

Some pages of this thesis may have been removed for copyright restrictions.

If you have discovered material in AURA which is unlawful e.g. breaches copyright, (either yours or that of a third party) or any other law, including but not limited to those relating to patent, trademark, confidentiality, data protection, obscenity, defamation, libel, then please read our [Takedown Policy](#) and [contact the service](#) immediately

**PRECISE ORBIT DETERMINATION AND ANALYSIS FROM
SATELLITE ALTIMETRY AND LASER RANGING
(Application of SEASAT data to atmospheric density evaluation)**

DEREK ANTHONY ROTHWELL

Doctor of Philosophy

THE UNIVERSITY OF ASTON IN BIRMINGHAM

December 1989

This copy of the thesis has been supplied on condition that anyone who consults it is understood to recognise that its copyright rests with its author and that no quotation from the thesis and no information derived from it may be published without the author's prior, written consent.

**PRECISE ORBIT DETERMINATION AND ANALYSIS FROM
SATELLITE ALTIMETRY AND LASER RANGING
(Application of SEASAT data to atmospheric density evaluation)**

DEREK ANTHONY ROTHWELL

Doctor of Philosophy

THE UNIVERSITY OF ASTON IN BIRMINGHAM

December 1989

This copy of the thesis has been supplied on condition that anyone who consults it is understood to recognise that its copyright rests with its author and that no quotation from the thesis and no information derived from it may be published without the author's prior, written consent.

THE UNIVERSITY OF ASTON IN BIRMINGHAM

PRECISE ORBIT DETERMINATION AND ANALYSIS FROM
SATELLITE ALTIMETRY AND LASER RANGING

(Application of SEASAT data to atmospheric density evaluation)

DEREK ANTHONY ROTHWELL

Doctor of Philosophy

December 1989

Thesis Summary

For optimum utilization of satellite-borne instrumentation, it is necessary to know precisely the orbital position of the spacecraft. The aim of this thesis is therefore two-fold – firstly to derive precise orbits with particular emphasis placed on the altimetric satellite SEASAT and secondly, to utilize the precise orbits, to improve upon atmospheric density determinations for satellite drag modelling purposes.

Part one of the thesis, on precise orbit determinations, is particularly concerned with the tracking data – satellite laser ranging, altimetry and crossover height differences – and how this data can be used to analyse errors in the orbit, the geoid and sea-surface topography. The outcome of this analysis is the determination of a low degree and order model for sea surface topography.

Part two, on the other hand, mainly concentrates on using the laser data to analyse and improve upon current atmospheric density models. In particular, the modelling of density changes associated with geomagnetic disturbances comes under scrutiny in this section. By introducing persistence modelling of a geomagnetic event and solving for certain geomagnetic parameters, a new density model is derived which performs significantly better than the state-of-the-art models over periods of severe geomagnetic storms at SEASAT heights. This is independently verified by application of the derived model to STARLETTE orbit determinations.

Keywords and Phrases

- Precise Orbit Determination
- Altimetry and Crossovers
- Geomagnetic Activity Modelling
- Satellite Laser Ranging
- Atmospheric Density Determination

Acknowledgements

I would like to express my gratitude to the following establishments and people :-

POL Bidston for supplying the SEASAT altimeter data; Delft University for supplying the NASA 'area tables' for SEASAT; World Data Centre C1 at RAL for supplying the raw auroral electrojet data; the SERC for supplying the research grant; Philip Moore for his patient supervision, but more importantly, for employing me in the first instance and last but by no means least, Lynn Burton for making such a good job of typing this thesis.

I would also like to acknowledge the help I received from Dr. Philip Moore on Chapters 6, 7 and 10 of this thesis.

List of Contents

	Page
Thesis Summary	2
Acknowledgments	3
Contents	4
List of Tables	7
List of Figures	10
CHAPTER 1 INTRODUCTION	13
PART ONE	
CHAPTER 2 SEASAT	16
2.1 Mission Description	16
2.2 History Of Orbital Improvements For Seasat	21
CHAPTER 3 SOFTWARE AND ITS DEVELOPMENT	23
3.1 The SATAN Software Package And Its Modifications	23
3.2 Force Model And Parameters	24
3.3 Least Squares And The Orbital Differential Correction Procedure	29
3.4 Multiple Drag Coefficients	33
3.5 Area Tables	37
CHAPTER 4 ALTIMETRY	44
4.1 Altimeter Data	44
4.2 Definitions	44
4.3 Altimetry As Tracking Data	46
4.4 Supplementing Sparse Laser Orbits With Altimetry	52
CHAPTER 5 CROSSOVERS	59
5.1 Formulation Of The Crossovers From Altimetry	59
5.2 Crossovers As Observational Data	61
5.3 Crossovers And Sparse Laser Orbits	63
5.4 Crossover Weighting Strategy	71
5.5 A Note On The Derivation Of The Crossovers	72

CHAPTER 6	RADIAL ORBIT ERROR DUE TO THE GRAVITY FIELD	73
6.1	The Disturbing Potential	73
6.2	Linear Radial Perturbations	74
6.3	Radial Orbit Error At A Crossover Point	85
CHAPTER 7	ERRORS ASSOCIATED WITH ALTIMETRY AND CROSSOVERS	86
7.1	The RMS Error Of Fit	86
7.2	Altimetry	87
7.3	Crossovers	93
7.4	Time Tag, Offset And Once and Twice Per Revolution Errors	97
CHAPTER 8	SEA SURFACE TOPOGRAPHY	102
8.1	Mathematical Formulation	103
8.2	Numerical Results	107
8.3	Discussion Of Results	108
PART TWO		
CHAPTER 9	DENSITY	117
9.1	The Atmosphere	118
9.2	Number Density	119
9.3	Solar Activity	121
9.4	Diurnal Variation	122
9.5	Geomagnetic Activity	122
CHAPTER 10	A COMPARISON OF ATMOSPHERIC DENSITY MODELS	124
10.1	Orbits Chosen For Analysis	124
10.2	Orbits Derived Relative to CIRA 72	125
10.3	Orbits Derived Relative to JS84	128
10.4	Modifications to CIRA 72 and JS84	134
10.5	Derivation Of The Partial Derivatives For Geomagnetic Modelling Parameters	136

10.6	Preliminary Results	141
10.7	MSIS Type Models	145
10.8	Discussion	147
CHAPTER 11	DENSITY DETERMINATION	149
11.1	Atmospheric Densities From Multiple Drag Coefficients	149
11.2	Relative Effective Densities	152
11.3	The Effect of Gravity Field And SRP Errors On The Density Values	162
11.4	Density Profiles	165
CHAPTER 12	NEW DENSITY MODELLING TECHNIQUES	172
12.1	Summation Techniques Applied to CIRA 72 and JS84	173
12.2	The Auroral Electroject, AE	175
12.3	Recovery Of Geomagnetic Modelling Coefficients	186
12.4	Further Computations Using JHA_1B_1	198
12.5	A Note On The Use Of The NASA 'Area-Tables' For Drag	213
12.6	Discussion	215
CHAPTER 13	CONCLUSIONS AND RECOMMENDATIONS	218
13.1	Conclusions	218
13.2	Recommendations For Further Work	221
REFERENCES		222
APPENDICES		
Appendix 1	Definitions Of Orbital Elements and Geometry	227
Appendix 2	Maxima And Minima For Altimeter Errors	230
Appendix 3	Helmert-Wolf Blocking	233

List of Tables

		Page
2.1	Characteristics of SEASAT laser tracking stations.	19
2.2	SEASAT characteristics.	21
3.1	Comparison of the laser residual rms and recovered C_R values for the six day arc spanning MJD 43728 to MJD 43734 for three forms of the drag parameter.	34
3.2	Comparison of recovered daily drag coefficients for the six day arc spanning MJD 43728 to MJD 43734 both with and without the NASA 'area tables' for SEASAT.	42
3.3	Comparison of the radial, along-track and cross-track components of position for the orbits of Table 3.2.	42
4.1	Laser data average for MJD 43728 to MJD 43734.	51
4.2	Orbital differences between orbits computed using 10 passes of Arequipa laser data supplemented with altimetry and the reference orbit.	53
5.1	Orbital comparisons for MJD 43770 to MJD 43776.	64
5.2	Orbital comparisons for MJD 43776 to MJD 43782.	66
5.3	Orbital comparisons for MJD 43770 to MJD 43776.	67
5.4	Orbital comparisons for MJD 43776 to MJD 43782.	72
7.1	Crossover residuals for MJD 43764 to MJD 43770.	94
7.2	Crossover residuals for MJD 43764 to MJD 43770.	95
7.3	Crossover residuals for MJD 43764 to MJD 43770.	96
7.4	Resulting time tag error, offset and once and twice per revolution terms for altimetry and crossovers for the arc MJD 43716 to MJD 43722.	100
8.1	Arcs used in the Helmert-Wolf Blocking solution for a sea-surface topography model.	107
8.2	Recovered coefficients for a 10×10 sea-surface topography model as derived from five SEASAT arcs.	115
8.3	Recovered coefficients for a 6×6 sea-surface topography model determined using five SEASAT arcs.	116
9.1	Orbital results for the arc MJD 43770 to MJD 43776 using the analytic and numeric versions of CIRA 72.	120
9.2	Radial, along-track and cross-track differences between the analytic and numeric versions of CIRA 72 for the arc of Table 9.1.	120
10.1	Orbital arcs used for density model comparisons.	125
10.2	Orbital results relative to CIRA 72 and single C_D .	126

10.3	Orbital results relative to CIRA 72 and linear C_D .	126
10.4	Orbital results relative to CIRA 72 and multiple C_D 's.	127
10.5	Orbital results relative to JS84 and single C_D .	133
10.6	Orbital results relative to JS84 and linear C_D .	133
10.7	Orbital results relative to JS84 and multiple C_D 's.	134
10.8	Solution of certain parameters in JS84 from MJD 43774 to MJD 43783 with drag coefficient model as described.	142
10.9	Orbital results relative to JS84 with $c = 4.2d^{-1}$ and single C_D .	143
10.10	Orbital results relative to JS84 using a value of infinity for c and two values for τ , τ_{84} and τ_{77} .	144
10.11	Orbital results relative to MSIS-83 and a single C_D .	146
11.1	Recovered drag coefficients and modelled effective densities for the 13 day arc spanning September 19 to October 2, 1978.	154
11.2	Observed and modelled relative densities for the 13 day arc as derived from four atmospheric models and equation (11.14).	154
11.3	Recovered drag coefficients and modelled effective densities for the 14 day arc spanning July 27 to August 10, 1978.	159
11.4	Observed and modelled relative effective densities as derived from Table 11.3 upon using equation (11.14).	159
11.5	Recovered drag coefficients for orbits with gravity field and SRP errors, using CIRA 72 and the NASA 'area tables'.	167
11.6	Observed densities from Table 11.5 and equation (11.14).	167
12.1	Orbital results relative to CIRA 72 using the summation formula of equation (12.1).	174
12.2	As for Table 12.1 but using JS84.	174
12.3	Orbital results relative to CIRA 72, $\hat{A}E$ index and summation formula (12.1).	182
12.4	Orbital results relative to CIRA 72 using the summation formula of equation (12.1) and the $\hat{A}E$ index with $A_1 = 36.14K$ and $B_1 = 0.054K$.	190
12.5	Orbital results relative to CIRA 72 using $\hat{A}E$ index and estimated values of 34.81K and 0.071K for A_1 and B_1 , respectively.	191
12.6	Orbital results relative to CIRA 72 with K_p index, summation formula equation (12.1) and estimated values of 38K and 0.031K for A_1 and B_1 , respectively.	196

12.7	Orbital results relative to JS84 with K_p index, summation formula equation (12.1) and estimated values of 87.07K, 24.86m, 0.00105, 0.338 and 0.023 for A'_1 , Z_1 , E_1 , A_2 and A_3 , respectively.	196
12.8	Orbital results for MJD 43776 to MJD 43782 using multiple drag coefficients as described in the text.	199
12.9	Orbital results using CIRA 72 and JHA_1B_1 for three 'independent' SEASAT arcs.	205
12.10	Orbital rms results for 17 STARLETTE arcs.	209
12.11	Orbital results relative to CIRA 72 using the summation formula of equation (12.1) when solving for a single drag coefficient in conjunction with the GEM-T1 gravity field and the corrected NASA 'area tables' for SEASAT.	214
12.12	As for Table 12.11 but using JS84.	214

List of Figures

		Page
2.1	SEASAT in-flight configuration.	17
2.2	Geographic distribution of SEASAT laser sites with 20° elevation cut-off.	20
3.1	Third Body Attraction.	27
3.2	Laser Range Measurement.	32
3.3	Orbital comparison for an arc computed both with and without the NASA 'area tables' for SEASAT when utilizing multiple C_D 's.	43
4.1	Altimetry.	45
4.2	Altimeter Height.	47
4.3	Orbital comparison of an arc computed with laser data only and laser data supplemented with $2m\sigma$ altimetry sampled at 30 second intervals.	54
4.4	Orbital comparison of an arc computed with laser data only and laser data supplemented with $0.5m\sigma$ altimetry sampled at 30 second intervals.	55
4.5	Laser Sites.	57
4.6	Altitude Variation for SEASAT.	58
5.1	Crossing-Arc Point.	59
5.2	Orbital comparison of the reference ephemeris of MJD 43770 to MJD 43776 versus the orbit computed using Arequipa laser data minus the last pass.	68
5.3	Orbital comparison of the reference ephemeris of MJD 43770 to MJD 43776 versus the orbit computed using Arequipa laser data minus the last pass supplemented with $2m\sigma$ altimetry.	69
5.4	Orbital comparison of the reference ephemeris of MJD 43770 to MJD 43776 versus the orbit computed using Arequipa laser data minus the last pass supplemented with $1.25m\sigma$ crossover data.	70
6.1	Spectral analysis of the radial orbit differences between ephemerides computed using the GEM-T1 and PGS-S3 gravity fields for the period MJD 43770 to MJD 43776.	82
6.2	Orbital comparison of the ephemerides computed using the GEM-T1 and PGS-S3 gravity fields for the period MJD 43770 to MJD 43776.	83
6.3	Spectral analysis of the radial orbit differences between ephemerides computed using the GEM-T1 and PGS-S3 gravity fields and the same state vector for MJD 43770 to MJD 43776.	84
6.4	Projection of Satellite ground track onto Earth's surface.	85

7.1	Spectral analysis of the altimeter residuals for MJD 43770 to MJD 43776.	90
7.2	Spectral analysis of the altimeter residuals for MJD 43770 to MJD 43776.	91
7.3	Spectral analysis of the altimeter residuals for MJD 43770 to MJD 43776.	92
8.1	Sea Surface Topography.	102
8.2	Contour plot of 6×6 sea surface topography model relative to the GEM-T1 derived 'mean' geoid as determined using five SEASAT arcs.	112
8.3	Contour plot of the 10×10 sea surface topography model as derived by Marsh et al.	113
8.4	Contour plot of the 6×6 sea surface topography model as derived by Engelis.	114
9.1	The Atmosphere.	118
10.1	Values of geomagnetic indices K_p and K'_p for the arcs of Table 10.1.	131
10.2	Recovered drag coefficients from CIRA 72 and K_p index for the 13 day arc MJD 43770 to MJD 43783.	132
11.1	Modelled density profiles for MJD 43770 to MJD 43783.	155
11.2	Observed density profiles for MJD 43770 to MJD 43783.	156
11.3	Modelled density profiles for MJD 43716 to MJD 43730.	160
11.4	Observed density profiles for MJD 43716 to MJD 43730.	161
11.5	Observed density profiles for MJD 43770 to MJD 43783.	168
11.6	Observed density profiles for MJD 43716 to MJD 43730.	169
11.7	Solar flux, $F_{10.7}$, and geomagnetic planetary index, K_p , for MJD 43770 to MJD 43783.	170
11.8	Solar flux, $F_{10.7}$, and geomagnetic planetary index, K_p , for MJD 43716 to MJD 43730.	171
12.1	Plots of K_p and AE indices for the period MJD 43722 to MJD 43796.	177
12.2	AE'_{t_c} index for the values (a) 1 and (b) 6 hours for t_c .	179
12.2	AE'_{t_c} index for the values (c) 12 and (d) 24 hours for t_c .	180
12.3	Geomagnetic planetary index, K_p , versus AE'_{12} index showing least squares fit.	184
12.4	K_p and AE'_{12} indices for the period MJD 43770 to MJD 43776.	185
12.5	Observed density profiles for the period MJD 43770 to MJD 43783.	201
12.6	Modelled density profiles for the period MJD 43770 to MJD 43783.	202

12.7	Observed density profiles for the period MJD 43716 to MJD 43730.	203
12.8	Modelled density profiles for the period MJD 43716 to MJD 43730.	204
12.9	Geomagnetic planetary index, K_p , for MJD 43805 to MJD 43810.	207
12.10	Geomagnetic planetary index, K_p , for MJD 45965 to MJD 46043.	210
12.11	Geomagnetic planetary index, K_p , for MJD 43467 to MJD 43473.	211
12.12	Geomagnetic planetary index, K_p , for MJD 45814 to MJD 45819.	212
A.1	Orbital ellipse.	227
A.2	Orientation of orbital ellipse in space.	228
A.3	Maxima and minima for altimeter errors.	230

CHAPTER 1

INTRODUCTION

Precise orbit determination is a pre-requisite for the useful application of satellite data to such diverse phenomena as space geodesy, oceanography and atmospheric density evaluation. Improvements in precise orbital determination are associated both with improved modelling techniques of the orbital perturbations and the availability of high quality tracking data, the latter often being the stimulus for the former. The motivation behind this thesis is thus twofold. Firstly, part one concentrates on the derivation of precise orbits from the inclusion of altimetry as tracking data whilst part two details improvements in atmospheric density modelling. Throughout, the satellite utilized for this study is SEASAT, being the best available source of altimetry and laser tracking data.

In detail, part one concentrates on the derivation of precise orbits using SEASAT data, with particular emphasis placed on altimetry, both in normal mode and as crossover height differences. In normal form, altimeter height measurements are contaminated by geoid uncertainties and are thus an inaccurate type of tracking data. Crossovers however, do not contain this geoid error, since it is the same on both tracks. This establishes crossover height differences as a more accurate form of tracking data with crossover residuals providing a good representation of global radial ephemeris error. To process, utilize and analyse both altimeter and crossover data, the existing software has been greatly modified and expanded. The data processing stage is described in chapter 3, together with other software modifications such as the implementation of multiple drag coefficients, various atmospheric density models and the NASA 'area tables' for SEASAT. The usefulness of the two types of altimetry in tracking data studies is investigated by analysis of orbits computed with both the full network of available laser range data and also a sparse amount. Results of this work are presented in chapters 4 and 5. Analysis of the altimeter and crossover residuals leads to information on the type of errors within the orbit, the geoid and the sea

surface topography, once the radial orbit error due to the gravity field has been separated. The mathematics necessary for this separation is developed in chapter 6 and the solution for once and twice per revolution errors, a constant altimeter range offset and an altimeter time tag bias is detailed in chapter 7. Chapter 8 reveals how altimetry can be used to determine a low degree and order model for sea surface topography, concluding part one of the thesis.

Part two is concerned with the crux of the research, namely that of using precise orbits to analyse and determine atmospheric densities at SEASAT heights. Densities are determined by analysing the variation within the recovered drag coefficients from long-arc orbits. By producing modelled and observed density profiles from this density determination work, it is possible to predict where a good orbital fit using a single drag scale factor will occur and hence gain insight into the applicability of certain density models.

Reliable along-track information, as supplied by the laser data, is a necessity for the drag coefficients to be well determined. At the outset of this research project, it was anticipated that altimetry would play an important role in this aspect, hence one of the reasons for its implementation into the software. However, analysis has shown that for adequate laser coverage, the supplementation of orbits with altimetry does not significantly affect the solution, especially in the along-track direction. In consideration of the extra computing time required to process altimetry, it was decided that orbits used in the subsequent density analyses should be computed using laser range data only.

Results of the density analyses and determinations can be found from chapter 9 onwards, wherein current state-of-the-art atmospheric models have been compared and found deficient in their representation of density changes associated with geomagnetic activity. In an attempt to rectify this problem, new variants of the geomagnetic models are derived using several different techniques. The uses of a smoothed geomagnetic planetary index, K_p' and a new geomagnetic index based on raw auroral electrojet data, the modelling of persistence of a geomagnetic event and

the derivation of coefficients within certain geomagnetic models using a combination of data from several SEASAT arcs, are all investigated. This results in the derivation of a new density model called $JH A_1 B_1$ which proves very successful in representing density changes associated with severe geomagnetic storms. Its validity is independently assessed by employing it in orbit determinations of STARLETTE.

It is anticipated and indeed hoped, that the work in this thesis, particularly in part two, will prove useful in improving the modelling of future non-altimetric and altimetric satellites such as ERS-1, thus enabling full use of the onboard instruments for their designated purposes.

CHAPTER 2

SEASAT

§2.1 Mission Description

The SEASAT satellite, launched on June 28, 1978 was a proof-of-concept mission to show that the monitoring of oceanographic phenomena and features could be achieved from space. During its operational lifetime of 104 days, six hours and 52 minutes [1], SEASAT collected an unprecedented amount of global data representing various oceanographic and atmospheric phenomena. The onboard equipment included a Synthetic Aperture Radar (SAR) to image the ocean surface, a Microwave Scatterometer System to measure surface wind speed and direction, a Scanning Multichannel Microwave Radiometer (SMMR) to measure sea surface temperature and atmospheric water content, a Radar Altimeter to measure significant wave height and the altitude of the spacecraft above the instantaneous sea level and a Visual and Infrared Radiometer to measure sea surface and cloud top temperatures. Also on board were an S-band Transponder, a TRANET/Geoceiver doppler beacon and a laser retroreflector array, all to assist in the tracking of the spacecraft. Figure 2.1 depicts the in-flight configuration of the satellite.

Of particular interest to the oceanographic community is the altimeter data, but to utilize it most effectively to model the marine geoid and dynamic ocean topography to decimetre accuracy, it is necessary to know the radial component of the spacecraft's position to a similar accuracy. Attempts to achieve this high level of orbital precision were based on data from a global network of high quality tracking stations which included Unified S-Band (USB), TRANET/Geoceiver doppler and laser stations.

Figure 2.1 : Seasat in-flight configuration.



The decimetre level of radial accuracy has not, as yet, been attained due mainly to errors in the modelling of the Earth's gravity field, solar radiation pressure (SRP) and atmospheric drag forces. However, the data collected from SEASAT has helped greatly in improving the models of the gravity field [2, 3, 4] and, as explained in the introduction, the second part of this thesis is concerned with using the SEASAT laser data to improve on the current atmospheric density models.

A list of the laser tracking stations together with their locations and assigned accuracies can be found in Table 2.1 [5]. Also listed in the table are the number of passes and observations obtained from each station although it should be noted, in view of their poor quality, certain stations were not used in any of the orbital determinations described subsequently. These included Helwan, San Fernando, Wettzell and Grasse. In addition, the data from Orroral had to be corrected for a range and time-dependent range bias for dates occurring prior to September 16 (MJD 43767, MJD being the modified Julian date) [5]. Figure 2.2 shows the observability circles for the laser sites as applied to SEASAT at a nominal height of 800km, with cut-off elevation for the laser ranges set at 20°. The diagram clearly shows the limited geographic distribution of the laser tracking data.

Table 2.1: Characteristics of SEASAT laser tracking stations

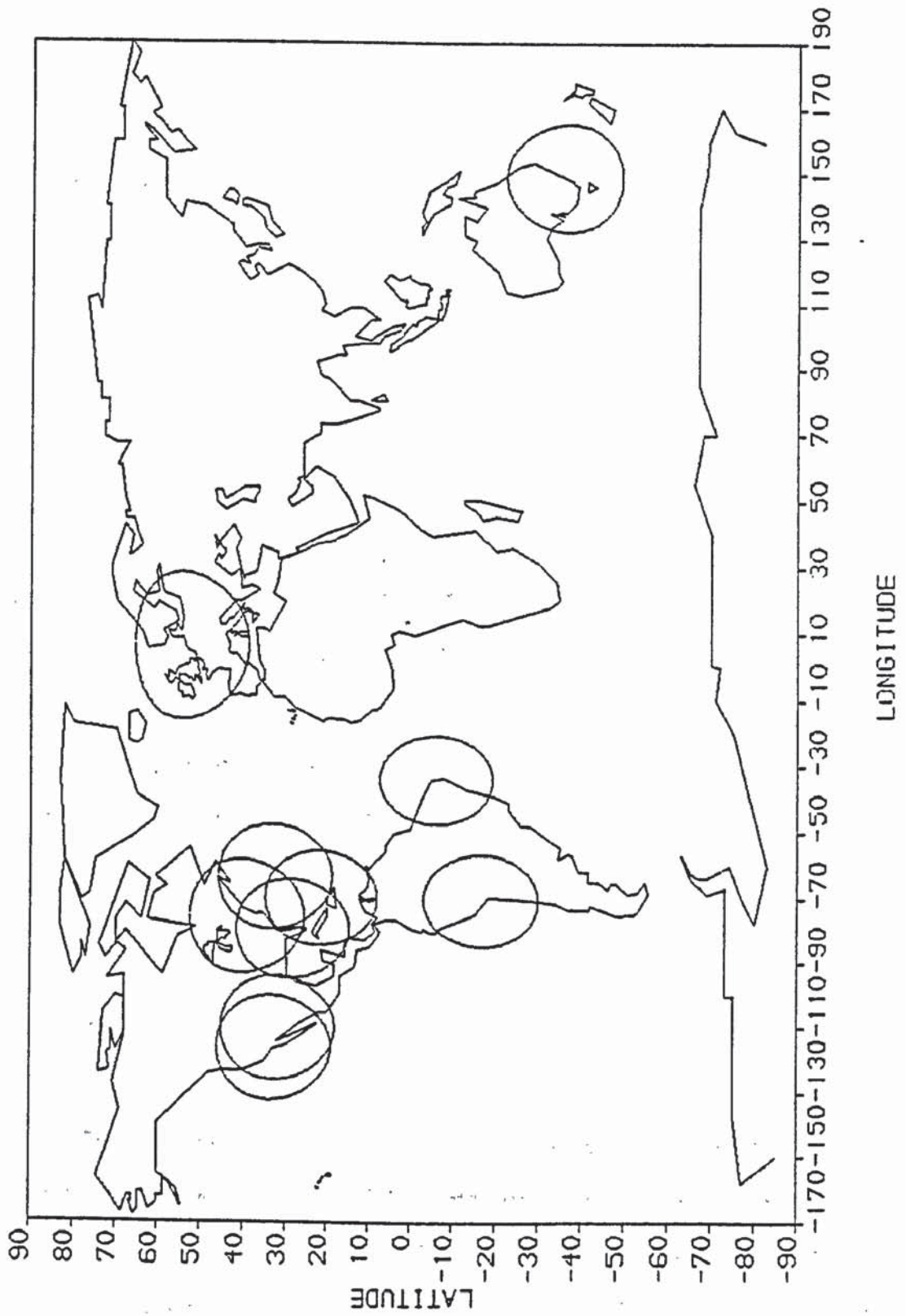
<u>Station</u>	<u>Location</u>	<u>Latitude</u> (deg)	<u>Longitude</u> (deg)	<u>Passes</u>	<u>Observations</u>	<u>Accuracy range</u> (cm)	<u>Assigned</u> σ (m)	<u>Weight, ω</u> **
7062	Otay Mountain, Calif.	32.60	243.16	120	20,965	≤ 10	0.15	44.44
7063	Greenbelt, Maryland	39.02	283.17	27	3,565	≤ 10	0.15	44.44
7067	Bermuda Island	32.35	295.34	72	5,828	≤ 10	0.15	44.44
7068	Grand Turk Island	21.46	288.87	44	4,679	≤ 10	0.15	44.44
7069	Patrick AFB, Florida	28.23	279.39	83	11,969	≤ 10	0.15	44.44
7801	Helwan, Egypt †			10	244	10-100	0.70	2.04
7804	San Fernando, Spain †			7	249	10-100	0.70	2.04
7833	Kootwijk, Netherlands	52.18	5.81	58	1,218	10-100	0.70	2.04
7834	Wetzell, W. Germany †			7	830	10-100	0.70	2.04
7842	Grasse, France †			9	297	10-100	0.70	2.04
7907	Arequipa, Peru	-16.47	288.51	119	5,152	50-100	0.50	4.00
7921	Mt. Hopkins, Arizona	31.68	249.12	28	627	50-100	0.70	2.04
7929	Natal, Brazil	-5.93	324.84	13	304	50-100	0.70	2.04
7943	Orroral, Australia	-35.62	148.95	36	1,125	50-100	0.70	2.04

† These stations were not used in any of the orbit determinations due to poor quality data

* See reference [1]

** The weight applies to the value given to each observational data set in the orbital correction procedure and is equal to $1/\sigma^2$, σ being the assigned standard deviation of the observations in metres.

Figure 2.2 : Geographic distribution of SEASAT laser sites with 20° elevation cut-off.



The orbits of SEASAT can be characterized by two distinct repeat periods plus an interim period. The launch orbit had a nominal 17-day closure at 1.67 sub-satellite track spacing whilst the final orbit, achieved on September 10 (MJD 43761) after various manoeuvres initiated on August 15 (MJD 43735), almost exactly repeated every three days [6]. Approximate orbital elements for the SEASAT trajectory, together with details of the satellite itself, are presented in Table 2.2 [7].

Table 2.2: SEASAT characteristics

$a \sim 7163\text{km}$	A	25.31m^2
$e \sim 0.001$	m	2195.0kg (August 15)
$i \sim 108^\circ.0$	A/m	$1.14 \times 10^{-2} \text{m}^2/\text{kg}$
$\dot{M} \sim 5153^\circ.3/\text{day}$	Shape	cylindrical with appendages

In Table 2.2, a is the semi-major axis of the orbital ellipse of eccentricity, e ; i the inclination of the orbital plane relative to the equatorial plane and \dot{M} the rate of change of the mean anomaly. (Full definitions, together with geometrical interpretation of all the orbital elements can be found in Appendix 1.) A is the average (constant) cross-sectional area of the spacecraft and m its mass on August 15, 1978. Note that the mass decreases slightly throughout the lifetime of the spacecraft due to fuel expenditure.

§2.2 History Of Orbital Improvements For SEASAT

One of the major advances in orbital improvements over the last few years has arisen from improved modelling of the Earth's gravity field. As mentioned in section 2.1, SEASAT data has helped considerably in this progress, from the tailored preliminary gravity solutions, PGS-S3 [2] and PGS-S4 [2], up to the state-of-the-art general purpose model GEM-T1 [3], (with subsequent versions GEM-T2 and GEM-T3 expected to be published in the near future). Radial rms accuracies of

SEASAT with PGS-S3 are of the order of 1.2m [3] compared with 50cm for GEM-T1 [3] and 30cm for GEM-T3 [4], approaching the required 10cm precision for optimum altimetric utilization. (Projected orbital accuracies of GEM-T3 applied to TOPEX trajectories show radial rms values of 15cm [4].) In conjunction with these gravity field improvements are substantial improvements in the long wavelength geoid, as expected since the latter is an equipotential surface of the gravity field supplemented with the rotational potential.

Other modelling improvements have not been so dramatic, particularly the determination of atmospheric densities for satellite drag purposes. This problem is addressed further from chapter 9 onwards.

The original model for the cross-sectional area, A , of SEASAT consisted of the constant value listed in Table 2.2 and the unrealistic assumption that the satellite could be approximated by a sphere. This approximation was employed in the drag and solar radiation pressure (SRP) force models but proved inadequate, especially for SRP. Hence, NASA commissioned the derivation of variable area models for both the drag and solar radiation pressure forces. These are given in tabular form and are subsequently referred to as the NASA 'area tables' [8] when utilized in orbit determinations. They are described in more detail in section 3.5.

CHAPTER 3

SOFTWARE AND ITS DEVELOPMENT

The software employed at Aston University for the orbit determinations used throughout this thesis is described in this chapter. Section 3.1 briefly outlines the main software modifications undertaken as part of this study, whilst subsequent sections reveal mathematical detail about the force modelling, the least squares differential correction procedure, multiple drag coefficients and the NASA 'area tables' for SEASAT [8].

§3.1 The SATAN Software Package And Its Modifications

The SATAN (SATellite ANalysis) software package [9] is a series of FORTRAN programs for analysing the orbits of satellites of low eccentricity. In its original form, SATAN generates an orbit by numerically integrating the equations of motion using an eighth-order Gauss-Jackson method [10]. The integration step length is constant with a value of 30 seconds being used throughout this thesis. By fitting the generated orbit to laser range observations using a least squares differential correction procedure, it was possible in the original form to solve for a state vector at epoch, a multiplicative factor, C_R , for solar reflectivity, a scale factor, C_D , for air-drag, a dragrate, \dot{C}_D , and certain other coefficients such as laser station coordinates and earth rotation parameters. The programs were written in such a way as to facilitate modifications, several of which have been undertaken as part of this study. These include modifications to air-drag, solar radiation pressure and the use of altimetry for tracking purposes. A preliminary study of sea-surface topography was also performed.

Air-drag, as computed in subroutine DRAG, has been modified to use and solve – for multiple drag coefficients since the extra degrees of freedom introduced to

the system by such a model, greatly improves the orbital fit. The subroutine has also been updated to accept a number of different atmospheric density models including CIRA 72 [11], JS84 [12], MSIS-1/2 [13,14], MSIS-83 [15] and DTM [16]. In two of these models, CIRA 72 and JS84, it is possible to estimate certain coefficients within the geomagnetic activity component. The details of this can be found from chapter 9 onwards. The incorporation of the NASA 'area tables' for SEASAT [8] for air-drag and normalized solar radiation pressure accelerations has also been achieved.

Altimetry has been introduced as tracking data, both in its normal form and as crossover height differences, the processing of each being described in [17]. Various software has been written for its analysis, for example the orbit correction program has been modified to solve for certain errors in the altimeter data including once- and twice-per-revolution terms, a time tag bias and a constant offset. In addition, programs have been developed to recover the spectral frequencies of the altimeter residuals and the sea surface topography, the latter by analysing data accumulated from several SEASAT arcs. As an integral part of the sea surface topography analysis any altimeter offset is estimated.

The force model and differential correction procedure incorporated into the original SATAN suite is now described (sections 3.2 and 3.3) with the modifications to the drag and solar radiation pressure models described in sections 3.4 and 3.5.

§3.2 Force Model And Parameters

The orbit generation program involves integration of the satellite's equations of motion using an eighth-order Gauss-Jackson numerical integrator [10]. These equations can be written succinctly as

$$\ddot{\mathbf{x}} = \mathbf{F}(\mathbf{x}, \dot{\mathbf{x}}, \mathbf{B}) \quad (3.1)$$

where \underline{x} is the position vector of the satellite at time t , $\dot{\underline{x}}$ and $\ddot{\underline{x}}$, the corresponding velocity and acceleration vectors respectively, whilst \underline{B} is the vector of all initial parameters within the accelerating force, \underline{E} . For instance, \underline{B} will consist, amongst others, of the initial state vector, gravity field coefficients, drag coefficient(s) and a solar reflectivity coefficient, C_R . In SATAN, the accelerating force, \underline{E} , models the gravitational attraction of the Earth, Sun, Moon, Venus, Mars, Jupiter and Saturn; earth tides; atmospheric drag and solar radiation pressure, both direct and earth reflected. Parameters and constants within each of these force models are governed according to the Merit Standards [18].

Reference Systems

The numerical integration is performed in an inertial reference frame based on the position of the equatorial plane and vernal equinox on Jan. 0.0 in the year 2000, simply referred to as J2000. However, the calculation of the acceleration due to the Earth's gravity field is most conveniently done in a reference frame fixed within the earth defined by the Greenwich Meridian and the true of date equatorial plane.

Transformation from J2000 to the true of date equator and equinox is performed by accounting for the effects of precession of the earth's spin axis about the pole of the ecliptic and the superimposed periodic motion known as nutation. This introduces two rotation matrices, P for precession and N for nutation. In addition, transformations from this true-of-date frame to the earth-fixed frame requires accounting for sidereal time and polar motion. This introduces a third rotation matrix, S . Hence, if \underline{x}_T is the earth fixed position vector and \underline{x}_{J2000} is the vector in J2000, then

$$\underline{x}_T = S \cdot N \cdot P \cdot \underline{x}_{J2000} \quad (3.2)$$

For a fuller explanation of the S , N and P rotation matrices, see [19].

At every step of the numerical integration, the position of the satellite is transformed, using equation (3.2), to the earth-fixed reference frame and the

acceleration of the gravity field is calculated. The acceleration is then transformed to the J2000 frame for the numerical integration step.

Earth Gravity

The acceleration due to the gravitational attraction of the Earth at an external point, \underline{x} , is expressed as the gradient of a potential V , where

$$V = \frac{GM_E}{r} \left(1 - \sum_{n=2}^{\infty} J_n \left(\frac{R_E}{r} \right)^n P_n(\sin \phi) + \sum_{\ell=2}^{\infty} \sum_{m=1}^{\ell} \left(\frac{R_E}{r} \right)^{\ell} P_{\ell m}(\sin \phi) [C_{\ell m} \cos m\lambda + S_{\ell m} \sin m\lambda] \right) \quad (3.3)$$

wherein G is the universal gravitational constant; M_E the mass of the earth of radius R_E ; r the radial distance of the point \underline{x} , the position of the satellite from the centre of the earth; ϕ the geocentric latitude of this point; λ its geocentric longitude; J_n the zonal harmonic coefficients of degree n ; $C_{\ell m}$ and $S_{\ell m}$ the tesseral harmonic coefficients of degree ℓ and order m , respectively and $P_n(\cdot)$ and $P_{\ell m}(\cdot)$ the Legendre and associated Legendre polynomials. For a derivation and more detailed explanation of equation (3.3) see Theory of Satellite Geodesy by Kaula [20].

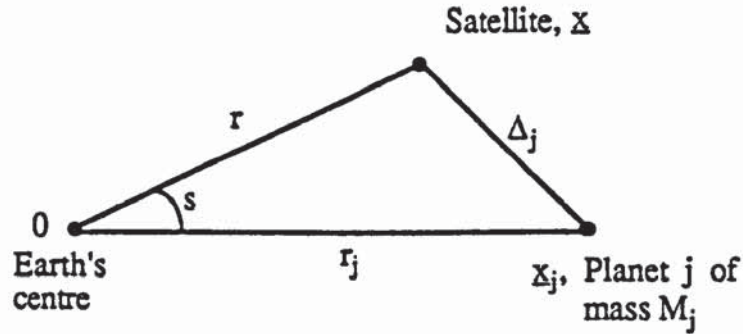
Third Body Attraction

Third body attraction is calculated for the Sun, Moon, Venus, Mars, Jupiter and Saturn. Referring to Figure 3.1 the accelerating force, $\ddot{\underline{x}}_{TB}$, at the point \underline{x} is given by [21]

$$\ddot{\underline{x}}_{TB} = \sum_j GM_j \left\{ \frac{\underline{x}_j - \underline{x}}{\Delta_j^3} - \frac{\underline{x}_j}{r_j^3} \right\} \quad (3.4)$$

where $r = |\underline{x}|$, $r_j = |\underline{x}_j|$ and $\Delta_j = |\underline{x} - \underline{x}_j|$. M_j represents the mass of the j^{th} body with the summation being taken over all those bodies just mentioned.

Figure 3.1: Third Body Attraction



Solid Earth And Ocean Tides

Time dependent tidal accelerations are caused by the lunar and solar gravitational forces acting on different parts of the rotating earth. These effects are supplemented by the effects of the orbit of the moon about the earth and the earth about the sun. For a rigid earth, the frequency independent tidal potential, ΔU_2 , due to the moon and sun is given by [22]

$$\Delta U_2(r) = \sum_j \frac{GM_j}{r_j^3} \frac{R_E^5}{r^3} k_2 \left(\frac{3}{2} \cos^2 S - \frac{1}{2} \right) \quad (3.5)$$

with notation as defined previously and by Figure 3.1. In equation (3.5), k_2 is the second degree Love number [23] and M_j represents either the mass of the moon or sun. The induced tidal acceleration (frequency independent) is found by taking the gradient of ΔU_2 . Frequency dependent solid earth tides (diurnal and semi-diurnal) are modelled as variations in the standard potential coefficients C_{2m} and S_{2m} using the Wahr model as given in the Merit Standards [18].

Ocean tides in SATAN, are modelled according to Schwiderski's model as presented in the Merit Standards [18].

Atmospheric Drag

The acceleration, \ddot{x}_D , due to the density of the atmosphere is modelled by assuming that drag can be expressed according to the classical equation from aerodynamics, namely

$$\ddot{\mathbf{x}}_D = -\frac{1}{2} \left(\frac{A}{m} \right) C_D \rho \mathbf{v}_r \mathbf{v}_r \quad (3.6)$$

where (A/m) is the cross-sectional area-to-mass ratio; C_D a scaling factor, called the drag coefficient; ρ the atmospheric density; \mathbf{v}_r the velocity of the spacecraft relative to the ambient atmosphere and $v_r = |\mathbf{v}_r|$. The density, ρ , is calculated from a static density model specified prior to orbit computation (see chapter 9 onwards).

Solar Radiation Pressure (SRP)

The acceleration due to direct SRP, $\ddot{\mathbf{x}}'_{SRP}$, is modelled by [24]

$$\ddot{\mathbf{x}}'_{SRP} = -\nu C_R \left(\frac{A}{m} \right) P \frac{AU^2}{|\mathbf{x} - \mathbf{x}_{SUN}|^2} \hat{\mathbf{x}}_S \quad (3.7)$$

where ν is the eclipse factor (which equals zero if the satellite is in the umbra, one if it is in total sunlight with a smoothing function to account for the transition between the two, i.e. when the satellite is in the penumbra); C_R is the solar reflectivity coefficient to account for the reflectivity characteristics of the spacecraft (normally taking a value of between 1.0 and 2.0); (A/m) the cross-sectional area-to-mass ratio; P the force per unit area exerted at the Earth by the Sun when its geocentric distance is one astronomical unit (AU) in km; \mathbf{x} the position of the satellite; \mathbf{x}_{SUN} the position of the sun and $\hat{\mathbf{x}}_S$ a unit vector from the satellite to the sun, all in the geocentric reference frame, J2000.

Earth reflected and infrared (IR) radiation are modelled by [25]

$$d\ddot{\mathbf{x}}_{SRP} = - \left\{ C_R \gamma P \cos \theta + P_{IR}/c \right\} \cos \alpha \left(\frac{A}{m} \right) \frac{dA}{\pi d^2} \mathbf{e}_d \quad (3.8)$$

where γ is the albedo (proportion of direct radiation which is reflected from the earth) of the surface element, dA ; θ the angle between the surface normal and the sun; P_{IR} the emitted infrared flux of the surface element; α the angle between the surface element's normal and the satellite; c the velocity of light; d the distance of the

$$\ddot{\mathbf{x}}_D = -\frac{1}{2} \left(\frac{A}{m} \right) C_D \rho \mathbf{v}_r \mathbf{v}_r \quad (3.6)$$

where (A/m) is the cross-sectional area-to-mass ratio; C_D a scaling factor, called the drag coefficient; ρ the atmospheric density; \mathbf{v}_r the velocity of the spacecraft relative to the ambient atmosphere and $v_r = |\mathbf{v}_r|$. The density, ρ , is calculated from a static density model specified prior to orbit computation (see chapter 9 onwards).

Solar Radiation Pressure (SRP)

The acceleration due to direct SRP, $\ddot{\mathbf{x}}'_{SRP}$, is modelled by [24]

$$\ddot{\mathbf{x}}'_{SRP} = -\nu C_R \left(\frac{A}{m} \right) P \frac{AU^2}{|\mathbf{x} - \mathbf{x}_{SUN}|^2} \hat{\mathbf{x}}_S \quad (3.7)$$

where ν is the eclipse factor (which equals zero if the satellite is in the umbra, one if it is in total sunlight with a smoothing function to account for the transition between the two, i.e. when the satellite is in the penumbra); C_R is the solar reflectivity coefficient to account for the reflectivity characteristics of the spacecraft (normally taking a value of between 1.0 and 2.0); (A/m) the cross-sectional area-to-mass ratio; P the force per unit area exerted at the Earth by the Sun when its geocentric distance is one astronomical unit (AU) in km; \mathbf{x} the position of the satellite; \mathbf{x}_{SUN} the position of the sun and $\hat{\mathbf{x}}_S$ a unit vector from the satellite to the sun, all in the geocentric reference frame, J2000.

Earth reflected and infrared (IR) radiation are modelled by [25]

$$d\ddot{\mathbf{x}}_{SRP} = - \left\{ C_R \gamma P \cos \theta + P_{IR}/c \right\} \cos \alpha \left(\frac{A}{m} \right) \frac{dA}{\pi d^2} \mathbf{e}_d \quad (3.8)$$

where γ is the albedo (proportion of direct radiation which is reflected from the earth) of the surface element, dA ; θ the angle between the surface normal and the sun; P_{IR} the emitted infrared flux of the surface element; α the angle between the surface element's normal and the satellite; c the velocity of light; d the distance of the

satellite from the surface element and e_d a unit vector from the satellite to the surface element. If $\theta > \pi/2$ then $\gamma = 0$. The total earth reflected and IR radiation should be calculated by integrating equation (3.8) over the surface of the earth visible to the satellite. This integration is in fact approximated by summing over 13 surface elements as in [25].

Total Force

The total accelerating force, \underline{E} , is the sum of all these terms and is given by

$$\ddot{\underline{x}} \equiv \underline{E}(\underline{x}, \dot{\underline{x}}, \underline{B}) = \underline{\nabla}V + \ddot{\underline{x}}_{TB} + \underline{\nabla}\Delta U_2 + \ddot{\underline{x}}_D + \ddot{\underline{x}}_{SRP} + \sum_{i=1}^{13} d\ddot{\underline{x}}_{SRP}^i \quad (3.9)$$

where $d\ddot{\underline{x}}_{SRP}^i$ is the accelerating force due to earth reflected and IR radiation for the i^{th} surface element. In equation (3.9) it is assumed that the potential coefficients of V have been corrected for frequency dependent solid earth tides and ocean tides.

§3.3 Least Squares And The Orbital Differential Correction Procedure

The orbital parameters and other coefficients estimated in the data reduction process are calculated using a least squares differential correction procedure. This is now described.

Assume there are N observations, d_i^o , of a type of distance measurement to a satellite, each with an 'a priori' standard deviation, σ_i . These measurements might comprise laser range observations, altimeter heights or crossover height differences for example. At the time of each observation, t_i , SATAN calculates a corresponding distance d_i^c , dependent on m initial conditions. This is written

$$d_i^c = d_i^c(\underline{P}), \quad i = 1, \dots, N \quad (3.10)$$

where \underline{P} is an m -vector with components p_j , $j = 1, \dots, m$. \underline{P} will include the state vector at epoch, the drag coefficient(s), the solar radiation pressure coefficient and all

other orbital or geodetic parameters, some of which may be estimated in the reduction procedure.

Assume \underline{P}^* is the value of \underline{P} sought in the data reduction procedure but that $\hat{\underline{P}}$ is the best available approximation prior to solution. Then

$$\underline{P}^* = \hat{\underline{P}} + \Delta\underline{P} \quad (3.11)$$

for some vector of corrections, $\Delta\underline{P}$. It is this vector which is being estimated.

The most accurate orbit is obtained when the computed distances d_i^c , most closely resemble the observed values d_i^o in the least-squares sense. This is equivalent to minimizing the function I given by

$$I = \sum_{i=1}^N \left[d_i^o - d_i^c(\underline{P}^*) \right]^2 \omega_i \quad (3.12)$$

where ω_i is a weight assigned to each observation depending on its 'a priori' accuracy. The value chosen is

$$\omega_i = \frac{1}{\sigma_i^2}. \quad (3.13)$$

I is minimized with respect to all the components of \underline{P} for which corrections are sought. This gives m' equations of the form

$$\frac{\partial I}{\partial p_j} = -2 \sum_{i=1}^N \omega_i \left(d_i^o - d_i^c(\underline{P}^*) \right) \frac{\partial d_i^c}{\partial p_j}(\underline{P}^*) \equiv 0 \quad (3.14)$$

for $j = 1, \dots, m'$ and $m' \leq m$. For brevity, $d_i^c(\underline{P}^*)$ is written as d_i^{*c} and $d_i^c(\hat{\underline{P}})$ as \hat{d}_i^c . Then, by Taylor's theorem and equation (3.11)

$$d_i^{*c} = \hat{d}_i^c + \Delta\underline{P} \cdot \tilde{\nabla} \hat{d}_i^c + 0(\Delta P^2) \quad (3.15)$$

wherein $\tilde{\nabla} \hat{d}_i^c$ refers to the m' -vector of partials $\partial \hat{d}_i^c / \partial p_j$, $j = 1, \dots, m'$. Also

$$\frac{\partial d_i^{*c}}{\partial p_j} = \frac{\partial \hat{d}_i^c}{\partial p_j} + 0(\Delta P). \quad (3.16)$$

Upon substituting (3.15) and (3.16) into (3.14)

$$\sum_{i=1}^N \omega_i \left(d_i^o - \hat{d}_i^c - \Delta P \cdot \tilde{\nabla} \hat{d}_i^c - 0(\Delta P^2) \right) \left(\frac{\partial \hat{d}_i^c}{\partial p_j} + 0(\Delta P) \right) = 0. \quad (3.17)$$

Assuming $(d_i^o - \hat{d}_i^c)$ is of the order $0(\Delta P)$, then to order $0(\Delta P)$ (3.17) can be

written

$$\sum_{i=1}^N \omega_i \Delta P \cdot \tilde{\nabla} \hat{d}_i^c \frac{\partial \hat{d}_i^c}{\partial p_j} = \sum_{i=1}^N \omega_i \left(d_i^o - \hat{d}_i^c \right) \frac{\partial \hat{d}_i^c}{\partial p_j} \quad (3.18)$$

for $j = 1, \dots, m'$. In matrix form this is

$$D \Delta P = \underline{b} \quad (3.19)$$

where D is the $m' \times m'$ matrix with elements $D_{kj} = \sum_{i=1}^N \omega_i \frac{\partial \hat{d}_i^c}{\partial p_k} \frac{\partial \hat{d}_i^c}{\partial p_j}$, ΔP is the

m' -vector of corrections and \underline{b} is the m' -vector with components $b_j = \sum_{i=1}^N \omega_i$

$(d_i^o - \hat{d}_i^c) \frac{\partial \hat{d}_i^c}{\partial p_j}$. Equation (3.19) represents the so called normal equations and has

a solution provided D is invertible. This turns out to be the case provided there are sufficient observations, since D is then a symmetric positive definite matrix.

In order to calculate D and \underline{b} in the programs, the partials $\partial \hat{d}_i^c / \partial p_j$ must be calculated for each observation time, t_i , together with \hat{d}_i^c itself. This is achieved using the eighth-order Gauss-Jackson numerical integrator [10] to derive both $\partial \hat{d}_i^c / \partial p_j$ and \hat{d}_i^c , assuming p_j is an orbital parameter, i.e. $p_j \in \underline{B}$. (If p_j is a

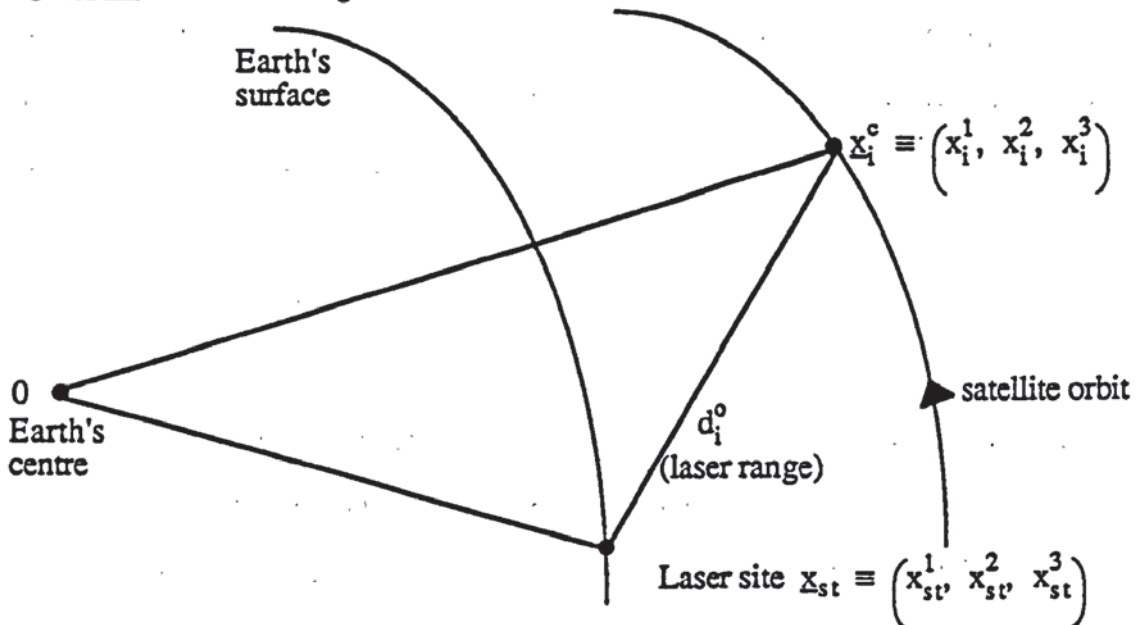
parameter that does not affect the orbital position, e.g. station coordinates, then $\partial \hat{d}_i^c / \partial p_j$ can be calculated directly from the definition of \hat{d}_i^c .)

The equations of motion have been expressed by equation (3.1). The solution of this at each observation time, t_i , gives the values \mathbf{x}_i^c and $\dot{\mathbf{x}}_i^c$. Using \mathbf{x}_i^c it is straightforward to calculate \hat{d}_i^c depending on the type of observation, d_i^o . For instance, if d_i^o is a laser range measurement then the one-way laser range \hat{d}_i^c is given by

$$\hat{d}_i^c = \sqrt{(x_i^1 - x_{st}^1)^2 + (x_i^2 - x_{st}^2)^2 + (x_i^3 - x_{st}^3)^2} \quad (3.20)$$

where $\mathbf{x}_i^c = (x_i^1, x_i^2, x_i^3)$ and $(x_{st}^1, x_{st}^2, x_{st}^3) \equiv \mathbf{x}_{st}$ give the coordinates of the laser site in J2000. (See Figure 3.2.) Note that \hat{d}_i^c could be calculated in the true of date reference frame since distances are invariant under rotation.

Figure 3.2 : Laser Range Measurement.



To calculate $\partial \hat{d}_i^c / \partial p_j$, for $p_j \in \underline{B}$, equation (3.1) must be differentiated with

respect to p_j . Hence

$$\frac{\partial \ddot{\mathbf{x}}}{\partial p_j} = \frac{\partial \underline{F}}{\partial \mathbf{x}} \frac{\partial \mathbf{x}}{\partial p_j} + \frac{\partial \underline{F}}{\partial \dot{\mathbf{x}}} \frac{\partial \dot{\mathbf{x}}}{\partial p_j} + \frac{\partial \underline{F}}{\partial p_j} \quad (3.21)$$

where $\partial E/\partial p_j$ are the explicit partial derivations. Since E is only weakly dependent on \dot{x} – it appears only in the drag force – the middle term of equation (3.21) can be omitted. Then, upon interchanging derivatives

$$\frac{d^2}{dt^2} \left(\frac{\partial x}{\partial p_j} \right) = \frac{\partial E}{\partial x} \cdot \frac{\partial x}{\partial p_j} + \frac{\partial E}{\partial p_j} \quad (3.22)$$

Equation (3.22) is a second order ordinary differential equation in $\partial x/\partial p_j$ and can be integrated using the Gauss–Jackson process to obtain $\partial x_i^c/\partial p_j$ at time, t_i . Again $\partial \hat{d}_i^c/\partial p_j$ can be obtained from these partials, depending on the type of observation.

For example, in the case of a laser range measurement, differentiating equation (3.20) yields

$$\frac{\partial \hat{d}_i^c}{\partial p_j} = \left\{ \left(x_i^1 - x_{st}^1 \right) \frac{\partial x_1^1}{\partial p_j} + \left(x_i^2 - x_{st}^2 \right) \frac{\partial x_1^2}{\partial p_j} + \left(x_i^3 - x_{st}^3 \right) \frac{\partial x_1^3}{\partial p_j} \right\} / \hat{d}_i^c \quad (3.23)$$

Similar calculations for the altimeter heights and crossover height differences can be found in the appropriate sections describing these forms of observations – chapter 4 for pure altimetry and chapter 5 for crossovers.

§3.4 Multiple Drag Coefficients

For long–arc analyses, typically a few days in length, large errors occur in the orbital solution of SEASAT when solving for either a single drag coefficient [6, 26] or a drag coefficient plus a dragrate [6]. Apparently, the current atmospheric density models are unable to cope with certain short–term variations in density such as those due to geomagnetic disturbances. The accuracies obtained when using a linear dragrate model are generally better than those obtained from the single coefficient model since the extra degree of freedom within the system helps to absorb some, though not all, of the along–track error. By introducing multiple drag coefficients to

the system, the number of degrees of freedom is increased, absorbing more of this error. This is a somewhat artificial means of absorbing unwanted along-track error, but can be justified by the improved orbital accuracies which are obtained. Table 3.1 shows the rms of fit to laser range observations, together with the recovered C_R values, for an arc computed using each of the three forms for the drag scale parameter.

Table 3.1: Comparison of the laser residual rms and recovered C_R values for the six day arc spanning MJD 43728 to MJD 43734 (August 8 to August 14, 1978). In each case, the orbit is relative to the GEM-T1 gravity field, the CIRA 72 atmospheric model and the NASA 'area tables' for SEASAT. Solution of each orbit required estimating for a state vector at epoch, a solar reflectivity coefficient, C_R , and the parameters within each of the drag models.

<u>Model For Drag Parameter</u>	<u>rms(m)</u>	<u>C_R</u>
constant drag (C_D)	2.40	0.93
linear dragrate (C_D, \dot{C}_D)	1.57	1.32
daily drag coefficients ($C_{D_i}, i = 1, \dots, 6$)	0.61	1.55

The orbit computed with the daily drag coefficients is regarded as the more acceptable, both in terms of the rms value and the recovered solar reflectivity factor, C_R . Numerous long-arc analyses, spanning the entire lifespan of SEASAT, have shown that the value of C_R is in the region 1.5 to 1.7, when utilizing a multiple drag coefficient model.

Software Description

The modifications to the software, to use and solve-for multiple drag coefficients, is now described.

The force model for air-drag is given by equation (3.6). Solving for the coefficient, C_D , as part of the orbital solution, results in absorption of some of the

errors in A , ρ and other along-track forces such as the gravity field and SRP. Hence C_D loses its physical significance, becoming a scaling factor for the inadequacies of the modelled along-track forces. By using multiple C_D 's more of this error can be absorbed, so improving the orbital fit.

The normal equations for the orbital solution are given by equation (3.19). The equation for the partials with respect to a single drag coefficient is therefore

$$\sum_{i=1}^N \omega_i (d_i^o - \hat{d}_i^c) \frac{\partial \hat{d}_i^c}{\partial C_D} = \sum_{i=1}^N \omega_i \left\{ \Delta P' \cdot \nabla' \hat{d}_i^c + \Delta C_D \frac{\partial \hat{d}_i^c}{\partial C_D} \right\} \frac{\partial \hat{d}_i^c}{\partial C_D} \quad (3.24)$$

where $\Delta P'$ is the vector of corrections to all parameters except C_D and $\nabla' \hat{d}_i^c$ is the vector of all partials except with respect to C_D .

However, if it is required to use and solve-for a number, $N_{DRAG} > 1$, of drag coefficients, C_{D_i} , $i = 1, \dots, N_{DRAG}$, each spanning a separate time interval of the arc length, this equation needs to be altered slightly.

A distance measurement, \hat{d}_{ij}^c , calculated at time t_i during the time spanned by C_{D_j} is dependent on the drag coefficient at this time plus all previous drag coefficients. For example :-

$$\left. \begin{aligned} \hat{d}_{i1}^c &= \hat{d}_{i1}^c (C_{D_1}), \\ \hat{d}_{i2}^c &= \hat{d}_{i2}^c (C_{D_1}, C_{D_2}), \\ \vdots & \\ \hat{d}_{ij}^c &= \hat{d}_{ij}^c (C_{D_1}, C_{D_2}, \dots, C_{D_j}), \\ \vdots & \\ \hat{d}_{iN_{DRAG}}^c &= \hat{d}_{iN_{DRAG}}^c (C_{D_1}, C_{D_2}, \dots, C_{D_{N_{DRAG}}}). \end{aligned} \right\} \quad (3.25)$$

Hence the drag coefficients are not strictly independent and if one is estimated, then all should be estimated. The notation for the partial derivatives is simplified by writing the drag coefficients in vector form. Thus

$$\left. \begin{aligned} \frac{\partial \hat{d}_{i1}^c}{\partial \underline{C}_D} &= \left(\frac{\partial \hat{d}_{i1}^c}{\partial C_{D_1}}, 0, \dots, 0 \right), \\ \frac{\partial \hat{d}_{i2}^c}{\partial \underline{C}_D} &= \left(\frac{\partial \hat{d}_{i2}^c}{\partial C_{D_1}}, \frac{\partial \hat{d}_{i2}^c}{\partial C_{D_2}}, 0, \dots, 0 \right), \\ &\vdots \\ \frac{\partial \hat{d}_{ij}^c}{\partial \underline{C}_D} &= \left(\frac{\partial \hat{d}_{ij}^c}{\partial C_{D_1}}, \frac{\partial \hat{d}_{ij}^c}{\partial C_{D_2}}, \dots, \frac{\partial \hat{d}_{ij}^c}{\partial C_{D_j}}, 0, \dots, 0 \right), \\ &\vdots \\ \frac{\partial \hat{d}_{iN_{DRAG}}^c}{\partial \underline{C}_D} &= \left(\frac{\partial \hat{d}_{iN_{DRAG}}^c}{\partial C_{D_1}}, \frac{\partial \hat{d}_{iN_{DRAG}}^c}{\partial C_{D_2}}, \dots, \frac{\partial \hat{d}_{iN_{DRAG}}^c}{\partial C_{D_{N_{DRAG}}}}, \right). \end{aligned} \right\} \quad (3.26)$$

Equations (3.26) can be written more succinctly as

$$\frac{\partial \hat{d}_i^c}{\partial \underline{C}_D} = \left(\frac{\partial \hat{d}_i^c}{\partial C_{D_1}}, \dots, \frac{\partial \hat{d}_i^c}{\partial C_{D_{N_{DRAG}}}} \right) \equiv \left(\frac{\partial \hat{d}_i^c}{\partial C_{D_j}} \right)_{j=1}^{N_{DRAG}} \quad (3.27)$$

where $\partial \hat{d}_i^c / \partial C_{D_j}$ is taken to be identically zero for all drag coefficients, C_{D_j} , after

which the observation occurs. Equation (3.24) then becomes

$$\sum_{i=1}^N \omega_i \left(d_i^o - \hat{d}_i^c \right) \frac{\partial \hat{d}_i^c}{\partial C_{D_j}} = \sum_{i=1}^N \omega_i \left(\Delta P' \cdot \underline{\nabla}' \hat{d}_i^c + \sum_{k=1}^{N_{DRAG}} \frac{\partial \hat{d}_i^c}{\partial C_{D_k}} \Delta C_{D_k} \right) \frac{\partial \hat{d}_i^c}{\partial C_{D_j}} \quad (3.28)$$

for $j = 1, \dots, N_{DRAG}$.

The above has been implemented into the software with time-intervals specified as input data. For convenience as much as anything, it is customary to use daily drag coefficients for SEASAT.

§3.5 Area Tables

As well as absorbing errors associated with density mismodelling, multiple drag coefficients can absorb errors due to the uncertainty in the spacecraft's cross-sectional area, A . The original SATAN package employs a spherical approximation for the cross-sectional area of SEASAT, in both the drag and the solar radiation pressure force models. However, close inspection of the in-flight configuration of SEASAT (Figure 2.1) shows this to be an over-simplification which could lead to large discrepancies between the modelled forces and the actual forces at any instant. The shape of SEASAT is basically cylindrical with appendages attached, the main ones being the solar panels with a surface area of 14.88m^2 and the SAR with a surface area of 28m^2 [27]. Since the satellite is stabilized, the body always points to the centre of the earth and so is perpendicular to the along-track direction. Hence, for air-drag purposes, this component of the satellite's cross-sectional area does not vary. The SAR is fixed relative to the body and points in the direction of motion, i.e. along-track, so the area of this component is also constant for drag purposes. However, the area presented by the solar panels in the direction of the velocity vector will vary because of their continuous rotation towards the sun. Hence, for drag purposes, the satellite area varies by about 25% throughout an orbital revolution, the average of which is pretty much the same from one day to the next. Consequently any error in the modelling of this area is virtually constant from one day to the next and scales the drag coefficients accordingly, not affecting their relative variation.

In the sun-satellite direction, the variation in cross-sectional area is more significant and is due to all three main spacecraft components. The area of the body and SAR in this direction, vary due to the satellite's orbital motion, whilst that of the

solar panels varies because they can only rotate about one axis. This limits the maximum area which can be presented to the sun at any particular instant. Variations of the spacecraft's area in the sun–satellite direction can cause large variations in the computed SRP force, very significant at SEASAT heights. In particular, this force can have a significant along–track component, any mismodelling of which will be absorbed by the drag coefficients. This can cause meaningless C_D values to be recovered, such as very small or even negative values.

To account for the variations in cross–sectional area, NASA commissioned the derivation of a set of tables for SEASAT [8], tabulating areas for drag and normalized accelerations for SRP at various viewing angles. These tables, which have been incorporated into the software to give a more realistic model for the satellite's cross–sectional area than the constant value assumed in the spherical satellite approximation, are now described.

The area tables have been derived in a coordinate system fixed within the satellite. This is the so called Body Coordinate Frame (BCF) and is given by three orthonormal vectors \hat{x}_{BCF} , \hat{y}_{BCF} and \hat{z}_{BCF} relative to the inertial reference system J2000. Specifically

$$\begin{aligned}\hat{z}_{BCF} &= -\dot{\mathbf{x}}(t)/|\dot{\mathbf{x}}(t)|, \\ \hat{y}_{BCF} &= (\hat{z}_{BCF} \times \mathbf{v}_u)/|\hat{z}_{BCF} \times \mathbf{v}_u|, \\ \hat{x}_{BCF} &= (\hat{y}_{BCF} \times \hat{z}_{BCF})/|\hat{y}_{BCF} \times \hat{z}_{BCF}|\end{aligned}$$

where $\mathbf{x}(t)$ is the satellite's position in J2000 at time t and \mathbf{v}_u is a unit vector in the direction of the satellite's velocity, $\dot{\mathbf{x}}(t)$, also at time t , i.e. $\mathbf{v}_u = \dot{\mathbf{x}}(t)/|\dot{\mathbf{x}}(t)|$.

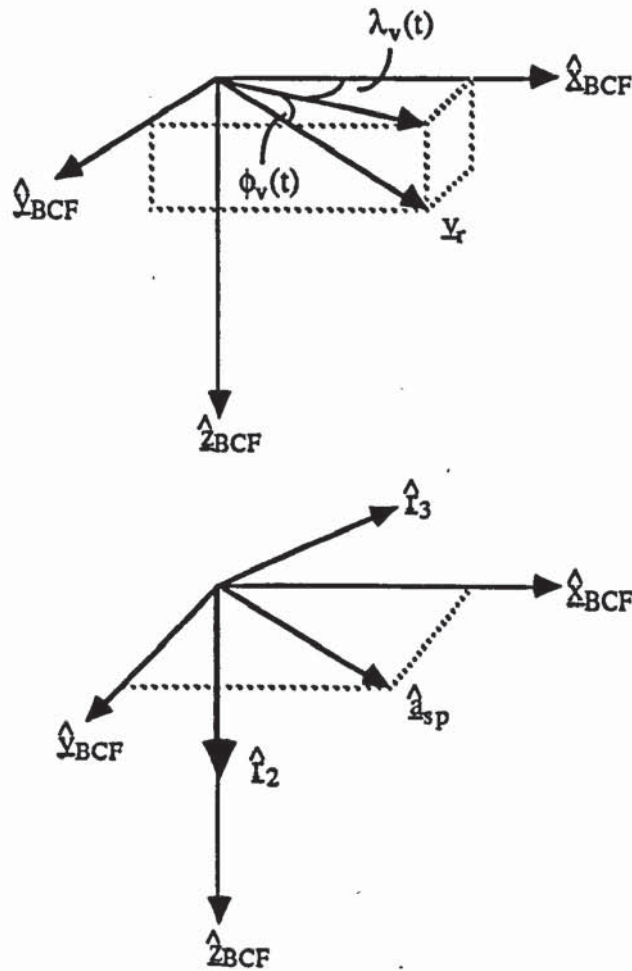
Computation of the area, A , for drag modelling at time t is performed by tri–linearly interpolating within the drag table for three different angles. The values of A are tabulated as a function of the latitude, ϕ_v , and longitude, λ_v , of the relative velocity vector, \mathbf{v}_r , in the J2000 system and also the right ascension, α_s , of the sun about the solar panel axis. These angles are given by

$$\phi_v(t) = \tan^{-1} \left[\frac{(\underline{v}_r \cdot \hat{\underline{z}}_{BCF})}{\sqrt{(\underline{v}_r \cdot \hat{\underline{x}}_{BCF})^2 + (\underline{v}_r \cdot \hat{\underline{y}}_{BCF})^2}} \right]$$

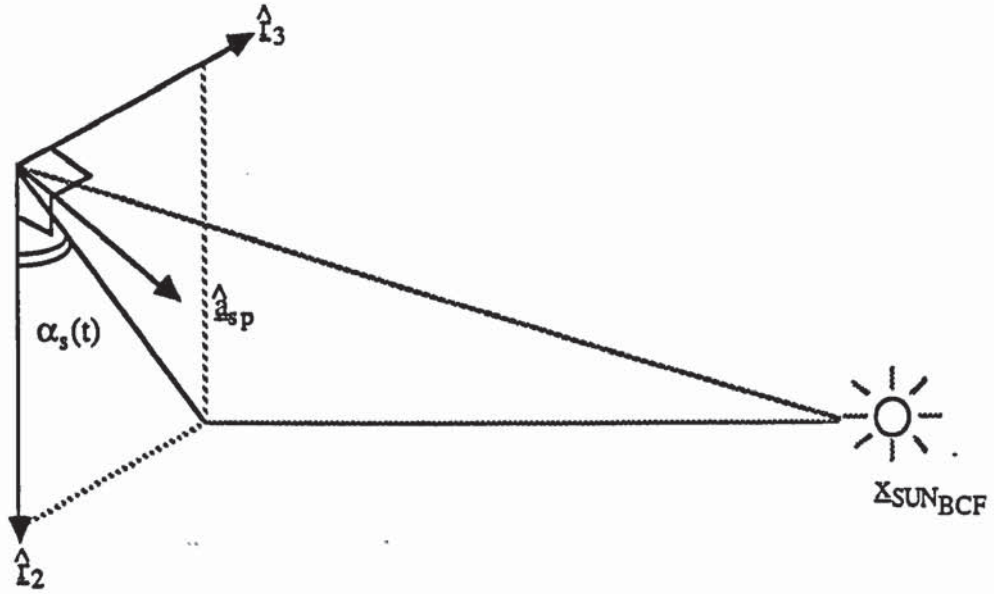
$$\lambda_v(t) = \tan^{-1} \left(\frac{\underline{v}_r \cdot \hat{\underline{y}}_{BCF}}{\underline{v}_r \cdot \hat{\underline{x}}_{BCF}} \right)$$

$$\alpha_s = \tan^{-1} \left(\frac{\hat{\underline{l}}_3 \cdot \underline{x}_{SUN_{BCF}}}{\hat{\underline{l}}_2 \cdot \underline{x}_{SUN_{BCF}}} \right)$$

where $\hat{\underline{l}}_3 = \hat{\underline{a}}_{sp} \times \hat{\underline{z}}_{BCF}$, $\hat{\underline{l}}_2 = \hat{\underline{l}}_3 \times \hat{\underline{a}}_{sp}$, $\hat{\underline{a}}_{sp}$ being the unit vector defining the direction of the solar panel rotation axis and $\underline{x}_{SUN_{BCF}}$ the position of the sun all in the BCF reference frame. Diagrammatically,



(Since for SEASAT, $\hat{\underline{a}}_{sp} = (x, y, 0)$ for $x, y \neq 0$).



For SRP modelling, the tables represent vectors of normalized accelerations in the BCF reference frame, written as $\Delta^* = (A_1^*, A_2^*, A_3^*)$. The acceleration $\ddot{\mathbf{x}}_{SRP}$, due to direct SRP is given by

$$\ddot{\mathbf{x}}_{SRP} = -\frac{\nu C_{RP}}{m} \frac{AU^2}{|\mathbf{x} - \mathbf{x}_{SUN}|^2} \frac{\Delta_{J2000}^*}{C_R^*} \quad (3.29)$$

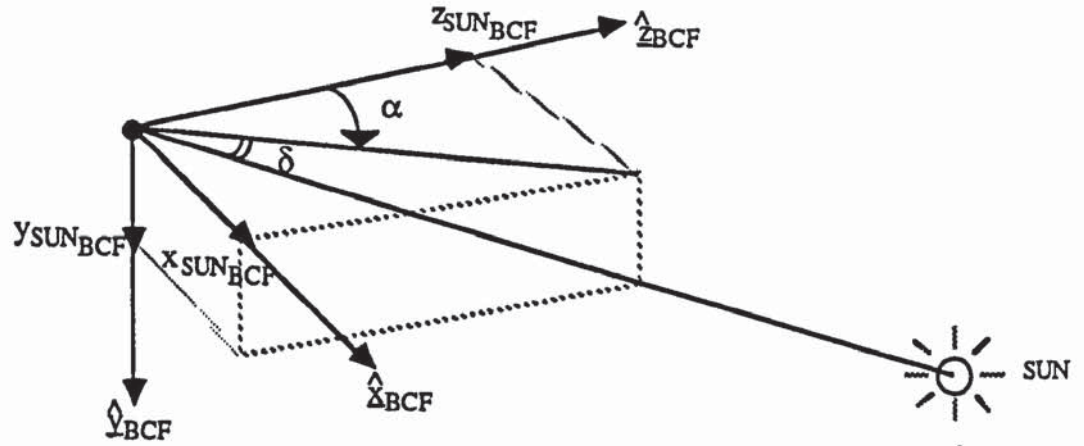
where C_R is the reflectivity coefficient being used, C_R^* is the effective reflectivity coefficient used in the derivation of the normalized accelerations, Δ_{J2000}^* is the normalized acceleration in J2000 and all other terms are as defined in equation (3.7). The values of A_i^* , $i = 1, 2, 3$ are tabulated for two angles, the right ascension, α , of the sun from the satellite and its declination, δ . These are defined to be

$$\alpha = \tan^{-1} \left(\frac{x_{SUN_BCF}}{z_{SUN_BCF}} \right) \quad 0 \leq \alpha < 360^\circ$$

$$\delta = \tan^{-1} \left(\frac{y_{SUN_BCF}}{\sqrt{(x_{SUN_BCF}^2 + z_{SUN_BCF}^2)}} \right) \quad -90^\circ \leq \delta \leq 90^\circ$$

where $\mathbf{x}_{SUN_BCF} = (x_{SUN_BCF}, y_{SUN_BCF}, z_{SUN_BCF})$.

Diagrammatically,



A bilinear interpolation is used to obtain the value of \hat{A}^* at the required time and position. This defines a vector in the BCF coordinate frame which needs to be rotated to J2000 to be used in equation(3.29), i.e.

$$\hat{A}_{J2000}^* = B \hat{A}^*$$

where B is the rotation matrix whose column vectors are \hat{x}_{BCF} , \hat{y}_{BCF} , \hat{z}_{BCF} .

By using the tables in orbit determinations it is assumed that mismodelling of the SRP force has been reduced, especially for the purposes of this study, in the along-track direction. Hence, variations in the recovered drag coefficients, when employing the area tables are not dominated by solar radiation, an important assumption for the work on density determinations described from chapter 9 onwards.

During initial testing of the area tables, the satellite was found to be fairly insensitive to the drag table areas with similar drag coefficients obtained when using either the drag area tables or a mean cross-sectional area. However, this is not the case for the normalized SRP accelerations which must be precisely derived for meaningful drag coefficients to be recovered.

The effect of the area tables is observed when computing an orbit both with and without them. Resulting drag coefficients for such an analysis are given in Table 3.2 together with the rms of fit to the laser data and the estimated SRP coefficient, C_R .

Table 3.2: Comparison of recovered daily drag coefficients for the six days arc spanning MJD 43728 to MJD 43734, both with and without the NASA 'area tables' for SEASAT. Both orbits are relative to the GEM-T1 gravity field and the CIRA 72 atmospheric model.

<u>Area model employed</u>	<u>rms(m)</u>	<u>C_R</u>	<u>No.Obs</u>	<u>C_{D1}</u>	<u>C_{D2}</u>	<u>C_{D3}</u>	<u>C_{D4}</u>	<u>C_{D5}</u>	<u>C_{D6}</u>
Spherical satellite	0.56	1.61	1488	0.85	1.63	1.40	0.47	1.72	1.57
NASA tables	0.61	1.55	1488	4.05	5.51	5.15	3.79	4.99	4.81

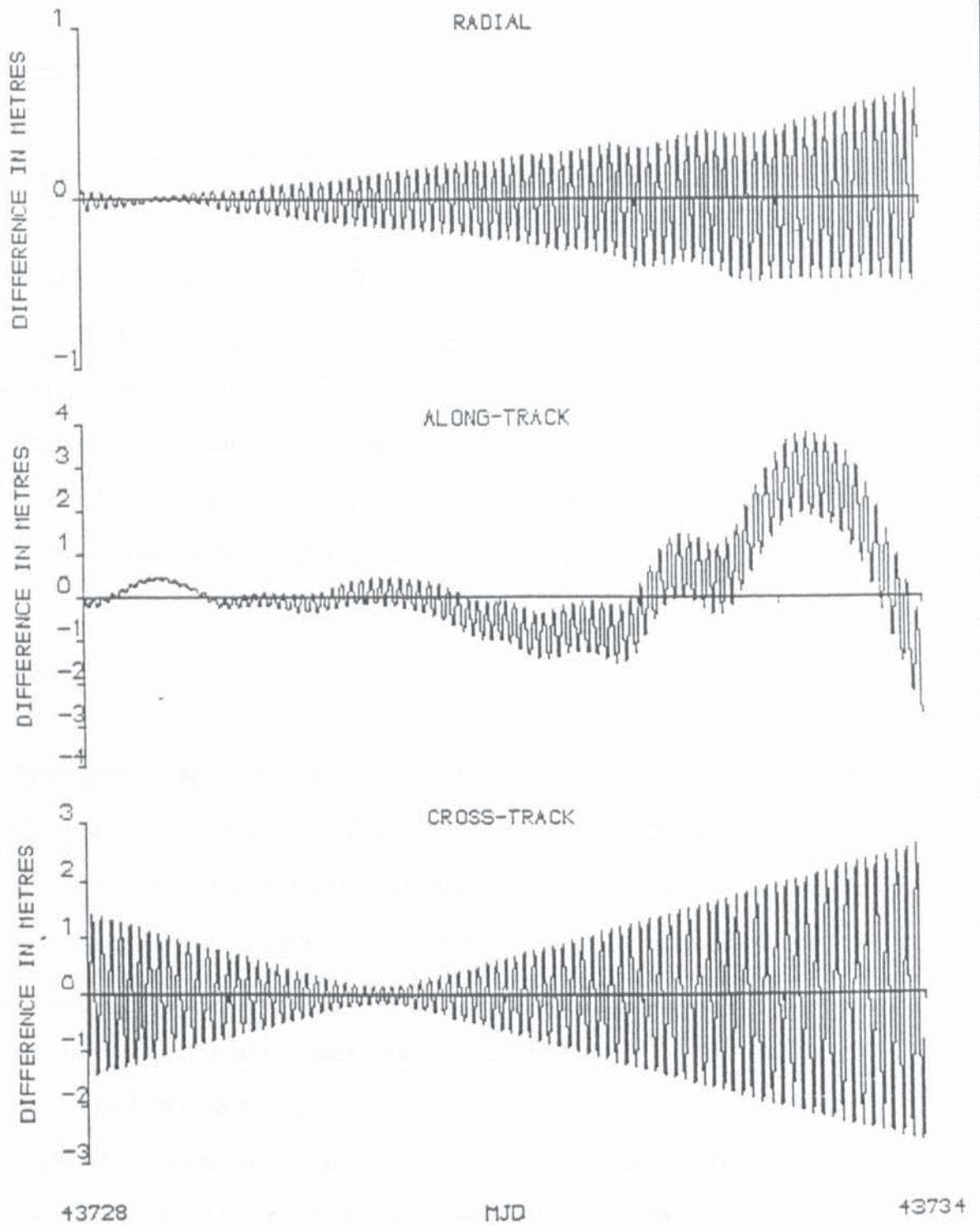
A remarkable similarity between the recovered C_R and rms values is noted for each of the models. This indicates little difference between the two orbits, a fact which is vindicated by a comparison of the radial, along-track and cross-track components of position for each ephemeris. Table 3.3 shows this comparison which is plotted in Figure 3.3.

Table 3.3: Comparison of the radial, along-track and cross-track components of position for the orbits of Table 3.2.

<u>Differences in metres(max/rms)</u>		
<u>Radial</u>	<u>Along-track</u>	<u>Cross-track</u>
0.64/0.21	3.76/1.10	2.64/0.95

As suggested earlier in the text, the drag coefficients have absorbed the along-track modelling errors to give orbits of a similar quality, with C_R being determined from the radial and cross-track components of SRP. The lower rms value of the spherical satellite model is not deemed significant. Of more importance is the variation within the recovered drag coefficients. Use of the area tables results in a variation by a factor of 1.5 whereas for the spherical satellite model, the variation is by a factor of 3.7. Also, according to Cook (1965) [28], a realistic value for C_D should be above 2.0 for a satellite which is basically cylindrical. In view of these observations, it was decided to adopt the NASA 'area tables' in all future orbital computations of SEASAT.

Figure 3.3 : Orbital comparison for an arc computed both with and without the NASA 'area tables' for SEASAT when utilizing multiple drag coefficients.



CHAPTER 4

ALTIMETRY

§4.1 Altimeter Data

The SEASAT altimeter data, spanning July 6, 1978 to October 9, 1978 (MJD 43695 to MJD 43790), was supplied by POL Bidston on three magnetic tapes called Geophysical Data Records (GDRs) [29]. These tapes were created by the Instrument Data Processing System at the Jet Propulsion Laboratory (JPL) in California, with the purpose of providing all necessary information for using altimetry as a radial observation of the satellite's orbit and/or to monitor various oceanographic phenomena. This chapter describes the processing necessary to obtain radial measurements and their subsequent use in SEASAT orbit determinations.

§4.2 Definitions

In the current study, the radial altimeter measurements are defined relative to the reference ellipsoid, an oblate spheroid of revolution whose surface approximates as closely as possible, that of the geoid, an equipotential surface of the Earth's gravitational field and centrifugal rotation. Intuitively, the geoid is the height that the mean sea level would attain if there were no ocean circulation phenomena, sea density variations or winds. In reality, there is a difference between the two and this is termed the sea surface topography.

Figure 4.1 depicts, in simple form, the concept of altimetry. To derive the satellite height above the reference ellipsoid, from the raw altimeter measurement, various corrections need to be added. These corrections, together with the raw measurement itself, are listed on the GDR tapes. The observed satellite height, h_1^o , at time t_1 is expressed by

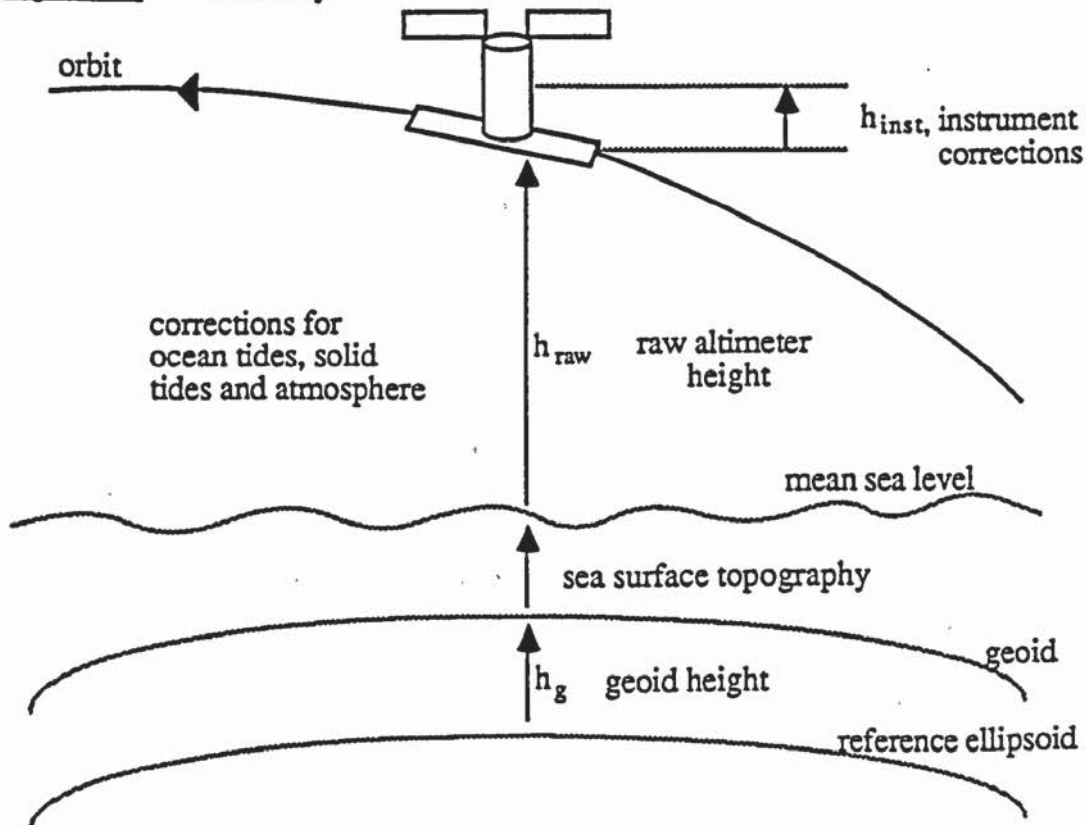
$$h_i^o = h_{\text{raw}} + h_g + h_{\text{bar}} + h_{\text{SETC}} + h_{\text{OETC}} + h_{\text{ionc}} + h_{\text{wet}} + h_{\text{dry}} + h_{\text{inst}} - 0.07h_{\frac{1}{3}} \quad (4.1)$$

where the terms on the right hand side of equation (4.1) are defined as follows:-

- h_{raw} : raw altimeter measurement above the instantaneous sea surface
- h_g : geoid height relative to the reference ellipsoid
- h_{bar} : barotropic correction
- h_{SETC} : solid earth tide correction
- h_{OETC} : (Schwiderski) ocean earth tide correction
- h_{ionc} : ionospheric delay correction
- h_{wet} : wet tropospheric correction
- h_{dry} : dry tropospheric correction
- h_{inst} : sum of corrections to account for the offset from the centre of gravity of the altimeter and any electronic delays
- $h_{\frac{1}{3}}$: significant wave height to accommodate sea state bias [30].

The geoid height, h_g , on the GDR tape is the so called GEM-10BD geoid based on the GEM-10B gravimetric geoid produced by Goddard Space Flight Centre [29].

Figure 4.1: Altimetry.



Close inspection of equation (4.1) reveals that there is no term to account for the sea surface topography. A mean sea surface height does exist on the GDR tapes, derived by James Marsh of Goddard Space Flight Centre (GSFC), using the NASA orbit from the 18 days of data spanning July 28, 1978 to August 14, 1978. Any geographically related error in the NASA orbit will however, propagate into these mean sea level heights and hence into the sea surface topography, values of which can be recovered by differencing the mean sea level and the geoid. Hence, it was decided not to use this correction term in the calculation of h_i^o and consequently, the altimeter residuals will contain an error component due to the omission of the sea surface topography. Analysis of the altimeter residuals can therefore lead to the determination of a model for sea surface topography. This is addressed in chapter 8.

The processing of equation (4.1) is performed using the FORTRAN program CONVERT, described in [17].

§4.3 Altimetry As Tracking Data

The radial information offered by the altimeter observations can be used to minimize errors in this component of the satellite's position. If the satellite's position, \mathbf{x}_i^c , is calculated at the time, t_i , of an altimeter observation, the height above the reference ellipsoid, h_i^c can be derived. Then the difference between h_i^o of equation (4.1) and h_i^c defines the altimeter residual, Δh , i.e. $\Delta h = h_i^o - h_i^c$. For consistency however, both values must be determined relative to the same reference ellipsoid. Since SATAN determines positions relative to the inertial frame J2000, the reference ellipsoid for the calculated position, h_i^c will be different to that for the observed position which is defined by the true of date equatorial plane and Greenwich Meridian. In order to calculate the altimeter residual therefore, h_i^c must be computed relative to this same ellipsoid. This is achieved by determining h_i^c from the true of date position, \mathbf{x}_i^t , where

$$\underline{x}_i^t = R \underline{x}_i^c \quad (4.2)$$

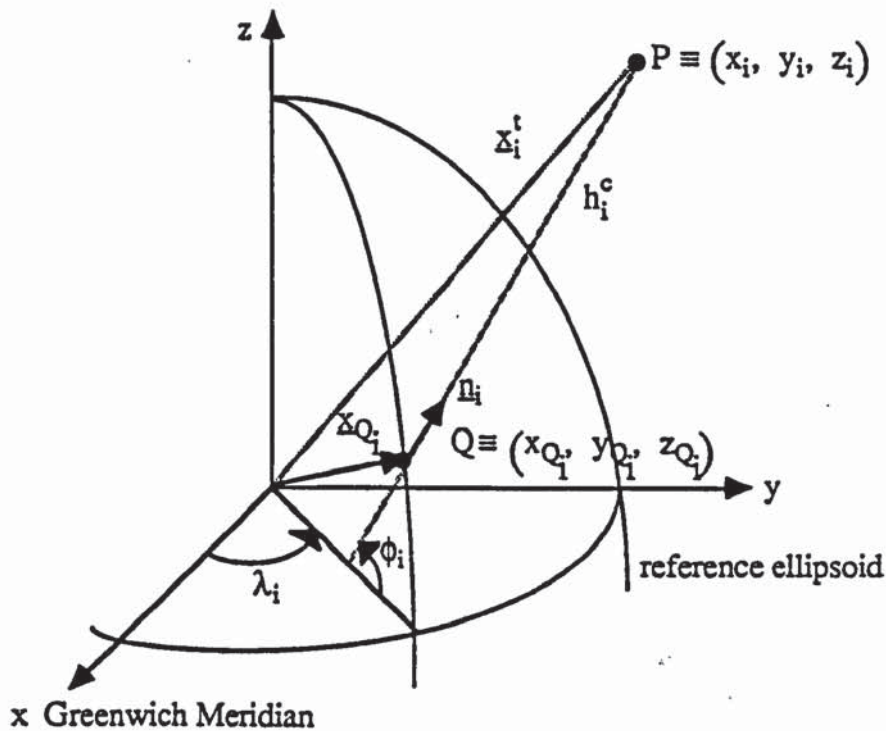
for the rotation matrix $R \equiv S.N.P.$ of equation (3.2), transforming J2000 coordinates to earth-fixed coordinates.

It should be noted here that such a transformation was not necessary on the laser range calculations since they are defined by vector differences which are invariant under rotation. For the altimeter height calculations, this does not hold, since the position of the reference ellipsoid varies under rotation.

The computed satellite height, h_i^c , is now derived from \underline{x}_i^t by referring to

Figure (4.2) [31].

Figure 4.2: Altimeter Height.



Assume the satellite is at point P , $(x_i, y_i, z_i) \equiv \underline{x}_i^t$, in the earth-fixed reference frame. It is desired to find the normal height, h_i^c , of P above the reference ellipsoid. Let Q be the point $(x_{Q_i}, y_{Q_i}, z_{Q_i})$, on this ellipsoid, obtained from the projection of P along the ellipsoid normal. Then from [31]

$$\underline{x}_{Q_i} \equiv \begin{pmatrix} x_{Q_i} \\ y_{Q_i} \\ z_{Q_i} \end{pmatrix} = N \begin{pmatrix} \cos \phi_i \cdot \cos \lambda_i \\ \cos \phi_i \cdot \sin \lambda_i \\ (1-e^2) \sin \phi_i \end{pmatrix} \quad (4.3)$$

wherein ϕ_i is the geodetic latitude, λ_i the geodetic longitude, e the eccentricity of the reference ellipsoid and N the radius of curvature in the prime vertical at (ϕ_i, λ_i) on the reference ellipsoid, given by

$$N = R_E / (\cos^2 \phi_i + (1 - e^2) \sin^2 \phi_i)^{\frac{1}{2}}. \quad (4.4)$$

In equation (4.4), R_E is the radius of the ellipsoid at the equator. From Figure (4.2)

$$\underline{x}_i^t = \underline{x}_{Q_i} + h_i^c \underline{n}_i \quad (4.5)$$

where \underline{n}_i is the unit normal at (ϕ_i, λ_i) on the ellipsoid, given by

$$\underline{n}_i = \begin{pmatrix} \cos \phi_i \cdot \cos \lambda_i \\ \cos \phi_i \cdot \sin \lambda_i \\ \sin \phi_i \end{pmatrix}. \quad (4.6)$$

Combining equations (4.3), (4.5) and (4.6)

$$\underline{x}_i^t \equiv \begin{pmatrix} x_i \\ y_i \\ z_i \end{pmatrix} = \begin{pmatrix} (N + h_i^c) \cos \phi_i \cos \lambda_i \\ (N + h_i^c) \cos \phi_i \sin \lambda_i \\ [(1 - e^2) N + h_i^c] \sin \phi_i \end{pmatrix}. \quad (4.7)$$

Using equation (4.7)

$$h_i^c = \frac{(x_i^2 + y_i^2)^{\frac{1}{2}}}{\cos \phi_i} - N \quad (4.8)$$

$$\phi_i = \tan^{-1} \left\{ \frac{z_i}{(x_i^2 + y_i^2)^{\frac{1}{2}}} \left(1 - \frac{e^2 N}{N + h_i^c} \right)^{-1} \right\} \quad (4.9)$$

$$\lambda_i = \tan^{-1} (y_i/x_i). \quad (4.10)$$

Equations (4.4), (4.8), (4.9) and (4.10) are solved iteratively, the procedure started by using the value of ϕ_i on the GDR tapes as initial input to the system.

The minimization of the altimeter residuals is performed by identifying h_i^o and h_i^c with d_i^o and \hat{d}_i^c , respectively, in section 3.3. Hence it is necessary to calculate the partial derivatives $\partial h_i^c / \partial p_j$ for each parameter, p_j , to be adjusted. Now

$$h_i^c = h_i^c(\mathbf{x}_i^t) \quad (4.11)$$

where $\mathbf{x}_i^t = \mathbf{x}_i^t(\mathbf{P})$ and \mathbf{P} contains the initial state vector, relative to J2000. From equations (4.11) and (4.2)

$$\frac{\partial h_i^c}{\partial p_j} = \nabla h_i^c \cdot \frac{\partial \mathbf{x}_i^t}{\partial p_j} \quad (4.12)$$

and
$$\frac{\partial \mathbf{x}_i^t}{\partial p_j} = \mathbf{R} \frac{\partial \mathbf{x}_i^f}{\partial p_j} \quad (4.13)$$

so that
$$\frac{\partial h_i^c}{\partial p_j} = \nabla h_i^c \cdot \mathbf{R} \frac{\partial \mathbf{x}_i^f}{\partial p_j}. \quad (4.14)$$

The partial derivatives $\partial \mathbf{x}_i^f / \partial p_j$ are determined as part of the orbit generation program, as is \mathbf{R} , so all that remains to be calculated is ∇h_i^c . From equations (4.4)

and (4.8)

$$h_i^c = \frac{(x_i^2 + y_i^2)^{\frac{1}{2}}}{\cos \phi_i} - R_E / (\cos^2 \phi_i + (1 - e^2) \sin^2 \phi_i)^{\frac{1}{2}}. \quad (4.15)$$

Dropping the i subscripts and differentiating with respect to x

$$\frac{\partial h^c}{\partial x} = \frac{x}{\cos \phi} \cdot \frac{1}{(x^2 + y^2)^{\frac{1}{2}}} + (x^2 + y^2)^{\frac{1}{2}} \frac{\sin \phi}{\cos^2 \phi} \frac{\partial \phi}{\partial x} - R_E e^2 F \frac{\partial \phi}{\partial x} \quad (4.16)$$

where
$$F = \frac{\sin \phi \cos \phi}{(1 - e^2 \sin^2 \phi)^{\frac{3}{2}}}.$$

Now
$$|F| = \left| \frac{\sin \phi \cos \phi}{(1 - e^2 \sin^2 \phi)^{\frac{3}{2}}} \right| \leq \frac{|\sin 2\phi|}{2|1 - e^2 \sin^2 \phi|^{\frac{3}{2}}} < \frac{(1 - e^2)^{-\frac{3}{2}}}{2}$$

therefore $|F| \approx \frac{1}{2} + O(e^2)$ and $R_E e^2 F \approx O(e^2)$. Therefore, the last term of equation (4.16) is small compared to the previous terms and is omitted. From equation (4.9)

$$\tan \phi = \frac{z}{(x^2 + y^2)^{\frac{1}{2}}} \left(1 - \frac{e^2 N}{N + h^c}\right)^{-1}. \quad (4.17)$$

Ignoring terms of order $O(e^2)$ and differentiating with respect to x yields

$$\frac{\partial \phi}{\partial x} \approx -\frac{zx}{(x^2 + y^2)^{\frac{1}{2}} r^2} \quad (4.18)$$

where $r^2 = x^2 + y^2 + z^2$. Substituting this into equation (4.16)

$$\frac{\partial h^c}{\partial x} \approx \frac{x}{\cos \phi} \left[\frac{1}{(x^2 + y^2)^{\frac{1}{2}}} - \frac{z \tan \phi}{r^2} \right] \quad (4.19)$$

and since h^c is symmetrical in x and y

$$\frac{\partial h^c}{\partial y} \approx \frac{y}{\cos \phi} \left[\frac{1}{(x^2 + y^2)^{\frac{1}{2}}} - \frac{z \tan \phi}{r^2} \right]. \quad (4.20)$$

Differentiating equation (4.15) with respect to z

$$\frac{\partial h^c}{\partial z} = (x^2 + y^2)^{\frac{1}{2}} \frac{\sin \phi}{\cos^2 \phi} \frac{\partial \phi}{\partial z} - R_E e^2 F \frac{\partial \phi}{\partial z} \quad (4.21)$$

which simplifies to

$$\frac{\partial h^c}{\partial z} \approx \sin \phi \quad (4.22)$$

upon ignoring terms of order $O(e^2)$. Equation (4.22) has been derived by solving for $\partial \phi / \partial z$ from equation (4.17) and substituting into equation (4.21).

Note that if a spherical earth approximation is adopted in determining the partial derivatives then equations (4.19) and (4.20) simplify to

$$\frac{\partial h^c}{\partial x} \approx \frac{x}{r} \quad (4.23)$$

and

$$\frac{\partial h^c}{\partial y} \approx \frac{y}{r}. \quad (4.24)$$

Having derived mathematically the altimeter residuals and partial derivatives and modified the software accordingly, altimetry can be used as tracking data in orbit determinations. It must however, be supplemented by laser range data. Orbits derived from altimetry alone, have little or no constraint in the along-track and cross-track directions causing the normal equations to be ill-conditioned and generally indeterminate.

Various experiments have been undertaken to test the usefulness of altimetry in laser orbits. Preliminary work involved supplementing orbits computed from the full network of laser tracking data over the periods being analysed. One such case was the six day arc spanning August 8, 1978 to August 14, 1978 (MJD 43728 to MJD 43734), with laser data coverage as listed in Table 4.1.

Table 4.1: Laser data coverage for MJD 43728 to MJD 43734.

<u>Station number</u>	<u>Number of passes</u>	<u>Number of observations accepted (3m rejection level)</u>	<u>Rms of fit to referenc orbit (m)</u>
7069	5	239	0.51
7062	10	414	0.30
7067	6	112	0.64
7907	12	465	1.07
7833	3	97	0.51
7929	1	12	1.08
7943	5	106	1.53

Total rms of fit to laser data for reference ephemeris = 0.50m.

In Table 4.1, the column headed 'rms of fit to reference orbit', refers to the accuracy of the observations at each laser site for the reference ephemeris, an orbit computed with all the laser data listed, when solving for a state vector at epoch, a solar reflectivity coefficient, C_R , and six daily drag coefficients. The gravity field employed was GEM-T1 and the atmospheric model, CIRA 72. Next, this reference orbit was supplemented with altimetry weighted with a standard deviation, σ , of 2m and sampled at a minimum of 30 second intervals. This had very little effect on the orbital solution, thus it was decided to increase the weight on the altimetry by applying an 'a priori' standard deviation of 0.5m. Both these ephemerides were compared radially, along-track and cross-track with the reference ephemeris, the results of which are plotted in Figures 4.3 and 4.4. Both figures confirm that the information altimetry contains in the along-track and cross-track directions is limited, whilst also showing that to affect the radial component, altimetry must be weighted unrealistically high. For a well determined laser orbit, the conclusion is that altimetry does not add much extra information to the solution. However, the small effect it does have, is investigated further in chapter 7.

In view of this and the computing time needed to process altimetry, there may seem little point in doing so, but the altimeter residuals have other uses apart from correcting orbital parameters. They can be used to analyse errors in the gravity field, geoid, orbit and sea surface topography, as well as determine the latter, as will be explained in chapter 8. The true worth of altimetry as tracking data is seen when it is supplemented to orbits computed from a sparse amount of laser data, subsequently referred to as sparse laser orbits.

§4.4 Supplementing Sparse Laser Orbits With Altimetry

SEASAT altimetry provides a near global set of observations, covering virtually all the ocean areas between latitude 70°S and 70°N, though much of that south of 60°S was contaminated by sea ice effects. Consequently, much useful

orbital information is contained therein. Section 4.3 showed that this information added little to an orbit derived from a good set of laser observations. However, as the amount of laser data is reduced, there will be a point when altimetry begins to provide the orbital information lacking in sparse laser range data. Experiments have been performed both in the Netherlands [25] and at Aston University to find the point where this occurs. Results of the work performed at Aston were presented in a paper at the UKGA-11 conference in Durham in April, 1987 [32].

Table 4.2 summarizes some of the results presented in Table 4.1 of [32] for the arc spanning MJD 43728 to MJD 43733.

Table 4.2: Orbital differences between orbits computed using 10 passes (425 observations) of Arequipa (7907) laser data supplemented with altimetry and the reference orbit.

Altimeter data		Orbital differences (max/rms)		
σ (m)	sampling interval (minutes)	radial (m)	along-track (m)	cross-track (m)
∞	—	5.66/2.55	117.2/24.81	0.95/0.66
2.0	1.0	1.62/0.68	29.85/6.24	1.13/0.77
1.0	1.0	1.32/0.58	17.43/4.32	1.00/0.68
0.5	1.0	1.35/0.60	12.01/3.64	0.52/0.35

Figure 4.3 : Orbital comparison of an arc computed with laser data only and laser data plus 2σ altimetry sampled at 30 second intervals.

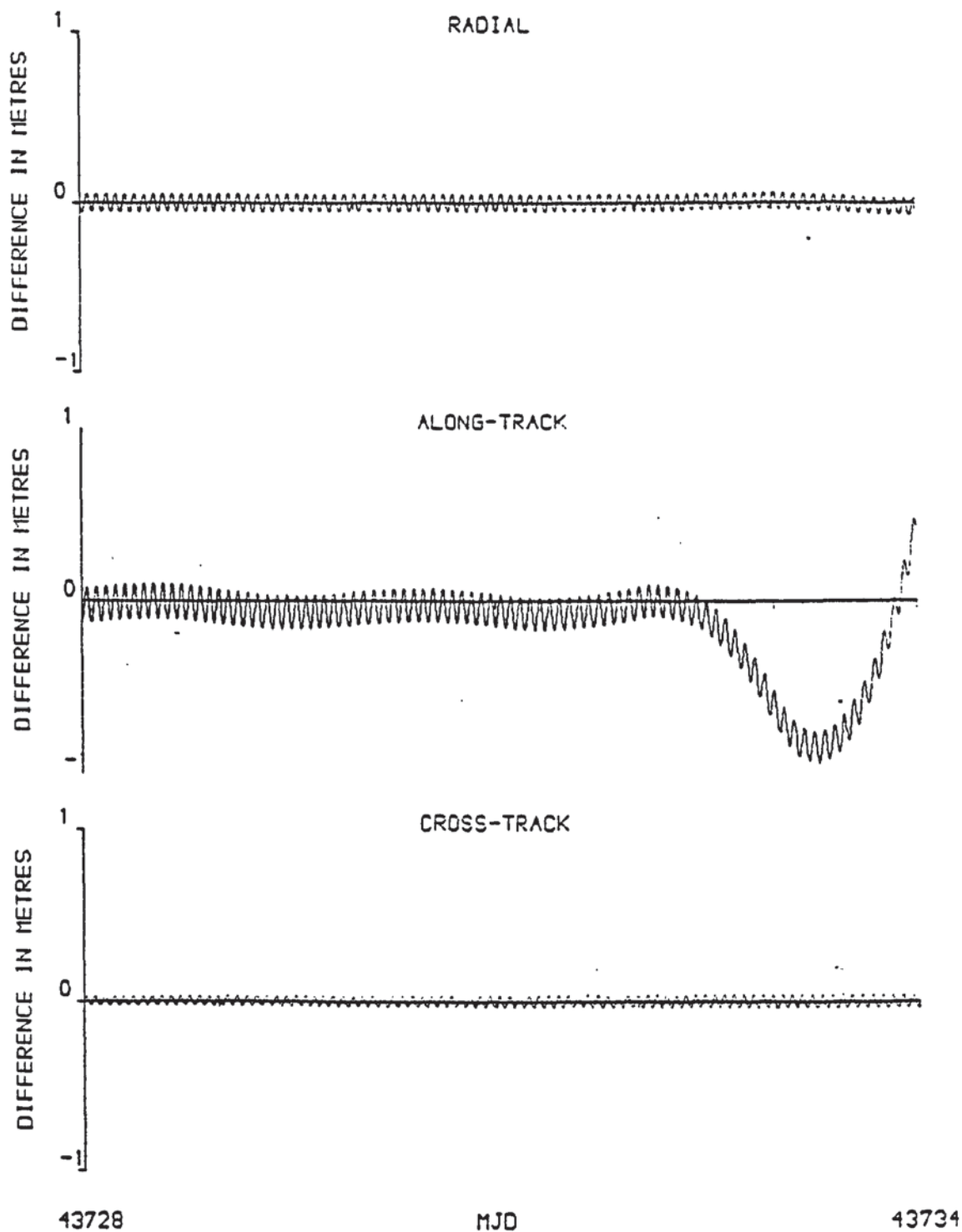


Figure 4.3 : Orbital comparison of an arc computed with laser data only and laser data plus $2m\sigma$ altimetry sampled at 30 second intervals.

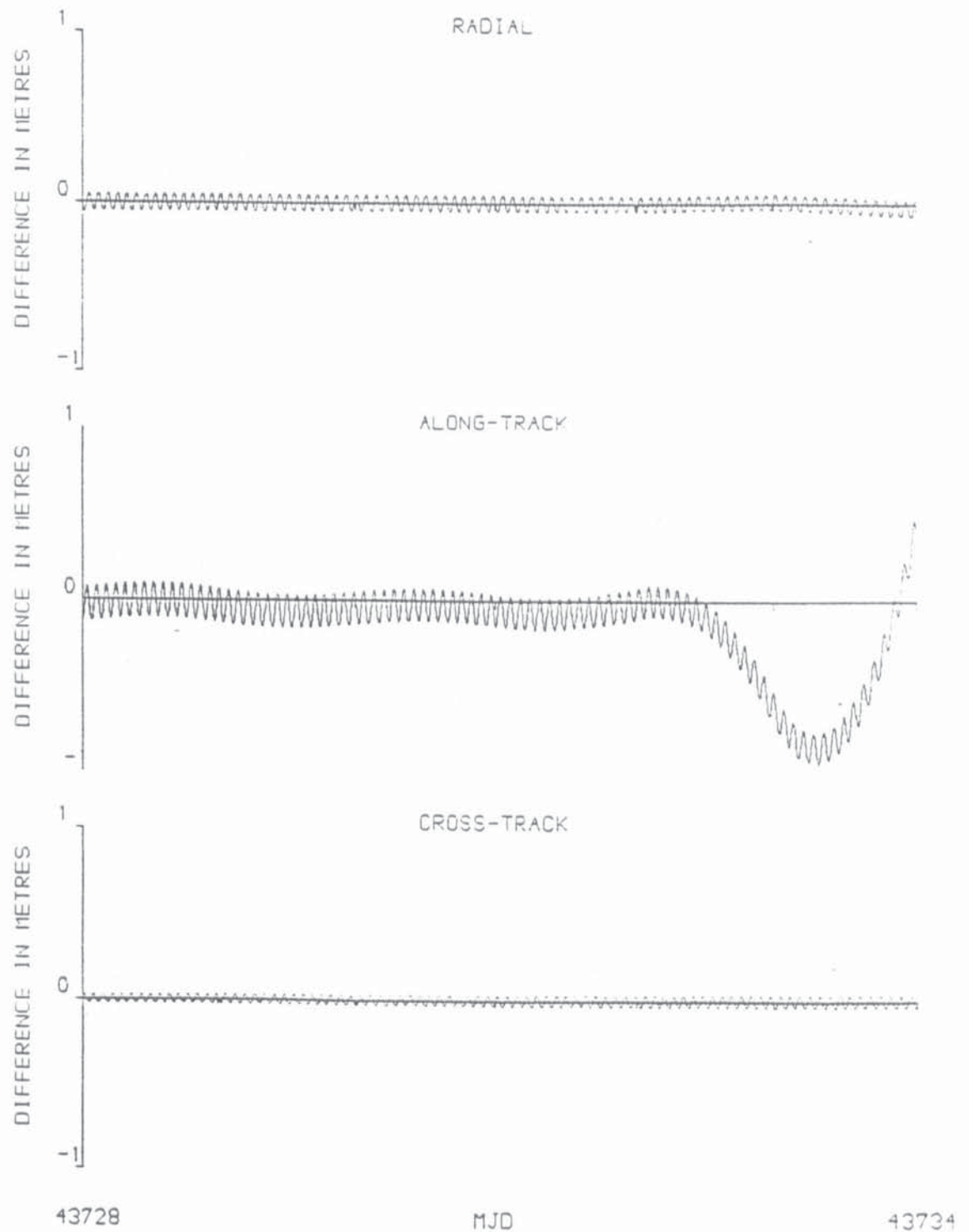
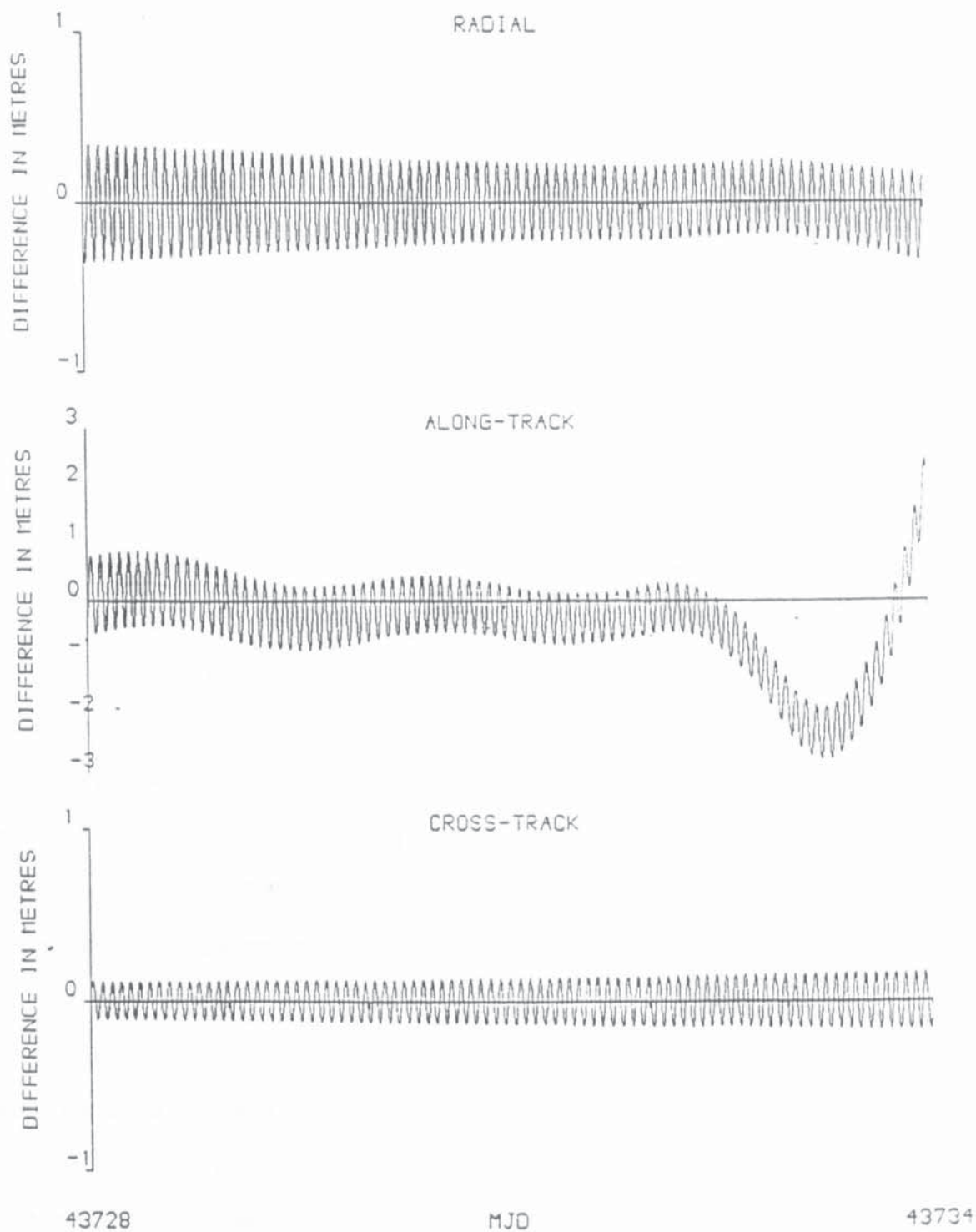


Figure 4.4 : Orbital comparison of an arc computed with laser data only and laser data plus 0.5mσ altimetry sampled at 30 second intervals.



In Table 4.2, the reference orbit refers to the orbit computed relative to the PGS-S3 gravity field [2], the CIRA 72 atmospheric model, a spherical satellite approximation for cross-sectional area modelling and daily drag coefficients when utilizing the full network of laser data. The results show that altimetry has a beneficial effect, both radially and to a lesser extent, along-track when it is supplemented to a very sparse network of laser observations. As the observational standard deviation, σ , is reduced on the altimeter, the orbital differences decrease with the Arequipa plus $0.5\text{m } \sigma$ altimetry orbit most closely approximating the reference orbit. For this orbit, the altimeter and laser data points are each of equal weight, whilst the ratio of altimeter to laser range measurements is of the order 10 : 1. Despite this predominance of altimetry, the laser range observations are still able to constrain the cross-track component of position. However, decreasing the 'a priori' standard deviation on the altimeter to 0.1m caused the laser data to have minimal effect and the solution failed to converge. Hence, care must be taken not to 'over-weight' the altimetry in such analyses.

Explanation for the orbital improvements radially is quite straightforward since altimetry provides direct information of this component. Along-track however, the improvement is not so easy to explain since the information from altimetry is limited in this direction. A little thought about the geometry of the situation may help to resolve this matter. Referring to Figure 4.5 it is seen that observations from the laser sites at each end of an arc help to fix all three components of the satellite's position at these points. This leaves the trajectory in a somewhat freer state in between. For the sparse laser orbits just mentioned, the length of the gaps between laser sites will obviously be larger than those for the orbits computed from the full laser network. Consequently, there will be longer periods unconstrained by observational data. Adding altimetry will help to fix the radial component of position during these periods directly, but the constraint along-track is a little more subtle. Due to the Earth's ellipticity and also to some extent, that of the satellite's orbit, the radial altimeter height above the reference ellipsoid will vary quite considerably

throughout the orbit (Figure 4.6). For instance, at the most northerly point of SEASAT's orbit, the altitude was approximately 810km. Conversely, at the most southerly point, it was near 824km whilst at the equator, it was near 798km. This variation helps to pin-point a group of radial altimeter observations in terms of their latitude, so providing some secondary along-track information.

Figure 4.5: Laser Sites.

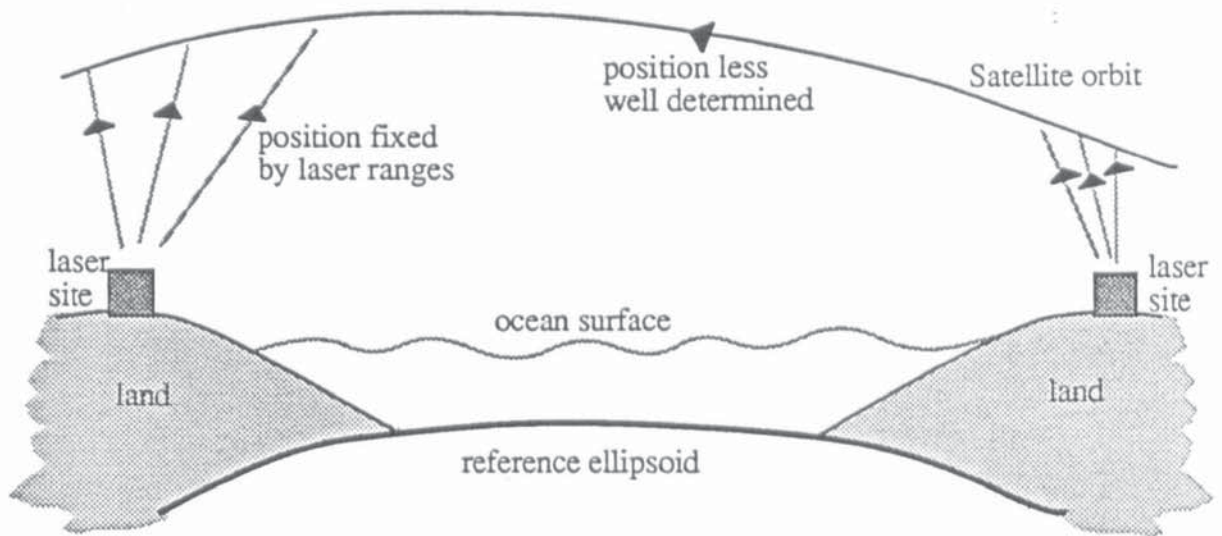
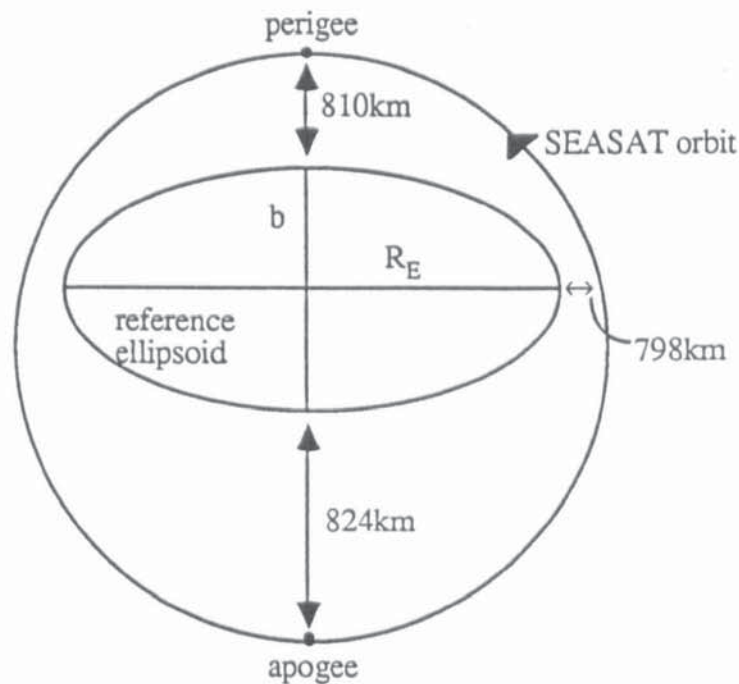


Figure 4.6: Altitude Variation for SEASAT.



R_E : semi-major axis of Earth's reference ellipsoid

b : semi-minor axis of Earth's reference ellipsoid

The practicality of supplementing altimetry to sparse laser orbits may be realized when the European Remote Sensing satellite, ERS-1 is launched, since there is some doubt as to the amount and distribution of laser coverage which will occur for this spacecraft. ERS-1 will also carry the Precise Range and Range-rate Experiment (PRARE) but as the name suggests, it is an experimental system. In the event of poor laser coverage or failure of PRARE, the results of Table 4.2 show that accurate orbits can still be obtained upon utilization of altimetry.

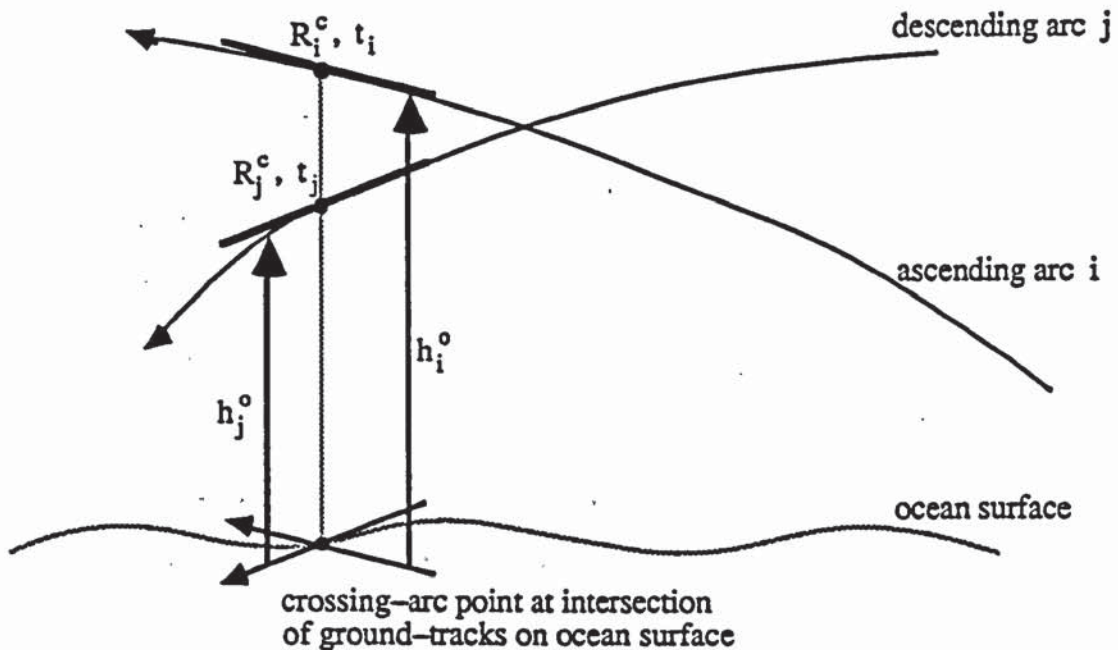
CHAPTER 5

CROSSOVERS

§5.1 Formulation Of The Crossovers From Altimetry

A crossover point occurs where ascending and descending satellite ground-tracks intersect, a satellite ground track being the projection of the satellite's trajectory onto the Earth's surface. Figure 5.1 [33] depicts in simple form, the crossing-arc point between two arcs, i and j .

Figure 5.1: Crossing-Arc Point.



In Figure 5.1, R_i^c and R_j^c refer to the calculated geodetic heights of the spacecraft at the crossover point for time t_i on the ascending arc and t_j on the descending arc, respectively. Observed h_i^o and h_j^o denote the corresponding altimeter measurements at these times, including all correction terms, as defined in equation (4.1), except the geoid correction. Numerical values for h_i^o and h_j^o are

found by interpolating within the GDR files at times t_i and t_j , respectively. The observed crossover height difference, C_{ij}^o , is then defined to be

$$C_{ij}^o = h_i^o - h_j^o \quad (5.1)$$

if t_i is earlier than t_j and

$$C_{ij}^o = h_j^o - h_i^o \quad (5.2)$$

if t_i is later than t_j . Similarly, the calculated crossover height difference, C_{ij}^c , is defined to be

$$C_{ij}^c = R_i^c - R_j^c \quad (5.3)$$

for t_i earlier than t_j and

$$C_{ij}^c = R_j^c - R_i^c \quad (5.4)$$

for t_i later than t_j . The crossover height residual, ΔC_{ij} , is then defined by

$$\Delta C_{ij} = C_{ij}^o - C_{ij}^c \quad (5.5)$$

Equation (5.1), for example, illustrates the reason for omission of the geoid correction in the definitions of h_i^o and h_j^o ; being identical on both tracks, it cancels in the equation. This cancellation removes a large part of the altimetric uncertainty from the crossover measurement, thus providing a more accurate form of radial observation than pure altimetry. For example, the precision of a crossover height measurement is governed by the precision of the altimeter plus the various correction terms, in particular that due to the ocean tides and results in a measurement accuracy of about 20cm rms. Conversely, an altimeter height measurement is greatly affected by the geoid accuracy which is precise to about 1m rms and therefore produces an observation with a total rms accuracy in excess of 1m. Apart from the orbital contribution, the measured crossover height difference includes time dependent terms such as the difference in the sea state bias and ocean tides for the two epochs. Sea surface topography has not been modelled in equation (4.1), so any difference in the time dependent or dynamic component (e.g. due to eddy currents) will propagate into the crossover residuals. Over periods of a few days, these oceanographic topography

variations however, are expected to be small, so that analogous to the geoid height, the sea surface topography is the same on both tracks. Consequently, the main contribution to the crossover height residuals, will be radial ephemeris error, but it should be noted that geographically correlated terms will cancel at the crossover points rendering part of this radial difference unobservable [34].

The processing of the crossovers is described in [17] and involves determining the two epochs of the crossover points from an initial reference ephemeris. Since this ephemeris is not updated at each iteration of an orbital solution and since in any event, this ephemeris is not the 'true' ephemeris, these epochs do not correspond to the 'true' crossover epochs that actually occurred for SEASAT. For an accurate reference ephemeris however, the computed epochs will be sufficiently near to the 'true' crossover epochs so that the geoid height is the same on both tracks at these points. Hence the crossovers described throughout this thesis are strictly speaking, only pseudo-crossovers and not 'true' crossovers.

§5.2 Crossovers As Observational Data

The minimization of the crossover height residuals using least squares can be used to solve for certain orbital and geodetic parameters as described in section 3.3. To do this, the partial derivatives of the residuals, with respect to these parameters, need to be determined. For instance, if p is an orbital parameter, then

$$\frac{\partial}{\partial p} (C_{ij}^o - C_{ij}^c) = - \frac{\partial}{\partial p} (R_i^c - R_j^c) \quad (5.6)$$

assuming that t_i is earlier than t_j , on using equation (5.3). The partial derivatives $\partial R_i^c / \partial p$ and $\partial R_j^c / \partial p$ are determined from equation (4.14) upon identifying R_i^c and R_j^c with h_i^c and h_j^c , respectively.

As for pure altimetry, crossovers provide mainly radial information on the measurement residuals but, unlike pure altimeter residuals, the crossover residuals are almost entirely a consequence of radial orbit error. Hence the rms of the crossover residuals provides an independent check on global radial orbital accuracy, whether crossovers are used in the orbital solution or not. The rms of the crossover residuals, R_c , can be written

$$R_c = \sqrt{\left(\sum_{k=1}^N \Delta C_k^2 / N \right)} \quad (5.7)$$

where $\Delta C_k = C_{ij}^o - C_{ij}^c$ is the residual of the k^{th} crossover out of the total N considered in a long-arc analysis. Writing ΔC_k as

$$\Delta C_k = (h_{1k}^o - h_{2k}^o) - (R_{1k}^c - R_{2k}^c) \quad (5.8)$$

where h_{1k}^o, h_{2k}^o refer to the observed altimeter measurements for the earlier and later arcs, respectively and R_{1k}^c, R_{2k}^c , the calculated geodetic heights for these two arcs,

then

$$R_c = \left(\sum_{k=1}^N \frac{[(h_{1k}^o - h_{2k}^o) - (R_{1k}^c - R_{2k}^c)]^2}{N} \right)^{\frac{1}{2}}. \quad (5.9)$$

Now let $h_{1k}^c = R_{1k}^c - h_g$ and $h_{2k}^c = R_{2k}^c - h_g$ where h_g is the precise geoid height at the crossover point. Then equation (5.9) can be written

$$R_c = \left(\sum_{k=1}^N \frac{[(h_{1k}^o - h_{1k}^c) - (h_{2k}^o - h_{2k}^c)]^2}{N} \right)^{\frac{1}{2}}. \quad (5.10)$$

Expanding (5.10) gives

$$R_c = \left(\sum_{k=1}^N \frac{(h_{1k}^o - h_{1k}^c)^2}{N} - \frac{2}{N} \sum_{k=1}^N (h_{1k}^o - h_{1k}^c)(h_{2k}^o - h_{2k}^c) + \sum_{k=1}^N \frac{(h_{2k}^o - h_{2k}^c)^2}{N} \right)^{\frac{1}{2}} \quad (5.11)$$

For a large sample, the first term in this expression can be expected to have value R_o^2 , where R_o is the rms of the orbital radial component, (this term is devoid of any geoid error). For large N , R_o can be considered independent of location so that the last term can also be expected to have the value R_o^2 . Similarly, the value of the central term can be expected to be zero so that

$$R_c \approx (2R_o^2)^{\frac{1}{2}} \quad (5.12)$$

giving $R_o \approx R_c / \sqrt{2}$. (5.13)

It should be noted that, although this values gives an independent check on the global radial orbit rms, it is only approximate, since part of the error is unobservable at the crossover points [34].

§5.3 Crossovers And Sparse Laser Orbits

As with pure altimetry, crossover data can be supplemented to orbits with spare laser data and the resulting ephemerides compared with reference ephemerides, determined from a full network of available laser data. One such orbit was the six day arc spanning September 19 to September 25, 1978 (MJD 43770 to MJD 43776). The reference ephemeris was obtained relative to the GEM-T1 gravity field, the NASA 'area tables' for SEASAT and the CIRA 72 atmospheric model, solving for a state vector at epoch, daily drag coefficients and a single solar reflectivity coefficient. Initial comparisons were made with orbits determined using laser data from the Arequipa station (7907) only, and then supplementing this data with either pure

altimetry sampled at half minute intervals or crossovers utilizing various weights. The weight applied to the Arequipa laser data was the nominal 0.5m standard deviation for this station as given in Table 2.1. Results of these comparisons are shown in Table 5.1.

Table 5.1: Orbital comparisons for MJD 43770 to MJD 43776.

Reference ephemeris versus	Difference in metres (max/rms)		
	<u>radial</u>	<u>along-track</u>	<u>cross-track</u>
Arequipa laser data only	0.79/0.30	5.95/1.81	1.21/0.76
Arequipa plus 2m σ altimetry †	0.45/0.13	5.52/1.93	1.25/0.77
Arequipa plus 1.25m σ crossovers †	0.51/0.24	10.28/2.39	1.07/0.66
Arequipa plus 0.5m σ altimetry *	0.42/0.15	3.81/1.52	2.62/1.80
Arequipa plus 0.3m σ crossovers *	0.35/0.10	6.53/1.73	1.07/0.65

The † and * symbols in Table 5.1 indicate a similar level of significance applied to altimetry and crossovers for the respective comparisons, i.e.

$$N_{\text{alt}} \omega_{\text{alt}} \approx N_{\text{cr}} \omega_{\text{cr}} \quad (5.14)$$

where N_{alt} (= 10,558), N_{cr} (= 4119) are the number of altimeter and crossover data points, respectively, for the six day arc and ω_{alt} and ω_{cr} their respective weights as given by equation (3.13).

Several points can be noted from Table 5.1. Both pure altimetry and crossovers have a beneficial effect, at least radially, on an orbit determined from sparse laser data. The Arequipa plus 2m σ altimetry orbit gives a closer fit to the reference orbit than the 'similarly weighted' Arequipa plus 1.25m σ crossover data. Increasing the weight of the pure altimetry does not improve the radial component of position, but the along-track component improves at the expense of a deterioration in the cross-track position.

However, increasing the weight on the crossovers to a similar level of significance continues to improve the radial component of position without affecting the cross-track component. The along-track component improves to a similar level of accuracy as that obtained from using the Arequipa data only.

It is difficult to infer any hard and fast conclusions from Table 5.1, but it does suggest that pure altimetry contains more along-track information than crossover data. This may be a consequence of the geometry as explained in section 4.4, but it should be noted that crossovers implicitly contain along-track information since they are a function of two epochs. If the along-track position is determined incorrectly, the crossover will be slightly out of place on both tracks, hence magnifying any error. Evidently, this type of along-track information is not as strong as that contained in the geometry of pure altimetry.

It was anticipated that crossovers would provide greater radial accuracy than pure altimetry since, being devoid of any geoid error, they are inherently more accurate. That this did not occur for the Arequipa plus $1.25\text{m } \sigma$ crossover orbit as compared to the Arequipa plus $2\text{m } \sigma$ altimetry orbit, could be due to non-similarity of weighting. Altimetry provides a good global coverage of observational data, whereas crossovers are predominantly at high latitudes. It is possible that the adopted weighting strategy has not provided enough significance to the low latitude crossovers. However, the radial accuracy of the Arequipa plus $0.3\text{m } \sigma$ crossover orbit is an improvement upon the Arequipa plus $0.5\text{m } \sigma$ altimetry orbit, showing that for more realistic weights of crossovers, they provide the anticipated improvement in radial orbit accuracy.

Finally, it should be noted that the cross-track component of position is in most agreement with the reference orbit when the Arequipa data is supplemented with crossovers (of any weight). This is strange, since crossovers do not contain strong cross-track information and is probably a quirk of the data. To confirm this, it was decided to repeat the above analysis on another six day arc, September 25 to October 1, 1978 (MJD 43776 to MJD 43782). For this arc, a reference ephemeris was

obtained as before, except that two half daily drag coefficients were estimated on MJD 43780, on account of the severe geomagnetic storm on this day. A comparison of the resulting reference ephemeris was made with an ephemeris determined using laser data excluding the NASA laser stations 7062, 7063, 7067, 7068 and 7069. This was the so called sparse laser orbit. Next, this sparse laser orbit was supplemented with $1\text{m } \sigma$ crossover data and compared with the reference orbit. The results of these tests, presented in Table 5.2, show that crossovers improve the sparse laser orbit both radially and along-track, but have a detrimental effect cross-track. Evidently, the good cross-track fit of the previous six day arc when using crossovers, must have been coincidental.

Table 5.2: Orbital comparisons for MJD 43776 to MJD 43782.

Reference ephemeris versus	Difference in metres (max/rms)		
	<u>radial</u>	<u>along-track</u>	<u>cross-track</u>
Sparse laser orbit	2.57/1.03	19.35/4.81	0.91/0.62
Sparse laser orbit plus $1\text{m } \sigma$ crossovers	0.35/0.18	6.59/2.63	1.20/0.84
Sparse laser orbit plus $0.5\text{m } \sigma$ crossovers	0.71/0.40	9.72/3.14	1.53/1.02
Sparse laser orbit plus $0.3\text{m } \sigma$ crossovers	1.90/1.23	16.53/5.19	2.27/1.44

Returning to Table 5.1, it is to be noticed that the level of orbital improvement of the Arequipa data, when supplemented with either altimetry or crossovers is slight. This is because the Arequipa only orbit, is itself fairly accurate. To place a more stringent test on the use of crossovers in sparse laser orbits, the decision was taken to omit the last pass of laser data from Arequipa and repeat the above experiments. Results of the ensuing comparisons are detailed in Table 5.3 and plotted graphically in Figures 5.2 to 5.4.

Table 5.3: Orbital comparisons for MJD 43770 to MJD 43776.

	Reference ephemeris versus	Difference in metres (max/rms)		
		<u>radial</u>	<u>along-track</u>	<u>cross-track</u>
(1)	Arequipa laser data minus pass on last day	12.24/2.48	613.12/113.06	1.26/0.75
(2)	As (1) but supplemented † with 2m σ altimetry	0.34/0.13	4.82/2.22	1.78/1.18
(3)	As (1) but supplemented † with 1.25m σ crossovers	0.51/0.27	4.90/2.07	1.24/0.78
(4)	As (1) but supplemented * with 0.5m σ altimetry	failure to converge		
(5)	As (1) but supplemented * with 0.3m σ crossovers	0.31/0.10	4.52/1.64	1.06/0.65

Again † and * refer to data of similar weights as defined by equation (5.14).

Once again, it is seen that the sparse laser orbit supplemented with 0.3m σ crossovers is in most agreement with the reference ephemeris. From Figure (5.2), the poor performance of the sparse laser orbit is due solely to the errors on the last day associated with an ill-determined drag coefficient. Supplementing this orbit with either 2m σ altimetry or crossovers constrains this coefficient to give highly accurate results. As before, the 2m σ altimetry performs better radially than the 'similarly weighted' 1.25m σ crossovers. However, increasing the weight of the altimetry to 0.5m standard deviation causes the system to become ill-conditioned and non-convergent. This is probably due to the limited cross-track information on the last day. The similarly weighted 0.3m σ crossover orbit does converge and gives the most accurate ephemeris probably because the low latitude crossovers have now been given a realistic weight.

Obviously, care must be taken not to over-weight pure altimetry in sparse laser orbits since it contains only radial and slight along-track information with no cross-track constraint. Caution must also be exercised with the weight applied to the crossovers since there will be a point when they also, become ill-conditioned. This is examined in the next section.

Figure 5.2 : Orbital comparison of the reference ephemeris of MJD 43770 to MJD 43776 versus the orbit computed using Arequipa laser data minus the last pass.

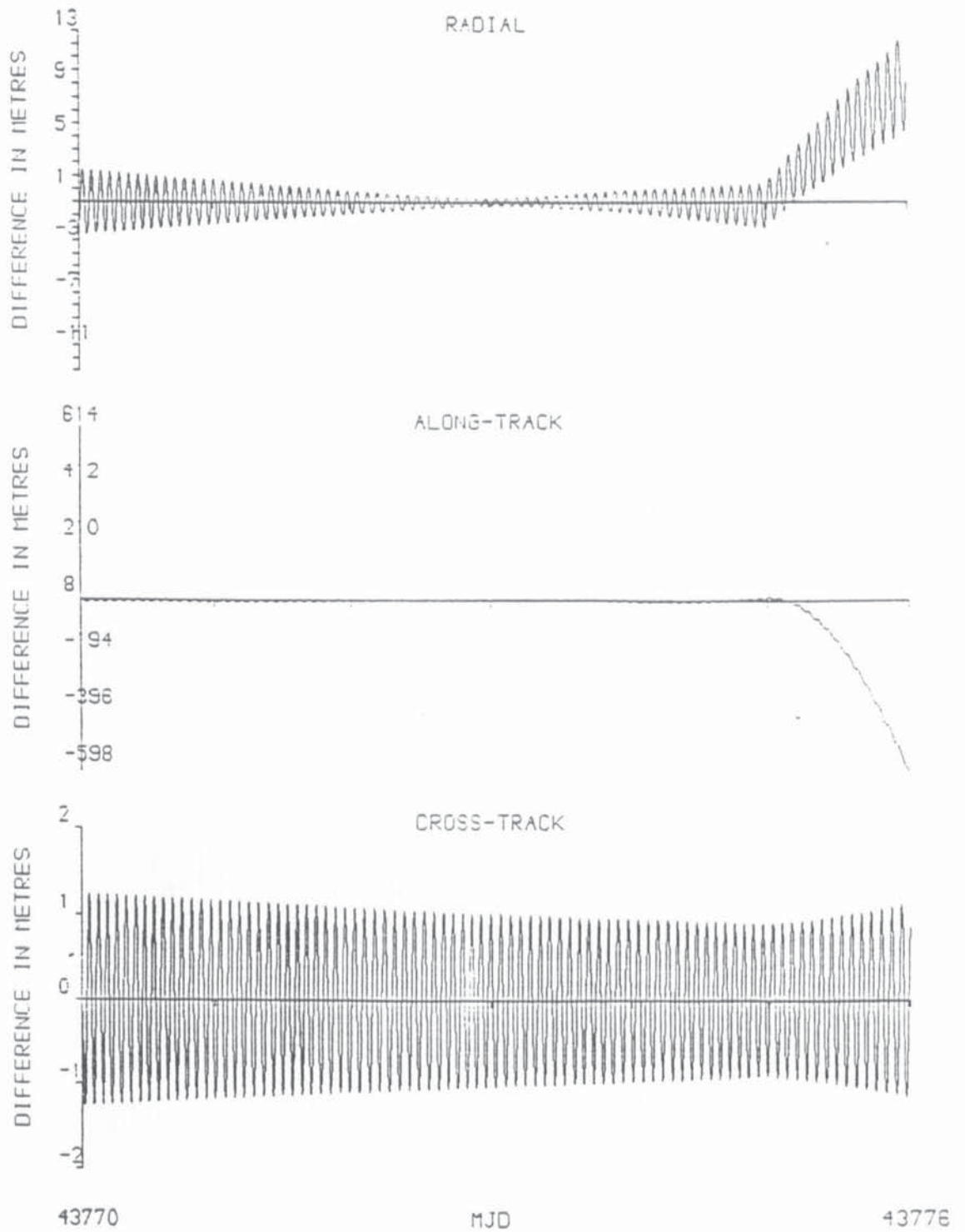


Figure 5.3 : Orbital comparison of the reference ephemeris of MJD 43770 to MJD 43776 versus the orbit computed using Arequipa laser data minus the last pass plus $2m\sigma$ altimetry.

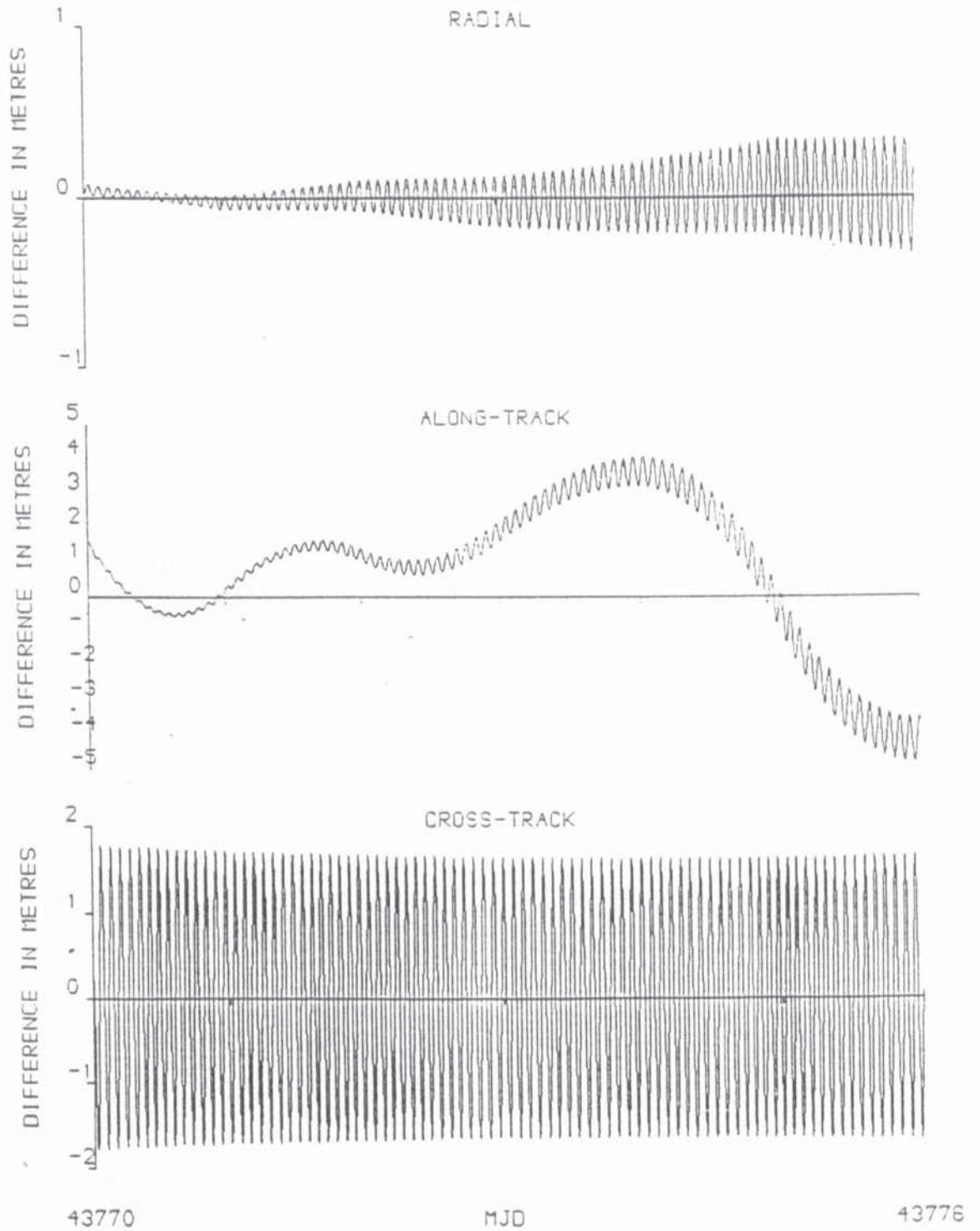
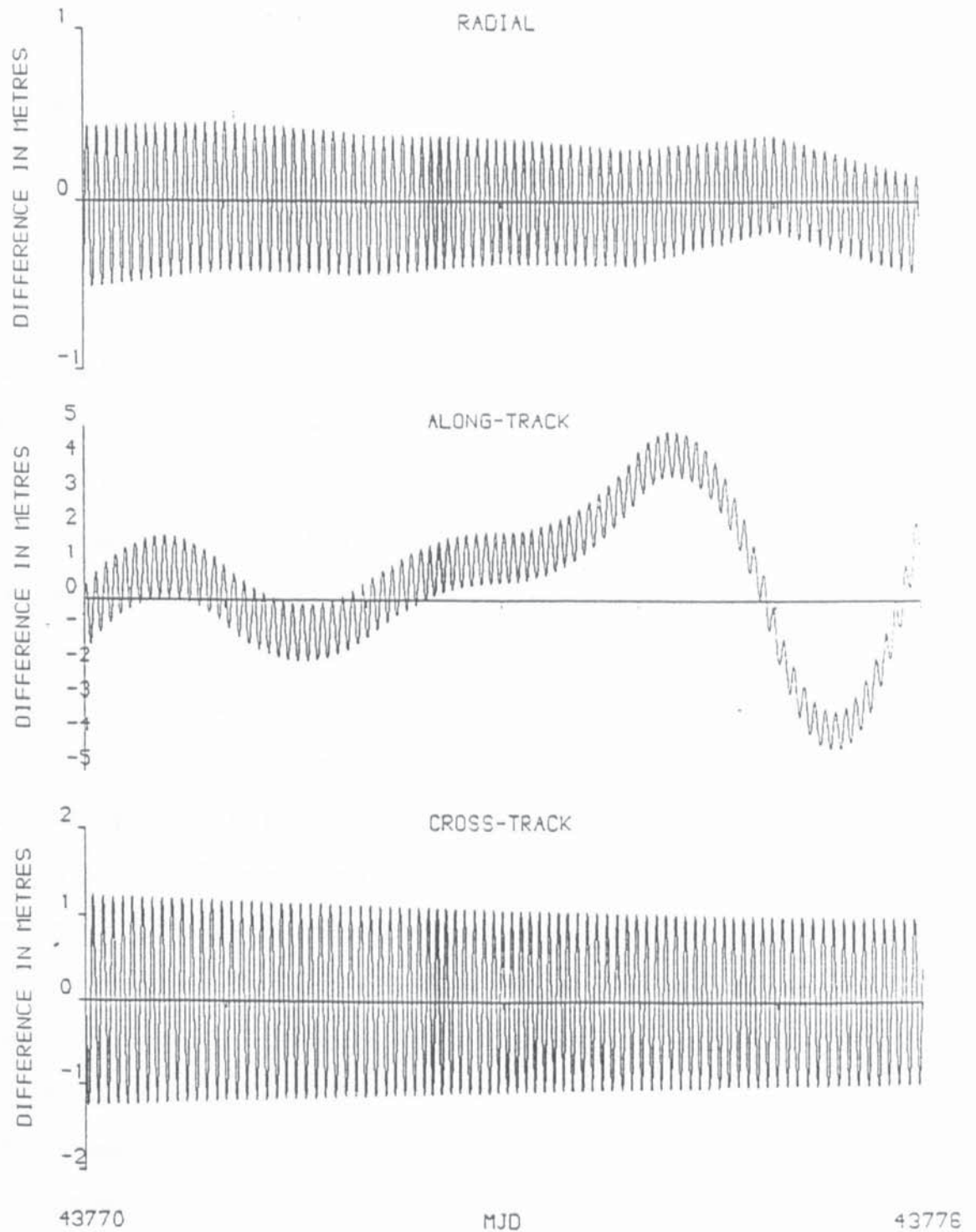


Figure 5.4 : Orbital comparison of the reference ephemeris of MJD 43770 to MJD 43776 versus the orbit computed using Arequipa laser data minus the last pass plus $1.25m\sigma$ crossover data.



The results of this section have shown that crossovers are equally, if not more useful than pure altimetry when used as tracking data in sparse laser orbits and their use can minimize the radial error.

§5.4 Crossover Weighting Strategy

The results of section 5.3 have shown a strong dependence, at least radially and along-track, on the weight applied to the crossovers. For instance, both Table 5.1 and Table 5.3 have shown that the most accurate sparse laser orbit for MJD 43770 to MJD43776 was obtained when supplemented with 0.3m σ crossover data. Upon increasing the weight of the crossovers to a standard deviation of 0.1m it was found that the cross-track component of position began to deviate considerably from the reference orbit, showing that the point where crossovers are over-weighted lies somewhere between a standard deviation of 0.3m and 0.1m for this orbit.

Other tests on ill-conditioning were performed using the MJD 43776 to MJD 43782 arc. Here the sparse laser orbit was supplemented in turn, with 1.0m σ , 0.5m σ and 0.3m σ crossover data. Comparison of the resulting orbits with the reference orbit have been presented in Table 5.2, clearly showing the deterioration in orbital accuracy as more significance is applied to the crossovers. The reason that this happens for a lower crossover weight than in the other orbital arc is unclear, but could be a consequence of the different laser data sets. Apparently, the distribution, both spatial and temporal, of the laser data, plays an important role in defining the optimum weight to be applied to the crossovers. If it is wished to supplement crossovers to orbits using the full network of available laser data, then the standard deviation applied to them should be of the order of 0.15m since their accuracy is comparable to that of the NASA laser stations as given in Table 2.1.

§5.5 A Note Of The Derivation Of The Crossovers

The analysis of section 5.3 was performed using crossovers which had been derived using reference ephemerides (see [17]). This may seem artificial in that if only a sparse network of laser data is available, a highly accurate initial orbit may not be obtainable. There are two solutions to this problem. Firstly, it is possible to supplement the sparse laser orbit with altimetry and derive an ephemeris which the comparisons of section 4.4 suggest is of good accuracy. Using this, it is then possible to derive the crossovers and apply them as in the previous analysis. A simpler solution is to calculate the crossovers from the sparse laser orbit directly, without resorting to the use of pure altimetry. Since the crossovers determined are not 'true' crossovers, but psuedo-crossovers, all that matters are the epochs and height difference. It is not that crucial for the latitudes and longitudes of the crossover points to be 'true', since for along-track errors of the order of tens of metres, the geoid component of any height measurement will still be the same on both tracks. Hence, as long as the sparse laser orbit is not 'bad' in the sense of the above along-track error, it is realistic to use it to determine the crossovers. Confirmation of this is shown in Table 5.4 where crossovers have been derived using the reference ephemeris and a sparse laser ephemeris. The results show there is virtually no difference between the two methods.

Table 5.4: Orbital comparisons for MJD 43776 to MJD 43782.

Reference ephemeris versus	Difference in metres(max/rms)		
	<u>radial</u>	<u>along-track</u>	<u>cross-track</u>
Sparse laser orbits plus 1m σ crossovers derived from reference ephemeris	0.35/0.18	6.59/2.63	1.20/0.84
Sparse laser orbit plus 1m σ crossovers derived from sparse laser orbit	0.34/0.18	6.56/2.63	1.20/0.84

CHAPTER 6

RADIAL ORBIT ERROR DUE TO THE GRAVITY FIELD

In this chapter the radial orbit error, Δr , associated with mis-modelling of the Earth's gravity field is developed, in order to obtain the dominant error frequencies for separation of orbital, geoidal and sea surface topography frequencies, in the altimeter residuals. Consequently, it is unnecessary to derive the exact amplitudes of these terms and thus Δr is only expanded to order e^0 in the eccentricity.

§6.1 The Disturbing Potential

The gravitational disturbing potential, V , has been expressed by Kaula [20] as

$$V = \sum_{\ell=2}^{\infty} \sum_{m=0}^{\ell} V_{\ell m} \quad (6.1)$$

where

$$V_{\ell m} = \frac{\mu R_E^{\ell}}{a^{\ell+1}} \sum_{p=0}^{\ell} F_{\ell mp}(i) \sum_{q=-\infty}^{\infty} G_{\ell pq}(e) \left\{ \begin{array}{l} \ell-m \text{ even} \\ \left[\begin{array}{l} C_{\ell m} \\ -S_{\ell m} \end{array} \right] \cos \psi_{\ell mpq} + \left[\begin{array}{l} S_{\ell m} \\ C_{\ell m} \end{array} \right] \sin \psi_{\ell mpq} \\ \ell-m \text{ odd} \quad \ell-m \text{ odd} \end{array} \right\} \quad (6.2)$$

wherein a is the semi-major axis of the orbital ellipse; μ the gravitational constant multiplied by the mass of the earth; R_E the radius of the earth at the equator; $F_{\ell mp}(i)$ inclination functions expressing the rotation, i , of the potential from the equatorial to the orbital plane; $G_{\ell pq}(e)$ eccentricity functions transforming from true to mean anomaly in an elliptic orbit; $C_{\ell m}$, $S_{\ell m}$ the spherical harmonic coefficients of degree ℓ and order m and

$$\psi_{\ell mpq} = (\ell - 2p + q)(\omega + M) - q\omega + m(\Omega - \theta_s). \quad (6.3)$$

In equation (6.3) ω is the argument of perigee, M the mean anomaly, Ω the argument of ascending node and θ_s the sidereal angle (see Appendix 1).

§6.2 Linear Radial Perturbations

Using the geometry of Figure A.1 (Appendix 1), the radial distance, r , is expressed in terms of the eccentric anomaly, E , by

$$r = a(1 - e \cos E). \quad (6.4)$$

Now equation (6.2) expresses the disturbing potential in terms of M , the mean anomaly. Hence it is necessary to transform equation (6.4) to the same element. For small eccentricity (as is the case for SEASAT), the transformation is simply given by $\cos E \approx \cos M$ so that

$$r = a(1 - e \cos M) + O(e^2). \quad (6.5)$$

A change in r due to an error in the harmonic coefficients $C_{\ell m}$, $S_{\ell m}$ is then (to order e^0)

$$\Delta r \approx \Delta a - a \Delta e \cos M + a e \Delta M \sin M \quad (6.6)$$

where Δa , Δe and ΔM are the corresponding errors in a , e and M due to errors $\Delta C_{\ell m}$, $\Delta S_{\ell m}$ in $C_{\ell m}$, $S_{\ell m}$, respectively. Equation (6.6) is of order e^0 since ΔM is of order e^{-1} , but is sufficient for analysis of the required frequencies. Δa , Δe and ΔM are found by solving Lagrange's planetary equations [20] with V as the disturbing potential.

Let ξ denote any of the Keplerian elements a , e , i , ω , Ω or M . Lagrange's planetary equations express $\dot{\xi}$ in terms of all the other elements plus the disturbing potential. Hence $\dot{\xi}$ can be written in the form

$$\dot{\xi} = L_{\xi}(a, e, i, \omega, \Omega, M; V, \mu) \quad (6.7)$$

with known function L_{ξ} . Consider a change in $\dot{\xi}$ due to an error in V . Then

$$\Delta \dot{\xi} = \sum_j \left(\frac{\partial L_\xi}{\partial \beta_j} + \sum_{i=1}^6 \frac{\partial L_\xi}{\partial C_i} \frac{\partial C_i}{\partial \beta_j} \right) \Delta \beta_j \quad (6.8)$$

where $C_i \in (a, e, i, \omega, \Omega, M)$ and $\beta_j \in (C_{\ell m}, S_{\ell m})_{\ell, m}$ i.e. it is assumed that the error in V is caused by an error in one or more of the harmonic coefficients which define V . For simplicity consider an error in a single coefficient, $C_{\ell m}$, say.

Then

$$\Delta \dot{\xi} = \frac{\partial L_\xi}{\partial C_{\ell m}} \Delta C_{\ell m} + \sum_{i=1}^6 \frac{\partial L_\xi}{\partial C_i} \frac{\partial C_i}{\partial C_{\ell m}} \Delta C_{\ell m} \quad (6.9)$$

or

$$\Delta \dot{\xi} = \frac{\partial L_\xi}{\partial C_{\ell m}} \Delta C_{\ell m} + \sum_{i=1}^6 \frac{\partial L_\xi}{\partial C_i} \Delta C_i \quad (6.10)$$

where

$$\Delta C_i = \frac{\partial C_i}{\partial C_{\ell m}} \Delta C_{\ell m}. \quad (6.11)$$

The first term of equation (6.10) represents the first order approximation of the error in $\dot{\xi}$, whilst the second term accounts for second order effects which arise from the interactions of the first order terms with all the harmonic coefficients. These terms are ignored in this first order analysis so that

$$\Delta \dot{\xi} \approx \frac{\partial L_\xi}{\partial C_{\ell m}} \Delta C_{\ell m}. \quad (6.12)$$

For example, if $\xi \equiv a$, then from [20]

$$\Delta \dot{a} \approx \frac{\partial}{\partial C_{\ell m}} \left(\frac{2}{na} \frac{\partial V}{\partial M} \right) \Delta C_{\ell m} \quad (6.13)$$

which upon substitution from equations (6.1) and (6.2) yields

$$\Delta \dot{a} \approx \frac{2\mu R_E^\ell}{na^{\ell+2}} \sum_{p=0}^{\ell} F_{\ell mp}(i) \sum_{q=-\infty}^{\infty} G_{\ell pq}(e) (\ell - 2p + q) \begin{cases} \Delta C_{\ell m} & \ell - m \text{ even} \\ -\Delta S_{\ell m} & \ell - m \text{ odd} \end{cases} \sin \psi_{\ell mpq} +$$

$$\left. \begin{array}{l} \Delta S_{\rho m} \\ \Delta C_{\rho m} \end{array} \right\} \cos \psi_{\rho m p q} \quad \begin{array}{l} \rho-m \text{ even} \\ \rho-m \text{ odd} \end{array} \quad (6.14)$$

In equation (6.14) the error $\Delta S_{\rho m}$ in $S_{\rho m}$ has also been included.

Equation (6.12) is integrated using the well-known method of linear perturbations (Kaula [20], Colombo [34] and Engelis [35]) in which the elements a , e and i are assumed fixed and ω , Ω and M are assumed to vary linearly with time, under the action of earth oblateness. However, for precise frequency recovery the elements used in this method should not be osculating elements but mean elements, that is, elements which define a secularly precessing reference ellipse in which all periodic variations due to the second degree harmonic, C_{20} , have been removed. As an example, the mean value of the semi-major axis, \bar{a} , given by Kozai [36] is

$$\bar{a} \approx a + \frac{3}{2} C_{20} \frac{R_E^2}{a} \sin^2 i \cos [2(\omega + M)] \quad (6.15)$$

where a , i , ω and M represent osculating values. The secularly precessing ellipse is then defined by

$$\bar{\omega} = \dot{\bar{\omega}}(t - t_0) + \bar{\omega}_0 \quad (6.16)$$

$$\bar{M} = \dot{\bar{M}}(t - t_0) + \bar{M}_0 \quad (6.17)$$

$$\bar{\Omega} - \theta_s = (\dot{\bar{\Omega}} - \dot{\theta}_s)(t - t_0) + (\bar{\Omega}_0 - \theta_{s,0}) \quad (6.18)$$

wherein
$$\dot{\bar{\omega}} \approx \frac{3}{4} \bar{n} C_{20} \left(\frac{R_E}{\bar{a}}\right)^2 (5 \cos^2 \bar{i} - 1) \quad (6.19)$$

$$\dot{\bar{M}} \approx \mu^{\frac{1}{2}} \bar{a}^{-\frac{3}{2}} \left[1 - \frac{3}{2} C_{20} \left(\frac{R_E}{\bar{a}}\right)^2 \left(1 - \frac{3}{2} \sin^2 \bar{i}\right) \right] \quad (6.20)$$

$$\dot{\bar{\Omega}} \approx \frac{3}{2} \bar{n} C_{20} \left(\frac{R_E}{\bar{a}}\right)^2 \cos \bar{i} \quad (6.21)$$

In equations (6.16) to (6.21) the bars signify mean elements; the 0 subscripts in equations (6.16) to (6.18) signify the values of those mean elements at time t_0 , from which all subsequent perturbations are derived; $\dot{\theta}_s$ is the rate of change of the

sidereal angle, i.e. the rotation rate of the earth; \bar{n} is the (mean) mean motion and all other symbols are as defined previously.

Equation (6.14) can now be integrated to give

$$\Delta a \approx \frac{2\mu R_E^\ell}{\bar{n} \bar{a}^{\ell+2}} \sum_{p=0}^{\ell} F_{\ell mp}(\dot{i}) \sum_{q=-\infty}^{\infty} G_{\ell pq}(\dot{e}) \left\{ \begin{array}{l} \left[\begin{array}{l} \Delta C_{\ell m} \\ -\Delta S_{\ell m} \end{array} \right]_{\substack{\ell-m \text{ even} \\ \ell-m \text{ odd}}} \cos \bar{\psi}_{\ell mpq} + \\ \left[\begin{array}{l} \Delta S_{\ell m} \\ \Delta C_{\ell m} \end{array} \right]_{\substack{\ell-m \text{ even} \\ \ell-m \text{ odd}}} \sin \bar{\psi}_{\ell mpq} \end{array} \right\} \frac{(\ell - 2p + q)}{\dot{\bar{\psi}}_{\ell mpq}} + K_1 \quad (6.22)$$

where K_1 is a constant to account for Δa being zero at time $t = t_0$. The summations in equation (6.22) are taken over all values of p, q for which $\dot{\bar{\psi}}_{\ell mpq} \equiv (\ell - 2p + q)(\dot{\bar{\omega}} + \dot{\bar{M}}) - q\dot{\bar{\omega}} + m(\dot{\bar{\Omega}} - \dot{\theta}_s)$ is non-zero. $\dot{\bar{\psi}}_{\ell mpq}$ can equal zero for all zonal terms ($m = 0$) and be near to zero at resonance. For the zonals, if $\bar{\psi}$ is zero then $\bar{\psi}$ must be constant and integration of equation (6.14) will lead to a secular term for the change in a , which for this analysis, is ignored. At pure resonance, the change in a would also be secular, but SEASAT only encounters shallow resonance. The frequency of such terms, is therefore low and the method of linear perturbations is as accurate as special perturbation methods for resonance, e.g. Gedeon [37].

The planetary equations for Δe and ΔM are solved similarly resulting in

$$\Delta e \approx \frac{\mu R_E^\ell}{\bar{n} \bar{a}^{\ell+3} \bar{e}} \sum_{p=0}^{\ell} F_{\ell mp}(\dot{i}) \sum_{q=-\infty}^{\infty} G_{\ell pq}(\dot{e})_q \left\{ \begin{array}{l} \left[\begin{array}{l} \Delta C_{\ell m} \\ -\Delta S_{\ell m} \end{array} \right]_{\substack{\ell-m \text{ even} \\ \ell-m \text{ odd}}} \cos \bar{\psi}_{\ell mpq} + \\ \left[\begin{array}{l} \Delta S_{\ell m} \\ \Delta C_{\ell m} \end{array} \right]_{\substack{\ell-m \text{ even} \\ \ell-m \text{ odd}}} \sin \bar{\psi}_{\ell mpq} \end{array} \right\} \frac{1}{\dot{\bar{\psi}}_{\ell mpq}} + K_2 \quad (6.23)$$

and

$$\Delta M \approx -\frac{\mu R_E^\ell}{\bar{a}^{\ell+3}} \sum_{p=0}^{\ell} F_{\ell mp}(\dot{i}) \sum_{q=-\infty}^{\infty} \frac{1}{\dot{\bar{\psi}}_{\ell mpq}} \left[G_{\ell pq}(\dot{e}) \left\{ \frac{3(\ell - 2p + q)}{\dot{\bar{\psi}}_{\ell mpq}} - \frac{2(\ell + 1)}{\bar{n}} \right\} \right]$$

$$+ \frac{\partial}{\partial e} G_{\ell pq}(\bar{e}) \cdot \frac{1}{n\bar{e}} \left[\begin{array}{c} \ell-m \text{ even} \\ \Delta C_{\ell m} \\ -\Delta S_{\ell m} \\ \ell-m \text{ odd} \end{array} \right] \sin \bar{\psi}_{\ell mpq} - \begin{array}{c} \ell-m \text{ even} \\ \Delta S_{\ell m} \\ \Delta C_{\ell m} \\ \ell-m \text{ odd} \end{array} \cos \bar{\psi}_{\ell mpq} \right] - \frac{3}{2} \frac{\bar{n}}{a} K_1 (t - t_0) + K_3 \quad (6.24)$$

where K_2 and K_3 are constants to account for Δe and ΔM being zero at time t_0 . In equation (6.24), ΔM contains the interaction of Δa with the inverse square component of force. Equations (6.22), (6.23) and (6.24) are substituted into equation (6.6) and truncated at order e^0 . The even zonals, odd zonals and tesserals ($m \neq 0$) are dealt with separately. For example, the periodic perturbations in r due to errors in the even zonal harmonic coefficients can be expressed, to order e^0 , by

$$\begin{aligned} \Delta r_{\ell,0} \text{ periodic; } \ell \text{ even} &\approx \Delta C_{\ell 0} \frac{\mu R_E^\ell}{\bar{n} \bar{a}^{\ell+2}} \left\{ 4 \sum_{p=0}^{\frac{\ell}{2}-1} F_{\ell 0p}(\bar{i}) \cos \bar{\psi}_{\ell 0p0} \frac{(\ell - 2p)}{\dot{\bar{\psi}}_{\ell 0p0}} \right. \\ &\quad \left. - \sum_{p=0}^{\ell} F_{\ell 0p}(\bar{i}) \sum_{q=\pm 1} \frac{d}{de} G_{\ell pq}(\bar{e}) \left[q \cos \bar{M} (\cos \bar{\psi}_{\ell 0pq} - \cos c_{\ell 0pq}) + \sin \bar{M} (\sin \bar{\psi}_{\ell 0pq} \right. \right. \\ &\quad \left. \left. - \sin c_{\ell 0pq}) \right] / \dot{\bar{\psi}}_{\ell 0pq} \right\} \quad (6.25) \end{aligned}$$

wherein $c_{\ell 0pq} = (\ell - 2p + q)(\bar{\omega}_0 + \bar{M}_0) - q\bar{\omega}_0 + m(\bar{\Omega}_0 - \theta_{s,0})$ gives the initial mean angular argument. Now

$$\begin{aligned} -\cos \bar{M} \cos \bar{\psi}_{\ell 0p-1} + \sin \bar{M} \sin \bar{\psi}_{\ell 0p-1} &= -\cos [(\ell - 2p)(\bar{\omega} + \bar{M})] \quad \text{and} \\ \cos \bar{M} \cos \bar{\psi}_{\ell 0p1} + \sin \bar{M} \sin \bar{\psi}_{\ell 0p1} &= \cos [(\ell - 2p)(\bar{\omega} + \bar{M})] \end{aligned}$$

so that the frequencies in equation (6.25) are at \bar{M} and $(\ell - 2p)(\bar{\omega} + \bar{M})$ for $p = 0, \dots, \ell/2 - 1$. These are equivalent to one cycle and $(\ell - 2p)$ cycles per revolution, respectively since $\bar{\omega}$ is small for SEASAT (approximately 1°/day). However, the lower even zonal harmonic terms are accurately known and such errors

are relatively small. Also, due to the altitude attenuation factor $\left(\frac{R_E}{\bar{a}}\right)^{\varrho}$, these errors become less significant for high ϱ .

Similarly, the odd zonals yield error frequencies of one cycle and $(\varrho - 2p)$ cycles per revolution, where $p \neq (\varrho \pm 1)/2$. Once again, because the lower odd zonal coefficients are accurately known, such errors are relatively small. The tesseral harmonics yield frequencies of one cycle per revolution and $(\varrho - 2p + q)(\dot{\bar{\omega}} + \dot{\bar{M}}) + m(\dot{\bar{\Omega}} - \dot{\bar{\theta}}_s)$. Since many of these coefficients are poorly determined, these terms may lead to large errors, particularly when $\dot{\bar{\psi}}_{\varrho mpq}$ is small, that is for low frequencies.

Hence it is concluded that the dominant radial orbit errors associated with gravity field mis-modelling occur near to one cycle per revolution, that is of low frequency. This confirms the earlier work of Marsh and Williamson [38] and Wagner [39] who show that the main radial orbit error occurs below two cycles per revolution. A similar analysis and conclusion was drawn by Engelis [35]. Both Wagner and Engelis have plotted spectral graphs to show the frequencies of these error terms.

Spectral graphs of this nature have also been derived using numerical rather than analytical techniques. Figure 6.1, for instance, shows the spectrum of the radial orbital differences between the coefficients (including the central term, μ) of the GEM-T1 and PGS-S3 gravity fields when applied to SEASAT. This graph has been obtained by converging the orbits using each gravity field and then comparing the radial differences which are plotted in Figure 6.2. As anticipated from the theory, the main error frequencies are seen to occur near to one cycle per revolution. If the spectrum is derived from numerical integrations using the same state vector for each gravity field, then the results are as plotted in Figure 6.3. Here, there is a large (6m) once per revolution term and a significant (60cm) twice per revolution term. Evidently, most of the once per revolution term can be accommodated by a change in the initial position, whilst all of the twice per revolution term can be so absorbed. Equation (6.6) shows how a change in the initial position can reduce the amplitude of the once per revolution term, i.e.

$$\Delta r_{11} = \Delta a_1 - \bar{a} \Delta e_1 \cos \bar{M} + \bar{a} \bar{e} \Delta M_1 \sin \bar{M} \quad (6.26)$$

Δr_{11} representing a first order change in r due to changes in the initial values of a , e and M , represented by Δa_1 , Δe_1 and ΔM_1 , respectively. Since the $\cos \bar{M}$ and $\sin \bar{M}$ terms are multiplied by Δe_1 and ΔM_1 , respectively, changes in e and M at the initial epoch can accommodate a once per revolution term. To explain the twice per revolution term of Figure 6.3, it is necessary to refer to Engelis [35] once more. His equation (32) is

$$\begin{aligned} \Delta r_2 \approx \bar{a} \bar{e} \left(\frac{3}{2} \frac{\bar{n}}{\bar{a}} \Delta a_0 \right) (t - t_0) \sin \bar{M} + \frac{1}{2} \bar{a} C_{20} \left(\frac{R_E}{\bar{a}} \right)^2 \left(\frac{3}{2} \frac{\bar{n}}{\bar{a}} \Delta a_0 + \tilde{M}^f + \tilde{\omega}^r \right) \\ \times (t - t_0) \sin^2 i \sin [2(\bar{M} + \bar{\omega})] \end{aligned} \quad (6.27)$$

where Δr_2 is the second order change in r due to interaction between a constant error in the semi-major axis, Δa_0 , with the central force term and second degree harmonic. In equation (6.27), \tilde{M}^f and $\tilde{\omega}^r$ represent long period and secular variations in M and ω due to resonance. Expressions for these terms can be found in Engelis [40]. Equation (34) of Engelis [35] shows that the second order radial error, Δr_{12} , due to an error in the initial position has the form

$$\begin{aligned} \Delta r_{12} = -\bar{a} \bar{e} \left(\frac{3}{2} \frac{\bar{n}}{\bar{a}} \Delta a_1 \right) (t - t_0) \sin \bar{M} - \frac{1}{2} \bar{a} C_{20} \left(\frac{R_E}{\bar{a}} \right)^2 \left(\frac{3}{2} \frac{\bar{n}}{\bar{a}} \Delta a_1 \right) \\ \times (t - t_0) \sin^2 i \sin [2(\bar{M} + \bar{\omega})] \end{aligned} \quad (6.28)$$

which is almost identical with equation (6.27) but with opposite sign. Hence adjustment of the initial state vector in the orbital solution can simultaneously remove both Δr_2 and Δr_{12} as must have occurred for Figure 6.1. In the case of Figure 6.3, the majority of the constant error in the semi-major axis arose from using different values for the central force term, μ for the two gravity fields. If the same value of μ

is used and the differences compared from the same state vector, then the once per revolution term reduces to 2m and the twice per revolution term to 20cm.

The above analysis is adequate for deriving the dominant frequencies of radial orbit errors due to errors in the gravity field. For precise amplitude recovery of these frequencies it is necessary to expand Δr to order e and include certain interaction terms, particularly those with the central force term and the second degree harmonic. Such an expansion can be found in either Engelis [35] or Wagner [39].

Figure 6.1 : Spectral analysis of the radial orbit differences between ephemerides computed using the GEM-T1 and PGS-S3 gravity fields for the period MJD 43770 to MJD 43776.

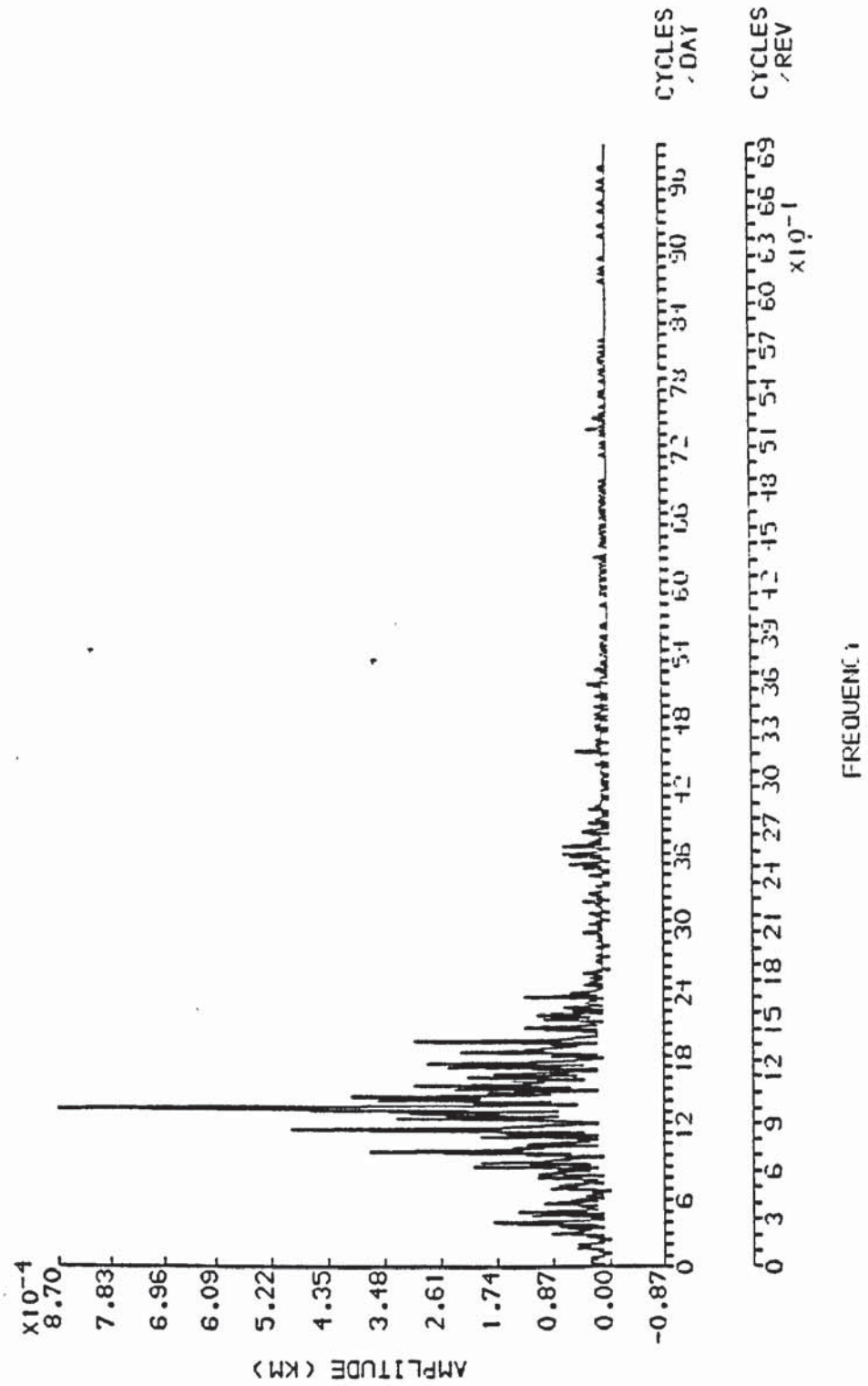


Figure 6.2 : Orbital comparison of the ephemerides computed using the GEM-T1 and PGS-S3 gravity fields for the period MJD 43770 to MJD 43776.

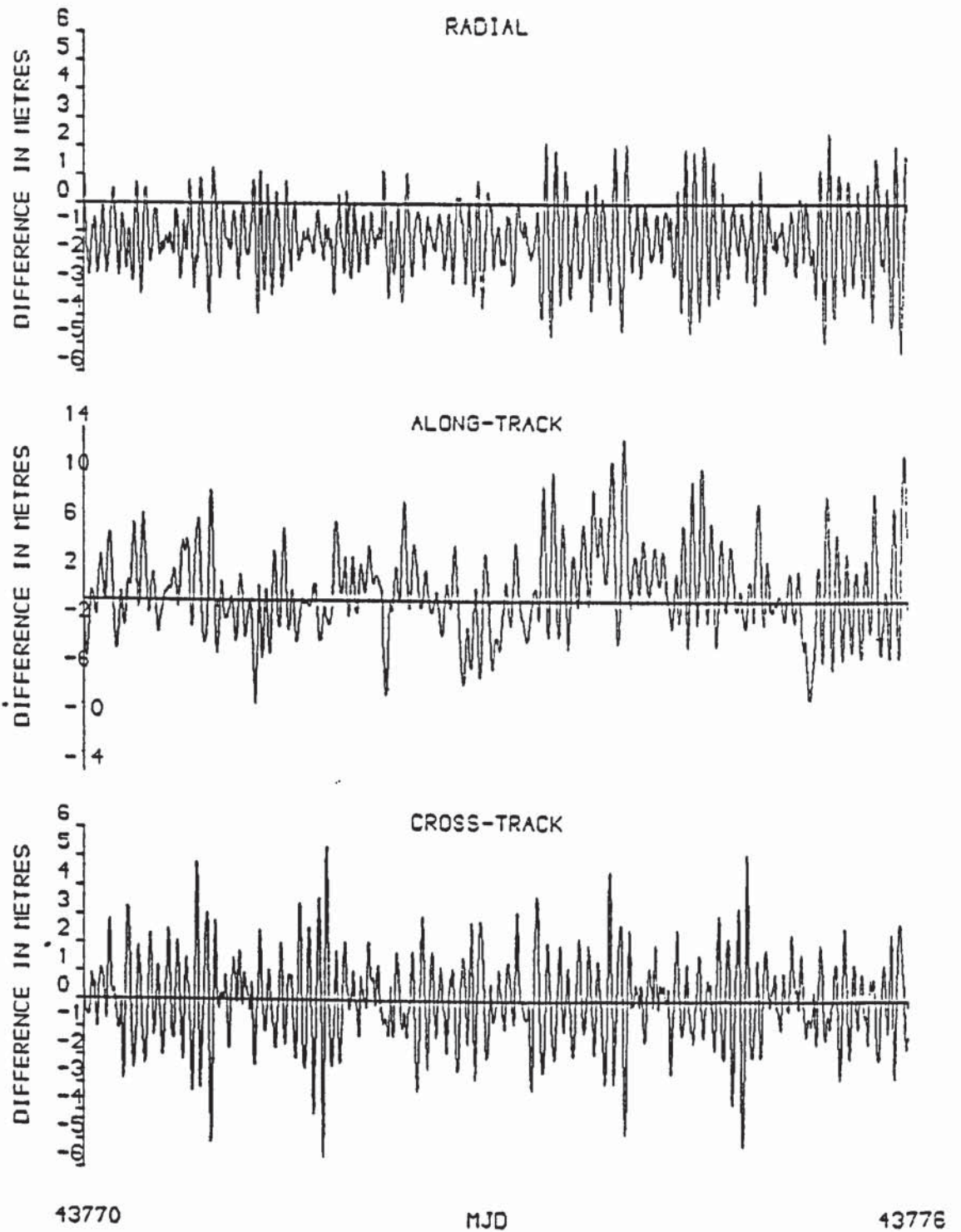
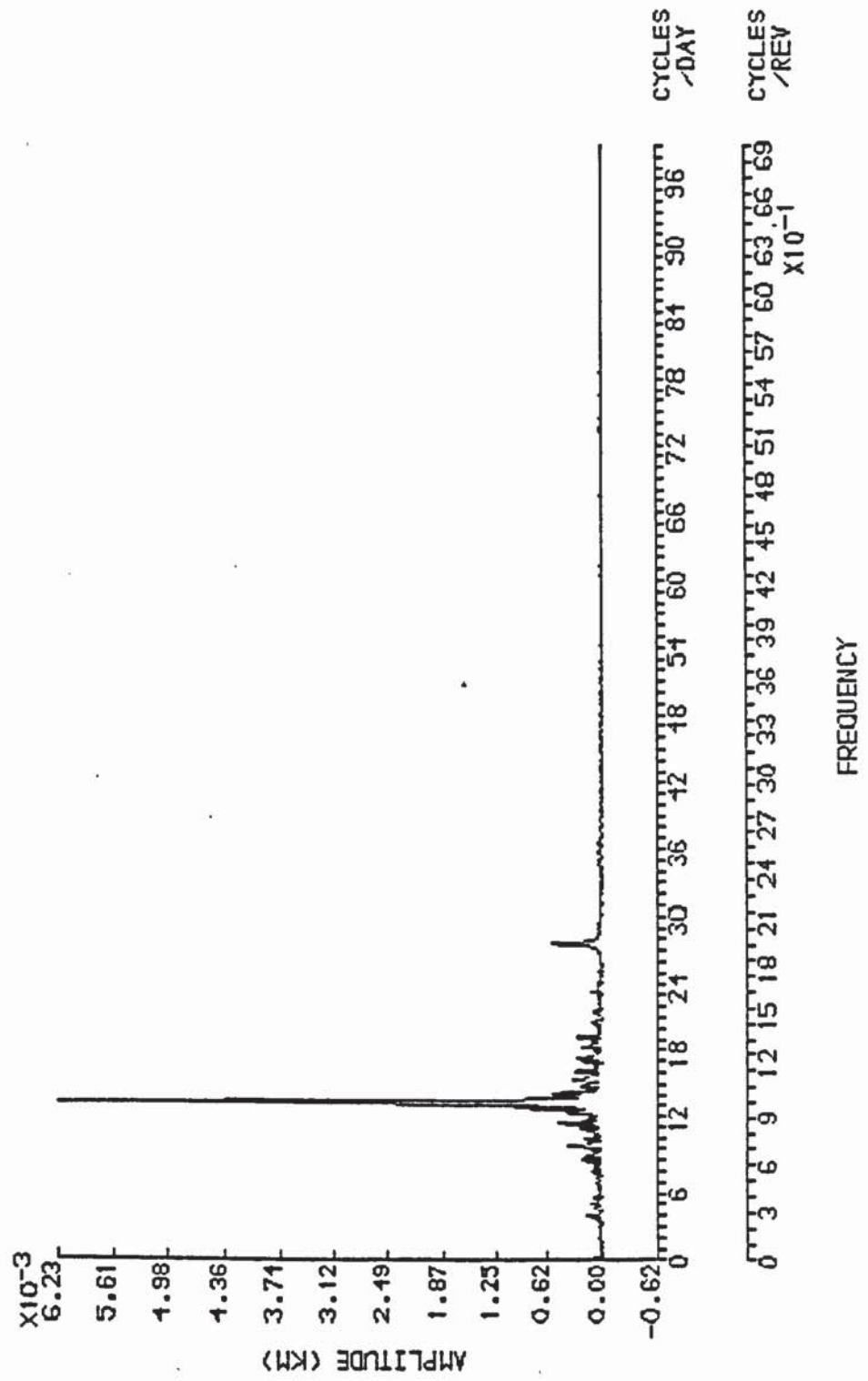


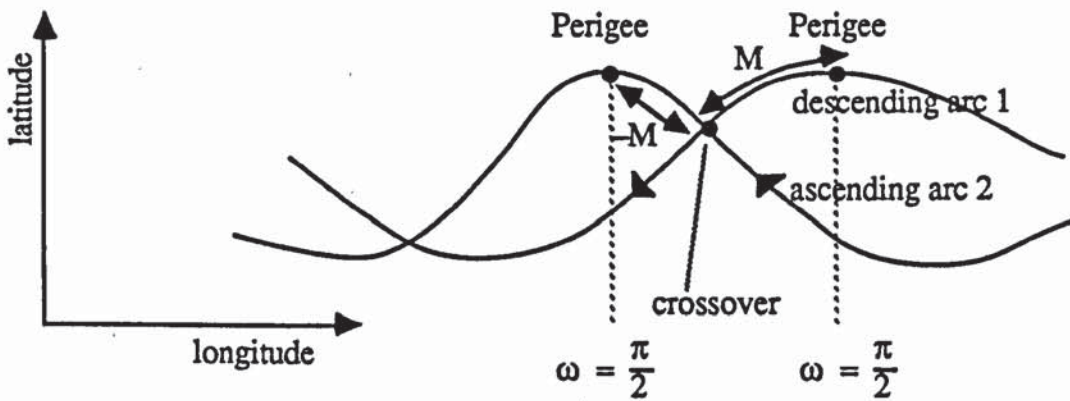
Figure 6.3 : Spectral analysis of the ephemerides computed using the GEM-T1 and PGS-S3 gravity fields and the same state vector for the period MJD 43770 to MJD 43776.



§6.3 Radial Orbit Error At A Crossover Point

For a near circular frozen orbit, that is an orbit with $\omega = \pi/2$, $\dot{\omega} \approx 0$ and e having a specific value (see Cook, 1966 [41]), the crossover points occur near to $M_1 = M$ on the descending arc and $M_2 = -M$ on the ascending arc (Figure 6.4).

Figure 6.4: Projection Of Satellite Ground Track Onto Earth's Surface For Inclination Greater Than 90° .



For each arc, the radial orbit error at the crossover, Δr_i , $i = 1, 2$ can be expressed by equation (6.6). Hence

$$\Delta r_1 \approx \Delta a - \bar{a} \Delta e \cos M_1 + \bar{a} \bar{e} \Delta M \sin M_1 \quad (6.29)$$

$$\Delta r_2 \approx \Delta a - \bar{a} \Delta e \cos M_2 + \bar{a} \bar{e} \Delta M \sin M_2. \quad (6.30)$$

SEASAT's orbit was not precisely frozen, nor a perfect repeat. Therefore $M_1 = M + \varepsilon$ and $M_2 = -M + \eta$ for small ε and η . Hence

$$\Delta r_1 - \Delta r_2 \approx 2\bar{a} \bar{e} \Delta M \cos\left(\frac{\varepsilon + \eta}{2}\right) \sin M + 2\bar{a} \Delta e \sin M \sin\left(\frac{\varepsilon + \eta}{2}\right). \quad (6.31)$$

If ε and η are small, equation (6.31) is approximately equal to $2\bar{a} \bar{e} \Delta M \sin M$, showing that the part of the radial orbit error associated with Δa and Δe is unobservable at the crossover point [34].

CHAPTER 7

ERRORS ASSOCIATED WITH ALTIMETRY AND CROSSOVERS

§7.1 The RMS Error Of Fit

The physical precision of the SEASAT altimeter, i.e. the precision of the raw altimeter measurement, was 10cm [1]. However, to use altimetry as a pseudo-radial orbit measurement, the geoid height above some reference surface, in this case the reference ellipsoid, must be added. This provides the largest source of uncertainty in the altimeter observations, producing an overall rms accuracy of between one and two metres. Thus, even though altimetry provides a more global distribution of tracking data than laser range observations, it is in general, not as accurate and leads to the higher rms values of laser plus altimeter orbits as compared to laser only orbits. However, sections 4.3 and 5.3 have shown that such orbits differ only slightly from reference orbits determined using laser data only. Hence the rms can sometimes be misleading as to the accuracy of an orbit. One way of viewing the rms is as a measure of orbital accuracy at points where data exists. The rms of the laser only orbits indicates good local accuracy near to the laser sites but is uninformative about the accuracy elsewhere in the orbit. For the laser plus altimeter orbits, the rms is much more global but is a combination of both orbital and geoidal accuracies. In order to obtain a global radial orbital rms it is preferable to use the value derived from the crossover residuals as described in section 5.2, even though some of the orbital error is unobservable by this method. Typical values of the rms radial error determined using the GEM-T1 gravity field when solving for daily drag coefficients over six day arcs, are in the region of 50 to 60cm. These values agree very well with those derived by Zandbergen et al [42] when analysing three day arcs.

§7.2 Altimetry

The altimeter residuals are mainly a consequence of errors in the orbit, the geoid and omission of sea surface topography. Spectral analysis of these residuals will recover the frequencies of the main error terms, giving an insight into their origin. To this end, the methodology devised by T. Ponman [43] which can reproduce spectral frequencies for irregularly sampled data such as altimetry, is utilized. By applying this method to various data sets from different gravity fields and geoids, graphs of the form of Figures 7.1 to 7.3 can be plotted.

Quantitative conclusions cannot be derived from these graphs since Ponman's method does not recover precise amplitudes and also, by using different gravity fields and geoids, different numbers of altimeter observations satisfy the rejection criteria. However, a qualitative feel for the nature of the errors, is possible. For instance, Figure 7.1 depicts the altimeter error frequencies for the six day arc spanning MJD 43770 to MJD 43776 determined relative to the GEM-T1 gravity field and derived geoid. Here, there is a large twice per revolution term and very little noise. Evidently, all of the orbital once per revolution error has been absorbed into the initial position. Since there is no sizeable orbital twice per revolution error (see chapter 6), the two cycles per revolution term in Figure 7.1 must be due to geoid error and sea surface topography omission. A similar conclusion can be drawn from figure 7.2 where the altimetry now refers to the GEM-10BD detailed geoid [44], for the same orbital arc. Once again, there is no once per revolution term but the twice per revolution term is larger. This must be a consequence of geoid error and not the fact that a different amount of data is accepted when using the two geoids, since in the case of the GEM-10BD geoid, less data is accepted. It can be concluded that the twice per revolution error is larger for GEM-10BD than for the GEM-T1 derived geoid. It should also be noted here, that all even zonal harmonic coefficients can contribute to the twice per revolution geoid error – it is not caused solely by C_{20} which is known very accurately. For instance, let h_g represent the geoid height with respect to the

reference ellipsoid. From [45] this can be represented by a spherical harmonic expansion of the disturbing potential and Bruns formula, i.e.

$$h_g = \frac{\mu}{r\gamma} \sum_{\ell=2}^{\infty} \left(\frac{R_E}{r}\right)^\ell \sum_{m=0}^{\ell} \left\{ C_{\ell m}^* \cos m\lambda + S_{\ell m} \sin m\lambda \right\} P_{\ell m}(\sin \phi) \quad (7.1)$$

where (ϕ, λ, r) are the geocentric coordinates of the subsatellite track, γ the normal gravity on the reference ellipsoid, $P_{\ell m}(\cdot)$ the associated Legendre functions and $C_{\ell m}^*$, $S_{\ell m}$ the harmonic coefficients of the disturbing potential. The $C_{\ell m}^*$ coefficients are related to the potential coefficients, $C_{\ell m}$, by

$$C_{\ell m}^* = C_{\ell m} - C_{\ell m}^{\text{ref}} \quad (7.2)$$

with all $C_{\ell m}^{\text{ref}}$ being zero except for the even degree zonal terms. (These coefficients represent the potential of the reference ellipsoid.) Using the transformations of Kaula [20], it is possible to map an error in h_g , due to errors $\Delta C_{\ell m}^*$ and $\Delta S_{\ell m}$ in $C_{\ell m}^*$ and $S_{\ell m}$, respectively, into the orbital plane. For a near circular orbit this produces a radial orbit error, $O_{\ell m}$, of the form [46]

$$O_{\ell m} = \sum_{p=0}^{\ell} F_{\ell mp}(i) [A_{\ell m} \cos \psi_{\ell mp} + B_{\ell m} \sin \psi_{\ell mp}] \quad (7.3)$$

for constants $A_{\ell m}$, $B_{\ell m}$ dependent upon $\Delta C_{\ell m}^*$, $\Delta S_{\ell m}$, μ , R_E , γ and a . In equation (7.3) $\psi_{\ell mp} = (\ell - 2p)(\omega + M) + m(\Omega - \theta_s)$. For the even zonal harmonic terms, $m = 0$ and ℓ is even. Hence as p takes on the values 0 upto ℓ , $(\ell - 2p)$ will take all even values between $-\ell$ and ℓ . In particular, it is seen that

all even zonal terms will contribute to an error term of frequency $2(\dot{\omega} + \dot{M})$ that is, twice per revolution.

Returning to Figure 7.2, it is also pertinent to note here, that there is an increased noise level when using GEM-10BD, with significant error frequencies at 3, 5, 6 and 7 cycles per revolution. This provides a strong case for the continued use of the GEM-T1 derived geoid in altimeter processing.

Figure 7.3 depicts the error frequencies for the same orbital arc as Figures 7.1 and 7.2, but now the orbit is determined relative to the PGS-S3 gravity field and GEM-T1 derived geoid. As explained above, this graph cannot be compared quantitatively with Figure 7.1, but it is apparent that PGS-S3 contains a more significant once per revolution error than GEM-T1, together with significant errors near to one cycle per revolution. Comparison of these two graphs shows clearly the orbital improvement due to the general purpose gravity field, GEM-T1 over the SEASAT tailored field, PGS-S3, for the three day repeat orbit. Similar graphs have also been plotted for arcs occurring during SEASAT's 17 day repeat orbit and show the same trends. However, one difference noticed, is a significant once per revolution term for the GEM-T1 gravity field over this period. Evidently, for the 17 day repeat orbit, it is not possible to absorb all of the orbital once per revolution term into the initial position, showing that GEM-T1 'fits' the three day repeat orbit to a higher level of accuracy.

Figure 7.1 : Spectral analysis of the altimeter residuals for the period MJD 43770 to MJD 43776 relative to the GEM-T1 gravity field and derived geoid, CIRA 72 atmospheric model, daily drag coefficients and NASA 'area tables' for SEASAT. Laser data nominally weighted. Altimetry weighted according to an 'a priori' standard deviation of 2m.

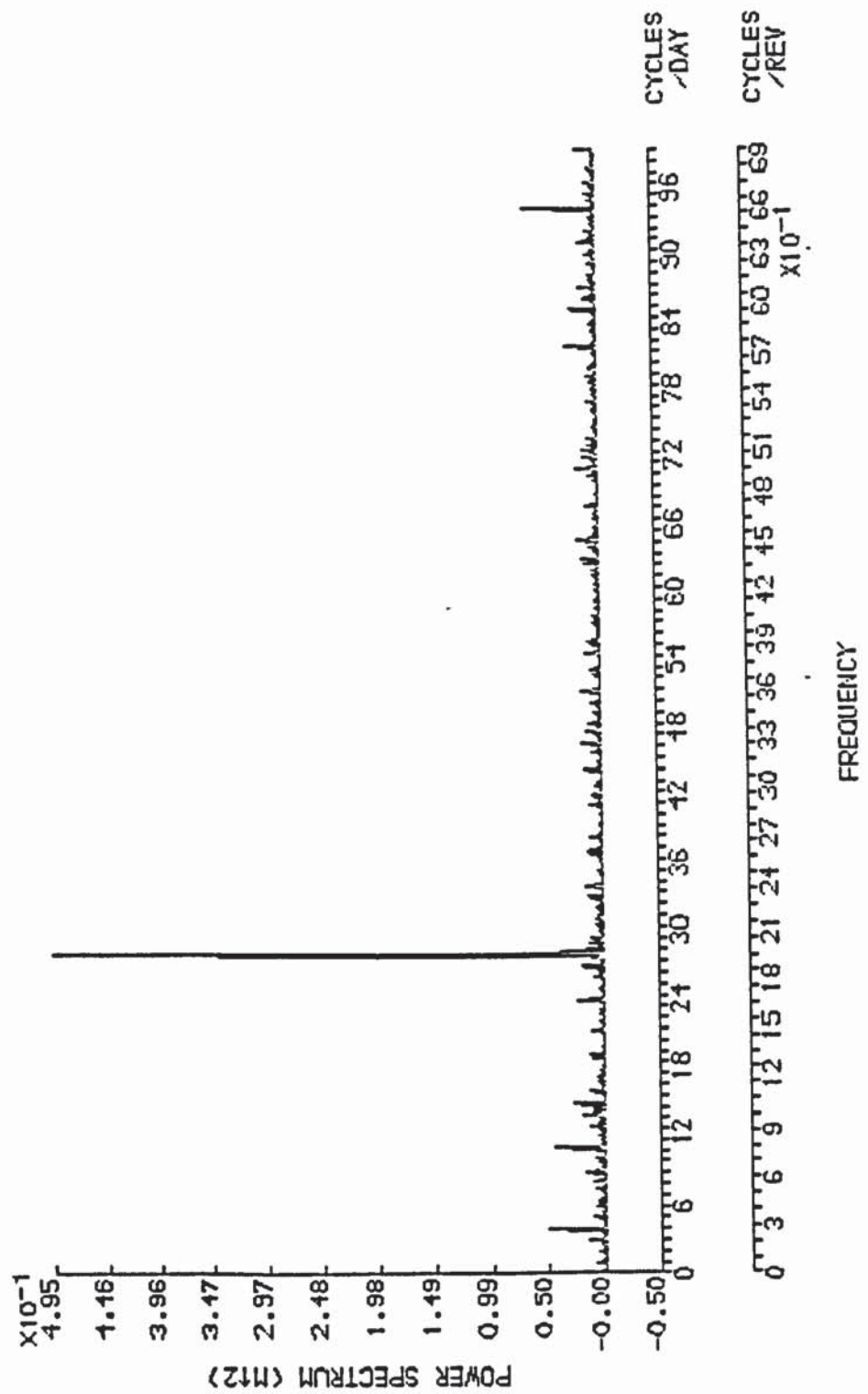


Figure 7.2 : As for Figure 7.1 except using GEM-10B geoid.

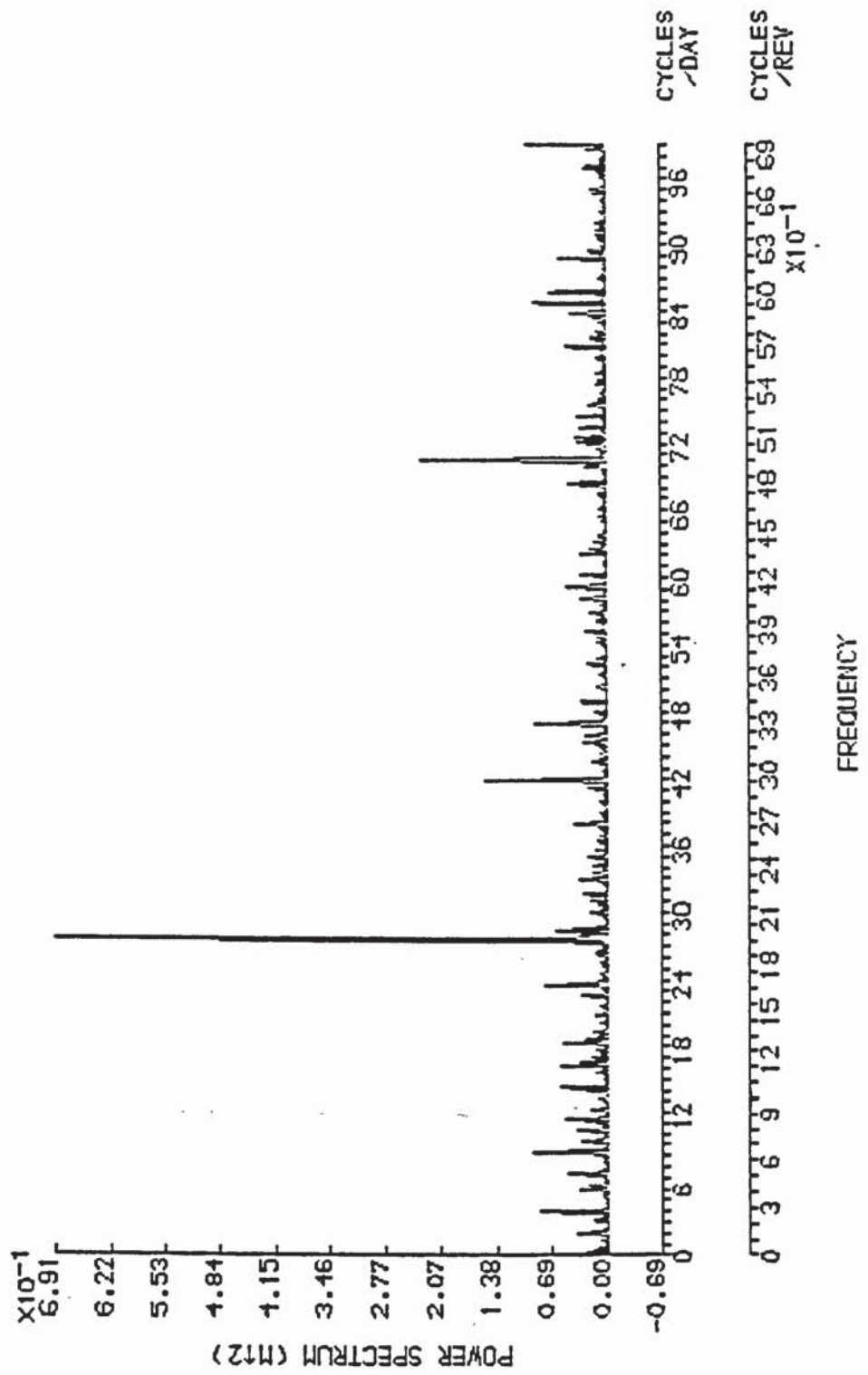
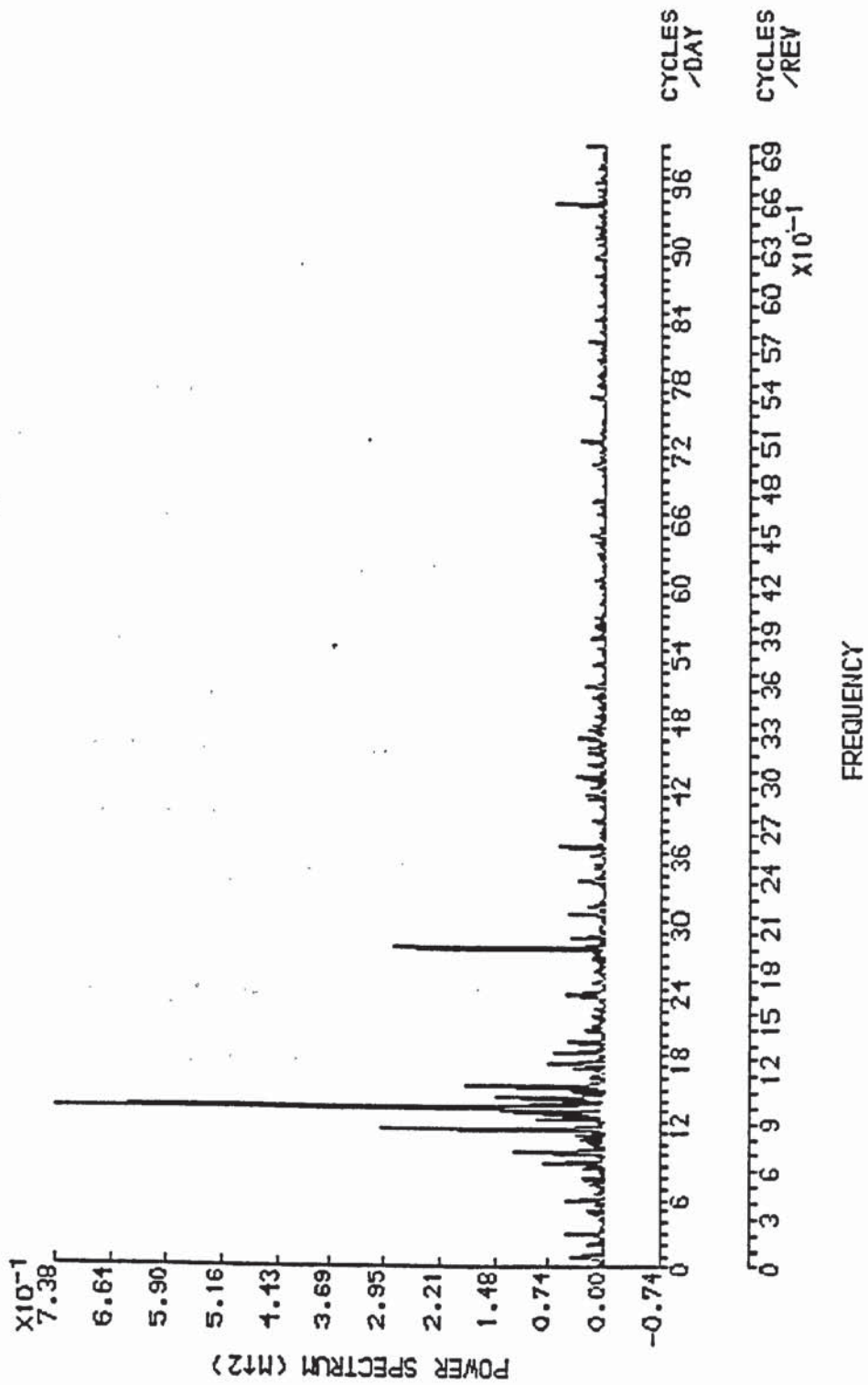


Figure 7.3 : As for Figure 7.1 except using the PGS-S3 gravity field.



§7.3 Crossovers

Since crossover residuals provide a measure of orbital error, it is possible to obtain an indication of the observable geographically related orbit error by analysing crossover residuals in blocks of latitude and longitude on the earth's surface. Such residuals are grouped together in various blocks and the rms and mean values of each block calculated. Table 7.1 illustrates the results for the six day arc spanning MJD 43764 to MJD 43770, determined relative to the GEM-T1 gravity field when estimating a state vector at epoch, daily drag coefficients and a single solar reflectivity coefficient. The orbit was derived from laser data only (nominal weight), that is, with zero weight applied to the crossovers. Note that there is a northern-southern hemisphere bias in the values of the means from each region, this bias being manifested as positive in the north and negative in the south. Further, the rms values are larger at the higher latitudes.

Table 7.2 details the same information but with crossover data included and assigned a 0.5m standard deviation. In this case, both mean and rms values decrease relative to their corresponding values in Table 7.1. Such an occurrence has also been observed by Wakker et al [5] who relate the offset to a time-dependent eccentricity error, the likely cause of which is solar radiation pressure mis-modelling resulting from poor quality data [47]. In the case of this arc, the poor data occurs on the last two days of the laser only solution. Adding crossovers, particularly over this period, helps to constrain the solar radiation pressure coefficient.

Table 7.1 : Crossover residuals for MJD 43764 to MJD 43770. Laser data weighted nominally. Zero weight applied to both altimetry and crossovers. Values are rms (cm), mean (cm) and number of crossovers, reading downwards.

LATITUDE > LONGITUDE	-60	-40	-20	0	20	40	60	80
0								
117.2477	68.7523	76.0086	13.0119	43.7500	0.0000	45.4245	52.6050	
-22.9912	-35.7546	-33.2556	4.5333	17.6500	138.3000	24.7667	36.8633	
30	34	33	9	3	2	1	3	30
84.2816	72.9077	62.3009	70.5008	57.0156	0.0000	0.0000	52.1635	
-22.7688	-59.0829	-38.3421	1.2800	14.3000	0.0000	0.0000	51.1238	
60	32	35	19	5	5	0	0	21
102.8753	60.7703	68.9123	115.5855	54.1216	0.0000	0.0000	0.0000	
-36.9353	-51.4968	-45.3300	-22.1800	-17.3300	-70.9000	0.0000	0.0000	
90	17	31	20	5	10	1	0	0
98.6887	61.5210	67.4960	63.7697	52.4867	0.0000	0.0000	0.0000	
-33.2000	-64.1906	-47.6889	-17.4375	-4.4333	-0.5000	0.0000	0.0000	
120	13	32	18	8	6	1	0	0
84.7430	53.0148	70.5062	77.4660	50.3034	66.5645	48.6409	56.8950	
-24.5130	-45.7440	2.6250	2.8750	15.3333	14.8182	16.0000	154.8333	
150	23	25	4	4	6	11	3	3
84.9884	86.9827	60.2656	26.6432	58.8219	106.8498	99.2250	88.6933	
-24.7000	-45.5958	-12.3214	-50.4143	34.7222	20.5000	-2.3308	29.1822	
180	36	24	14	7	9	15	26	28
89.0282	44.5223	56.3090	46.9645	46.0788	57.6210	87.6295	66.1118	
-38.0193	-28.6500	-8.1857	0.4333	-0.1000	40.5000	44.1583	51.1576	
210	57	28	21	6	11	17	24	33
81.8281	68.6987	65.6529	29.5640	75.5365	80.0777	76.2407	86.4238	
-51.7046	-30.5759	-33.5235	-9.7667	9.1857	37.8316	58.2278	45.2310	
240	65	29	17	6	14	19	18	29
77.5294	75.3987	64.6208	77.8609	40.6013	31.2336	0.0000	97.8369	
-16.0038	-41.6909	-2.2000	26.4700	20.1100	11.7333	121.8000	23.3533	
270	52	33	19	10	10	3	1	15
64.1725	56.0539	88.0686	4.4000	23.9309	54.6920	17.8793	70.2418	
-38.6550	-45.4842	-17.1636	22.3000	-29.8000	16.9800	44.8333	51.7692	
300	40	19	11	2	3	15	3	26
101.7347	73.0015	35.8249	0.0000	47.5402	69.5733	56.4980	85.0111	
-24.6315	-28.5741	-15.0333	-16.6000	-29.1857	27.9714	32.8667	16.1750	
330	54	27	9	1	7	14	27	16
96.1301	71.4824	60.2781	29.7983	45.7051	36.3876	40.4582	49.3674	
-19.3489	-31.8345	-7.0789	-9.9200	8.5444	10.9889	53.7889	44.8451	
360	47	29	19	5	9	9	18	51

Table 7.2 : As for Table 7.1 except using crossovers with an assigned standard deviation of 0.5m.

LATITUDE >	-80	-60	-40	-20	0	20	40	60	80
0	110.2432	67.2309	72.4811	6.0780	45.6500	0.0000	48.4865	47.4829	
	-17.3061	-14.2909	-18.2222	5.2667	12.5500	86.2000	1.7667	14.3667	
	33	33	9	3	2		1	3	30
30	83.3856	67.1993	57.4695	69.4757	56.4917	0.0000	0.0000	49.3746	
	2.1438	-38.0371	-23.8000	4.8000	12.1200	0.0000	0.0000	32.7810	
	32	35	19	5	5		0	0	21
60	102.0119	53.2454	71.4081	111.4954	51.6007	0.0000	0.0000	0.0000	
	-24.7222	-28.9968	-40.4048	-18.3000	-19.4300	-75.1000	0.0000	0.0000	
	18	31	21	5	10		1	0	0
90	92.6116	64.0369	60.7791	59.4340	51.3775	0.0000	0.0000	0.0000	
	-14.4385	-48.3529	-28.2833	-11.4375	-4.4333	-4.2000	0.0000	0.0000	
	13	34	18	8	6		1	0	0
120	94.6293	45.5245	60.7428	73.1247	47.9948	65.3349	54.6757	59.3731	
	-16.5731	-21.9600	15.3250	6.3250	13.9833	4.3636	4.1333	139.1000	
	26	25	4	4	6		11	3	3
150	79.8053	88.2659	55.8039	24.3723	61.9950	107.9868	100.3261	80.1145	
	-18.7286	-25.2208	-0.8429	-29.3429	32.0556	5.3800	-27.6038	16.1393	
	35	24	14	7	9		15	26	28
180	91.1777	41.6565	51.4265	43.3759	42.6999	53.3099	80.9279	56.5356	
	-26.1603	-7.4286	4.8381	1.8500	-4.1182	25.3647	20.3583	24.5879	
	63	28	21	6	11		17	24	33
210	77.9222	63.8374	65.7579	25.7854	72.7721	74.7039	69.9622	79.7245	
	-24.1515	-9.1345	-20.2294	-7.7500	3.5357	23.0158	36.7111	17.9310	
	66	29	17	6	14		19	18	29
240	76.6838	79.3396	62.3939	71.5966	39.9034	26.6842	0.0000	92.1211	
	-1.5731	-20.6800	15.0421	29.4500	18.2400	3.7000	97.7000	26.4733	
	52	35	19	10	10		3	1	15
270	69.1644	59.0245	84.5766	4.6000	24.0351	51.6970	10.8086	69.3223	
	-24.6732	-25.3737	-3.3455	34.9000	-25.9000	-3.7800	19.2000	35.7071	
	41	19	11	2	3		15	3	28
300	92.1965	70.9387	30.6262	0.0000	41.7145	64.7848	51.0531	78.1752	
	-22.1151	-8.8037	-4.8111	-12.2000	-31.2286	13.0857	4.4667	-13.0500	
	53	27	9	1	7		14	27	16
330	96.1822	65.9586	60.4314	36.6628	46.0035	30.2535	36.8746	42.2592	
	-3.9347	-11.0828	5.2526	-7.1200	5.0333	-2.0889	30.8222	21.1157	
	49	29	19	5	9		9	18	51
360									

Table 7.2 : As for Table 7.1 except using crossovers with an assigned standard deviation of 0.5m.

LATITUDE > LONGITUDE	-80	-60	-40	-20	0	20	40	60	80
0	110.2432	67.2309	72.4811	6.0780	45.6500	45.6500	0.0000	48.4865	47.4829
	-17.3061	-14.2909	-18.2222	5.2667	12.5500	12.5500	86.2000	1.7667	14.3667
	33	33	9	3	2	2	1	3	30
30	83.3856	67.1993	57.4695	69.4757	56.4917	0.0000	0.0000	0.0000	49.3746
	2.1438	-38.0371	-23.8000	4.8000	12.1200	0.0000	0.0000	0.0000	32.7810
	32	35	19	5	5	0	0	0	21
60	102.0119	53.2454	71.4081	111.4954	51.6007	0.0000	0.0000	0.0000	0.0000
	-24.7222	-28.9968	-40.4048	-18.3000	-19.4300	-75.1000	0.0000	0.0000	0.0000
	18	31	21	5	10	1	0	0	0
90	92.6116	64.0369	60.7791	59.4340	51.3775	0.0000	0.0000	0.0000	0.0000
	-14.4385	-48.3529	-28.2833	-11.4375	-4.4333	-4.2000	0.0000	0.0000	0.0000
	13	34	18	8	6	1	0	0	0
120	94.6293	45.5245	60.7428	73.1247	47.9948	65.3349	54.6757	59.3731	138.1000
	-16.5731	-21.9600	15.3250	6.3250	13.9833	4.3636	4.1333	138.1000	3
	26	25	4	4	6	11	3	3	3
150	79.8053	88.2659	55.8039	24.3723	61.9950	107.9868	100.3261	80.1145	16.1393
	-18.7286	-25.2208	-0.8429	-29.3429	32.0556	5.3800	-27.6038	16.1393	28
	35	24	14	7	9	15	26	28	28
180	91.1777	41.6565	51.4285	43.3759	42.6999	53.3099	80.9279	56.5356	24.5879
	-26.1603	-7.4286	4.8381	1.8500	-4.1182	25.3647	20.3583	24.5879	33
	63	28	21	6	11	17	24	33	33
210	77.9222	63.8374	65.7579	25.7854	72.7721	74.7039	69.9622	79.7245	17.9310
	-24.1515	-9.1345	-20.2294	-7.7500	3.5357	23.0158	36.7111	17.9310	29
	66	29	17	6	14	19	18	29	29
240	76.6838	79.3396	62.3939	71.5966	39.9034	26.6842	0.0000	92.1211	26.4733
	-1.5731	-20.6800	15.0421	29.4500	18.2400	3.7000	97.7000	26.4733	15
	52	35	19	10	10	3	1	15	15
270	69.1644	59.0245	84.5766	4.6000	24.0351	51.6970	10.8086	69.3223	35.7071
	-24.6732	-25.3737	-3.3455	34.9000	-25.9000	-3.7800	19.2000	35.7071	28
	41	19	11	2	3	15	3	28	28
300	92.1965	70.9387	30.6262	0.0000	41.7145	64.7848	51.0531	78.1752	-13.0500
	-22.1151	-8.8037	-4.8111	-12.2000	-31.2286	13.0857	4.4667	-13.0500	16
	53	27	9	1	7	14	27	16	16
330	96.1822	65.9586	60.4314	36.6628	46.0035	30.2535	36.8746	42.2592	21.1157
	-3.9347	-11.0828	5.2526	-7.1200	5.0333	-2.0889	30.8222	21.1157	51
	49	29	19	5	9	9	18	51	51
360									

Table 7.3 : As for Table 7.1 except using alimtetry with an assigned standard deviation of 1m.

LATITUDE > LONGITUDE	-80	-60	-40	-20	0	20	40	60	80
0									
109.9747	66.7634	75.5394	10.1339	40.6500	0.0000	49.6243	47.3696		
-17.2182	-14.8636	-18.4333	6.7667	12.1500	80.4000	0.0000	0.3667	13.9433	
33	33	9	3	2	1	3	30		
30									
83.5829	67.9488	58.4539	66.7829	52.1889	0.0000	0.0000	49.6089		
2.2281	-38.5143	-24.2842	5.7800	10.9600	0.0000	0.0000	32.6571		
32	35	19	5	5	0	0	21		
60									
101.1455	53.6535	74.0298	115.1619	53.0708	0.0000	0.0000	0.0000	0.0000	
-24.7167	-29.5645	-41.3714	-17.3200	-22.5600	-70.5000	0.0000	0.0000	0.0000	
18	31	21	5	10	1	0	0		
90									
93.0932	65.5821	63.0352	63.8411	54.7546	0.0000	0.0000	0.0000	0.0000	
-14.5385	-49.0529	-29.4611	-11.5375	-5.9500	0.4000	0.0000	0.0000	0.0000	
13	34	18	8	6	1	0	0		
120									
95.0815	46.6946	63.3355	75.8966	48.1663	62.6631	54.5510	59.3658		
-16.3038	-21.9560	17.5250	8.8250	12.3833	4.7091	6.5000	138.6333		
26	25	4	4	6	11	3	3		
150									
84.6032	90.6778	57.3319	22.5724	58.0648	103.8755	98.4731	80.0696		
-23.2000	-24.9375	-0.1143	-26.0143	30.3111	5.3133	-27.1692	15.3536		
36	24	14	7	9	15	26	28		
180									
91.0653	42.6749	52.3574	44.6348	41.3759	52.7804	80.4981	56.1602		
-25.3603	-6.6321	5.8524	4.9667	-3.8091	25.2588	20.7125	23.8879		
63	28	21	6	11	17	24	33		
210									
77.7847	62.3472	64.1396	25.8699	74.9430	75.8010	72.1553	79.4430		
-23.1727	-8.5310	-19.3529	-4.6000	3.2571	23.8579	37.1667	17.3104		
66	29	17	6	14	19	18	29		
240									
76.3788	80.3195	65.4251	73.9342	39.6661	26.4890	0.0000	92.1792		
-1.1135	-19.3771	16.8158	32.2800	17.2000	8.1333	99.5000	26.0333		
52	35	19	10	10	3	1	15		
270									
69.1292	60.9268	88.4396	4.7500	27.5415	51.4942	7.9776	69.4199		
-24.3366	-25.3895	-2.7909	40.1500	-27.2333	-2.9133	17.4667	35.1929		
41	19	11	2	3	15	3	28		
300									
92.5127	70.3796	33.4631	0.0000	43.8958	67.7140	51.7933	77.6987		
-21.7491	-9.1333	-3.4111	-7.1000	-34.7429	12.7571	4.4444	-13.5500		
53	27	9	1	7	14	27	16		
330									
96.0601	66.4335	56.9359	33.7833	45.9319	32.4833	36.5530	42.1762		
-3.8225	-11.6103	4.1842	-6.2200	4.3222	-2.7556	30.5444	20.5000		
49	29	19	5	9	9	18	51		
360									

Consequently, supplementing the laser only orbit with pure altimetry should have a similar effect. Results of this analysis are presented in Table 7.3 where altimetry has been utilized with a standard deviation of 1m. The table shows very good agreement with Table 7.2 proving that a more global set of data helps to reduce the north-south bias which occurs in the crossover residuals due to poor determination of the solar radiation pressure coefficient.

The example cited above is an extreme case and the offset quite large. In some cases the bias is much smaller, zero or even negative in the north and positive in the south. For instance, there is only a very small offset in the laser only orbit of MJD 43770 to MJD 43776 and adding altimetry or crossovers has little effect. However, this orbit has been derived from a much better laser tracking data set so that the solar radiation pressure coefficient is well-determined.

§7.4 Time Tag, Offset And Once And Twice Per Revolution Errors

As yet unmentioned, is the effect of a timing error on the altimeter measurements. Such an error will cause the calculated satellite position to be earlier or later than the corresponding altimeter height measurement, depending on the sign of the error. Whichever is the case, the resulting altimeter residuals will experience two maxima and two minima (see Appendix 2). This determines a twice per revolution error and consequently, a time tag bias on the altimeter is indistinguishable from a geoid or sea surface topography error at this frequency. However, calibration of the SEASAT altimeter resulted in the derivation of a -79.4ms time tag bias which has been removed from the time tags on the GDR tapes [29]. Any residual error, should therefore be small, but cannot be recovered from altimetry directly. A combination of pure altimetry and crossovers is needed to separate a twice per revolution term from a time tag error on the altimeter measurements. At the crossover point, the twice per revolution error in the geoid and sea surface topography will be

the same on both tracks and hence unobservable. The time tag error however, would propagate into an orbital error and so will be observable from the crossovers.

In practice it is possible to use pure altimetry to determine once and twice per revolution terms as well as a constant offset, whilst using the crossovers to determine a time tag bias plus the portion of the once per revolution error which is observable at the crossover (see section 6.3). In this method, the various terms are estimated from altimetry and crossovers separately.

Let Δh_i denote the i^{th} altimeter residual and Δh_i^m the modelled residual given by

$$\Delta h_i^m = A_1 \cos M_i + B_1 \sin M_i + A_2 \cos 2M_i + B_2 \sin 2M_i + C_0 \quad (7.4)$$

wherein M_i is the mean anomaly of the i^{th} observation and A_1, B_1, A_2, B_2 and C_0 are the coefficients to be determined. Solution of these coefficients is achieved using a least squares fit of Δh_i^m to Δh_i for $i = 1, \dots, N$; N being the total number of altimeter residuals satisfying the rejection criterion. Then

$$\min \sum_{i=1}^N (\Delta h_i - \Delta h_i^m)^2$$

is equivalent to solving

$$\sum_{i=1}^N (\Delta h_i - \Delta h_i^m) \frac{\partial \Delta h_i^m}{\partial p} = 0$$

for $p \in (A_1, B_1, A_2, B_2, C_0)$. This results in the solution

$$\begin{pmatrix} A_1 \\ B_1 \\ A_2 \\ B_2 \\ C_0 \end{pmatrix} = D^{-1} \begin{pmatrix} \sum_{i=1}^N \Delta h_i \cos M_i \\ \sum_{i=1}^N \Delta h_i \sin M_i \\ \sum_{i=1}^N \Delta h_i \cos 2M_i \\ \sum_{i=1}^N \Delta h_i \sin 2M_i \\ \sum_{i=1}^N \Delta h_i \end{pmatrix} \quad (7.5)$$

where D is the 5×5 matrix with elements $D_{kj} = \sum_{i=1}^N \frac{\partial \Delta h_i^m}{\partial p_k} \frac{\partial \Delta h_i^m}{\partial p_j}$ for

$k, j = 1, \dots, 5$ where $p_1 \equiv A_1$, $p_2 \equiv B_1$, $p_3 \equiv A_2$, $p_4 \equiv B_2$ and $p_5 \equiv C_0$.

Similarly, let ΔC_i denote the i^{th} crossover residual and ΔC_i^m the modelled crossover residual given by

$$\Delta C_i^m = \Delta \dot{C}_i \Delta t + A'_1 S_i \quad (7.6)$$

wherein $\Delta \dot{C}_i$ is the difference in the rate of change of the spacecraft altitude at the i^{th} crossover point; Δt the constant time tag bias to be determined; A'_1 the amplitude of the part of the once per revolution term observable at the crossover point, $S_i = \sin M_{1i} - \sin M_{2i}$ and M_{1i} and M_{2i} represent the mean anomaly at the i^{th} crossover point for the ascending and descending arcs, respectively. Minimization of the discrepancies between ΔC_i and ΔC_i^m in a least squares sense results in the

solution

$$\begin{pmatrix} \Delta t \\ A'_1 \end{pmatrix} = \begin{pmatrix} \sum_{i=1}^{N'} \Delta \dot{C}_i^2 & \sum_{i=1}^{N'} \Delta \dot{C}_i S_i \\ \sum_{i=1}^{N'} \Delta \dot{C}_i S_i & \sum_{i=1}^{N'} S_i^2 \end{pmatrix}^{-1} \begin{pmatrix} \sum_{i=1}^{N'} \Delta C_i \Delta \dot{C}_i \\ \sum_{i=1}^{N'} \Delta C_i S_i \end{pmatrix} \quad (7.7)$$

where N' denotes the total number of crossovers satisfying the rejection criterion. Note that the term, $\Delta\dot{C}_i$, is calculated as part of the crossover processing program, CROSS [17].

Results of this analysis, for the arc spanning MJD 43716 to MJD 43722 are given in Table 7.4.

Table 7.4: Resulting time tag error, offset and once and twice per revolution terms for altimetry and crossovers for the arc MJD 43716 to MJD 43722. Orbital solution computed relative to the GEM-T1 gravity field and derived geoid.

Number of altimeter observations, $N = 9722$

Number of crossover observations, $N' = 3737$

Values derived from altimetry :-	<u>Value (cm)</u>	<u>Standard error</u> (cm)
Offset (C_0)	94	2
1/rev (cos term), A_1	-4	2
1/rev (sin term), B_1	44	3
2/rev (cos term), A_2	-75	3
2/rev (sin term), B_2	-5	2

Values derived from crossovers :-

1/rev (sin term only), A'_1	-3	1
Time tag bias, Δt	0.41ms	0.13ms

The large offset of 94cm in Table 7.4 is a consequence of the altimeter height bias, miscalculation of the semi-major axis of the reference ellipsoid (Marsh et al derive a value of 72cm [48]) plus any constant height in the sea surface topography. The once per revolution term represents orbit error whilst the large twice per revolution term represents sea surface topography and maybe geoid error. Such a

term could be reduced upon the introduction of a model for sea surface topography in equation (4.1).

It is also encouraging to note the small time tag bias as derived from the crossover data, thus confirming the value on the GDR tapes. Further analysis of the time tag bias is beyond the scope of this thesis and is anyway unlikely to contradict the GDR value, given the extensive analysis of SEASAT in the early 1980's [38].

A more realistic solution than the one described above, would be obtained by combining the two data sets and solving for the terms simultaneously.

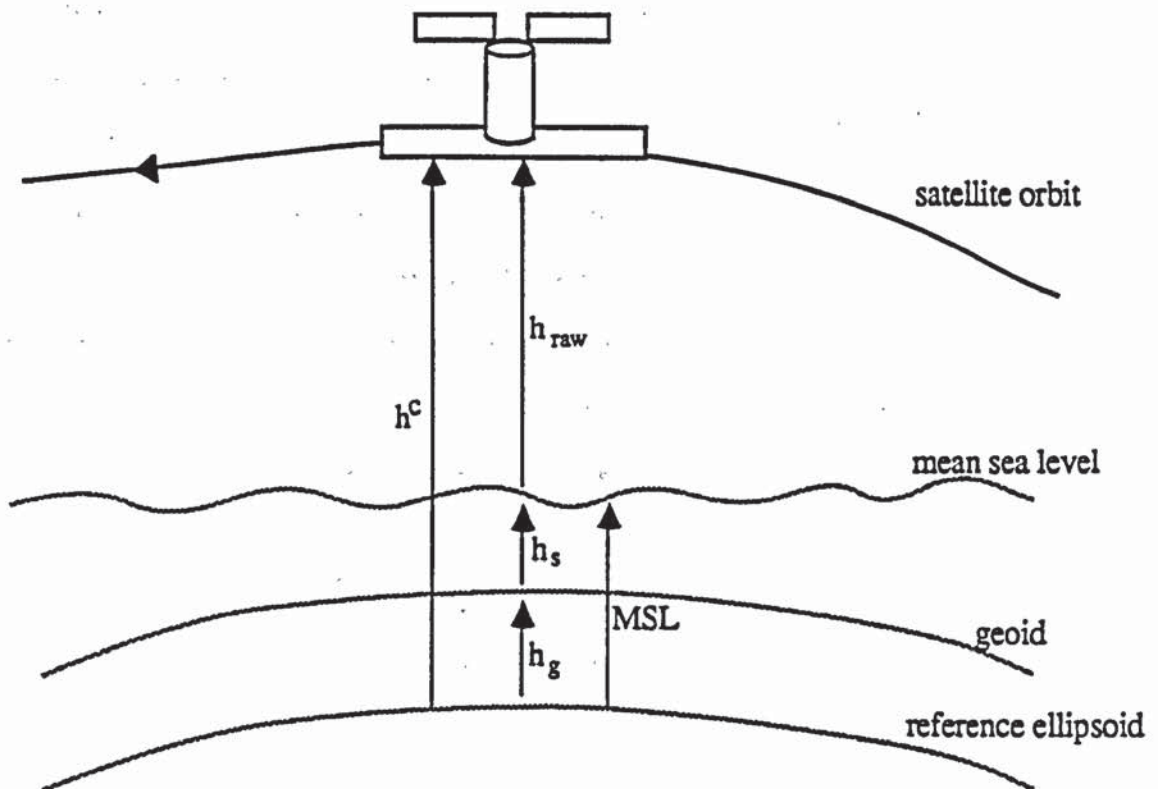
CHAPTER 8

SEA SURFACE TOPOGRAPHY

The sea surface topography is the difference in height between the oceanic geoid and the mean sea level, caused by ocean circulation phenomena, water density variations and winds. This height varies with season and so can be considered in one of two ways. The dynamic sea surface topography or DST can be regarded as the instantaneous value or at least the value averaged over a short period of time, whilst the stationary sea surface topography or SST can be regarded as the mean of DST over a long period of time, (at least one year). The model determined for sea surface topography, in this chapter, utilizes SEASAT altimetry over a 70 day period and so will be the DST for this time span.

Figure 8.1 depicts the sea surface topography in relation to the oceanic geoid and reference ellipsoid.

Figure 8.1: Sea Surface Topography.



In Figure 8.1, h_{raw} refers to the raw altimeter height above the instantaneous sea level; h^c the calculated geodetic height; h_g the geoid height above the reference ellipsoid; h_s the instantaneous sea surface topography and MSL the height of the mean sea level above the reference ellipsoid. Note that h_s is positive if the mean sea level is above the geoid and negative otherwise.

§8.1 Mathematical Formulation

The altimeter residual is assumed to be a sum of errors from the orbit, the geoid, non-modelling of the sea surface topography plus any remaining timing error on the altimeter (known to be small, as shown in chapter 7). Other correction terms of equation (4.1) are assumed exact for this analysis. This assumption may be false over certain parts of the earth for the ocean tidal corrections, but in general will be valid.

Chapter 6 showed that the orbital error frequencies occur near to one cycle per revolution, so that higher frequency terms in the altimeter residuals must be due to geoid error and non-modelling of the sea surface topography. Hence it is possible to derive the sea surface topography relative to some fixed (exact) geoid by assuming that any ocean tidal errors appear as random noise and are small. The method adopted is to expand the sea surface topography in terms of surface spherical harmonics, the most natural functions, as they characterize behaviour on a sphere. The coefficients of this expansion can then be recovered using a least squares method upon fitting the model to observed altimeter residuals. From Figure 8.1, the observed sea surface topography, $h_{s_i}^o$, at time t_i is

$$\left. \begin{aligned}
 h_{s_i}^o &\approx \text{MSL}_i - h_{g_i} \\
 &\approx h_i^c - (h_{raw_i} + \text{corrections}) - h_{g_i} \\
 &\approx h_i^c - h_i^o \\
 &\approx -(\text{altimeter residual})_i
 \end{aligned} \right\} \quad (8.1)$$

wherein the i subscript refers to the i^{th} observation and h_i^o is the observed altimeter height of equation (4.1). The sea surface topography model $h_{s_i}^c$, is given

by

$$h_{s_i}^c = \sum_{n=0}^{\infty} \sum_{m=0}^n (C'_{nm} \cos m\lambda_i + S'_{nm} \sin m\lambda_i) P_{nm}(\sin \phi_i) \quad (8.2)$$

wherein λ_i is the geographic longitude of the i^{th} observation; ϕ_i its geographic latitude; $P_{nm}(\cdot)$ the associated Legendre functions of degree n and order m and C'_{nm} , S'_{nm} are the coefficients to be determined. The least squares process involves minimizing the function I , where

$$I = \sum_{i=1}^N (h_{s_i}^o - h_{s_i}^c)^2, \quad (8.3)$$

N being the total number of altimeter observations that satisfy the rejection criterion.

Equation (8.2) can be written more compactly as

$$h_{s_i}^c = \sum_{n=0}^{\infty} \sum_{m=0}^n \sum_{\alpha=1}^2 c_{nm}^{\alpha} Y_{nm_i}^{\alpha} \quad (8.4)$$

$$\text{where } c_{nm}^{\alpha} = \begin{cases} C'_{nm} ; \\ S'_{nm} ; \end{cases} \quad Y_{nm_i}^{\alpha} = \begin{cases} P_{nm}(\sin \phi_i) \cos m\lambda_i ; & \alpha = 1 \\ P_{nm}(\sin \phi_i) \sin m\lambda_i ; & \alpha = 2. \end{cases}$$

Simplification of the computer coding of this model is achieved by reducing the three summation signs in equation (8.4) to just one. Define a new variable, k , by

$$k = n^2 + n + 2m + \alpha \quad (8.5)$$

where $\alpha = 1, 2$ for each value of $m = 0, \dots, n$ and $n = 0, \dots, \infty$. Then

$$h_{s_i}^c = \sum_{k=1}^{\infty} K_k \tilde{Y}_{k_i} \quad (8.6)$$

where $K_k = c_{nm}^\alpha$ and $\tilde{Y}_{k_i} = Y_{nm_i}^\alpha$ for k defined by equation (8.5). For example, $m = n = 0$ and $\alpha = 1$, correspond to $k = 1$ so that $K_1 \equiv C'_{00}$. Likewise, $K_2 \equiv S'_{00}$, etc. It is pertinent to note here, that all terms of the form S'_{n0} are zero. They are kept in the numbering system only as a simplification of the computer coding and are not actually solved for in the minimization of I . In practice, equation (8.6) must be terminated at some integer, k_{\max} , determined by the maximum degree, n_{\max} and order, m_{\max} , of the harmonic expansion. Then equation (8.3) can be written

$$I = \sum_{i=1}^N \left[h_{s_i}^o - \sum_{k=1}^{k_{\max}} K_k \tilde{Y}_{k_i} \right]^2. \quad (8.7)$$

Minimization of this is equivalent to solving

$$\frac{\partial I}{\partial K_j} = -2 \sum_{i=1}^N \left[h_{s_i}^o - \sum_{k=1}^{k_{\max}} K_k \tilde{Y}_{k_i} \right] \tilde{Y}_{j_i} = 0 \quad (8.8)$$

for $j = 1, \dots, k_{\max}$. Upon rearranging, equation (8.8) can be written as

$$\sum_{i=1}^N \left(\sum_{k=1}^{k_{\max}} K_k \tilde{Y}_{k_i} \right) \tilde{Y}_{j_i} = \sum_{i=1}^N h_{s_i}^o \tilde{Y}_{j_i} \quad (8.9)$$

for $j = 1, \dots, k_{\max}$. In matrix form this reduces to

$$AK = b \quad (8.10)$$

$$\text{where } b_j = \sum_{i=1}^N h_{s_i}^o \tilde{Y}_{j_i}, \quad A_{\rho j} = \sum_{i=1}^N \tilde{Y}_{\rho_i} \tilde{Y}_{j_i}, \quad \rho, j = 1, \dots, k_{\max} \text{ for}$$

$$\mathbf{b} = (b_j)_{j=1}^{k_{\max}}, \quad \mathbf{A} = [A_{\rho j}]_{\rho, j=1}^{k_{\max}}, \quad \text{and } \mathbf{K} = (K_j)_{j=1}^{k_{\max}}.$$

\mathbf{A} is a symmetric positive definite matrix and so can be inverted to give the solution

$$\mathbf{K} = \mathbf{A}^{-1} \mathbf{b}. \quad (8.11)$$

Equation (8.10) expresses the normal equations for the coefficients of the harmonic expansion for the sea surface topography. These equations could be incorporated into the orbital normal equations with all the other parameters to be estimated, but the solution would then be orbit dependent and determined from only a limited number of altimeter observations. For a better determined solution, it is preferable to combine data from several orbital arcs having initially removed all of the orbit dependent parameters. This procedure is called the Helmert–Wolf Blocking Process and is described in more detail in Appendix 3.

The procedure is applied to several reference orbits determined throughout the operational lifetime of SEASAT, where in this context, a reference orbit is a six day arc in which a state vector at epoch, daily drag coefficients and a solar radiation pressure coefficient are all estimated. The data used in these arcs includes all laser data, weighted nominally as given in Table 2.1, crossover data, weighted with a standard deviation of 0.5m and altimetry, weighted with a standard deviation of 2m so as not to affect the orbital solution. (The state vector, drag coefficients and solar radiation pressure coefficient are the so called orbit dependent parameters which are removed as a result of the Helmert–Wolf process.) Throughout the computations, the GEM–T1 gravity field and derived geoid were employed.

Each orbital arc is converged, using the procedure outlined in [17] and the normal equations (8.10) separated using the Helmert–Wolf process. These equations are stored and added to those from previous arcs. Once all have been stored and

summed, they can be solved using an appropriate method for matrix inversion. That chosen for this work is due to Choleski [49].

§8.2 Numerical Results

The method described in section 8.1 has been applied to five SEASAT arcs, the details of which are listed in Table 8.1.

Table 8.1: Arcs used in the Helmert–Wolf Blocking solution for a sea surface topography model.

<u>Orbit</u>	<u>Repeat Period</u>	<u>Number of Altimeter Points</u>
MJD 43716–22	17–day	9722
MJD 43722–28	17–day	10112
MJD 43728–34	17–day	9483
MJD 43764–70	3–day	7186
MJD 43770–76	3–day	<u>10558</u>
	Total	47061

Use of this data, should provide sufficient coverage of both the 17 day and 3 day repeat orbits, with the addition of extra data not expected to significantly alter the results. For solution, the rejection level on the altimeter residuals was set at 5m after removing a 70cm range bias from the observed altimeter heights [48].

Equation (8.7) has been implemented into the software with k_{\max} determined from $n_{\max} = m_{\max} = 10$, that is with $k_{\max} = 132$. This determines a sea surface topography model up to degree and order 10, but initial tests have shown the 'a posteriori' standard errors on some of the coefficients to be large (Table 8.2), as large as the coefficients themselves in fact. Such coefficients have not been well determined, probably due to a measure of inseparability between them. A more modest approach is to determine a model upto degree and order six only. With

hindsight, this model should be more representative of the actual sea surface topography at these wavelengths since the method assumes that the geoid is known exactly, and upto degree and order six this is a fair assumption for the GEM-T1 derived geoid.

The results will be contaminated in three ways. There will be the near once per revolution orbit error which cannot be separated from the once per revolution sea surface topography terms; there will be aliasing of the high frequency sea surface topography terms into the low frequency terms due to omission and there will be the effect of the altimeter time tag bias and other temporal variations, such as tidal errors. Determination of the once and near once per revolution coefficients, C'_{10} , C'_{11} and S'_{11} will absorb some of the near once per revolution orbit error, aliasing their recovered values which may be unrepresentative therefore, of the actual sea surface topography values. However, total omission of these first degree terms is inadmissible due to aliasing into other terms. It was therefore decided to solve for these coefficients bearing in mind these facts. The aliasing of the high frequency terms is not deemed too serious, since it is known from oceanographic studies that the sea surface topography has most of its power at the longer wavelengths [50]. The remaining altimeter time tag bias, as determined from crossovers (section 7.4) is of the order of 1ms, which translates into a 7mm radial orbit error. Considering the method has various underlying assumptions concerning the geoid and orbital accuracy, this level of error is deemed insignificant. Other temporal errors, such as tides, should be random in nature and thus unlikely to be absorbed into the solution.

The resulting 6 x 6 model coefficients are listed in Table 8.3 with contour plot being given in Figure 8.2.

§8.3 Discussion Of Results

Table 8.3 gives the recovered coefficients and standard errors for the sea surface topography model upto degree and order six. The $C'(0, 0)$ term represents

an altimeter range offset and is not necessarily a component of the DST. The value recovered is 15.78cm which, when added to the 70cm already removed from the altimeter residuals produces a total range bias of 85.78cm, in reasonable agreement with the 72cm offset determined by Marsh et al [48]. The $C'(2, 0)$ term is -51cm in Table 8.3, in fair agreement with the -42cm determined by Marsh et al (however see below). In contrast, the value recovered by Engelis [50] is -23cm but this could be a consequence of the different geoids and definitions used in each of the methods. For instance, Engelis employs a GEM-L1 derived geoid [51] for referencing the sea surface topography, whereas the method of section 8.1 uses a GEM-T1 derived geoid whilst Marsh et al derive the geoid in a simultaneous solution with SST. In both section 8.1 and Marsh et al the geoid does not include the permanent tidal effects of the sun and moon which will be experienced by the altimeter signals. The geoid used for referencing the sea surface topography should include these terms. The 'zero' geoid is defined as an equipotential surface of the Earth's gravitational field and centrifugal rotation that would exist without the direct influence of the sun and moon, but including the indirect effect due to the permanent yielding of an elastic earth. The 'mean' geoid however, is that equipotential surface that would exist with the sun and moon present [52]. In order to obtain the 'zero' GEM-T1 derived geoid it is necessary to add the quantity

$$c_1 = -0.198k_2 \left(\frac{3}{2} \sin^2\phi - \frac{1}{2} \right) \text{ metres}$$

to the geoid heights [53], where k_2 is the second degree Love number (= 0.30) and ϕ is the geocentric latitude. Then, to obtain the 'mean' geoid the quantity

$$c_2 = -0.198 \left(\frac{3}{2} \sin^2\phi - \frac{1}{2} \right) \text{ metres}$$

must be added. This is equivalent to adding 25.74cm to the recovered value of $C'(2, 0)$ resulting in a value of $\sim -25\text{cm}$, relative to the 'mean' GEM-T1 derived geoid. A final tidal correction which should also have been applied is a zero frequency correction to the sea surface heights due to the vertical displacement of the ocean bottom. (See Rowlands [54].) This correction is equivalent to adding another 12cm to the value of $C'(2, 0)$ thus yielding a final derived value of $\sim -13\text{cm}$. This value is in disagreement with the value derived by Engelis but there is confusion as to the precise definition he uses for the geoid. Engelis accounts for the vertical displacement of the ocean bottom plus the induced solid earth deformation, c_1 . It is unclear from the literature though, whether he includes the correction c_2 in the derivation of his -23cm for $C'(2, 0)$. Assuming that Marsh et al account for the vertical displacement of the ocean bottom then their value of -42cm agrees very well with the value of -39cm obtained in this chapter (when also accounting for that correction term). The contour plot of Figure 8.2 has been drawn using the value of -13cm for $C'(2, 0)$ since this refers to the 'mean' geoid. However, the contour plots of Figures 8.3 and 8.4 have been drawn using the values of -42cm and -23cm , respectively, for $C'(2, 0)$.

With hindsight, correction for these tidal terms would have been simpler at the altimeter data processing stage where the geoid height is calculated. However, if a model for sea surface topography is to be introduced to equation (4.1), such terms can automatically be accounted for there.

Comparison of some of the other coefficients shows marked differences between all three methods, but it is encouraging to note that the majority of the coefficients of largest amplitude in Table 8.3, agree with those of Marsh et al. For instance, the method of section 8.1 has recovered the $C'(6, 0)$, $C'(2, 1)$ and $S'(4, 4)$ terms with similar amplitudes to those derived at GSFC. This must account for the high level of qualitative agreement between Figure 8.2 and Figure 8.3, which show the contour plots for these two models. Figure 8.4 depicts the plot for the model by Engelis and again, there is good qualitative agreement with the other two

plots. For example, all models show virtually the same topographic mounts and troughs, although some are slightly displaced and have differing amplitudes for each of the plots, especially that due to Engelis. Again, this is a likely consequence of the geoid definitions adopted in each method.

Discrepancies between model coefficients is related to the methodology employed in each solution. Marsh et al use a heavily edited altimeter data set sampled at 15 second intervals, giving a spatial distribution of approximately 100km between measurements. Surface gravimetry is used and a simultaneous solution for a 10×10 sea surface topography model and gravity field terms is performed. Further, the sea surface topography is constrained relative to the oceanographic solution of Levitus [55], allowing determination of a 10×10 field. Such a method will therefore separate the gravity field and in particular the geoid terms, which would otherwise contaminate the sea surface topography. By definition, this method is more sophisticated than that presented here but such a method could not be performed at Aston without the use of land gravimetry and this data is not available at the present time.

Conversely, the method adopted by Engelis is non-dynamic relying on removal of the long-wavelength orbit error by averaging the repeat arcs and simultaneously minimizing the crossover discrepancies in a least squares sense. For the non-repeat era, a similar method is used whereby the crossover discrepancies are minimized in four separate regions.

It should be emphasized that the method presented in section 8.1 is merely a preliminary engineering exercise to show how altimetry can be applied in analysing oceanographic phenomena. It is not intended to recover precise DST and should not be viewed as such. However, the foundation of a capability has been developed at Aston for more detailed studies in the future, especially for ERS-1.

Figure 8.2 : Contour plot of a 6×6 sea surface topography model relative to the GEM-T1 derived 'mean' geoid as determined using five SEASAT arcs.



Figure 8.3 : Contour plot of a 10×10 sea surface topography model as derived by Marsh et al [48].



Figure 8.4 : Contour plot of a 6×6 sea surface topography model as derived by Engelis [50].



Table 8.2 : Recovered coefficients for a 10×10 sea surface topography model as derived from five SEASAT arcs.

MAXIMUM DEGREE AND ORDER OF EXPANSION = 10
TOTAL NUMBER OF PARAMETERS EVALUATED = 121

INDEX (K)	COEFFICIENT	VALUE (CM)	STANDARD ERROR (CM)	INDEX (K)	COEFFICIENT	VALUE (CM)	STANDARD ERROR (CM)
1	C' 0 0	-3.36581	5.11305	68	S' 7 3	25.46039	3.44081
3	C' 1 0	7.92285	5.62739	69	C' 7 4	-8.85654	2.54431
5	C' 1 1	-19.80134	3.29699	70	S' 7 6	-15.60704	2.52786
6	S' 1 1	5.92686	5.87815	71	C' 7 7	6.05463	2.56764
7	C' 2 0	-25.00054	3.70552	72	S' 7 7	0.02830	2.04679
9	C' 2 1	-20.02843	2.50997	73	C' 8 0	7.50339	2.97090
10	S' 2 1	12.11013	7.98443	75	C' 8 1	1.09560	1.80513
11	C' 2 2	-23.86980	4.74131	76	S' 8 1	-7.23045	2.69517
12	S' 2 2	-20.05993	3.32850	77	C' 8 2	2.23728	2.77998
13	C' 3 0	10.08461	3.20114	78	S' 8 2	-6.58523	1.80390
15	C' 3 1	0.69912	2.60652	79	C' 8 3	-3.14904	1.88296
16	S' 3 1	22.34387	6.43625	80	S' 8 3	-6.79549	2.27524
17	C' 3 2	-32.34626	6.73774	81	C' 8 4	19.09508	2.61074
18	S' 3 2	-16.74736	3.16460	82	S' 8 4	7.22753	2.46580
19	C' 3 3	9.78124	2.92699	83	C' 8 5	-13.64873	2.83706
20	S' 3 3	-23.14040	4.08368	84	S' 8 5	23.47363	1.30741
21	C' 4 0	-16.66808	4.92395	85	C' 8 6	-15.50910	2.62144
23	C' 4 1	13.26571	2.33211	86	S' 8 6	-10.48571	2.45415
24	S' 4 1	9.83002	3.26753	87	C' 8 7	3.38325	2.40627
25	C' 4 2	-15.01410	6.66727	88	S' 8 7	-7.61982	2.22864
26	S' 4 2	-10.20354	3.20499	89	C' 8 8	7.63002	2.26017
27	C' 4 3	1.00496	3.45530	90	S' 8 8	3.05156	1.91255
28	S' 4 3	-32.95891	5.38291	91	C' 9 0	1.23899	2.63527
29	C' 4 4	3.83148	2.76998	93	C' 9 1	0.39479	1.74575
30	S' 4 4	-15.01301	3.56783	94	S' 9 1	3.58035	2.41857
31	C' 5 0	-18.81849	4.35192	95	C' 9 2	-2.41595	2.13778
33	C' 5 1	-4.25942	1.94791	96	S' 9 2	1.22445	1.76620
34	S' 5 1	-5.48750	3.72843	97	C' 9 3	-6.87914	1.68704
35	C' 5 2	-11.76989	4.54581	98	S' 9 3	7.03146	2.27713
36	S' 5 2	-0.31400	2.69625	99	C' 9 4	11.57250	1.72453
37	C' 5 3	6.50611	3.54598	100	S' 9 4	-5.86693	1.90785
38	S' 5 3	-23.04960	5.76529	101	C' 9 5	-15.24724	2.19521
39	C' 5 4	11.08038	3.90820	102	S' 9 5	13.80697	2.24520
40	S' 5 4	4.15180	3.02506	103	C' 9 6	-24.79069	2.50993
41	C' 5 5	0.29744	2.63628	104	S' 9 6	-5.65962	2.28238
42	S' 5 5	-1.74758	3.16145	105	C' 9 7	0.26568	2.24925
43	C' 6 0	6.61605	3.32969	106	S' 9 7	-7.33144	2.04428
45	C' 6 1	-7.52719	2.16926	107	C' 9 8	10.22288	2.15668
46	S' 6 1	-23.16048	4.46922	108	S' 9 8	7.41135	2.04056
47	C' 6 2	-8.02423	2.59678	109	C' 9 9	8.48870	2.04892
48	S' 6 2	0.88277	2.06504	110	S' 9 9	4.66141	1.97500
49	C' 6 3	13.95107	3.24501	111	C' 10 0	-5.90460	2.35100
50	S' 6 3	-17.69743	4.49025	113	C' 10 1	4.56088	2.57712
51	C' 6 4	25.22598	4.27298	114	S' 10 1	1.26172	2.24972
52	S' 6 4	23.16637	3.46413	115	C' 10 2	-3.39676	1.69149
53	C' 6 5	-2.03173	2.64164	116	S' 10 2	0.43984	1.54177
54	S' 6 5	9.53078	3.14300	117	C' 10 3	-1.71908	1.48639
55	C' 6 6	4.79340	2.82399	118	S' 10 3	5.62679	1.69123
56	S' 6 6	-5.78896	2.42225	119	C' 10 4	6.44240	1.51711
57	C' 7 0	3.28799	3.11461	120	S' 10 4	-7.07424	1.56018
59	C' 7 1	-0.60311	1.86585	121	C' 10 5	-6.06431	1.62363
60	S' 7 1	-17.68343	3.67738	122	S' 10 5	3.14790	1.53645
61	C' 7 2	0.41622	2.93550	123	C' 10 6	-13.14337	1.79757
62	S' 7 2	0.13934	3.02684	124	S' 10 6	-8.10748	1.75991
62	C' 7 3	7.39266	2.36044	125	C' 10 7	-1.07495	1.84965
64	S' 7 3	-19.28034	2.69570	126	S' 10 7	-5.21012	1.78225
65	C' 7 4	22.14856	3.21936	127	C' 10 8	-3.52651	1.74616
66	S' 7 4	22.70981	3.51183	128	S' 10 8	2.23157	1.76387
67	C' 7 5	-11.60681	3.04307	129	C' 10 9	-9.38465	1.86237
				130	S' 10 9	11.78696	1.67671
				131	C' 10 10	-1.27739	1.72143
				132	S' 10 10	-0.94310	1.89001

Table 8.3 : Recovered coefficients for a 6×6 sea surface topography model as derived from five SEASAT arcs.

MAXIMUM DEGREE AND ORDER OF EXPANSION = 6

TOTAL NUMBER OF PARAMETERS EVALUATED = 49

INDEX (k)	COEFFICIENT	VALUE (cm)	STANDARD ERROR (cm)
1	C' 0 0	-15.78378	2.20124
3	C' 1 0	-13.87815	2.14648
5	C' 1 1	-6.63967	1.91592
6	S' 1 1	-20.17560	2.36805
7	C' 2 0	-51.42929	1.72106
9	C' 2 1	-10.66097	1.61827
10	S' 2 1	-7.48703	2.76029
11	C' 2 2	-2.06860	2.08179
12	S' 2 2	-7.58432	1.90746
13	C' 3 0	7.96496	1.70300
15	C' 3 1	-1.98534	1.59584
16	S' 3 1	-14.31960	2.34474
17	C' 3 2	0.58516	2.35167
18	S' 3 2	-1.52029	1.81364
19	C' 3 3	4.03687	1.82018
20	S' 3 3	0.74719	1.94160
21	C' 4 0	0.54259	1.94528
23	C' 4 1	5.84981	1.51387
24	S' 4 1	-7.64642	1.59723
25	C' 4 2	15.08968	2.12952
26	S' 4 2	-1.27809	1.83019
27	C' 4 3	-6.60788	1.83826
28	S' 4 3	-1.86741	2.04104
29	C' 4 4	-4.84317	1.62077
30	S' 4 4	-12.01962	1.87686
31	C' 5 0	0.22761	1.98066
33	C' 5 1	-3.84842	1.28375
34	S' 5 1	-0.00544	1.71535
35	C' 5 2	5.43717	1.64303
36	S' 5 2	1.23434	1.54818
37	C' 5 3	-5.45165	1.65692
38	S' 5 3	3.57818	1.94261
39	C' 5 4	-5.93535	1.82183
40	S' 5 4	-5.52697	1.76655
41	C' 5 5	5.04286	1.69673
42	S' 5 5	-0.58840	1.73126
43	C' 6 0	14.05591	1.71243
45	C' 6 1	-5.85064	1.32941
46	S' 6 1	-1.65355	1.75025
47	C' 6 2	-1.41642	1.34871
48	S' 6 2	-0.96051	1.33411
49	C' 6 3	0.87113	1.45989
50	S' 6 3	2.86656	1.53651
51	C' 6 4	3.64714	1.57704
52	S' 6 4	-0.92748	1.53937
53	C' 6 5	5.34524	1.58065
54	S' 6 5	-1.58725	1.61254
55	C' 6 6	6.03507	1.68515
56	S' 6 6	0.71660	1.56113

CHAPTER 9

DENSITY

This chapter introduces the second part of this thesis; namely that of atmospheric density analysis and determination using SEASAT data. As will be seen later, precise orbit determination is a pre-requisite for accurate density recovery, hence the significance of part one of this thesis. However, results from earlier chapters have shown that altimetry has little effect on orbits determined with a good set of laser tracking data, a fact that was not foreseen at the outset of this research – it was initially anticipated that altimetry would provide extra orbital information which would prove useful in density analysis. Since this is not the case and in consideration of the extra computing time required to process altimetry, it was decided to perform the density analyses of the remaining chapters using laser data only.

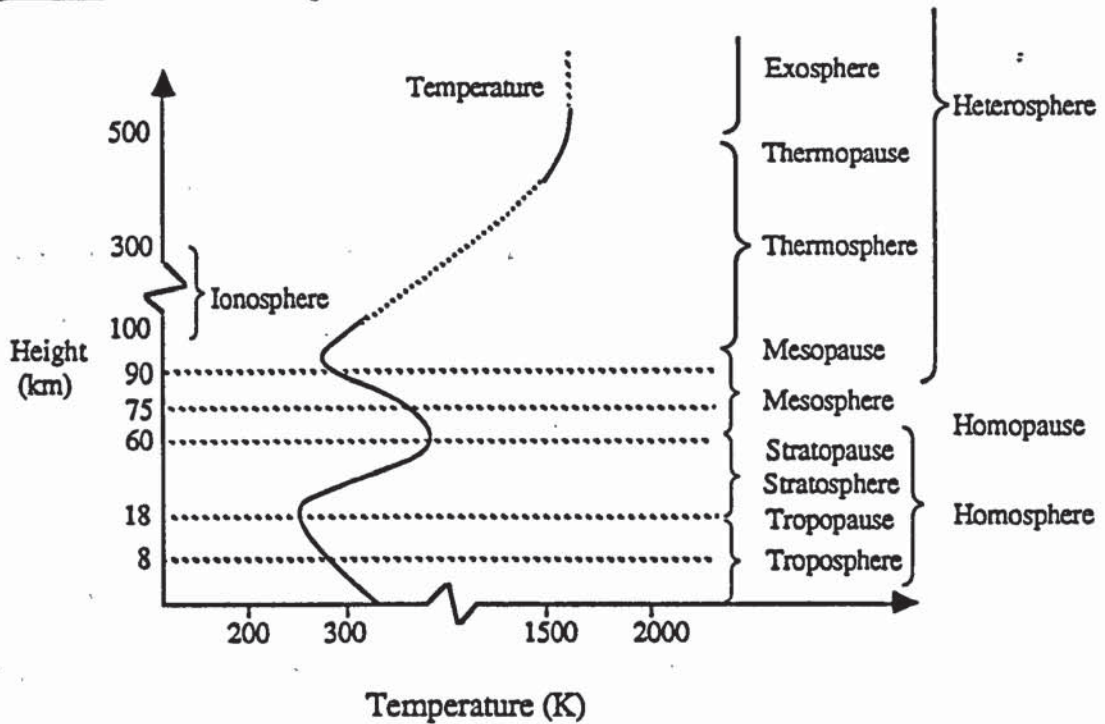
Chapter 10 compares current state-of-the-art atmospheric models showing that large discrepancies exist, particularly in the representation of a density change associated with geomagnetic activity. In chapter 11, densities are derived at SEASAT heights by utilizing the recovered drag coefficients from long-arc solutions. Finally, chapter 12 reveals how these derived density values can be applied to new modelling techniques. This leads to the investigation of using a new index for geomagnetic activity modelling, namely the auroral electrojet index and the estimation of certain coefficients in geomagnetic activity models.

To introduce the subject, this chapter addresses a few basic concepts about density, the atmosphere and describes the CIRA 72 atmospheric model [11], commonly adopted in orbital analyses.

§9.1 The Atmosphere

The atmosphere can be regarded as a series of several layers or 'spheres' defined in one of two ways, either on a thermal basis, or the basis of chemical composition. Both definitions are illustrated by the following diagram.

Figure 9.1: The Atmosphere.



The troposphere, stratosphere, mesosphere, thermosphere and exosphere are defined on a thermal basis; the layers between them are named by substituting the suffix 'pause' for the suffix 'sphere'. If the classification is by chemical composition, the main regions are the heterosphere, where a number of processes such as diffusion, mixing and photodissociation occur and the homosphere where the composition is unchanging. The homopause is the region between the two, where the composition begins to change.

For satellite orbital analysts, the main region of interest is the thermosphere where the temperature increases with height until it reaches a constant value at the exosphere. The heat input to the thermosphere has various effects upon the chemical composition in this region due to diffusion, mixing, photodissociation and ionisation.

Hence in terms of chemical composition the thermosphere is also called the heterosphere. Just below it is the homopause, an important layer since it provides the boundary conditions from which the diffusion equation is integrated in order to determine the number density of each individual atmospheric constituent within the thermosphere.

§9.2 Number Density

Above the height of the homopause (at about 100km in general) the composition of the atmosphere is dependent upon the temperature. The number density of each atmospheric constituent obeys the diffusion equation :-

$$\frac{dn_i}{n_i} = - \frac{M_i g}{R_* T} dz - \frac{dT}{T} (1 + \alpha_i') \quad (9.1)$$

where n_i is the number density of species i , of molecular mass M_i ; R_* the universal gas constant; g the gravitational acceleration of the earth at height z above ground level; T the temperature at this height and α_i' the diffusion constant of species i . The main atmospheric constituents of the thermosphere are Hydrogen (H_2), Helium (He), Argon (Ar), Nitrogen (N_2), and Oxygen; Oxygen occurring in both atomic (O) and molecular (O_2) forms. The proportion of each varies with altitude and temperature, but for SEASAT heights the dominant constituents are generally Helium and atomic Oxygen as can be observed from Figure 2 p.262 of CIRA 1972 [11] for instance.

In CIRA 72, Jacchia gives an expression for the temperature profile T , used in equation (9.1). The form of this profile necessitates numerical integration of the diffusion equation. However, Walker [56] has derived an analytical approximation by modifying T slightly :-

$$T = T_\infty - (T_\infty - T_{125}) \exp \left[-s(z-125)(R_E+125)/(R_E+z) \right] \quad (9.2)$$

where T_{∞} is the asymptotic exospheric temperature; T_{125} the temperature at 125km, the height of the homopause in this case; s a parameter variable with T_{∞} and R_E the radius of the earth. It is the analytic approximation which is implemented in the SATAN software package. However, both numeric and analytic versions give almost exactly the same results as verified by Tables 9.1 and 9.2 which show the orbital differences for the two versions when applied to the three day SEASAT arc spanning MJD 43770 to MJD 43773. Both orbits are relative to the GEM-T1 gravity field, the NASA 'area tables' for SEASAT and utilize daily drag coefficients, C_{D_i} , $i = 1, 2, 3$ and a single solar reflectivity coefficient, C_R .

Table 9.1: Orbital results for the arc MJD 43770 to MJD 43773 using the analytic and numeric versions of CIRA 72.

<u>Model</u>	<u>rms(cm)</u>	<u>C_{D_1}</u>	<u>C_{D_2}</u>	<u>C_{D_3}</u>	<u>C_R</u>
Analytic	50.81	2.70	2.54	2.25	1.63
Numeric	50.80	2.73	2.56	2.28	1.63

Table 9.2: Radial, along-track and cross-track differences between the analytic and numeric versions of CIRA 72 for the arc of Table 9.1.

<u>Differences in metres (max/rms)</u>		
<u>Radial</u>	<u>Along-track</u>	<u>Cross-track</u>
0.005/0.002	0.013/0.004	0.0005/0.0003

The solution of equation (9.1) using the analytic approximation to T (equation (9.2)) has been derived since certain partial derivatives of the number densities are required later when coefficients are estimated in the density models. It is detailed in section 10.5

Returning to equation (9.2), T_{∞} is a function of several variables, notably the level of solar activity as measured by the solar flux, the local solar time and the geomagnetic activity. Each is now described in turn.

§9.3 Solar Activity

The extreme ultraviolet radiation or EUV emitted from the sun is responsible for heating the upper atmosphere. This radiation comprises two components, one due to the solar disc, variable over a period of 11 years and the other due to active regions on the disc itself. These active regions are caused by areas of higher temperature due to the formation of sun-spots and solar rotation. This component varies rapidly from day to day and has a 27 day cycle, commensurate with the solar rotation rate.

The most readily available index for the EUV is the 10.7cm solar flux or $F_{10.7}$ measured in units of $10^{-22} \text{ Wm}^{-2} \text{ Hz}^{-1}$. This index is measured at daily intervals and consists of the two EUV components, which can be separated by statistical methods. An increase in the EUV emissions as indicated by an increase in the $F_{10.7}$ index causes an increase in the temperature of the thermosphere and exosphere. The reaction of the atmosphere due to each component of the EUV is different but has been empirically modelled by Jacchia (in CIRA 1972 [11]) as

$$T_c = 379 + 3.24 \bar{F}_{10.7} + 1.3 (F_{10.7} - \bar{F}_{10.7}) \text{ K} \quad (9.3)$$

for zero geomagnetic activity, i.e. $K_p = 0$ (see section 9.5). In equation (9.3) $\bar{F}_{10.7}$ is the mean of $F_{10.7}$ taken over four solar rotations (108 days) centred on the day in question and T_c represents the night-time minimum of the exospheric temperature in degrees Kelvin. The first two terms of the equation model the temperature variation due to the disc component, whilst the last term models the day to day variation of the active region component.

§9.4 Diurnal Variation

The position of the sun with respect to the atmosphere has a significant effect on the exospheric temperature due to heating by the EUV. Satellite drag observations have shown that the maximum densities occur at around 2pm local solar time (LST) and at a latitude approximately equal to the sun's declination, δ_o . Similarly, minimum densities are seen to occur at around 3am LST with a latitude of $-\delta_o$. This is the so called diurnal variation, the temperature T_p of which, is modelled by a function of T_c in CIRA (1972) [11].

§9.5 Geomagnetic Activity

The earth can be regarded as a huge magnet having an associated magnetic field, the first approximation to which is a dipole orientated along the spin axis. Successive approximations incorporate multipoles and cause the magnetic poles to be misaligned from the spin poles. The geomagnetic field pervades the region close to the earth, extending outwards in what is called the magnetosphere, the radius of which varies but is several earth radii. The field controls the motion of the charged particles in the atmosphere and so affects the temperature and density.

Variations within the geomagnetic activity such as that due to interaction with the solar wind, cause temperature changes due to particle precipitation in the auroral zones and subsequent joule heating in the atmosphere. This in turn causes the density variations observed during geomagnetic storms and is an important part of atmospheric density modelling.

Several empirical indices have been used to describe the level of geomagnetic activity [57], one of the most common being the geomagnetic planetary index, K_p . This is an average value from 12 world-wide observatories and provides a uniform index over the globe. CIRA 72 incorporates this index into the model for the change in exospheric temperature, $\Delta_G T_{\infty}$, associated with a geomagnetic disturbance as

$$\Delta_G T_{\infty} = (A_1 K_p + B_1 \exp(K_p)) \quad (9.5)$$

where $A_1 = 28.0$ K, $B_1 = 0.03$ K and $\Delta_G T_{\infty}$ is lagged at 6.7 hours behind the K_p input.

This is a very simple representation of geomagnetic activity and attempts to model the effects as observed from low resolution satellite drag data. In no way does it attempt to represent the actual physics of the phenomenon which in reality are very complex. For instance, high resolution in-situ data collected from satellites such as ESRO 4 have shown that at the outset of a geomagnetic storm, there is an immediate increase of temperature and density in the thermosphere above the auroral zone and that the atmospheric perturbation propagates, reaching the equatorial regions considerably weakened some hours later. This transport of energy is complex and very difficult to model – one of the reasons why geomagnetic disturbances cause large uncertainties in density models. More advanced models of the geomagnetic effect, such as those due to Slowey [12, 58], attempt to take these features into account by introducing terms dependent on the latitude, longitude and time of propagation (delay time). A fuller description of Slowey's models can be found in chapter 10.

Jacchia's model for exospheric temperature T_{∞} , is the sum of the diurnal term, T_{ϱ} , and the geomagnetic variation, i.e.

$$T_{\infty} = T_{\varrho} + \Delta_G T_{\infty} \quad (9.6)$$

This value is used in the temperature profile equation (9.2) to determine the number density in equation (9.1).

The importance of the geomagnetic activity component on density can readily be seen from Table 5 of CIRA (1972) p.291, where at 800km for instance and a solar flux level of $\sim 125 \times 10^{-22} \text{ Wm}^{-2} \text{ Hz}^{-1}$, an increase of 100k can cause the density to virtually double. Such a temperature increase occurs for K_p above 4, i.e. for moderate geomagnetic activity and above. This is more significant than at 400km for example, where the density increase for the same activity is only about 50 per cent.

CHAPTER 10

A COMPARISON OF ATMOSPHERIC DENSITY MODELS

At the outset of this research project, all orbit computations utilized the CIRA 72 atmospheric density model [11]. Other models such as DTM [16] and MSIS-1/2 [13,14] were already implemented into the SATAN software package, but were not employed as a rule as CIRA 72 proved adequate for most orbital analyses, particularly if multiple drag coefficients were estimated as part of the orbital solution. Later, MSIS-83 [15] was added to the software, together with the modified geomagnetic activity component to CIRA 72, due to Slowey, JS84 [12]. At this stage it was decided that a comparison of the models was required in order to assess which performed 'the best' in most situations.

Initial work involved analysing the effects of Slowey's model, JS84, for geomagnetic activity, as implemented in CIRA 72, in place of equation (9.5). This led to experimentation and modification of the time constant, c , in JS84 and certain other parameters within both CIRA 72 and JS84. The mathematics involved is outlined in section 10.5.

Finally, it was decided to analyse the performance of the MSIS type models as a different approach is adopted to CIRA 72, in modelling the total density. MSIS-83 was chosen for this work, in view of it being an updated version of the MSIS-1/2 model.

§10.1 Orbits Chosen For Analysis

To obtain a representative sample of atmospheric conditions, orbital arcs were chosen from the entire operational life-span of SEASAT. Table 10.1 lists the main characteristics of the arcs involved. Each orbit was derived relative to the GEM-T1 gravity field and employed the NASA 'area tables' for drag force modelling and

normalized SRP accelerations. The parameters solved for in each orbit were a state vector at epoch, a single solar reflectivity coefficient, C_R and either a single drag coefficient, C_D , a dragrate (C_D, \dot{C}_D) or multiple drag coefficients, as specified.

Table 10.1: Orbital arcs used for density model comparisons.

<u>Orbital Arc</u> <u>Identification Number</u>	<u>Start</u> <u>Epoch(MJD)</u>	<u>Length of Arc</u> <u>in days</u>	<u>Repeat Period</u> <u>in days</u>
1	43722.0	6	17
2	43728.0	6	17
3	43748.5	6.75	interim
4	43764.0	6	3
5	43770.0	6	3
6	43774.0	9	3
7	43778.0	4	3
8	43784.0	5	3
9	43791.0	5	3

§10.2 Orbits Derived Relative To CIRA 72

Analysis of CIRA 72 involved computing many of the orbital arcs listed in Table 10.1, with all three forms for the drag parameter, that is, single C_D , linear C_D and multiple C_D 's. Tables 10.2 to 10.4 present the results of those arcs tested in this manner.

Table 10.2: Orbital results relative to CIRA 72 and single C_D .

<u>Orbital Arc</u>	<u>Rms (m)</u>	<u>C_D</u>	<u>C_R</u>	<u>Number of observations</u>
1	1.33	4.23	1.51	972
2	2.45	3.58	0.93	1488
3	1.59	2.15	1.38	1481
4	3.38	2.05	0.62	1101
5	5.32	2.58	1.69	1993
6	23.69	3.72	2.76	2165
7	7.78	3.90	1.73	1005
8	3.05	4.28	1.82	978
9	1.70	3.35	1.71	933

Table 10.3: Orbital results relative to CIRA 72 and linear C_D .

<u>Orbital Arc</u>	<u>Rms (m)</u>	<u>C_D</u>	<u>\dot{C}_D</u>	<u>C_R</u>	<u>Number of observations</u>
1	0.88	4.90	-0.10	1.75	971
2	1.57	5.02	-0.27	1.32	1488
3	1.50	1.98	0.04	1.35	1481
4	0.91	3.57	-0.26	1.54	1101
5	2.24	1.71	0.28	1.42	1992
6	12.67	2.85	0.15	1.64	2161
7					
8	1.41	4.73	-0.19	1.71	978
9	1.64	3.40	-0.02	1.73	933

Table 10.4: Orbital results relative to CIRA 72 and multiple C_D 's .

<u>Orbital Arc</u>	<u>Rms (m)</u>	<u>C_D range</u>	<u>C_R</u>	<u>Number of observations</u>
2	0.51	3.79–5.54	1.57	1448
3*	0.67	2.65–3.58	1.55	1481
4	0.45	1.57–3.52	1.43	1000
5	0.55	2.03–3.03	1.58	1956
6	2.51	2.33–4.08	1.51	2096

* All arcs utilized daily drag coefficients except for arc 3 which employed a final drag coefficient spanning 1.75 days.

Several conclusions can be drawn from these three tables. Firstly, the rms of fit when employing a single drag scale factor, is generally very poor (Table 10.2). This is most evident for arcs 6 and 7 which experience a severe geomagnetic storm on MJD 43780 (Figure 10.1), where the 3 hour global geomagnetic index, K_p , reaches a value of 8.0. There is also a large variation between arcs, in the recovered C_R values, for the single C_D parametrization. Evidently, some of the along-track modelling error has been absorbed by the solar radiation pressure coefficient. This is vindicated by the results of the linear drag model (Table 10.3) in which the rms of fit reduces for each arc and the recovered C_R values became more consistent than for Table 10.2. Apparently the extra degree of freedom within the system has helped to accommodate more of the along-track error, reducing the contamination of C_R . Similarly, the multiple drag coefficient model accommodates the along-track error to an even greater extent, with sub-metre rms values being obtained in all cases except arc 6. Again, this is attributed to the severe geomagnetic storm over this period. For multiple drag coefficients, the recovered C_R values show less variation than for the linear drag model with a range of 1.43 to 1.58 for the five arcs of Table 10.4.

These results justify the use of multiple drag coefficients in long-arc orbital determinations and indicate the inadequacy of a single drag coefficient

parametrization. However, it must be remembered that multiple drag coefficients are purely an artificial device to absorb errors in atmospheric density modelling and have no other geophysical significance. The aim of the ensuing density analysis is to strive towards the accuracies achieved with multiple drag coefficients, when using a single drag coefficient only.

§10.3 Orbits Derived Relative To JS84

Variation of the recovered multiple drag coefficients shows a marked correlation with variation in the geomagnetic index, K_p , as observed in Figure 10.2 for the orbital arc spanning MJD 43770 to MJD 43783. This phenomenon has been noticed by Wakker et al [6] and Noomen [59]. Apparently, short-term density variations associated with geomagnetic disturbances cause large uncertainties in density modelling which multiple drag coefficient solutions attempt to accommodate. It is the geomagnetic activity component therefore, which has come under scrutiny and is the main concern of the remainder of this study.

The first step towards geomagnetic activity modelling improvement was to implement Slowey's 1984 model, JS84 [12] into the CIRA 72 model. The components of this model are now described.

JS84 models the change in the logarithm of the number density, $\Delta_G \log_{10} n_i$, due to geomagnetic activity for each individual atmosphere constituent, i , by

$$\Delta_G \log_{10} n_i = \Delta_T \log_{10} n_i + \Delta_H \log_{10} n_i + \Delta_e \log_{10} n_i \quad (10.1)$$

where $\Delta_T \log_{10} n_i$ is the thermal component, $\Delta_H \log_{10} n_i$ the component due to the change in the height of the homopause and $\Delta_e \log_{10} n_i$ the component due to the equatorial wave, in which the number densities of all constituents increase in the same proportion centred on the equator.

The thermal component is evaluated assuming an increase in exospheric temperature $\Delta_G T_\infty$, given by

$$\Delta_G T_\infty = A F(\phi, \lambda) \quad (10.2)$$

where $A = A'_1 K'_p [1 + A_3 \exp(A_2 K'_p)]$ (10.3)

with $A'_1 \equiv 57.5K$, $A_2 \equiv 0.4$, $A_3 \equiv 0.027$

and $F = 0.1425 + 0.8137 \sin^n \phi +$
 $\cos^2 \phi (0.1184 \sin \lambda - 0.03604 + \cos \lambda) +$
 $\sin 2\phi (-0.07354 \sin \lambda + 0.1038 \cos \lambda) +$
 $\sin^4 \phi \sin 2\phi (0.3706 \sin \lambda - 0.1441 \cos \lambda).$ (10.4)

In equations (10.2) and (10.4), ϕ and λ represent the geomagnetic latitude and local magnetic time, respectively. Persistence is modelled in equation (10.3) by assuming K'_p to be the weighted mean of the lagged 3-hourly K_p geomagnetic index taken over the 41 values in the preceding five day interval :-

$$K'_p(t + \tau_{84}) = \frac{\sum_{t_i=t-5}^t K_p(t_i) e^{-c(t-t_i)}}{\sum_{t_i=t-5}^t e^{-c(t-t_i)}} \quad (10.5)$$

where t is the time in days, c the time constant equal to $1.0d^{-1}$ and τ_{84} is the time lag given by

$$\tau_{84} = 0.05 + 0.1 \cos^2 \phi \quad (\text{day}). \quad (10.6)$$

In equation (10.4) n takes the form $5.0 - K'_p/3.0$.

The model for the homopause variation is

$$\Delta_H \log_{10} n_i = \alpha_i \Delta z_H \quad (10.7)$$

where Δz_H (metres) is calculated from

$$\Delta z_H = Z_1 \Delta_G T_\infty$$

with $Z_1 \equiv 22.0$ and the α_i 's given by

$$\alpha(\text{Ar}) = + 3.07 \times 10^{-5} \quad (\text{mks})$$

$$\alpha(\text{O}_2) = + 1.03 \times 10^{-5} \quad (\text{mks})$$

$$\alpha(\text{N}_2) = 0.0$$

$$\alpha(\text{O}) = - 5.75 \times 10^{-5} \quad (\text{mks})$$

$$\alpha(\text{He}) = - 6.30 \times 10^{-5} \quad (\text{mks}).$$

Finally, the equatorial wave component is given by

$$\Delta_e \log_{10} n_i = E_1 \tanh [0.006(z - 100.0)] A \cos^2 \phi \quad (10.9)$$

where $E_1 \equiv 6.55 \times 10^{-4}$, z is the height in km and A is as in equation (10.3).

Figure (10.1) plots the K'_p index compared with the instantaneous K_p index for the periods spanning the orbital arcs of Table 10.1.

Results of computing these orbits with JS84 implemented in CIRA 72 are tabulated below.

Figure 10.1 : Values of geomagnetic indices K_p (full line) and K'_p (discontinuous line) for the arcs of Table 10.1. Horizontal scale is days from MJD 43700.

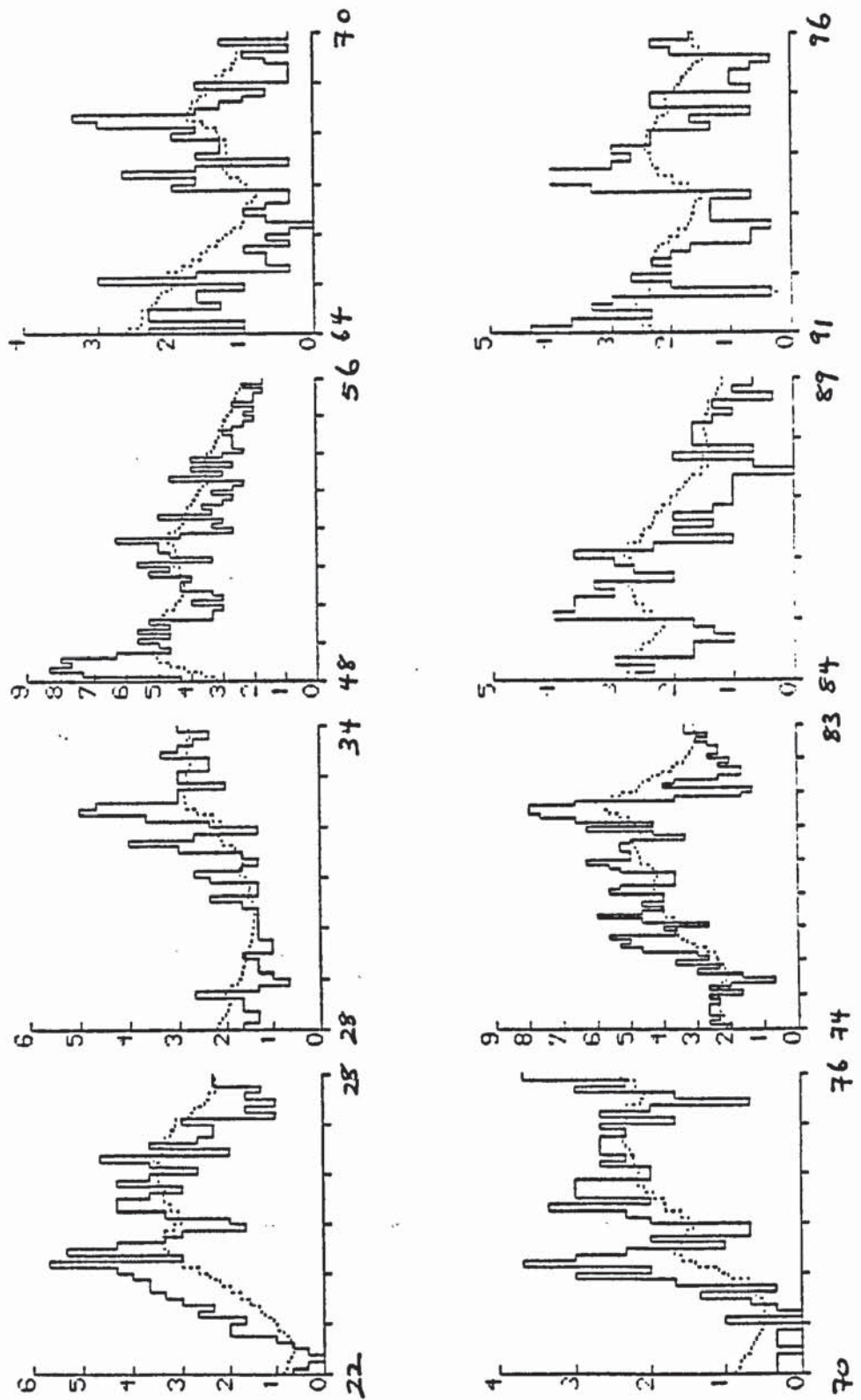


Figure 10.2 : Recovered drag coefficients from CIRA 72 and K_p index for the 13 day arc MJD 43770 to MJD 43783.

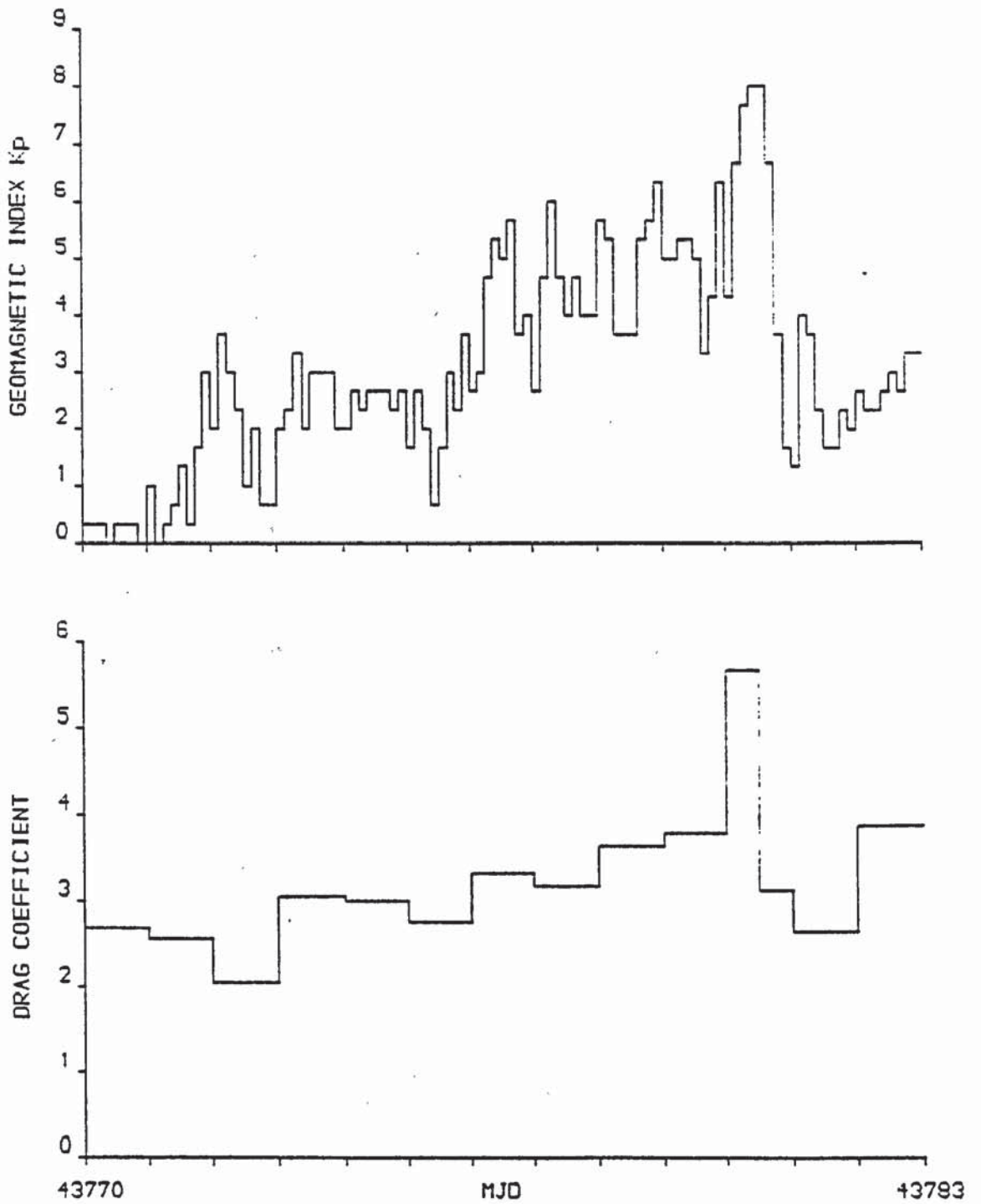


Table 10.5: Orbital results relative to JS84 and single C_D .

<u>Orbital Arc</u>	<u>Rms (m)</u>	<u>C_D</u>	<u>C_R</u>	<u>Number of observations</u>
1	2.83	4.26	0.97	972
2	1.61	4.83	1.34	1488
3	1.08	2.66	1.54	1481
4	2.77	2.67	1.15	1101
5	6.35	3.08	1.83	1993
6	34.38	5.12	3.71	2165
7	8.32	5.90	3.45	1005
8	8.00	4.70	1.95	978
9	4.19	3.78	1.61	933

Table 10.6: Orbital results relative to JS84 and linear C_D .

<u>Orbital Arc</u>	<u>Rms (m)</u>	<u>C_D</u>	<u>\dot{C}_D</u>	<u>C_R</u>	<u>Number of observations</u>
1	0.97	7.75	-0.45	2.08	971
2					
3					
4	1.38	3.61	-0.17	1.66	1101
5	1.60	1.81	0.39	1.52	1993
6	16.62	3.44	0.30	2.10	2165
7					
8	2.82	6.05	-0.56	1.69	978
9	1.03	3.30	0.22	1.36	933

Table 10.7: Orbital results relative to JS84 and multiple C_D 's .

<u>Orbital Arc</u>	<u>Rms (m)</u>	<u>C_D range</u>	<u>C_R</u>	<u>Number of observations</u>
2	0.58	4.40–6.57	1.58	1488
3*	0.60	2.23–3.08	1.57	1480
5	0.60	2.31–3.49	1.60	1990
6	1.06	2.40–6.80	1.71	2164
8	0.36	3.61–5.80	1.69	973

*All arcs employed daily C_D 's except arc 3 which used a final drag coefficient of 1.75 days in length.

Tables 10.5 to 10.7 reveal much the same pattern as Tables 10.2 to 10.4 with the most accurate orbits being obtained when multiple drag coefficients are employed as part of the orbital solution. The results, when solving for a single drag coefficient, are still poor in some cases (Table 10.5), for instance arcs 5, 6, 7, 8 and 9. Evidently, the more complex geomagnetic activity modelling as derived by Slowey, has not improved upon the simple form given in CIRA 72 (equation (9.5)), at least for SEASAT heights.

It is pertinent to note here, the similarities in results, between CIRA 72 and JS84, for the orbital arcs 2, 3 and 5 when using multiple drag coefficients (compare Tables 10.4 and 10.7). From this, one concludes that multiple drag coefficients absorb the errors in any density model, resulting in orbits of a similar quality. This is an important observation for the density determination work of the next chapter.

§10.4 Modifications To CIRA 72 And JS84

CIRA 72 is a general purpose satellite drag based density model but, as explained in sections 10.2 and 10.3, is inaccurate in representing short-term density variations associated with geomagnetic disturbances. The incorporation of the JS84

geomagnetic model into the software was a direct response to this deficiency, but as Table 10.5 shows, there has been no improvement. This may be a consequence of the height at which JS84 is being applied – approximately 800km. In general, the data used in the derivation of JS84 came from lower in the atmosphere, in particular the model incorporated ESRO 4 data collected in the 240–320km height band. Extrapolation to higher altitudes might therefore prove erroneous with certain coefficients inapplicable at such heights.

Therefore, in order to apply JS84 to SEASAT heights, it was decided that modification of some of the coefficients might prove beneficial and also indicate the main modelling deficiencies. This modification involved solving for certain geomagnetic coefficients as part of the orbital solution.

The accelerating force, \underline{F} , on the satellite can be written

$$\underline{F} = \underline{F}(\underline{B}, \rho) \quad (10.10)$$

where \underline{B} is a vector of parameters upon which \underline{F} depends, for instance gravitational coefficients, position, SRP coefficient, etc. and ρ is the atmospheric density, dependent upon the exospheric temperature, T_{∞} . From equation (9.6), T_{∞} is a function of $\Delta_G T_{\infty}$, the component due to geomagnetic activity. Hence equation (10.10) can be written

$$\underline{F} = \underline{F}(\underline{B}, \rho(T_{\infty}(\Delta_G T_{\infty}(\underline{P})), \underline{P}^*)) \quad (10.11)$$

where \underline{P} is a vector of all parameters in the geomagnetic activity model and \underline{P}^* a vector of parameters defining other atmospheric density characteristics, e.g. diurnal variation, semi-annual variation, etc. Then, for $p \in \underline{P}$, the chain rules gives

$$\frac{\partial \underline{F}}{\partial p} = \frac{\partial \underline{F}}{\partial \rho} \cdot \frac{\partial \rho}{\partial p} \quad (10.12)$$

Using equation (10.12), it is possible to solve for individual $p \in \mathcal{P}$ by the method of least squares outlined in section (3.3). In order to do this, it is necessary to derive a form for $\partial E/\partial p$. This is now described.

§10.5 Derivation Of The Partial Derivatives For Geomagnetic Modelling Parameters

To calculate the partial derivatives $\partial E/\partial p$, it is necessary to solve the diffusion equation (9.1). SATAN adopts the analytic approximation given by Walker [56] in which the temperature profile, $T(z)$, is given by equation (9.2). Equation (9.1) is integrated from the height of the homopause, taken to be 125km. Hence

$$\int_{n_i(125)}^{n_i} \frac{dn_i}{n_i} = -\frac{M_i}{R_*} \int_{125}^z \frac{g(z)}{T(z)} dz - (1 + \alpha'_i) \int_{T_{125}}^T \frac{dT}{T} \quad (10.13)$$

wherein $n_i(125)$ is the number density of species i at 125km and all other notation is as defined previously. From [11] $g(z) = 9.80665 R_E^2 / (R_E + z)^2 \text{ ms}^{-2}$ so that substitution of $g(z)$ and $T(z)$ into equation (10.13) yields

$$\ln[n_i] - \ln[n_i(125)] = I + (1 + \alpha'_i) \ln\left[\frac{T_{125}}{T}\right] \quad (10.14)$$

upon integration. In equation (10.14)

$$I = -\frac{M_i 9.80665 R_E^2}{R_* T_\infty} \int_{125}^z \frac{(R_E + z)^{-2}}{(1 - A \exp[-sz'])} dz \quad (10.15)$$

where $A = \frac{T_\infty - T_{125}}{T_\infty}$ (10.16)

and $z' = \frac{(z - 125)(R_E + 125)}{(R_E + z)}$ (10.17)

I is integrated using the substitution $u = 1 - A \exp[-sz']$:-

$$I = -\frac{M_i 9.80665 R_E^2}{R_* T_\infty} \int_{1-A}^{1-A \exp[-sz']} \frac{du}{s(R_E + 125)^2 u(1-u)} \quad (10.18)$$

$$= -\frac{M_i g(125)}{sR_* T_\infty} \left\{ \ln \left[\frac{T}{T_{125}} \right] + \frac{s(z-125)(R_E + 125)}{(R_E + z)} \right\} \quad (10.19)$$

where $g(125)$ is the value of $g(z)$ at $z = 125$ km. Hence the solution to equation (10.13) is given by

$$\ln[n_i] = \ln[n_i(125)] + \left(\frac{M_i g(125)}{sR_* T_\infty} + 1 + \alpha'_i \right) \ln \left[\frac{T_{125}}{T} \right] - \frac{M_i g(125)}{R_* T_\infty} z'. \quad (10.20)$$

This equation expresses the natural logarithm of the number density of species i as derived from integrating the diffusion equation with boundary conditions at 125km. This applies to N_2 , O_2 , O and He . For H , diffusive equilibrium occurs above 500km. Hence equation (9.1) must be integrated from 500km. The method is similar, resulting in the equation

$$\ln[n_H] = \ln[n_H(500)] + \left(\frac{M_H g(125)}{sR_* T_\infty} + 1 \right) \ln \left[\frac{T_{500}}{T} \right] - \frac{M_H g(125) (z-500)(R_E + 125)^2}{R_* T_\infty (R_E + 500)(R_E + z)} \quad (10.21)$$

wherein the subscript H refers to hydrogen. (Equation (10.21) has been derived assuming a value of zero for α'_H .) The total atmospheric density, ρ , is then calculated from

$$\rho = \sum_{i=1}^{N_s} \frac{n_i M_i}{A_v} \quad (10.22)$$

where N_s is the total number of atmospheric constituents each with corresponding number density, n_i and molecular mass, M_i . A_v is Avogadro's number.

As an illustration of the mathematics involved in calculating $\partial F/\partial p$, equation (10.12) is developed for the coefficient, A'_1 in JS84. For this parameter

$$\frac{\partial F}{\partial A'_1} = \frac{\partial F}{\partial \rho} \cdot \frac{\partial \rho}{\partial A'_1} \quad (10.23)$$

From equation (3.6), $\partial F/\partial \rho$ is simply

$$\frac{\partial F}{\partial \rho} = -\frac{1}{2} \left(\frac{A}{m} \right) C_D v_r v_r \quad (10.24)$$

with notation as previously defined, whilst $\partial \rho/\partial A'_1$ is given by

$$\frac{\partial \rho}{\partial A'_1} = \sum_{i=1}^{N_s} \frac{\partial n_i}{\partial A'_1} \frac{M_i}{A_v} \quad (10.25)$$

Let $L'_i = \ln[n_i]$ whence $n_i = e^{L'_i}$ and in particular

$$\frac{\partial n_i}{\partial A'_1} = n_i \frac{\partial L'_i}{\partial A'_1} \quad (10.26)$$

In JS84, L'_i is calculated by solving the diffusion equation (9.1) and adding the corrections for the homopause height variation and the equatorial wave. Thus

$$L'_i = L_i + \Delta_H \ln[n_i] + \Delta_e \ln[n_i] \quad (10.27)$$

where L_i is the natural logarithm of n_i as given by equation (10.20) or in the case of hydrogen, equation (10.21), $\Delta_H \ln[n_i]$ is the homopause correction and $\Delta_e \ln[n_i]$ the equatorial wave correction. From equations (10.7), (10.8) and (10.9)

$$\Delta_H \ln[n_i] = \ln[10] \cdot \alpha_i \cdot Z_1 \cdot \Delta_G T_\infty \quad (10.28)$$

and
$$\Delta_e \ln[n_i] = \ln[10] \cdot E_1 \cdot \tanh [0.006 (z - 100.0)] \cdot A \cdot \cos^2 \phi \quad (10.29)$$

with notation as already defined. Therefore, differentiating equation (10.27) with respect to A'_1 yields

$$\frac{\partial L'_i}{\partial A'_1} = \frac{\partial L_i}{\partial A'_1} + \ln[10] \alpha_i Z_1 \frac{\partial}{\partial A'_1} (\Delta_G T_\infty) + \ln[10] \cdot E_1 \cdot \tanh[0.006(z-100)] \cdot \cos^2 \phi \frac{\partial A}{\partial A'_1} \quad (10.30)$$

$$\text{where} \quad \frac{\partial}{\partial A'_1} (\Delta_G T_\infty) = K'_p [1 + A_3 \exp(A_2 K'_p)] \cdot F(\phi, \lambda) \quad (10.31)$$

$$\text{and} \quad \frac{\partial A}{\partial A'_1} = K'_p [1 + A_3 \exp(A_2 K'_p)] \quad (10.32)$$

upon differentiating equations (10.2) and (10.3), respectively. The first term of equation (10.30) is calculated using the Chain Rule,

$$\frac{\partial L_i}{\partial A'_1} = \frac{\partial L_i}{\partial T_\infty} \cdot \frac{\partial T_\infty}{\partial A'_1} \quad (10.33)$$

For N_2 , O_2 , O and He , $\partial L_i / \partial T_\infty$ is calculated by differentiating equation (10.20) with respect to T_∞ whilst for H , equation (10.21) is differentiated. The resulting equations are

$$\begin{aligned} \frac{\partial L_i}{\partial T_\infty} = & \frac{\partial}{\partial T_\infty} [\ln n_i (125)] + \frac{\partial}{\partial T_\infty} \left(\frac{1}{sH_i} \right) \ln \left[\frac{T_{125}}{T} \right] + \left(1 + \alpha'_i + \frac{1}{sH_i} \right) \cdot \\ & \frac{\partial}{\partial T_\infty} \left[\ln \left(\frac{T_{125}}{T} \right) \right] - \frac{\partial}{\partial T_\infty} \left(\frac{1}{H_i} \right) \cdot z' \end{aligned} \quad (10.34)$$

for N_2 , O_2 , O , He and

$$\begin{aligned} \frac{\partial L_H}{\partial T_\infty} = & \frac{\partial}{\partial T_\infty} [\ln n_H (500)] + \frac{\partial}{\partial T_\infty} \left(\frac{1}{sH_H} \right) \ln \left[\frac{T_{500}}{T} \right] + \left(1 + \frac{1}{sH_H} \right) \frac{\partial}{\partial T_\infty} \left[\ln \left(\frac{T_{500}}{T} \right) \right] \\ & - \frac{\partial}{\partial T_\infty} \left(\frac{1}{H_H} \right) \cdot \frac{(z-500)(R_E+125)^2}{(R_E+500)(R_E+z)} \end{aligned} \quad (10.35)$$

for hydrogen. In equations (10.34) and (10.35)

$$\frac{1}{H_i} = \frac{M_i g(125)}{R_* T_\infty} \quad \text{and} \quad \frac{1}{H_H} = \frac{M_H g(125)}{R_* T_\infty}.$$

The explicit form for $s \equiv s(T_\infty)$ is given by [60] as

$$s = 0.0057 + \frac{17.6}{T_\infty + 244.0} \quad (10.36)$$

so that

$$\frac{\partial s}{\partial T_\infty} = \frac{-17.6}{(T_\infty + 244.0)^2} \quad (10.37)$$

Also from [60],

$$\log_{10} [n_i(125)] = a_i + \frac{b_i}{T_\infty + c_i} \quad (10.38)$$

for constants a_i , b_i and c_i dependent upon species, i , so that

$$\frac{\partial}{\partial T_\infty} [\ln n_i(125)] = \frac{-b_i}{(T_\infty + c_i)^2} \ln[10]. \quad (10.39)$$

From [11] the equation for the hydrogen concentration at 500km, $n_H(500)$, is

$$\log_{10} n_H(500) = 79.13 - 39.4 \log_{10} T_{500} + 5.5 (\log_{10} T_{500})^2 \quad (10.40)$$

yielding

$$\frac{\partial}{\partial T_\infty} [\ln n_H(500)] = \frac{\ln[10]}{T_{500}} (-39.4 + 11 \log_{10} T_{500}) \frac{\partial T_{500}}{\partial T_\infty} \quad (10.41)$$

upon differentiation with respect to T_∞ .

Next

$$\frac{\partial}{\partial T_\infty} \left(\frac{1}{sH_i} \right) = -\frac{1}{sH_i} \left[\frac{1}{s} \frac{\partial s}{\partial T_\infty} + \frac{1}{H_i} \frac{\partial H_i}{\partial T_\infty} \right] \quad (10.42)$$

where

$$\frac{\partial H_i}{\partial T_\infty} = \frac{R_*}{M_i g(125)}. \quad (10.43)$$

Equations (10.42) and (10.43) hold for all species, i , including H. Also

$$\frac{\partial}{\partial T_\infty} \left\{ \ln \left[\frac{T_{125}}{T} \right] \right\} = \frac{1}{T_{125}} \frac{\partial T_{125}}{\partial T_\infty} - \frac{1}{T} \frac{\partial T}{\partial T_\infty} \quad (10.44)$$

where T_{125} is given in [11] as

$$T_{125} = a + b T_{\infty} + c \exp(k T_{\infty}) \quad (10.45)$$

for constants a, b, c and k . Therefore

$$\frac{\partial T_{125}}{\partial T_{\infty}} = b + ck \exp(k T_{\infty}) . \quad (10.46)$$

$\partial T/\partial T_{\infty}$ is calculated by differentiating equation (9.2) with respect to T_{∞} :-

$$\frac{\partial T}{\partial T_{\infty}} = 1 - \left(1 - \frac{\partial T_{125}}{\partial T_{\infty}}\right) \exp[-sz'] + (T_{\infty} - T_{125}) z' \exp[-sz'] \frac{\partial s}{\partial T_{\infty}} . \quad (10.47)$$

By substituting $z = 500$ into equation (9.2)

$$T_{500} = T_{\infty} - (T_{\infty} - T_{125}) \exp[-sz'_{500}]$$

where

$$z'_{500} = \frac{(500 - 125)(R_E + 125)}{(R_E + 500)} . \quad (10.48)$$

Hence $\partial T_{500}/\partial T_{\infty}$ is given by

$$\frac{\partial T_{500}}{\partial T_{\infty}} = 1 - \left(1 - \frac{\partial T_{125}}{\partial T_{\infty}}\right) \exp[-sz'_{500}] + (T_{\infty} - T_{125}) z'_{500} \exp[-sz'_{500}] \frac{\partial s}{\partial T_{\infty}} . \quad (10.49)$$

Finally,

$$\frac{\partial}{\partial T_{\infty}} \left(\frac{1}{H_i}\right) = -\frac{1}{H_i^2} \frac{\partial H_i}{\partial T_{\infty}} \quad (10.50)$$

for all species. These equations solve equations (10.34) and (10.35) so all that remains to calculate is $\partial T_{\infty}/\partial A'_1$. But $T_{\infty} = T_2 + \Delta_G T_{\infty}$ so that

$$\frac{\partial T_{\infty}}{\partial A'_1} = \frac{\partial}{\partial A'_1} (\Delta_G T_{\infty}) \quad (10.51)$$

which is given by equation (10.31).

§10.6 Preliminary Results

The evaluation of equation (10.12) has been undertaken for the coefficients A_1 and B_1 in the formula for $\Delta_G T_{\infty}$ in CIRA 72, equation (9.5), and also for

the parameters c , the time constant, A'_1 , Z_1 , E_1 , A_2 and A_3 in JS84, (equations (10.3) to (10.9)). Some of this processing is utilized later in this thesis, when new models for geomagnetic activity are derived, in particular, solving for A_1 and B_1 in equation (9.5). However, some initial experiments were performed on the coefficients in JS84 and several conclusions drawn.

Firstly, it is not possible to estimate all the coefficients from one orbital arc, simultaneously. Likewise, if drag coefficients are also estimated, certain parameters such as A'_1 are difficult to derive on account of the high correlation between the two. This occurs because both A'_1 and the drag coefficients have the same effect of scaling the derived density values. Successful determination of one, requires that the other must be constrained in most circumstances. Also, estimation of the time constant, c , requires a very accurate initial approximation on account of the high non-linearity of equation (10.5). Consequently, much of the analysis performed on c was executed using various fixed values instead of actually deriving a value. Results of this preliminary work are presented in Table 10.8.

Table 10.8: Solution of certain parameters in JS84 from arc 6 (MJD 43774 to MJD 43783) with drag coefficient model as described.

<u>Orbital Description</u>	<u>Rms (m)</u>	<u>C_D range</u>	<u>C_R</u>	<u>Number of observations</u>	<u>Notes</u>
Daily C_D 's. Solve for :- \underline{x} , $\dot{\underline{x}}$, $\underline{C_D}$, C_R , c	0.59	3.14–5.45	1.68	2163	$c \rightarrow 4.2d^{-1}$
Daily C_D 's, $c = 4.2d^{-1}$ (fixed). Solve for :- \underline{x} , $\dot{\underline{x}}$, $\underline{C_D}$, C_R , A_2	0.61	3.14–5.35	1.67	2164	$A_2 \rightarrow 0.41$
Single C_D . Solve for :- \underline{x} , $\dot{\underline{x}}$, C_D , C_R , A'_1 , A_2 , c	3.37	1.82	1.44	2096	$c \rightarrow 4.7d^{-1}$ $A'_1 \rightarrow 144$ $A_2 \rightarrow 0.33$
Single C_D . Solve for :- \underline{x} , $\dot{\underline{x}}$, C_D , C_R , A'_1	4.63	2.22	1.52	2098	$A'_1 \rightarrow 117$

Arc 6 was analysed as it provided excellent variation in geomagnetic conditions over a large time span (Figure (10.1)). Using this period, Table 10.8 indicates that a time constant of $c = 1.0d^{-1}$ is too small and that $c = 4.2d^{-1}$ is more appropriate for SEASAT heights. It was therefore decided to apply this value to all the arcs listed in Table 10.1 when solving for a single drag coefficient, so that its performance could be compared to CIRA 72 and the original JS84. Results of this analysis are presented in Table 10.9.

Table 10.8 also indicates that A'_1 might be too small, i.e. that JS84, underestimates the density change associated with geomagnetic activity at 800km.

Estimating A_2 with c fixed at $4.2d^{-1}$ has little effect, either on A_2 itself or the orbit.

Results of solving for Z_1, E_1 and A_3 have not been produced at this stage since these coefficients are also highly correlated with A'_1 . This is to be expected when one considers that equations (10.2), (10.8) and (10.9), are all dependent upon the amplitude function A (equation (10.3)).

Table 10.9: Orbital results relative to JS84 with $c = 4.2d^{-1}$ and single C_D .

<u>Orbital arc</u>	<u>Rms (m)</u>	<u>C_D</u>	<u>C_R</u>	<u>Number of observations</u>
1	1.05	5.27	1.70	972
2	2.01	4.34	1.12	1488
3	1.51	2.60	1.44	1481
4	3.66	2.25	0.67	1101
5	6.28	2.89	1.77	1993
6				
7	5.12	5.09	2.55	1005
8	5.19	4.81	1.91	978
9	1.51	3.77	1.65	933

The use of $c = 4.2d^{-1}$ in JS84 has shown significant improvement over $c = 1.0d^{-1}$ in four out of eight arcs with one (arc 5) remaining virtually unchanged. Apparently, the smoothed index, $K'_p(c = 1.0d^{-1})$, is not applicable in many instances and Figure (10.1) may help to explain why. In most cases, the K'_p index all but removes the extreme geomagnetic variations and in particular it seems to have the effect of reducing the significance of 'blocks' of K_p . These blocks are noticeable in arcs 7, 8 and 9, precisely those arcs for which $c = 1.0d^{-1}$ performs badly.

To assess the effects of a further increase in the value of c , it was decided to recompute the eight arcs of Table 10.9 using a value of infinity. This is equivalent to using the instantaneous values of K_p as opposed to K'_p (see equation (10.5)). JS84 then takes on a very similar form to the geomagnetic activity component of J77 [61] which employs a time lag τ_{77} , equal to $0.1 + 0.2 \cos^2\phi$ (day). Consequently, both this value for τ and the value given by equation (10.6) were analysed, the results of which are presented in Table 10.10.

Table 10.10: Orbital results relative to JS84 using a value of infinity for c and two values for τ , $\tau_{84} = 0.05 + 0.1 \cos^2\phi$ (day) and $\tau_{77} = 0.1 + 0.2\cos^2\phi$ (day).

<u>Orbital</u> Arc	<u>Rms (m)</u>	<u>τ_{84}</u>		<u>τ_{77}</u>		<u>Number</u> of observations	
		<u>C_D</u>	<u>C_R</u>	<u>Rms (m)</u>	<u>C_D</u>		<u>C_R</u>
1	0.99	5.47	1.86	0.88	5.51	1.76	972
2	2.40	3.99	0.98	2.18	4.15	1.05	1488
3	1.85	2.52	1.41	1.66	2.52	1.41	1481
4	3.98	2.07	0.50	3.81	2.15	0.58	1101
5	6.63	2.81	1.74	6.44	2.83	1.74	1993
6							
7	1.56	4.61	2.07	4.97	4.61	1.96	1005
8	4.22	4.84	1.91	4.36	4.84	1.91	978
9	1.79	3.72	1.69	1.32	3.72	1.69	933

Both values of τ give results of a similar quality to those of CIRA 72 (Table 10.2) and JS84 with $c = 4.2d^{-1}$ (Table 10.9), except for the case of arc 7 with τ_{84} . For arc 7 the rms of fit is greatly reduced, the value being 1.56m on using τ_{84} compared to the value of 4.97m with τ_{77} . This is a significant improvement. Confirmation that the reduced time lag was responsible for this improvement was obtained when arc 7 was recomputed relative to CIRA 72 using τ_{84} for the time lag. The rms of fit reduced to 1.31m with recovered C_D of 3.85 and C_R of 1.84. However, this is not conclusive evidence that such a time lag is the required value overall, since the 3-hourly geomagnetic index, K_p , is too coarse to give anything but a crude indication.

§10.7 MSIS Type Models

The method of atmospheric density modelling adopted in the MSIS type models [13, 14, 15, 62] is different to the approach of CIRA 72. Such models, derived using in situ measurements, are more complex and attempt to represent the physical composition and temperature to a much greater accuracy than the drag based CIRA 72. There are many coefficients in the models, derived by assuming that the physics of the situation can be represented in terms of a spherical harmonic expansion. Consequently, the MSIS type models are generally more capable of representing individual constituent number densities.

One of the differences between CIRA 72, JS84 and the MSIS type models is the way in which persistence of a geomagnetic event is introduced into the modelling. CIRA 72 does not model persistence, JS84 attempts to account for it by smoothing the geomagnetic index, K_p , whereas the MSIS type models [15, 62] have a component which averages the effects of the activity itself. As seen in sections (10.2), (10.3) and (10.6), there are instances when CIRA 72 and JS84 are inaccurate, thus it was decided that an MSIS type model should also be analysed and compared with the results from CIRA 72 and JS84. The model chosen for this task

was the 1983 version, MSIS-83 [15], since it is an updated version of MSIS-1/2 [13,14] and also has a formulation for geomagnetic persistence. Results, both with (MSIS-83A) and without (MSIS-83) this persistence modelling, are presented in Table 10.11.

Table 10.11: Orbital results relative to MSIS-83 and a single C_D . MSIS-83 refers to the simple formula for geomagnetic activity (equation A23 of Hedin, [15]) whilst MSIS-83A refers to the summation formula A24.

<u>Orbital</u> <u>Arc</u>	<u>MSIS-83</u>				<u>MSIS-83A</u>			
	<u>Rms (m)</u>	<u>C_D</u>	<u>C_R</u>	<u>Number</u> <u>of observations</u>	<u>Rms (m)</u>	<u>C_D</u>	<u>C_R</u>	<u>Number</u> <u>of observations</u>
1	1.50	4.84	1.92	972	0.89	4.71	1.84	972
2	2.01	3.42	1.12	1488	1.84	3.51	1.17	1488
3	1.74	2.38	1.39	1481	1.34	2.40	1.44	1481
4	4.05	1.93	0.55	1101	3.74	2.06	0.69	1101
5	7.06	2.63	1.63	1928	6.40	2.66	1.61	1917
6								
7	5.06	4.75	1.89	1005	1.28	5.09	2.15	1005
8	6.07	5.19	1.98	978	6.27	5.11	1.95	978
9	3.06	3.98	1.64	933	3.04	3.97	1.62	933

These results are of a similar quality to those of Tables 10.2 and 10.9, with certain arcs (1, 2 and 3) improving over those relative to CIRA 72 and JS84 and others deteriorating (8 and 9). Hence, the overall modelling of total density, the sole requirement for satellite drag purposes, is in general, no better than for CIRA 72. Combined with the extra computing time required to utilize MSIS-83, this advocates the continued use of CIRA 72 in orbit determinations.

There is also a similarity in both the rms values and recovered C_R values between the two MSIS-83 versions, with MSIS-83A proving slightly the better. However, a significant improvement in the rms values occurs for arc 7 where MSIS-83A is by far the most accurate model examined. This confirms the findings of Hedin [15] that the model performs well over large well-defined geomagnetic storms, but is only comparable to the simpler model in the majority of situations.

§10.8 Discussion

Results of computing SEASAT arcs with various density models, when estimating a single drag coefficient, have been compared. Models employed, included the simple drag based CIRA 72, CIRA 72 modified with JS84 for geomagnetic activity modelling and two versions of MSIS-83. The results have shown that, in general, CIRA 72 performs as good as, if not better, than the more recent and complex models in representing the overall total atmospheric density. A great deal of progress is therefore required in order to attain the orbital accuracies obtained when employing multiple drag coefficients in the orbital solution. Evidently, the short-term density variations associated with geomagnetic activity are very difficult to accommodate with the later models not proving too successful. There are several explanations for this. Firstly, attempts to represent the dynamics of the atmosphere by static density models is an oversimplification which causes large uncertainties at SEASAT heights. Further, the majority of data employed in the derivation of the models analysed is from lower in the atmosphere (below 400km in general), where geomagnetic disturbances and hence temperature and density changes are not as significant as at 800km (section 9.5). Extrapolation to SEASAT heights might therefore prove inadequate as was suggested when A'_1 was estimated in Table 10.8, indicating that the density may be underestimated at such altitudes. Also, the parametrization of geomagnetic activity using K_p might be erroneous for certain periods. For example, arc 5 is very poorly determined for all the models analysed

whereas all the other arcs have a reasonable fit for at least one model. This could be the consequence of either poor data or the inadequacy of K_p in representing the geomagnetic effect over this period. This is investigated further in chapter 12.

Much of the work of this chapter has been summarized and published in a paper entitled "A Comparison of Geomagnetic Activity Models using SEASAT Laser Range Data", [26].

CHAPTER 11

DENSITY DETERMINATION

Figure 10.2 shows a marked correlation between the recovered drag coefficients and the geomagnetic planetary index, K_p , for the period MJD 43770 to MJD 43783. The implication is that the variation in the drag coefficients is in some way related to the variation in atmospheric density associated with geomagnetic activity. A similar correlation has also been observed by Wakker et al [6] and Noomen [59]. It has been noted that multiple drag coefficients absorb along-track modelling errors and, as shown in chapter 10, highly accurate orbits are derived in this way. Further, very similar orbits were obtained when using different density models provided multiple drag coefficients were estimated as part of the orbital solution. This suggests that multiple drag coefficients absorb errors in such a way as to produce an orbit as close to the real orbit as possible. Variation in the recovered values must therefore implicitly contain information about the true orbit and in particular about the true density.

This chapter aims to recover true atmospheric densities over daily intervals by analysing the variation in drag coefficients recovered from long-arc solutions of SEASAT laser data. Section 11.1 develops the mathematics necessary for such an analysis with the results of applying this method to two arcs presented in section 11.2. Section 11.3 assesses the effects of errors in some of the assumptions implicit in section 11.1, namely that the gravitational and SRP forces are modelled precisely.

§11.1 Atmospheric Densities From Multiple Drag Coefficients

Assume the modelled along-track position of the spacecraft at time $t = t_i$, is T_i^M , whilst the actual position is T_i^T . After a time interval $\Delta t_i = t_{i+1} - t_i$, the modelled along-track position, T_{i+1}^M , can be written as

$$T_{i+1}^M = T_i^M + \Delta T_i^M \quad (11.1)$$

where ΔT_i^M represents the total modelled along-track perturbation due to all forces (i.e. drag, gravity, SRP and third body attraction). An analogous equation exists for T_{i+1}^T . Although the estimated position at any instant may differ from the true position, this difference is assumed negligible for precise orbits derived from laser range data where the rms of fit is typically below one metre when estimating for multiple drag coefficients as part of the orbital solution (Table 10.4, Marsh et al [3] and Zandbergen et al [42]). Hence it is reasonable to equate

$$\Delta T_i^T = \Delta T_i^M . \quad (11.2)$$

Assuming that third body attraction is modelled exactly, expansion of equation (11.2) into the principal sources of along-track perturbation gives

$$\Delta T_i^T(\text{DRAG}) + \Delta T_i^T(\text{GRAVITY}) + \Delta T_i^T(\text{SRP}) = \Delta T_i^M(\text{DRAG}) + \Delta T_i^M(\text{GRAVITY}) + \Delta T_i^M(\text{SRP}) \quad (11.3)$$

where the terms in brackets refer to the force concerned. If, in the first instance, all along-track mis-modelling is attributed to atmospheric effects then

$$\Delta T_i^T(\text{DRAG}) = \Delta T_i^M(\text{DRAG}). \quad (11.4)$$

Equation (11.4) basically expresses, in mathematical form, the observation made at the end of section (10.3), namely that multiple drag coefficients absorb deficiencies in atmospheric modelling.

Now, representing ΔT in angular form

$$\frac{d}{dt}(\Delta T) \simeq \Delta n = -\frac{3}{2} \frac{n}{a} \Delta a \quad (11.5)$$

upon using Kepler's Third Law and dropping the T and M superscripts and the i subscript for brevity of notation. In equation (11.5), Δn and Δa are the corresponding changes in the mean motion, n , and the semi-major axis, a ,

respectively, due to atmospheric drag over a certain period of time. But, from King-Hele [63]

$$\frac{da}{dt} = \frac{2a^2v}{\mu} F_T \quad . \quad (11.6)$$

where v is the satellite velocity, μ the gravitational constant and F_T the along-track force given by

$$F_T = -\frac{1}{2} \left(\frac{A}{m} \right) C_D v_r^2 \rho . \quad (11.7)$$

In equation (11.7), the notation is as defined for equation (3.6). Integration of equation (11.6) gives

$$\Delta a = -\frac{C_{D_i}}{\mu} \int_{t_i}^t a^2 v \left(\frac{A}{m} \right) v_r^2 \rho dt' \quad (11.8)$$

where C_{D_i} is the drag coefficient assumed constant over the interval $[t_i, t]$. Hence, integration of equation (11.5) yields

$$\Delta T_i = \frac{3C_{D_i}}{2\mu} \int_{t_i}^{t_{i+1}} \frac{n}{a} \int_{t_i}^t a^2 v \left(\frac{A}{m} \right) v_r^2 \rho dt' dt \quad (11.9)$$

upon substitution of equation (11.8). In equation (11.9) C_{D_i} is now assumed constant over Δt_i . To recover density variation it is necessary to represent equation (11.9) in terms of an effective density, $\bar{\rho}_i$, defined by

$$\Delta T_i = \frac{3C_{D_i}}{2\mu} \bar{\rho}_i I_i \quad (11.10)$$

where

$$I_i = \int_{t_i}^{t_{i+1}} \frac{n}{a} \int_{t_i}^t a^2 v \left(\frac{A}{m} \right) v_r^2 dt' dt. \quad (11.11)$$

From equations (11.4) and (11.10),

$$C_D^T \bar{\rho}_i^T I_i^T = C_{D_1}^M \bar{\rho}_i^M I_i^M \quad (11.12)$$

there being only one true drag coefficient, C_D^T . For precise laser orbits, $I_i^T \approx I_i^M$ so that

$$C_D^T \bar{\rho}_i^T = C_{D_1}^M \bar{\rho}_i^M. \quad (11.13)$$

Since C_D^T is unknown, the absolute true effective density, $\bar{\rho}_i^T$, cannot be determined. However, the relative effective density is given by

$$\frac{\Delta \bar{\rho}_i^T}{\bar{\rho}_i^T} \equiv \frac{\bar{\rho}_{i+1}^T - \bar{\rho}_i^T}{\bar{\rho}_i^T} = \frac{C_{D_{i+1}}^M \bar{\rho}_{i+1}^M - C_{D_i}^M \bar{\rho}_i^M}{C_{D_i}^M \bar{\rho}_i^M} \quad (11.14)$$

upon using equation (11.13)

Note that equation (11.14) could have been written immediately upon assuming $C_{D_1}^M$ absorbs density modelling errors, but the identification of $\bar{\rho}_i$ (equation (11.10)) as the effective density is easily overlooked. Simply taking $\bar{\rho}_i$ as the average density over Δt_i will lead to anomalous results since $C_{D_1}^M$ is a scale factor to adjust the along-track position so as to satisfy equation (11.4).

§11.2 Relative Effective Densities

The method developed in section (11.1) has been applied to two long-arc SEASAT laser orbits with relative effective densities being determined over daily intervals in the main. One orbit was a 14 day arc spanning July 27 to August 10, 1978 (MJD 43716 to MJD 43730), the other a 13 day arc spanning September 19 to October 2, 1978 (MJD 43770 to MJD 43783). The former of these two arcs occurred during the 17 day repeat period, the latter during the 3 day repeat. Both orbital arcs were initially computed relative to the GEM-T1 gravity field in conjunction with the NASA 'area tables' for SEASAT and daily drag coefficients for all days except MJD

43780. On MJD 43780, two half daily coefficients were utilized because of the severe geomagnetic storm over this period. All orbital solutions involved estimating a state vector at epoch, a solar radiation pressure coefficient, C_R and multiple drag coefficients as described above.

Validation of the method was assessed by comparing the observed or 'true' densities as derived from several atmospheric density models. Equation (11.14) implies independence from the atmospheric model so that the observed densities derived from alternative models should be comparable.

The 13 day arc was computed relative to the atmospheric models CIRA 72, MSIS-83A (described in chapter 10), DTM and JS84, the results of which are presented in Tables 11.1 and 11.2. Figures 11.1 and 11.2 depict the density variations relative to $\bar{\rho}_1$, for the modelled and observed values, respectively, upon using

$$\bar{\rho}_{i+1} = \bar{\rho}_1 \prod_{j=1}^i (1 + \alpha_j) \quad (11.15)$$

where $\alpha_j = \Delta\rho_j/\bar{\rho}_j$ of Table 11.2. These graphs show the so called density profiles.

Table 11.1: Recovered drag coefficients and modelled effective densities for the 13 day arc spanning September 19 to October 2, 1978 (MJD 43770 to MJD 43783) using the GEM-T1 gravity field and NASA 'area tables' for SEASAT.

		CIRA 72 $C_R=1.62$, rms = 97cm		MSIS-83A $C_R=1.60$, rms = 83cm		DTM $C_R=1.63$, rms = 82cm		JS84 $C_R=1.65$, rms = 98cm	
i	Span of C_D 's	C_{D_i}	$\bar{\rho}_i \times 10^{14}$ (kgm ⁻³)	C_{D_i}	$\bar{\rho}_i \times 10^{14}$ (kgm ⁻³)	C_{D_i}	$\bar{\rho}_i \times 10^{14}$ (kgm ⁻³)	C_{D_i}	$\bar{\rho}_i \times 10^{14}$ (kgm ⁻³)
1	43770-71	2.69	1.29	2.53	1.31	2.53	1.34	2.60	1.29
2	71-72	2.57	1.35	2.47	1.41	2.37	1.45	2.69	1.33
3	72-73	2.06	1.94	2.22	1.75	2.17	1.86	2.59	1.50
4	73-74	3.04	1.79	3.22	1.78	3.18	1.81	3.52	1.62
5	74-75	2.99	2.15	3.44	1.91	3.39	1.93	3.66	1.84
6	75-76	2.75	2.03	2.90	1.83	2.86	1.86	2.87	1.83
7	76-77	3.31	2.39	3.97	2.06	3.79	2.17	4.55	1.84
8	77-78	3.16	2.75	4.18	2.22	4.15	2.25	4.30	2.17
9	78-79	3.63	2.83	4.51	2.26	4.44	2.28	4.41	2.31
10	79-80	3.78	3.34	5.19	2.37	5.23	2.35	4.94	2.45
11	80-80.5	5.67	2.99	4.92	2.86	6.69	2.47	6.63	2.52
12	80.5-81	3.11	7.11	5.41	4.72	8.02	3.04	7.11	3.19
13	81-82	2.64	2.23	3.33	1.92	3.17	1.80	2.14	2.55
14	82-83	3.86	1.93	3.97	1.70	4.13	1.77	4.05	1.95

Table 11.2: Observed (O) and modelled (M) relative densities for the 13 day arc as derived from four atmospheric models and equation (11.14).

		CIRA72		MSIS-83A		DTM		JS84	
i		O	M	O	M	O	M	O	M
1		0.0	+0.05	+0.05	+0.08	+0.01	+0.08	+0.07	+0.03
2		+0.15	+0.44	+0.12	+0.25	+0.18	+0.29	+0.08	+0.12
3		+0.37	-0.07	+0.47	+0.01	+0.42	-0.03	+0.47	+0.08
4		+0.18	+0.20	+0.15	+0.08	+0.14	+0.07	+0.18	+0.14
5		-0.13	-0.06	-0.20	-0.04	-0.19	-0.04	-0.22	-0.01
6		+0.42	+0.18	+0.54	+0.13	+0.55	+0.17	+0.59	0.0
7		+0.11	+0.15	+0.14	+0.08	+0.13	+0.04	+0.12	+0.18
8		+0.18	+0.03	+0.10	+0.02	+0.09	+0.02	+0.09	+0.07
9		+0.23	+0.18	+0.21	+0.05	+0.21	+0.03	+0.19	+0.06
10		+0.34	-0.11	+0.15	+0.21	+0.35	+0.05	+0.38	+0.03
11		+0.31	+1.38	+0.81	+0.65	+0.47	+0.23	+0.36	+0.27
12		-0.73	-0.69	-0.75	-0.59	-0.77	-0.41	-0.76	-0.20
13		+0.27	-0.13	+0.06	-0.11	+0.28	-0.02	+0.44	-0.24

Figure 11.1: Modelled density profiles for MJD 43770 to MJD 43783.

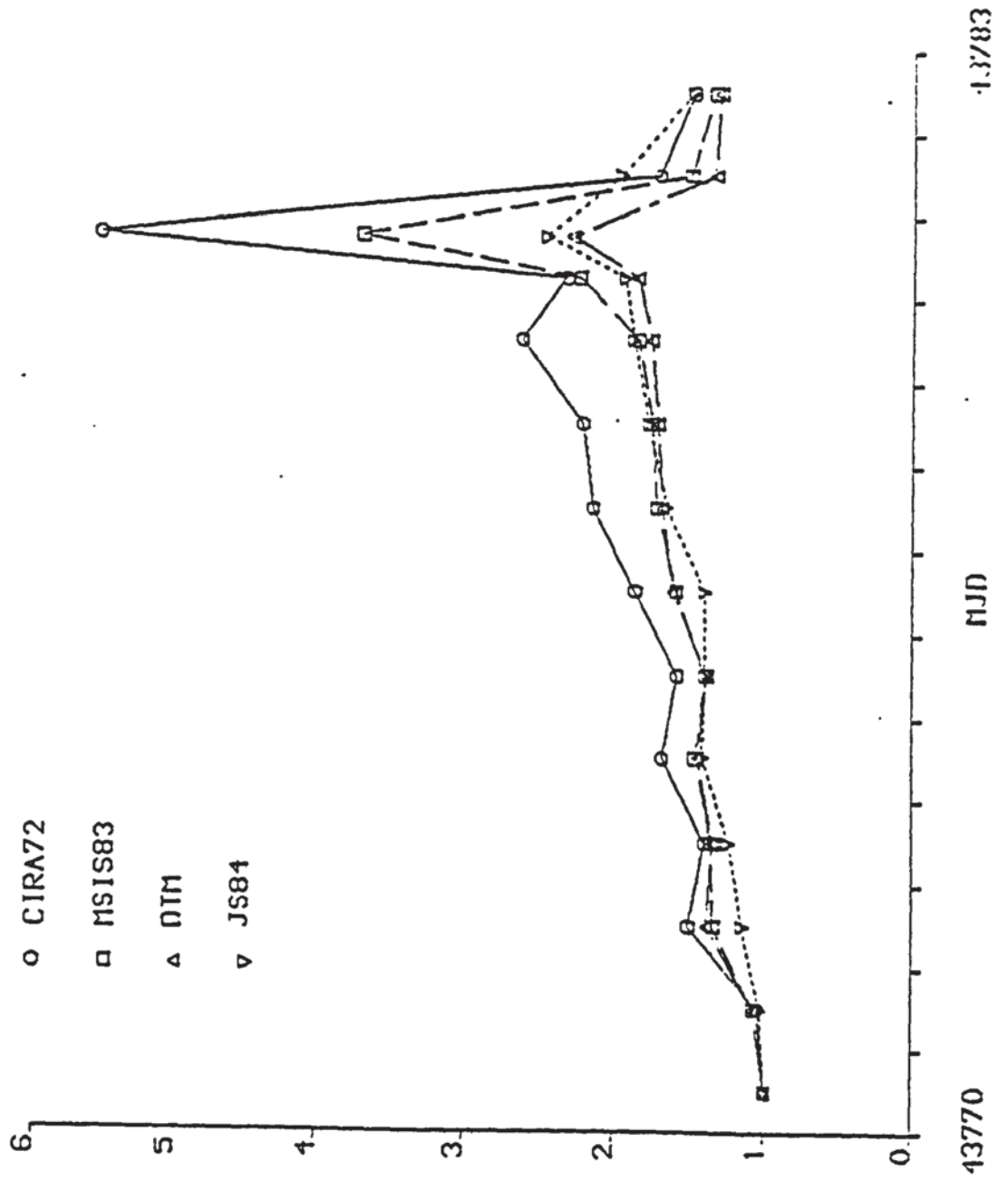
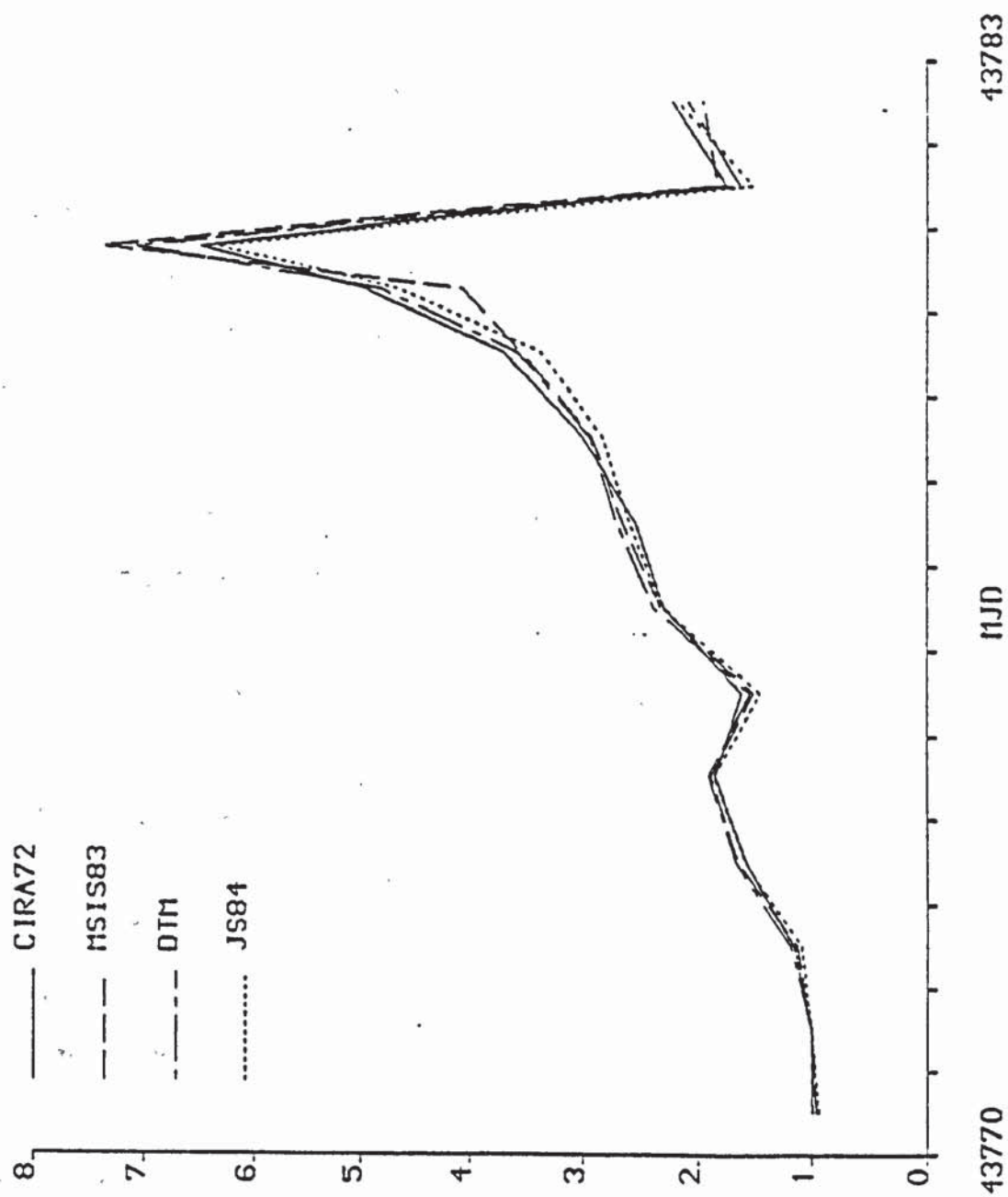


Figure 11.2: Observed density profiles for MJD 43770 to MJD 43783.



The observed density profiles of Figure 11.2 show excellent agreement between all models, with a slight discrepancy over the period of the two half-daily drag coefficients. (This is attributed primarily to the limited amount of data and shows the difficulty in deriving densities over periods of less than a day. Density values are only meaningful if the drag coefficients have been well-determined, a criterion which places a limit on the time span of their derivation. Consequently, this study was restricted to determining daily relative densities except on MJD 43780.) On a cautionary note, the last drag coefficient from any orbit is less well-determined than previous values as there is no subsequent data to act as a constraint. Results from the last day of any analysis should not be judged too critically.

In comparison, the modelled variations of Figure 11.1 exhibit considerable differences with only CIRA 72 (full line) approaching the level of increase as predicted from the data. Also, the modelled densities increase over the first ten days, at a rate less than the required variation. Such an error is unlikely to be systematic, as the total change in observed and modelled densities are in accord over the full 13 day period.

Figures 11.1 and 11.2 also reveal where a good orbital fit with a single drag scale factor will occur. For instance, MSIS-83A performs well over MJD 43778 to MJD 43782 with a single drag coefficient (Table 10.11). From the figures, it is apparent that, apart from scale, the shapes of the observed and MSIS-83A modelled density profiles over this period, are basically similar. Conversely, the poor performance of a single drag coefficient over MJD 43770 to MJD 43776 and MJD 43774 to MJD 43783 with any density model (Tables 10.2, 10.5, 10.9, 10.10 and 10.11), can be explained since all models fail to match the observed profiles over these periods, even allowing for a scale difference. In particular, these figures reveal the inadequacy of the K_p index in representing the change in density due to geomagnetic activity over MJD 43772. This confirms the hypothesis of section 10.8 which suggested that in certain instances, K_p might be unrepresentative of actual density change. Apparently the increase in K_p on MJD 43772 does not correspond

to an increase in density and hence no density model based on the K_p index, will be able to represent the true variation over this period.

Equivalent results for the 14 day arc, relative to CIRA 72 and MSIS-83A only, were also analysed. They are presented in Tables 11.3 and 11.4. In order to synchronize the observed profiles, the density variations were determined relative to $\bar{\rho}_2$ in this case to eliminate the offset introduced by the difference in the initial $C_D \bar{\rho}$ product. This offset is attributed to the differences in along-track position as derived from the initial state vectors, since the modelled densities are similar over MJD 43716 (Table 11.3). Hence results from the first day of an orbit should also be treated with caution. The method is therefore most applicable to long-arc orbits which give maximum constraint on the intermediate drag coefficients. For this reason the above analysis was restricted to two arcs only, since other arcs of comparable length could not be extracted from the limited SEASAT data set.

As shown in Figure 11.3, both profiles of modelled density for MJD 43722 to MJD 43728, agree well with the observed profile of Figure 11.4, as expected from the low rms values in Tables 10.2 and 10.11.

Both arcs have confirmed the validity of the method, with near identical observed profiles being derived irrespective of the density model used.

Table 11.3: Recovered drag coefficients and modelled effective densities for the 14 day arc spanning July 27 to August 10, 1978 (MJD 43716 to MJD 43730), using the GEM-T1 gravity field and NASA 'area tables'.

		CIRA 72 $C_R = 1.63$ crms = 86cm		MSIS-83A $C_R = 1.58$ rms = 90cm	
i	Span of C_{D_i} 's	C_{D_i}	$\bar{\rho}_i^M \times 10^{14}$ (kgm^{-3})	C_{D_i}	$\bar{\rho}_i^M \times 10^{14}$ (kgm^{-3})
1	43716-17	5.64	0.54	4.25	0.63
2	17-18	4.64	0.58	4.10	0.68
3	18-19	6.59	0.47	5.08	0.59
4	19-20	5.32	0.51	4.44	0.61
5	20-21	5.25	0.45	4.02	0.55
6	21-22	5.48	0.48	4.42	0.60
7	22-23	4.93	0.48	3.90	0.57
8	23-24	4.73	0.59	4.12	0.67
9	24-25	4.27	0.87	4.66	0.82
10	25-26	4.29	0.70	4.02	0.75
11	26-27	4.29	0.82	4.57	0.79
12	27-28	4.93	0.68	4.12	0.75
13	28-29	3.92	0.67	3.39	0.75
14	29-30	5.81	0.62	4.79	0.74

Table 11.4: Observed (O) and modelled (M) relative effective densities as derived from Table 11.3 upon using equation (11.14).

		CIRA 72		MSIS-83A	
i		O	M	O	M
1		-0.12	+0.07	+0.05	+0.08
2		+0.14	-0.20	+0.08	-0.13
3		-0.11	+0.10	-0.11	+0.02
4		-0.13	-0.12	-0.18	-0.09
5		+0.12	+0.07	+0.20	+0.09
6		-0.11	-0.01	-0.17	-0.06
7		+0.19	+0.24	+0.24	+0.18
8		+0.32	+0.46	+0.40	+0.23
9		-0.19	-0.19	-0.21	-0.09
10		+0.18	+0.18	+0.19	+0.05
11		-0.06	-0.18	-0.14	-0.05
12		-0.21	-0.01	-0.17	0.0
13		+0.37	-0.07	+0.40	0.0

Figure 11.3 : Modelled density profiles for MJD 43716 to MJD 43730.

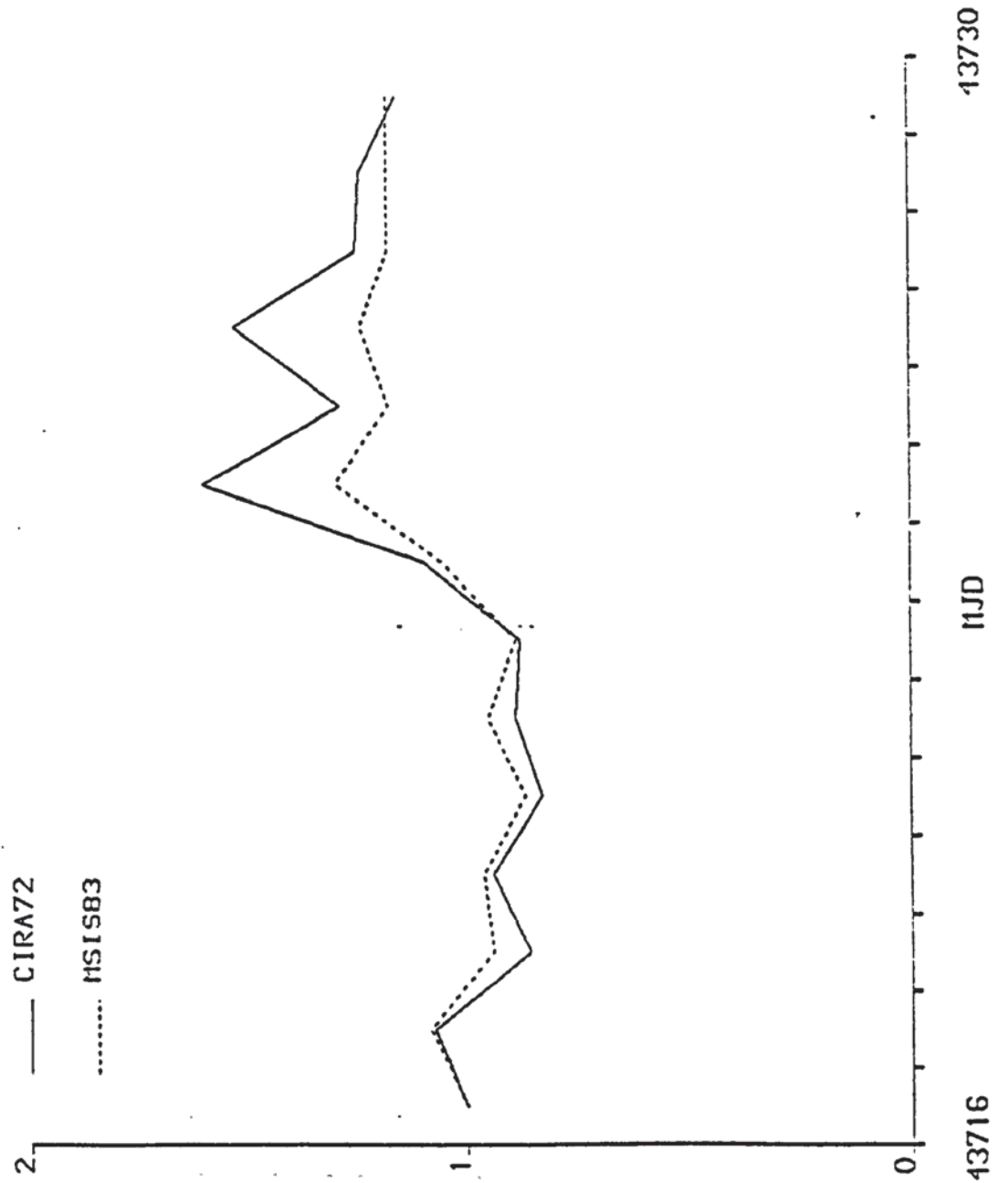
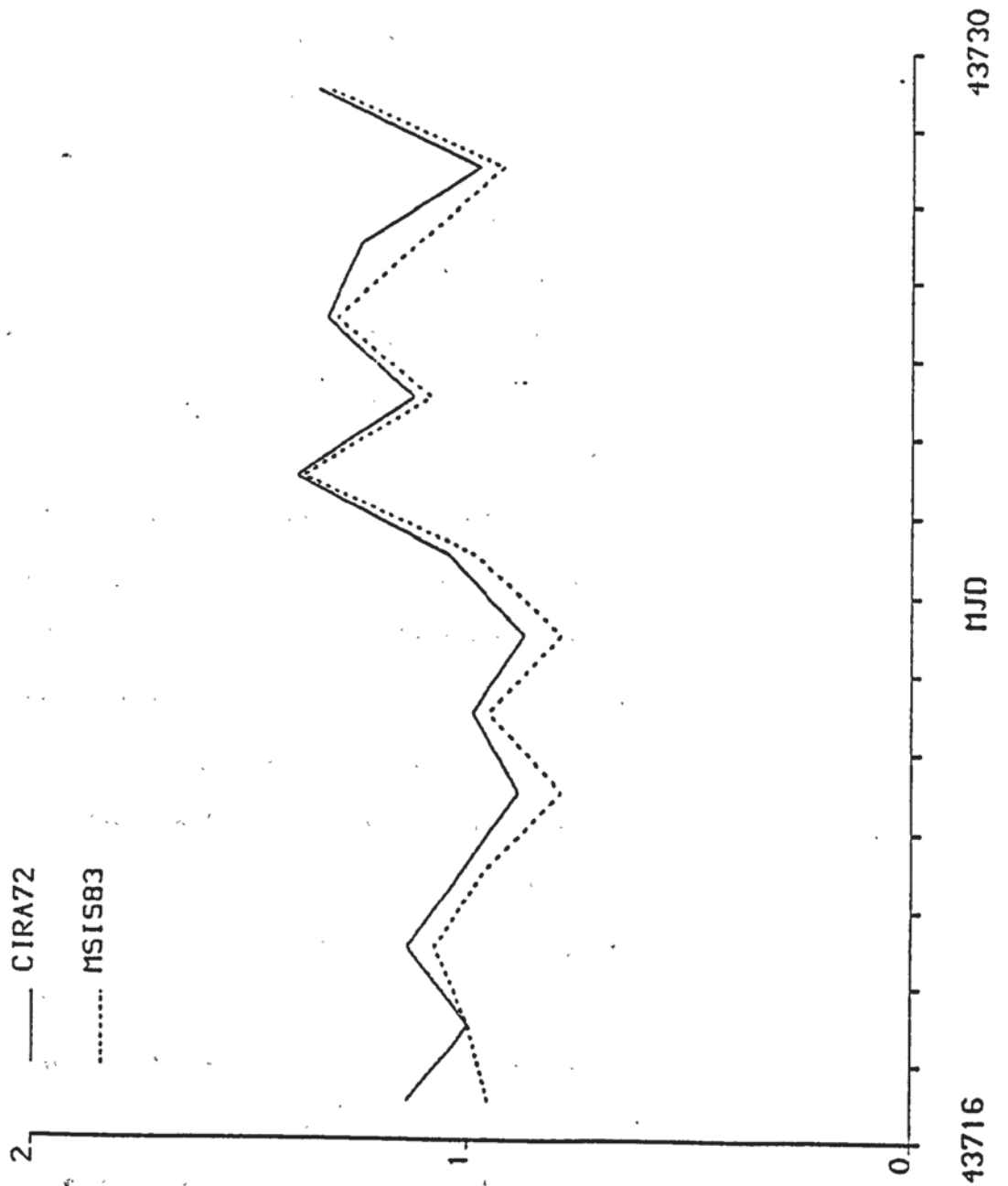


Figure 11.4 : Observed density profiles for MJD 43716 to MJD 43730.



§11.3 The Effect Of Gravity Field And SRP Errors On The Density Values

The method of density determination developed in section 11.1 assumes that no errors exist in either gravity field or SRP modelling. The orbits of section 11.2 are highly accurate, both in terms of the rms of fit to laser range data and the consistency within the recovered C_R values. Due to this accuracy, it was decided that the assumptions of section 11.1 were basically valid. This section is concerned with assessing the effects of non-negligible errors in both gravity and SRP forces on the derived density values.

Gravity field error effects were assessed by recomputing the two arcs of section 11.2 relative to the tailored SEASAT gravity field, PGS-S3 [2], whilst SRP error effects were assessed by using a fixed value of 1.5 for C_R in conjunction with the GEM-T1 gravity field. For both cases, the orbits were derived relative to the CIRA 72 atmospheric model only, again using the NASA 'area tables' for SEASAT. The results are presented in Tables 11.5 and 11.6 with graphical plots being given in Figures 11.5 and 11.6. Also plotted for comparison, are the profiles determined from GEM-T1 with CIRA 72. Note that the profiles are relative to $\bar{\rho}_2$ due to large discrepancies in the first drag coefficient from each of the models.

For the 13 day arc (Figure 11.5), there is good agreement in shape at least, between all three profiles, indicating that small gravity field and SRP errors have little effect on the derived densities over this period. This is attributed to the relatively high level of base density, a response to the level of solar activity for this time span (Figure 11.7). One discrepancy however, is the scale offset on the profile derived relative to the PGS-S3 gravity field. This disappears upon calculating the densities relative to $\bar{\rho}_3$ and is due to the inter-dependence between the first two drag coefficients of this orbit – the very high initial value causes the second one to be low, to compensate. Evidently, the initial along-track position as given by the state vector at epoch, contaminates the first two coefficients in this case. Such deficiencies however, are expected to be reduced for the significantly more accurate GEM-T1

gravity field. As a measure of the orbital improvement with GEM-T1, the rms of fit to the laser measurements for the 13 day arc when using GEM-T1 with CIRA 72 is 0.97m compared to 1.52m for PGS-S3 with CIRA 72, (Tables 11.1 and 11.5).

Conversely, the PGS-S3 profile for the 14 day arc, deviates significantly from the GEM-T1 based profiles (Figure 11.6). Over this period, the low solar activity (Figure 11.8) and hence low base density, gives more significance to gravity field errors. However, a small error in C_R , again has little effect. This is explained upon examination of the recovered drag coefficients, $C_{D_i}^{1.5}$, from the 14 day arc with C_R fixed at 1.5, (Table 11.5). Comparison with the values $C_{D_i}^M$, from the same orbit with C_R allowed to vary, (Table 11.3), shows an almost constant scale factor difference, $(1 - \beta)$. Hence from equation (11.14)

$$\begin{aligned} \left(\frac{\bar{\rho}_{i+1}^T - \bar{\rho}_i^T}{\bar{\rho}_i^T} \right)_{C_R = 1.5} &= \frac{C_{D_{i+1}}^{1.5} \bar{\rho}_{i+1}^{1.5} - C_{D_i}^{1.5} \bar{\rho}_i^{1.5}}{C_{D_i}^{1.5} \bar{\rho}_i^{1.5}} \\ &= \frac{(1 - \beta) [C_{D_{i+1}}^M \bar{\rho}_{i+1}^M - C_{D_i}^M \bar{\rho}_i^M]}{(1 - \beta) C_{D_i}^M \bar{\rho}_i^M} \\ &= \frac{(\bar{\rho}_{i+1}^T - \bar{\rho}_i^T)}{\bar{\rho}_i^T} \Bigg|_{C_R \text{ allowed to vary}} \end{aligned}$$

since $\bar{\rho}_i^{1.5} = \bar{\rho}_i^M$ where $\bar{\rho}_i^{1.5}$ is the modelled effective density over the i^{th} interval for the orbit with $C_R = 1.5$. Hence, both models for C_R give the same results for relative density, irrespective of the level of base density. The point at which an error in C_R is sufficient to corrupt the solution will depend on when the recovered drag coefficients are no longer scaled by a constant $(1 - \beta)$, relative to the original, values.

This modification to C_R effectively scales the radial, along-track and cross-track perturbations identically. In practice, this is unrealistic since along-track errors due to SRP will be absorbed within the drag coefficients with C_R constrained by

radial and cross-track effects. Thus equation (11.13) can be incorrect and should be replaced by

$$C_D^T \bar{\rho}_i^T = C_{D_i}^M \bar{\rho}_i^M + \delta_i \quad (11.16)$$

where δ_i is the required correction for SRP absorption in $C_{D_i}^M$. Equation (11.14)

then becomes

$$\frac{\bar{\rho}_{i+1}^T - \bar{\rho}_i^T}{\bar{\rho}_i^T} = \frac{C_{D_{i+1}}^M \bar{\rho}_{i+1}^M - C_{D_i}^M \bar{\rho}_i^M + \delta_{i+1} - \delta_i}{C_{D_i}^M \bar{\rho}_i^M + \delta_i} \quad (11.17)$$

where $i = 1$ is adopted in the denominator. Over consecutive days, $\delta_{i+1} \approx \delta_i$ given the slowly varying orbital geometry. Letting $\delta_i = \gamma C_{D_i}^M \bar{\rho}_i^M$ for some constant γ ,

then

$$\begin{aligned} \bar{\rho}_{i+1}^T &= \left\{ \frac{C_{D_{i+1}}^M \bar{\rho}_{i+1}^M - C_{D_i}^M \bar{\rho}_i^M}{(1 + \gamma) C_{D_i}^M \bar{\rho}_i^M} \right\} \bar{\rho}_i^T + \bar{\rho}_i^T \\ &= \left\{ \frac{C_{D_{i+1}}^M \bar{\rho}_{i+1}^M - C_{D_i}^M \bar{\rho}_i^M}{(1 + \gamma) C_{D_i}^M \bar{\rho}_i^M} \right\} \bar{\rho}_i^T + \left\{ \frac{C_{D_i}^M \bar{\rho}_i^M - C_{D_{i-1}}^M \bar{\rho}_{i-1}^M}{(1 + \gamma) C_{D_i}^M \bar{\rho}_i^M} \right\} \bar{\rho}_i^T + \bar{\rho}_{i-1}^T \end{aligned} \quad (11.18)$$

with the final result

$$\bar{\rho}_{i+1}^T = \left\{ 1 + \frac{1}{1 + \gamma} \sum_{j=1}^i B_j \right\} \bar{\rho}_1^T \quad (11.19)$$

where

$$B_j = \frac{(C_{D_{j+1}}^M \bar{\rho}_{j+1}^M - C_{D_j}^M \bar{\rho}_j^M)}{C_{D_i}^M \bar{\rho}_i^M} .$$

Simplifying equation (11.19) gives

$$\bar{\rho}_{i+1}^T = \left\{ 1 + \frac{1}{1 + \gamma} \frac{(C_{D_{j+1}}^M \bar{\rho}_{j+1}^M - C_{D_1}^M \bar{\rho}_1^M)}{C_{D_i}^M \bar{\rho}_i^M} \right\} \bar{\rho}_1^T \quad (11.20)$$

For $\gamma = 0$, equations (11.14) and (11.20) are equivalent. From equation (11.20) it is seen that precise SRP modelling is crucial for density determinations. Use of the NASA 'area tables' for normalized solar radiation pressure accelerations is

a direct response to this criterion. The tables were derived for SEASAT in consideration of the visibility, reflectivity and diffusivity of a surface for various orientations of the spacecraft and thus are expected to reduce along-track SRP errors. However, comparison of the recovered drag coefficients from the two arcs analysed, show this not to be the case. Averaging the first six coefficients from each arc (to reduce uncertainties due to geomagnetic variation) then relative to CIRA 72, a mean value of 5.49 is obtained for the earlier arc compared with 2.68 for the later one. In comparison, values of 4.39 and 2.80 were derived relative to MSIS-83A, respectively. Although partly a response to the differing levels of solar activity (Figures 11.7 and 11.8), the higher values during the earlier arc indicate absorption of SRP effects, particularly as the NASA tables yield larger along-track perturbations during the early part of SEASAT's operational life. However, the close correspondence between the observed and modelled densities over MJD 43716 to MJD 43730 indicates that this absorption has been by a near-constant scale factor, as expected for a period of low density variability. For the more interesting 13 day arc, the drag coefficients have more physical realism and coupled with the higher level of base density, are not expected to be influenced by SRP to any significant extent.

§11.4 Density Profiles

The method of density determination can be used to plot observed or 'true' density profiles over long-arc orbits. Such profiles have been plotted for two long-arc SEASAT laser orbits, using daily drag coefficients in the main. Although coarse, the profiles show the general trend of the 'true' density variation, with very similar results being obtained for any atmospheric model (provided that a good gravity field is employed). Gravity field and SRP errors were shown to be negligible over high levels of the base density as determined by the level of solar activity. For lower levels however, gravity field errors become more important but, by using the GEM-T1 model, it is anticipated that they are minimal. The development of more

accurate gravity models such as GEM-T3 for instance, (soon to be published), should enable the recovery of more reliable density values for even lower levels of base density and hopefully shorter time intervals than one day. Future work of this nature could be performed using ERS-1 data, which hopefully, will cover a longer time span than the SEASAT data, thereby experiencing a large degree of atmospheric variability and conditions.

Comparison of modelled and observed density profiles reveals the reason for poor orbits being obtained, in many cases when estimating a single drag coefficient only. However, by such a comparison, it is possible to predict where a good orbital fit to a single drag scale factor will occur. This technique has implications for new density modelling, since the observed profile indicates the shape that a modelled profile should follow. Use is made of this observation in the next and penultimate chapter in which new density modelling techniques are examined.

The work of this chapter has been published in a paper entitled "The Determination of Relative Effective Atmospheric Densities at 800km using SEASAT Laser Range Data", [64].

Table 11.5: Recovered drag coefficients for orbits with gravity field and SRP errors, using CIRA 72 and the NASA 'area tables'.

i	13 day arc (MJD 43770 to MJD 43783)		14 day arc (MJD 43716 to MJD 43730)	
	PGS-S3 $C_R = 1.65$ rms = 1.52m	$C_R = 1.5,$ (GEM-T1) rms = 1.61m	PGS-S3 $C_R = 1.60$ rms = 1.63m	$C_R = 1.5,$ (GEM-T1) rms = 0.99m
1	3.25	2.15	5.23	5.39
2	2.22	2.60	4.35	4.32
3	2.06	2.01	7.63	6.35
4	3.28	2.99	4.92	5.02
5	2.77	2.93	4.67	5.13
6	2.83	2.75	5.37	5.06
7	3.42	3.28	5.90	4.68
8	3.07	3.13	4.09	4.46
9	3.56	3.60	3.89	4.15
10	3.95	3.78	5.26	4.04
11	5.65	5.40	3.91	4.16
12	3.03	3.30	4.00	4.71
13	2.53	2.43	4.71	3.62
14	4.82	3.40	6.38	4.99

Table 11.6: Observed densities from Table 11.5 and equation (11.14).

i	13 day arc (MJD 43770 to MJD 43783)		14 day arc (MJD 43716 to MJD 43730)	
	PGS-S3	$C_R = 1.5$	PGS-S3	$C_R = 1.5$
1	-0.29	+0.27	-0.11	-0.14
2	+0.34	+0.11	+0.41	+0.18
3	+0.47	+0.38	-0.29	-0.13
4	+0.01	+0.18	-0.17	-0.10
5	-0.04	-0.12	+0.24	+0.06
6	+0.42	+0.40	+0.09	-0.08
7	+0.04	+0.10	-0.14	+0.18
8	+0.19	+0.19	+0.39	+0.36
9	+0.31	+0.24	+0.09	-0.21
10	+0.28	+0.28	-0.13	+0.21
11	+0.28	+0.45	-0.16	-0.07
12	-0.74	-0.77	+0.17	-0.24
13	+0.64	+0.21	+0.26	+0.28

Figure 11.5: Observed density profiles for MJD 43770 to MJD 43783.

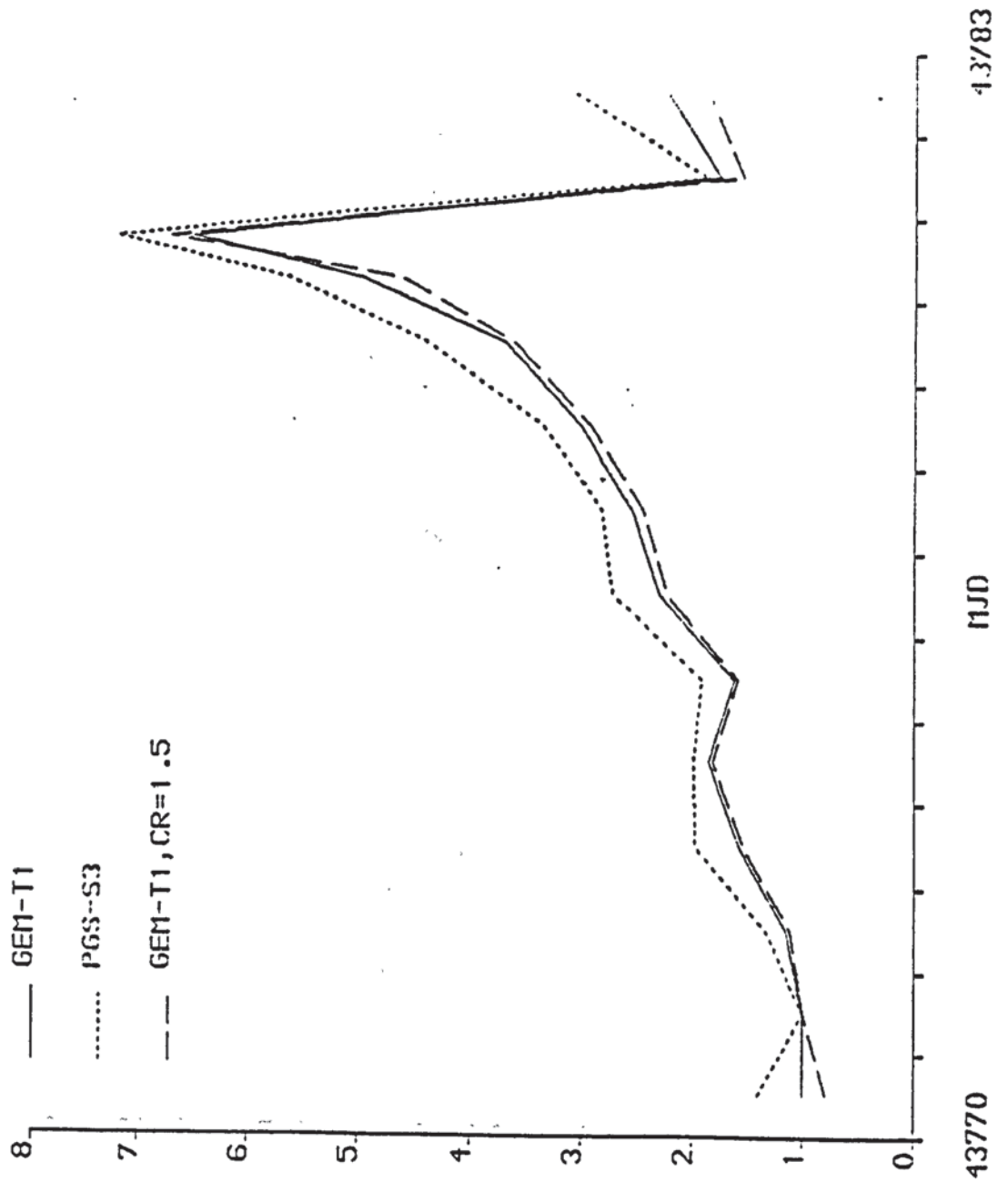


Figure 11.6 : Observed density profiles for MJD 43716 to MJD 43730.

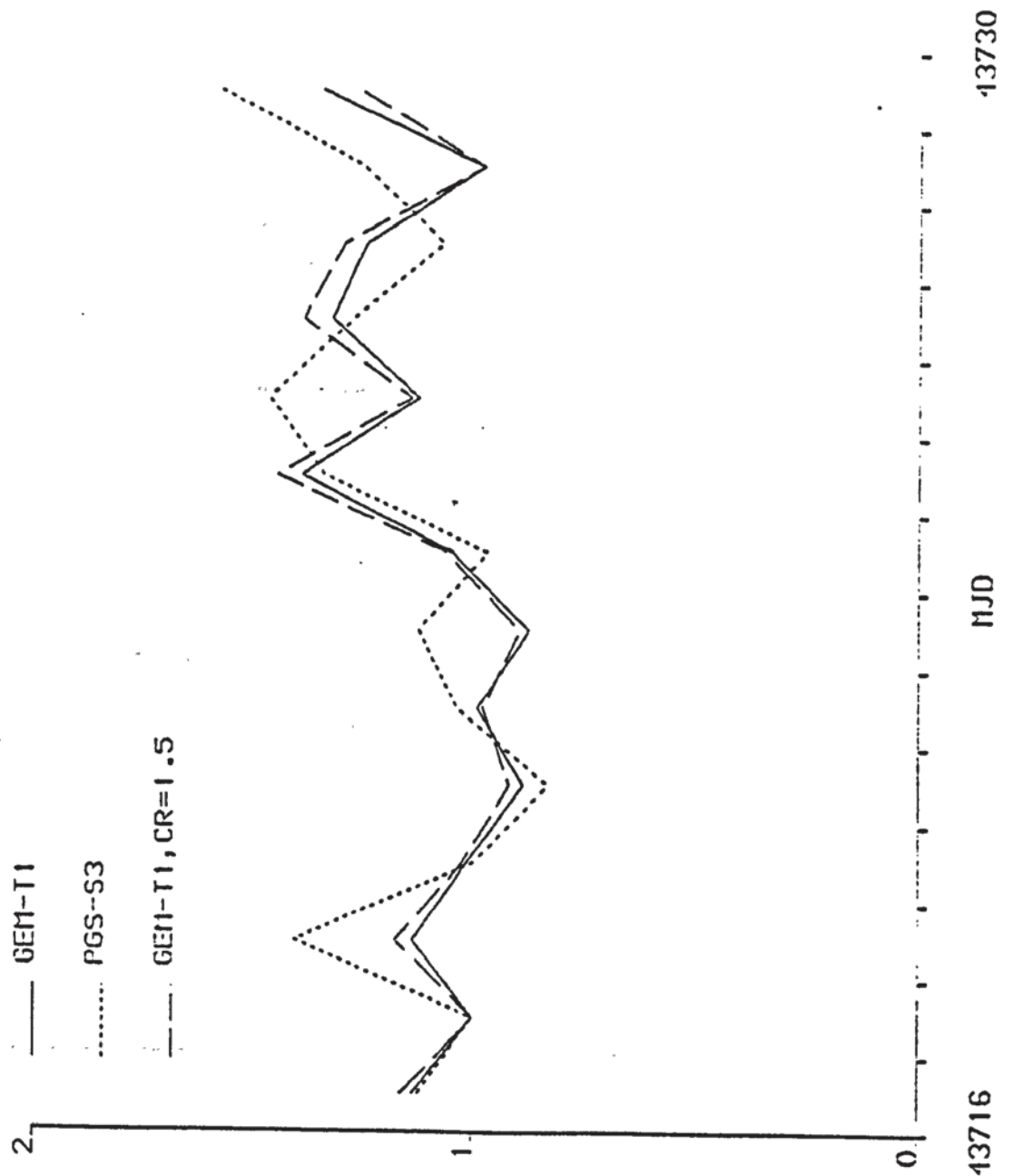


Figure 11.7: Solar flux, $F_{10.7}$ and geomagnetic planetary index, K_p , for MJD 43770 to MJD 43783.

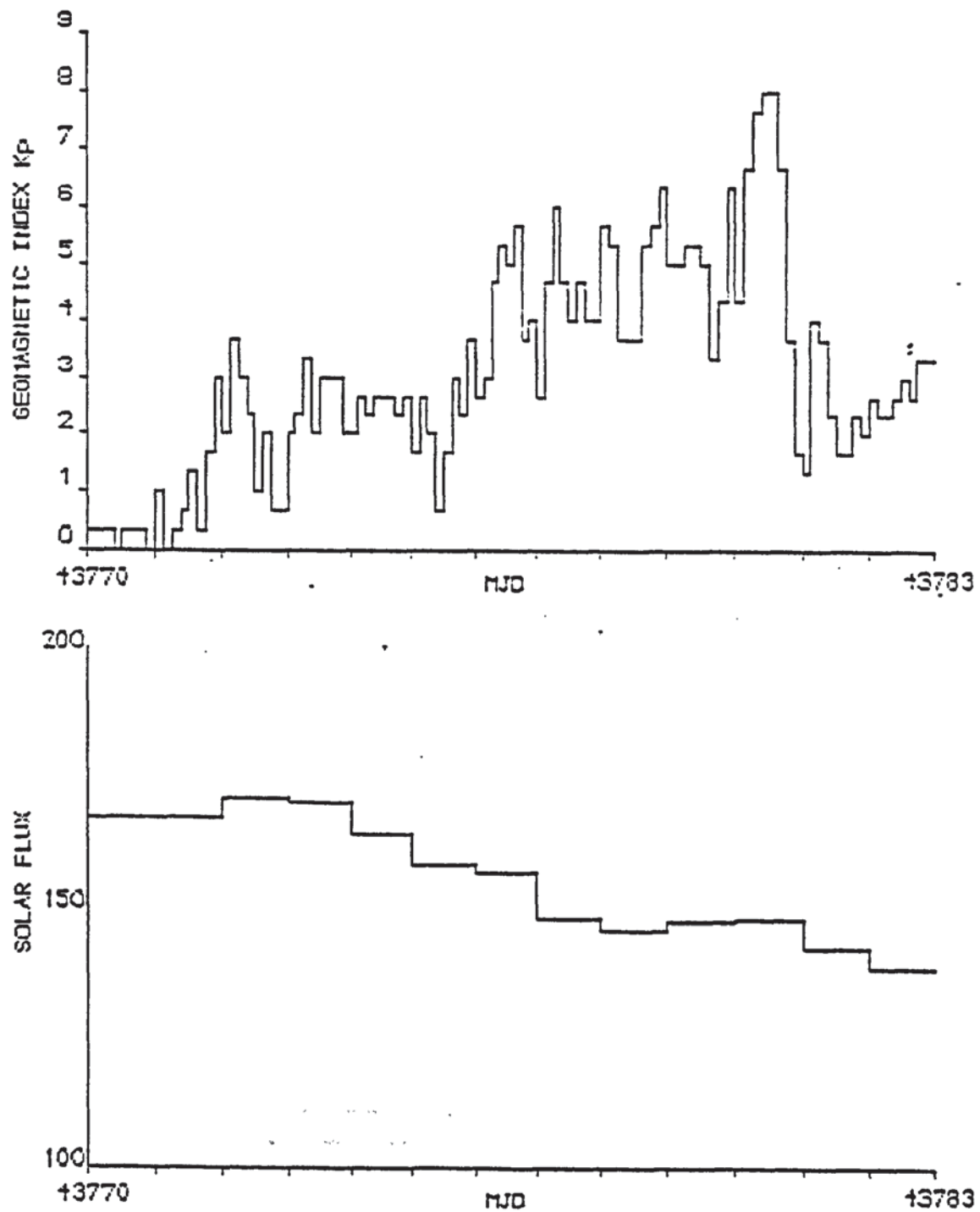
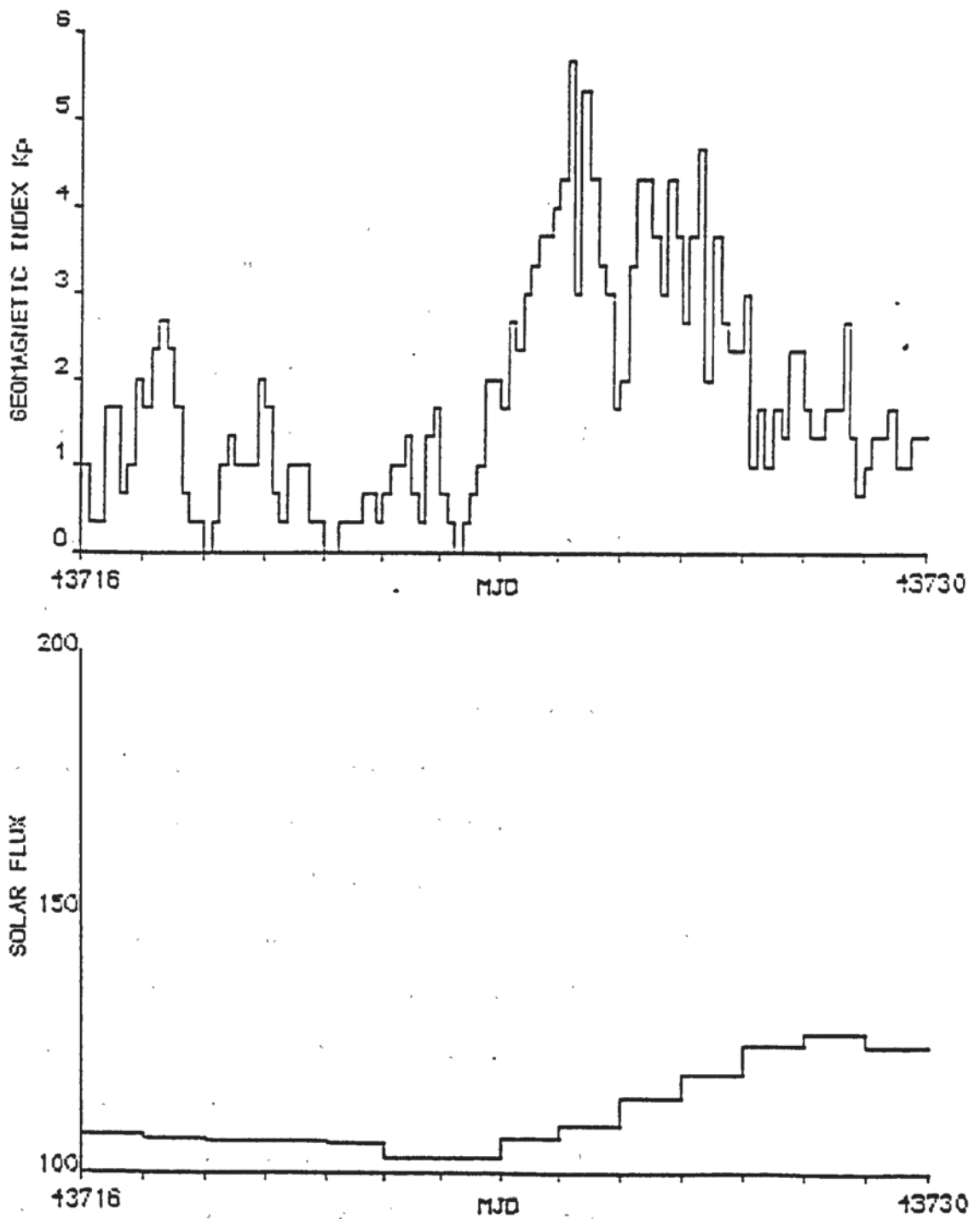


Figure 11.8: Solar flux, $F_{10.7}$ and geomagnetic planetary index, K_p , for MJD 43716 to MJD 43730.



CHAPTER 12

NEW DENSITY MODELLING TECHNIQUES

As gravity field models continue to improve, the errors associated with other forces, such as air-drag, will increase in significance, even when estimating for multiple drag coefficients. In order to attain the decimetre accuracy required for altimeter satellites, there will be a need in the near future, for improved modelling of these forces. This chapter aims to address this requirement for the drag force.

Chapters 10 and 11 have shown that current atmospheric density models are deficient in their representation of density changes associated with geomagnetic activity. It was seen that several of the more recent and more complex models for the geomagnetic activity component of the density model, performed no better than the simple drag based CIRA 72 density model, when employed in orbits using a single drag coefficient.

Nevertheless, CIRA 72 is itself deficient in modelling the persistence of a geomagnetic event. This aspect is examined in section 12.1. In that section, persistence is introduced to the CIRA 72 model using a summation formula, similar to that used by Hedin in his MSIS-83 model [15].

As suggested in chapter 10 and verified in chapter 11, there are instances (MJD 43772 for example), when the geomagnetic planetary index, K_p , does not represent the actual density variation associated with geomagnetic activity. In response to this deficiency it was decided to assess the performance of an alternative index representing geomagnetic activity, the Auroral Electrojet or AE index. Definitions and subsequent modelling of this index are described in section 12.2.

Finally, the decision was made to estimate certain coefficients in the CIRA 72 and JS84 geomagnetic models, plus some of their variants. This analysis is addressed in section 12.3.

An assessment of the performance of the model derived in section 12.3 and discussion of its merits are presented in sections 12.4 and 12.5, respectively.

§12.1 Summation Techniques Applied To CIRA 72 And JS84

The summation formula given by equation A.24 of MSIS-83 [15] is designed to introduce persistence of a geomagnetic event into density modelling. Persistence is not modelled in CIRA 72, whilst in JS84, it is accounted for by smoothing the K_p index. This has the unwanted effect of all but removing the extremes of geomagnetic variation. Hence the decision was taken to introduce persistence, both to CIRA 72 and JS84, by using a summation formula of the geomagnetic effect $\overline{\Delta}_G(\cdot)$, similar to that used in MSIS-83, as follows :-

$$\overline{\Delta}_G(t + \tau) = \frac{\Delta_G(a_1) + \sum_{i=1}^4 \Delta_G(a_{i+1}) \exp(-c0.125i)}{1 + \sum_{i=1}^4 \exp(-c0.125i)} . \quad (12.1)$$

In equation (12.1), τ is identically set to zero in accordance with the time lag of MSIS-83; $\Delta_G(\cdot)$ is to be identified with $\Delta_G T_{\infty}$ in CIRA 72 (equation (9.5)) and the components of $\Delta_G \log n_i$ in JS84 (equation (10.1)); a_1 is the K_p index at time t hrs, a_2 at $t-3$ hrs, a_3 at $t-6$ hrs, etc. and c is set at $3.0d^{-1}$ giving a time constant of 8 hrs, in close agreement with the values recommended by Hedin [15] in his summation formula A.24. (Hedin employs separate time constants for each atmospheric constituent, but an average value was chosen here to simplify the procedure.)

Results of computing the orbital arcs defined in chapter 10, relative to both CIRA 72 and JS84, with the summation formula of equation (12.1) and a single drag scale factor, are presented in Tables 12.1 and 12.2, respectively.

Table 12.1: Orbital results relative to CIRA 72 using the summation formula of equation (12.1) when solving for a single drag coefficient in conjunction with the GEM-T1 gravity field and NASA 'area tables' for SEASAT.

<u>Orbital Arc</u>	<u>Rms(m)</u>	<u>C_D</u>	<u>C_R</u>	<u>Number or Observations</u>
1	0.91	4.58	1.73	972
2	2.54	3.46	0.88	1488
3	1.73	2.21	1.40	1481
4	3.86	1.95	0.51	1101
5	5.56	2.57	1.71	1993
6				
7	2.44	4.08	2.22	1005
8	2.78	4.36	1.83	978
9	1.44	3.34	1.70	933

Table 12.2: As for Table 12.1 but using JS84.

<u>Orbital Arc</u>	<u>Rms(m)</u>	<u>C_D</u>	<u>C_R</u>	<u>Number or Observations</u>
1	0.83	5.49	1.84	972
2	2.20	4.15	1.04	1488
3	1.71	2.55	1.41	1481
4	3.87	2.13	0.56	1101
5	6.75	2.84	1.75	1993
6				
7	2.98	4.82	2.37	1005
8	4.58	4.83	1.91	978
9	1.92	3.71	1.68	933

Employing the rms of fit to the laser range residuals as the sole guide to orbital accuracy, equation (12.1) applied to CIRA 72 improves on the original model (Table 10.2) in four of the eight arcs tested. However, the level of orbital improvement far outweighs the degradation in accuracy, with arc 7 improving by 5.34m (primarily a response to the reduced time lag), arc 1 by 42cm, arc 8 by 30cm and arc 9 by 26cm. The degradations are 48cm in arc 4, 24cm in arc 5, 14cm in arc 3 and 9cm in arc 2. A similar pattern is noted when equation 12.1 is applied to JS84 (compare Tables 12.2 and 10.5).

Comparison of Tables 12.1 and 12.2 reveals similar levels of accuracy apart from arc 8, where CIRA 72 performs significantly better. Although tentative, these results demonstrate that the introduction of persistence through a summation formula such as equation (12.1), can lead to more realistic drag force modelling. The summation in equation (12.1) over the preceding 12 hour interval was purely arbitrary but computations made by extending the summation over 24 hours had negligible effect.

§12.2 The Auroral Electrojet, AE

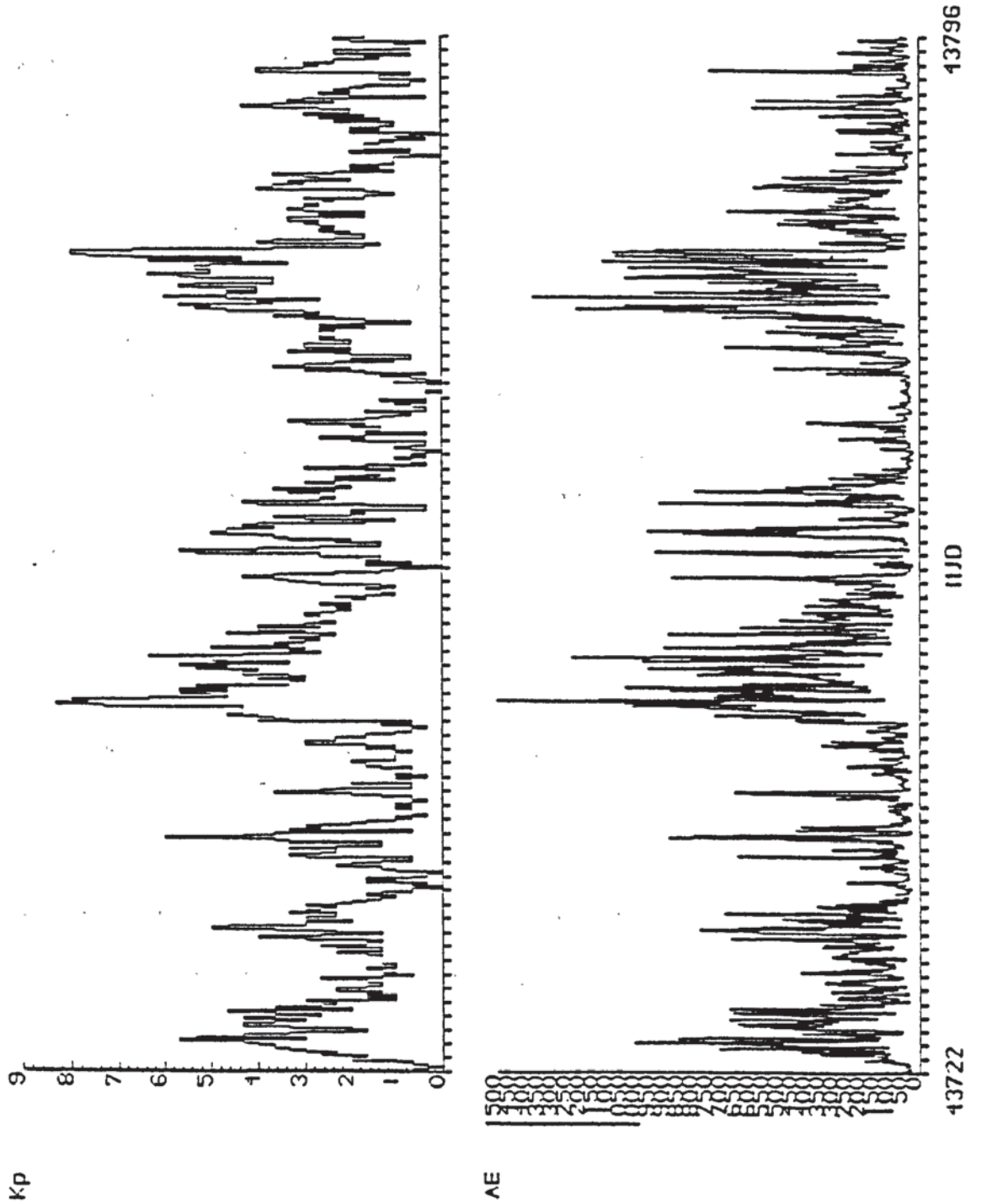
As mentioned in section 9.5, the earth's magnetic field extends, in approximately dipole fashion, to distances of a few earth radii, beyond which it is influenced by the solar wind. This influence causes the field to be confined within a boundary known as the magnetopause, the whole structure being called the magnetosphere. On the day side, this structure extends to about 10 earth radii whilst on the night side, the field is drawn out into a long tail which extends at least as far as the moon's orbit, 60 earth radii away.

Various upper atmospheric phenomena are linked with the structure of the magnetosphere and with the population of energetic particles contained therein. For instance, there is a domain of "auroral" particles intersecting the earth's surface in two bands, encircling the geomagnetic poles. These bands may be identified with the

"auroral ovals" which are the loci of precipitation of energetic particles causing aurora. Particle precipitation induces ionospheric currents which, through Joule dissipation is a significant heat source for the global thermosphere. Hence, the energy input to the auroral regions is related to the temperature changes associated with geomagnetic activity and can therefore be used for geomagnetic modelling purposes. An index, based on this energy input, is published by the World Data Centre A at hourly intervals. It is called the Auroral Electrojet or AE index and is a global measure of the auroral zone activity resulting from enhanced ionospheric currents during a magnetic disturbance [65, 66]. AE is a summation of the magnitudes of the auroral electrojet indices AL and AU, which are designed to measure the strengths of ionospheric currents in the westward and eastward electrojets, respectively [67]. This index can be used in place of the K_p index, in modelling geomagnetic activity, though it should be noted that it is not regularly computed.

Figure 12.1 plots the AE index for the period spanning August 2 to October 15, 1978 (MJD 43722 to MJD 43796), a period covering all orbits of chapters 10 and 11. Also plotted for comparison, is the 3 hourly K_p index for the same period. As seen from the figure, the AE index shows a close correspondence with the K_p index for the vast majority of geomagnetic storms, as is to be anticipated since both indices measure geomagnetic activity. It should therefore be possible to derive a model representing geomagnetic activity, based on the AE index. However, the erratic behaviour of the 1 hourly AE values suggests that, initially, some form of smoothing is necessary, since the atmosphere cannot react to such short-term geomagnetic fluctuations. Such a smoothing function has been defined by Nisbet et al [67] in his attempt to relate neutral air density variations to magnetic activity.

Figure 12.1 : Plots of K_p and AE indices for the period MJD 43722 to MJD 43796.



The function is given by

$$AE'_{t_c}(t) = \frac{1}{t_c} \int_{-\infty}^t AE(t') e^{-(t-t')/t_c} dt' \quad (12.2)$$

where t_c is a time constant in hours and $AE(t')$ is the auroral electrojet index at time t' hours. The time constant, t_c , effectively defines a level of smoothing and also implicitly models persistence of the AE activity. The value used however, is open to contention. Nisbet's work involved assessing various values ranging from 1 hour upto 24 hours and his results suggested a smaller value is required for the onset of a storm as compared to the decay of a storm. This indicates that the atmosphere reacts more quickly to the onset of a geomagnetic disturbance, but that its return to quiet time levels is much slower, corroborating the need for some form of persistence.

Figures 12.2(a) to (d) depict the AE'_{t_c} index for the values $t_c = 1, 6, 12$ and 24 hours, respectively, where AE'_{t_c} has been defined according to the approximation of equation (12.2) given by

$$AE'_{t_c}(t) = \frac{1}{t_c} \sum_{i=0}^{5t_c} AE(t - 5t_c + i) \exp[-(5t_c - i)/t_c] \quad (12.3)$$

where the increment i is in hourly intervals. The summation is terminated at $5t_c$ hours prior to the current time t , as beyond this, the exponential term is negligible.

Figure 12.2 : AE'_{t_c} index for the values (a) 1 and (b) 6 hours for t_c .

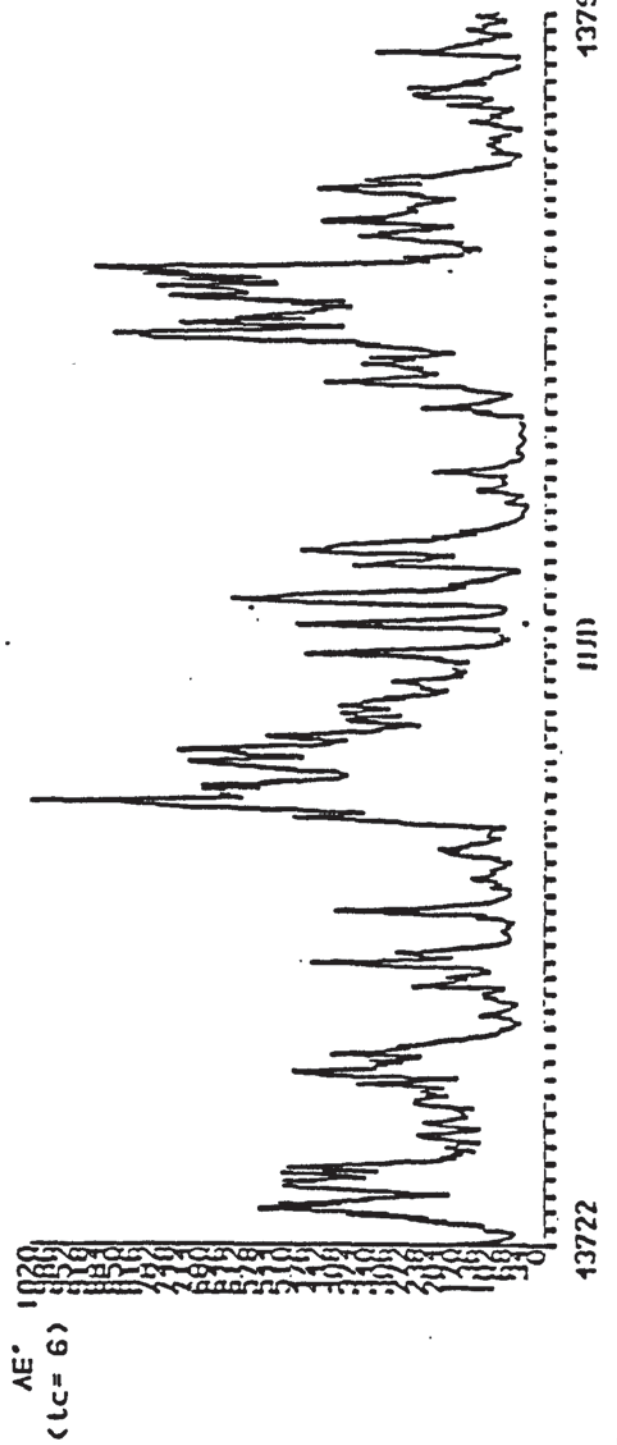
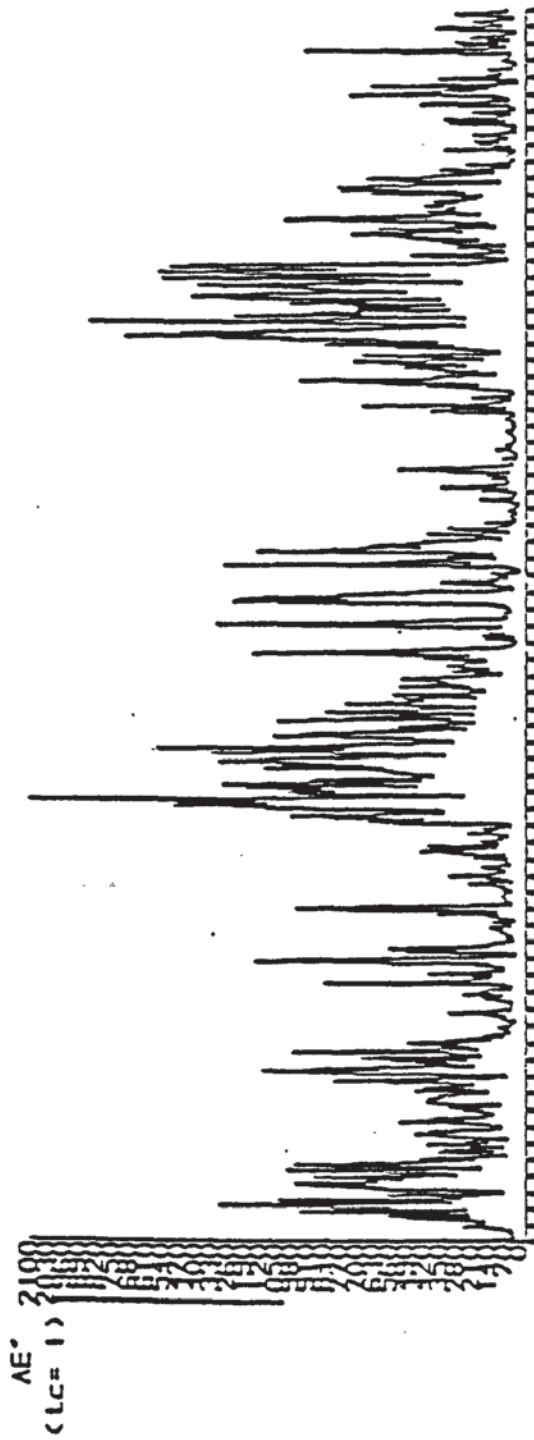


Figure 12.2 : AE'_{t_c} index for the values (a) 1 and (b) 6 hours for t_c .

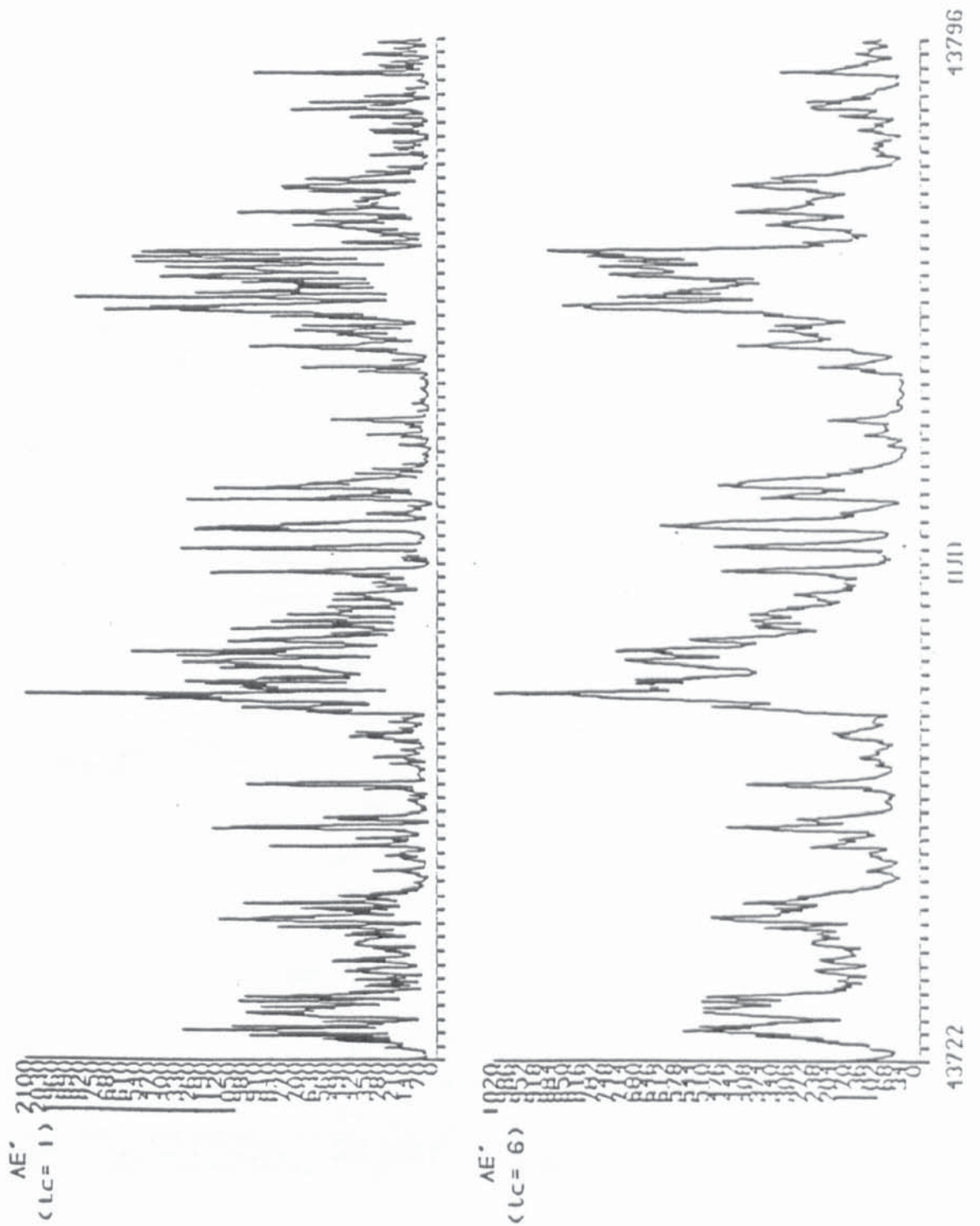
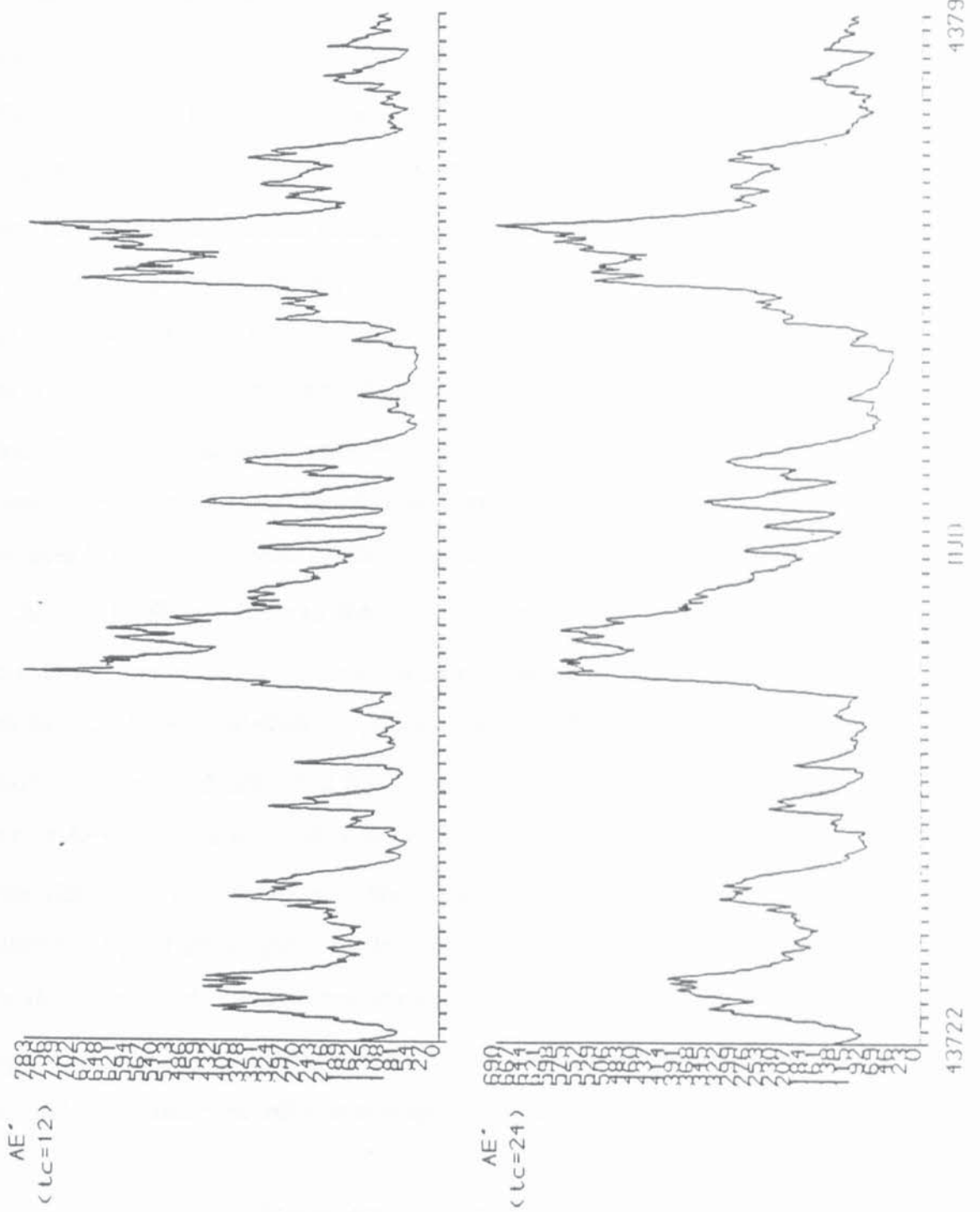


Figure 12.2 : AE'_{t_c} index for the values (c) 12 and (d) 24 hours for t_c .



All the graphs reveal a similar overall trend for the shape of the geomagnetic variation. However, Figure 12.2(a) shows that the value $t_c = 1$ hour, has little effect in smoothing the AE index, whilst a value of 24 hours has removed a good deal of the extreme variation (Figure 12.2 (d)). That value of t_c chosen for initial analysis was decided upon, by comparing the AE'_{t_c} profiles with the observed density profiles of chapter 11. For the value $t_c = 6$ hours, there is a large peak in the index during MJD 43776 (approximately $3/4$ of the way along the horizontal scale in Figure 12.2(b)), which is almost as significant as the peak during MJD 43780. Since this does not correspond with the observed density profile for this period (Figure 11.2), $t_c = 6$ hours was excluded from the subsequent analyses. Further, from Figures 12.2(c) and (d), the nearest profile to that required, is given by $t_c = 24$ hours. However, this value under-estimates the density drop on MJD 43781 whereas $t_c = 12$ hours is more appropriate here. Likewise, the profile of the AE'_{24} index over MJD 43748 to MJD 43756 is not as expected from the K_p data, whereas the AE'_{12} index is similar to the K_p profile for this period (Figure 12.1). Consequently, initial analysis of an index based on the AE data, was performed with a value of $t_c = 12$ hours in equation (12.3). This also happens to be the median value of those analysed by Nisbet et al [67]. For this index, (Figure 12.2(c)), there is a near one-to-one correspondence with the K_p index (Figure 12.1), at least to within a scale difference. A scaled form of this index, can therefore be implemented directly in place of K_p for geomagnetic modelling purposes in equation (9.5). Figure 12.3 plots the correspondence between various K_p and AE'_{12} values as taken from Figures 12.1 and 12.2(c). Clearly, there is a linear scale difference by a factor of almost $1/100.0$. Hence the index chosen for initial analysis, \hat{AE} , is given by

$$\hat{AE}(t) = AE'_{12}(t)/100.0. \quad (12.4)$$

In view of the results of section 12.1, where persistence is best modelled by a summation of the geomagnetic effect, the decision was taken to implement this index

in place of K_p in the CIRA 72 atmospheric model when using the summation formula of equation (12.1). Initially, the values of A_1 and B_1 , in equation (9.5) were taken to be the CIRA 72 values of 28K and 0.03K, respectively.

Results of computing eight of the nine orbital arcs defined in chapter 10, relative to this new model, solving for a single drag coefficient, are given in Table 12.3.

Table 12.3: Orbital results relative to CIRA 72, $\hat{A}E$ index and summation formula equation (12.1), when solving for a single drag coefficient. GEM-T1 gravity field and NASA 'area tables' for SEASAT utilized.

<u>Orbital Arc</u>	<u>Rms(m)</u>	<u>C_D</u>	<u>C_R</u>	<u>Number of Observations</u>
1	3.23	2.93	0.64	972
2	1.97	3.85	1.17	1488
3	2.21	1.80	1.40	1481
4	2.92	2.66	1.09	1102
5	4.31	2.91	1.81	1993
6				
7	5.64	3.78	2.53	1005
8	2.41	4.26	1.73	978
9	3.79	3.86	1.65	933

Comparison of these results with those of the original CIRA 72 model (Table 10.2) show rms improvements in five of the eight arcs tested, though some are only marginal improvements. Strictly speaking, this model should be compared to CIRA 72 when using the summation formula (equation (12.1)) with the K_p index (Table 12.1). In this comparison, only four of the eight arcs improve when using the $\hat{A}E$ index and several of those that deteriorate, arcs 1 and 9, for instance, do so severely.

However, this index is not totally without worth and will be examined more closely in the next section when certain coefficients are determined in the modelling.

Of particular interest to this analysis is the result of arc 5 (MJD 43770 to MJD 43776), where an rms of 4.31m has now been obtained. This is the lowest yet recorded for this arc and gives an indication that density variation due to geomagnetic activity over this period, is much better represented by an index based on the Auroral Electrojet than K_p . Examination of the AE'_{12} profile over this period may help to explain this phenomenon (Figure 12.4). This figure shows, in more detail, the AE'_{12} index for MJD 43770 to MJD 43776 (and also the K_p index for comparison). The AE'_{12} index is in better agreement with the observed density profile for this period (Figure 11.2), than the K_p profile. Hence, a form of modelling based on AE'_{12} will be preferred over this period than a model based on K_p .

Various experiments were also performed with values of 3, 6, 18 and 24 hours for t_c . Using these values, certain arcs improved relative to $t_c = 12$ hours, whilst others deteriorated in accuracy. No value performed significantly better than any other and consequently, $t_c = 12$ hours was adopted as the nominal time constant for the subsequent coefficient retrieval.

(One possibility for future research, is a more thorough investigation into the optimum time constant, t_c , particularly for the onset and decay of a geomagnetic storm where different values should ideally be utilized. For instance, a model could be developed which uses a smaller value of t_c at the beginning of a geomagnetic disturbance, being increased toward the end. However, the problems of discontinuity which this introduces must be overcome.)

Figure 12.3 :..Geomagnetic planetary index, K_p , versus AE'_{12} index showing least squares fit.

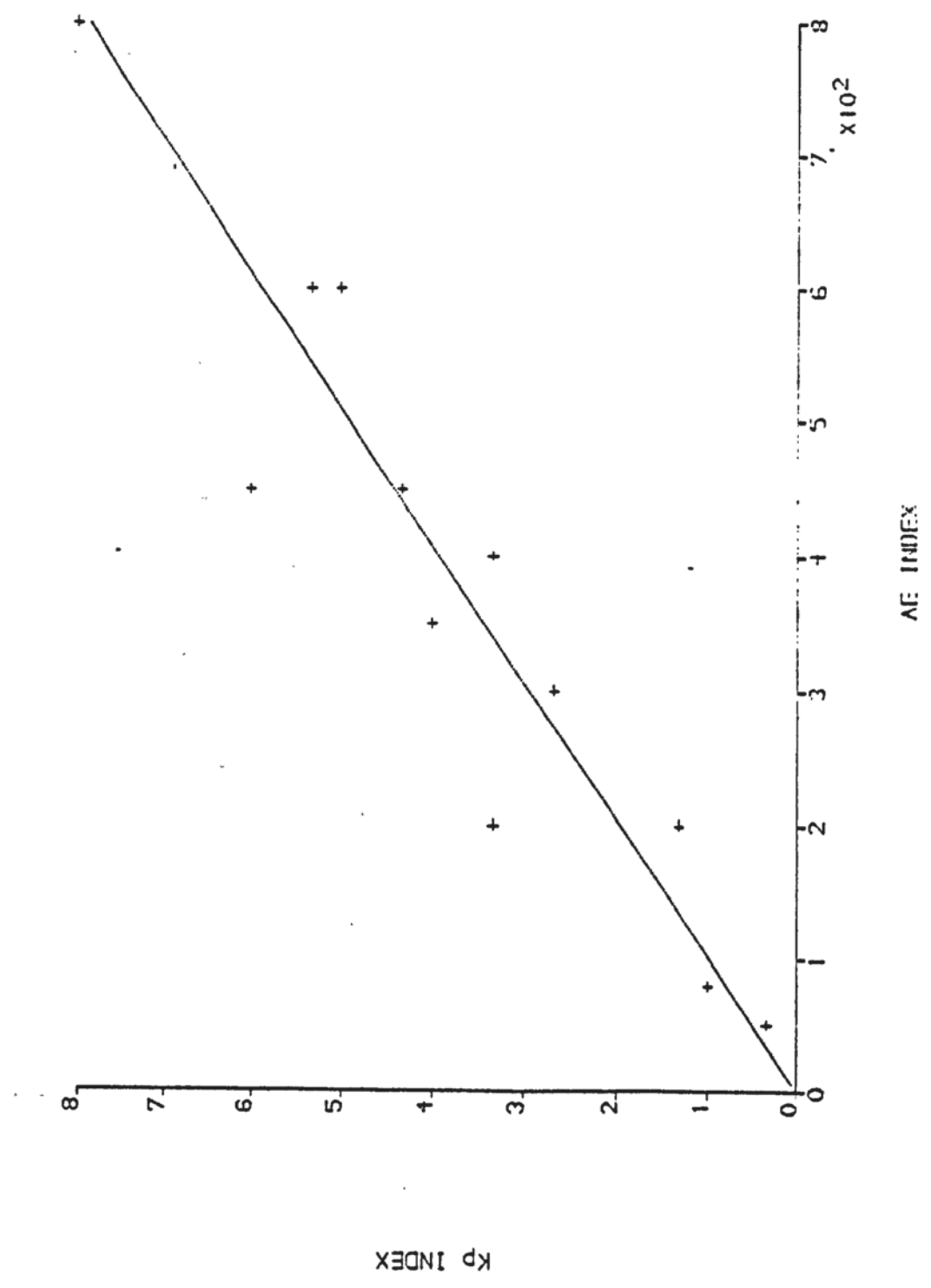
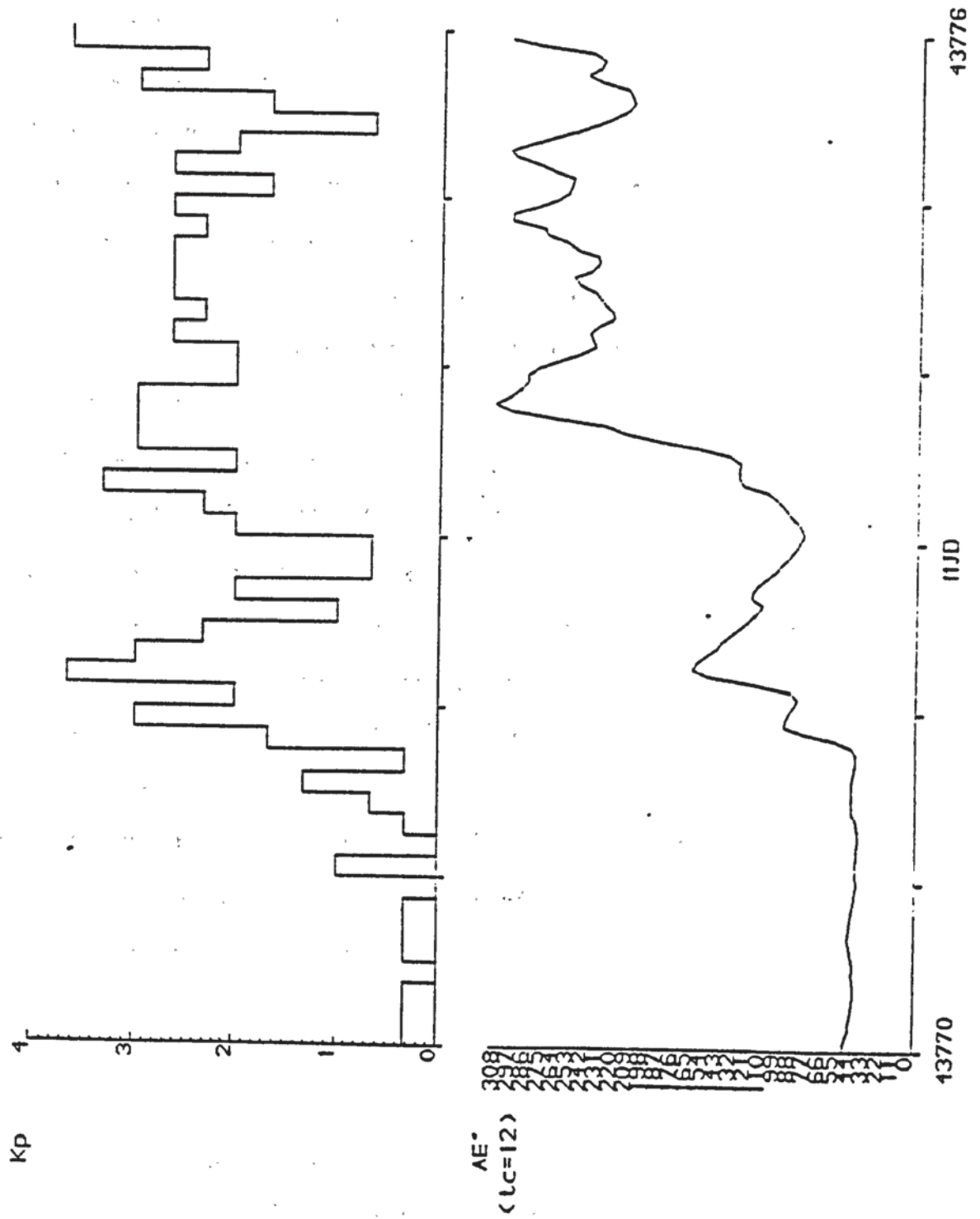


Figure 12.4 : K_p and AE'_{12} indices for the period MJD 43770 to MJD 43776.



§12.3 Recovery Of Geomagnetic Modelling Coefficients

Models Using The AE Index

Section 12.2 revealed that an index based on raw AE data can be used to model geomagnetic density variations to a similar standard as the K_p data in many instances. The smoothed AE index, \hat{AE} , was implemented into a version of CIRA 72, whose geomagnetic modelling coefficients A_1 and B_1 (equation (9.5)), were based on K_p data. A decision was therefore taken to allow A_1 and B_1 to vary when employing \hat{AE} , so that more realistic solutions would be obtained. Partial derivatives for A_1 and B_1 have already been described and implemented into the software. Nevertheless, it was still necessary to develop a method of solution for A_1 and B_1 using all eight orbital arcs of Table 12.3.

The method chosen, could have been the Helmert–Wolf Procedure described in Appendix 3, A_1 and B_1 being the outer parameters. However, such a method removes the inner parameters from the solution and usually requires no second iteration. Since a second iteration would provide a check on the convergence of the solution it was considered unwise to remove the inner parameters in this way. Hence a slight variation of the Helmert–Wolf Procedure was developed which would enable solution for a state vector at epoch, a single drag coefficient and an SRP coefficient from each orbital arc, as well as for A_1 and B_1 . This solution provides the values from which to iterate a second time. Such a method is now described.

Let the normal equations from arc i , where $i = 1, \dots, 9, i \neq 6$, be written as

$$\tilde{A}_i \underline{x}_i = \underline{b}_i \quad (12.5)$$

where \underline{x}_i is the vector of corrections to the state vector at epoch, x_i , the drag coefficient, C_{D_i} , and the SRP coefficient, C_{R_i} , for arc i and also to A_1 and B_1 . \tilde{A}_i is the 10×10 matrix of partial derivatives and \underline{b}_i is the 10–vector whose

components are the sum of the observation residuals multiplied by the partial derivatives as defined in equation (3.19). Equation (12.5) is partitioned thus

$$\begin{pmatrix} \hat{A}_i & \bar{A}_i \\ \bar{A}_i^T & A_i^{AB} \end{pmatrix} \begin{pmatrix} \Delta \hat{\Delta}_i \\ \Delta \Delta B \end{pmatrix} = \begin{pmatrix} \hat{b}_i \\ b_i^{AB} \end{pmatrix} \quad (12.6)$$

where
$$\hat{A}_i = \left(\sum_{j=1}^{N_i} \left(\frac{\partial r_j}{\partial p_l} \right) \left(\frac{\partial r_j}{\partial p_k} \right) \right)_{l,k=1}^8 \quad \text{for } p_l, p_k \in \hat{\Delta}_i$$

and the transpose of $\hat{\Delta}_i \equiv (x_i, y_i, z_i, \dot{x}_i, \dot{y}_i, \dot{z}_i, C_{D_i}, C_{R_i})$ is the state vector at epoch plus C_{D_i} and C_{R_i} for arc i . $\Delta \hat{\Delta}_i$ is the correction to this 8-vector whilst N_i is the number of observations from arc i and

$$\bar{A}_i^T = \begin{pmatrix} \sum_{j=1}^{N_i} \left(\frac{\partial r_j}{\partial x_i} \right) \left(\frac{\partial r_j}{\partial A_1} \right) & \dots & \sum_{j=1}^{N_i} \left(\frac{\partial r_j}{\partial C_{R_i}} \right) \left(\frac{\partial r_j}{\partial A_1} \right) \\ \sum_{j=1}^{N_i} \left(\frac{\partial r_j}{\partial x_i} \right) \left(\frac{\partial r_j}{\partial B_1} \right) & \dots & \sum_{j=1}^{N_i} \left(\frac{\partial r_j}{\partial C_{R_i}} \right) \left(\frac{\partial r_j}{\partial B_1} \right) \end{pmatrix}_{2 \times 8}$$

$$A_i^{AB} = \begin{pmatrix} \sum_{j=1}^{N_i} \left(\frac{\partial r_j}{\partial A_1} \right)^2 & \sum_{j=1}^{N_i} \left(\frac{\partial r_j}{\partial A_1} \right) \left(\frac{\partial r_j}{\partial B_1} \right) \\ \sum_{j=1}^{N_i} \left(\frac{\partial r_j}{\partial A_1} \right) \left(\frac{\partial r_j}{\partial B_1} \right) & \sum_{j=1}^{N_i} \left(\frac{\partial r_j}{\partial B_1} \right)^2 \end{pmatrix}_{2 \times 2}$$

$$\Delta \Delta B = \begin{pmatrix} \Delta A_1 \\ \Delta B_1 \end{pmatrix}, \quad b_i^{AB} = \begin{pmatrix} b_i^A \\ b_i^B \end{pmatrix}$$

where

$$\sum_{\substack{i=1 \\ i \neq 6}}^9 A_i^{AB} = \begin{pmatrix} \sum_{j=1}^{N'} \left(\frac{\partial r_j}{\partial A_1} \right)^2 & \sum_{j=1}^{N'} \left(\frac{\partial r_j}{\partial A_1} \right) \left(\frac{\partial r_j}{\partial B_1} \right) \\ \sum_{j=1}^{N'} \left(\frac{\partial r_j}{\partial B_1} \right) \left(\frac{\partial r_j}{\partial A_1} \right) & \sum_{j=1}^{N'} \left(\frac{\partial r_j}{\partial B_1} \right)^2 \end{pmatrix}_{2 \times 2}$$

$$\sum_{\substack{i=1 \\ i \neq 6}}^9 b_i^{AB} = \begin{pmatrix} \sum_{\substack{i=1 \\ i \neq 6}}^9 b_i^A \\ \sum_{\substack{i=1 \\ i \neq 6}}^9 b_i^B \end{pmatrix},$$

$$\sum_{\substack{i=1 \\ i \neq 6}}^9 b_i^A = \sum_{j=1}^{N'} (r_j^o - r_j^c) \frac{\partial r_j}{\partial A_1},$$

$$\sum_{\substack{i=1 \\ i \neq 6}}^9 b_i^B = \sum_{j=1}^{N'} (r_j^o - r_j^c) \frac{\partial r_j}{\partial B_1}$$

and

$$N' = \sum_{\substack{i=1 \\ i \neq 6}}^9 N_i.$$

Inversion of equation (12.7) determines the 66-vector $(\Delta \hat{X}_1, \dots, \Delta \hat{X}_9, \Delta A_1, \Delta B_1)^T$ and in particular corrections to A_1 and B_1 .

This method of solution using two iterations has been applied to the model described in section 12.2 using the $\hat{A}E$ index to represent geomagnetic activity and the summation formula equation (12.1), to represent persistence. The resulting values for the coefficients A_1 and B_1 converged to the following :-

$$A_1 = 36.14 \pm 0.22K,$$

$$B_1 = 0.054 \pm 0.0008K.$$

These values were then used to recompute the orbits of Table 12.3 relative to the same atmospheric model. Results are presented in Table 12.4.

Table 12.4: Orbital results relative to CIRA 72 using the summation formula of equation (12.1) and the \hat{AE} index with $A_1 = 36.14K$ and $B_1 = 0.054K$. Single drag coefficient estimated when utilizing the GEM-T1 gravity field and NASA 'area tables' for SEASAT.

<u>Orbital Arc</u>	<u>Rms(m)</u>	<u>C_D</u>	<u>C_R</u>	<u>N_i</u>
1	3.72	2.05	0.33	972
2	2.27	3.25	1.03	1488
3	2.95	1.26	1.31	1481
4	2.54	2.63	1.19	1102
5	2.89	2.68	1.75	1993
6				
7	3.16	2.53	1.96	1005
8	2.25	3.78	1.59	978
9	3.72	3.63	1.70	933

These results are not as accurate as hoped in that no orbital arc has an rms of fit to the laser observations of below 2m. Conversely, no orbital arc has an rms of fit over 4m, something not achieved for any of the previous modelling techniques. In particular, it is noted that the rms of fit for arc 5 is below 3m, confirming once again that the AE'_{12} profile fits the predicted density profile very well over this period. Also, the reduced rms of this arc is evidence for the predicted profile being in good agreement with the actual density profile. However, this vast orbital improvement has been to the detriment of arcs 1 and 9 which are now poorly determined. These two arcs are instances where the \hat{AE} index does not represent the necessary density variation associated with geomagnetic activity.

Overall, the effect of this form of modelling and method of solution has been to remove the extremes – none of the orbits are particularly accurate but conversely, none are particularly poor. This could be a consequence of oversmoothing the raw AE data, in a similar manner to how Slowey's smoothing of the K_p index all but removes any geomagnetic variation. The summation formula of equation (12.1)

effectively smooths the density variation associated with geomagnetic activity, whilst equation (12.3) also smooths the AE index itself. The above modelling has utilized both these forms of smoothing in an attempt to represent persistence and remove erratic behaviour from the index. Since the smoothing introduced by equation (12.3) implicitly defines a certain amount of persistence, it was decided to recompute the orbits of Table 12.4 omitting the summation formula of equation (12.1) from the modelling. That is, the next model analysed was CIRA 72 using the $\hat{A}E$ index with no summation formula and A_1 and B_1 re-estimated using equations (12.5) to (12.7). This analysis yielded the following converged values for A_1 and B_1 :-

$$A_1 = 34.81K$$

$$B_1 = 0.071K$$

Results of the ensuing orbital computations relative to this model are presented in Table 12.5.

Table 12.5: Orbital results relative to CIRA 72 using $\hat{A}E$ index and estimated values of 34.81K and 0.071K for A_1 and B_1 , respectively. Single drag coefficient estimated when using the GEM-T1 gravity field and NASA 'area tables' for SEASAT.

<u>Orbital Arc</u>	<u>Rms(m)</u>	<u>C_D</u>	<u>C_R</u>	<u>N_i</u>
1	3.48	2.27	0.47	972
2	2.33	3.25	1.01	1488
3	3.21	1.26	1.26	1481
4	2.91	2.54	1.06	1102
5	2.88	2.68	1.74	1993
6				
7	1.33	2.43	1.69	1005
8	1.97	3.89	1.63	978
9	3.42	3.67	1.69	933

Compared with Table 12.4, these results show rms improvements in four cases with two others remaining virtually the same. Also, arcs 7 and 8 have rms

values below 2m, whilst the worst rms of 3.48m is still lower than the worst of Table 12.4 (3.72m). It is thus concluded that the latter model for geomagnetic activity is to be preferred over that of Table 12.4, probably due to the oversmoothing within the previous model. It should be stressed however, that arcs 1, 3 and 9 performed badly once again, as seems to be the case with all models based on the AE index. Consequently, it was decided to re-examine geomagnetic modelling techniques based on the K_p index.

Models Using The K_p index

In a similar manner to the solution of A_1 and B_1 with the $\hat{A}E$ index, geomagnetic coefficients were also estimated for the models of section 12.1, that is A_1 and B_1 in CIRA 72 and A'_1 , Z_1 , E_1 , A_2 and A_3 in JS84 both with the summation formula (equation (12.1)). The method of solution for A_1 and B_1 is as described in equations (12.5) to (12.7). The parameters in JS84 are solved similarly except that they must be constrained due to high correlation between the coefficients. The mathematics of this constraint method, Least Squares Collocation, is explained fully by Moritz [68] but is briefly outlined below.

Least Squares Collocation involves minimizing the function Q defined by

$$Q = \mathbf{r}^T \mathbf{W} \mathbf{r} + \mathbf{z}^T \overline{\mathbf{W}} \mathbf{z} \quad (12.8)$$

where \mathbf{r} is the vector of observation residuals; \mathbf{W} the diagonal weight matrix associated with \mathbf{r} ; \mathbf{z} the vector of small changes to the original values of the constrained parameters and $\overline{\mathbf{W}}$ the diagonal weight matrix whose elements are $\overline{w}_j = 1/\overline{\sigma}_j^2$; $\overline{\sigma}_j$ being the 'a priori' standard error of $z_j \in \mathbf{z}$. Given no 'a priori' knowledge $\overline{\sigma}_j$ was set at $2\frac{1}{2}\%$ of the original parameter value for this analysis.

Let N be the number of observation residuals and M the number of constrained parameters. Then

$$Q = \sum_{i=1}^N (r_i^o - r_i^c)^2 w_i + \sum_{j=1}^M (p_{oj} - p_j)^2 \bar{w}_j \quad (12.9)$$

where p_{oj} is the 'a priori' value of parameter j and p_j the estimated value after solution; r_i^o the i^{th} observed laser range and r_i^c its corresponding computed value and w_i the diagonal elements of W . Now $r_i^c \equiv r_i^c(\mathbf{x})$ where \mathbf{x} is the vector of all orbital and geodetic parameters, some of which are to be constrained in the orbital solution. Let $\mathbf{x} = [\mathbf{y}, \mathbf{p}]$ be the partitioning of \mathbf{x} into those components, \mathbf{y} , which are unconstrained and those, \mathbf{p} , which are constrained. Then $\Delta\mathbf{x} = [\Delta\mathbf{y}, \Delta\mathbf{p}]$. The least squares methodology is to minimize Q with respect to each component of \mathbf{x} , thus

$$\frac{\partial Q}{\partial x_k} = -2 \sum_{i=1}^N (r_i^o - r_i^c) \frac{\partial r_i^c}{\partial x_k} w_i - 2 \sum_{j=1}^M (p_{oj} - p_j) \frac{\partial p_j}{\partial x_k} \bar{w}_j \equiv 0 \quad (12.10)$$

where $\mathbf{x} = (x_k)_{k=1}^{\ell}$, ℓ being the total number of estimated orbital and geodetic parameters. If $x_k = p_s$ for some value of s , then $\partial p_s / \partial x_k = 1$, otherwise it is identically zero. Therefore

$$\sum_{i=1}^N (r_i^o - r_i^c) \frac{\partial r_i^c}{\partial p_s} w_i + (p_{os} - p_s) \bar{w}_s = 0 \quad (12.11)$$

if $x_k = p_s$ for some value of s and

$$\sum_{i=1}^N (r_i^o - r_i^c) \frac{\partial r_i^c}{\partial x_k} w_i = 0 \quad (12.12)$$

if $x_k \neq p_j$, all $j = 1, \dots, M$. Prior to the $(n + 1)^{\text{th}}$ iteration, $n \geq 0$, \hat{r}_i^c and p_j^n are the most accurate estimates of r_i^c and p_j , respectively, such that

$$r_i^c = \hat{r}_i^c + \Delta y \cdot \frac{\partial \hat{r}_i^c}{\partial y} + \Delta p \cdot \frac{\partial \hat{r}_i^c}{\partial p}$$

and $p_j = p_j^n + \Delta p_j$, where $\Delta p = (\Delta p_j)_{j=1}^M$. Upon substitution into equations (12.11) and (12.12) these yield

$$\begin{aligned} & \sum_{i=1}^N \left(\frac{\partial \hat{r}_i^c}{\partial y} \cdot \Delta y + \frac{\partial \hat{r}_i^c}{\partial p} \cdot \Delta p \right) \frac{\partial \hat{r}_i^c}{\partial p_s} w_i + \Delta p_s \bar{w}_s \\ & = \sum_{i=1}^N \left(r_i^o - \hat{r}_i^c \right) \frac{\partial \hat{r}_i^c}{\partial p_s} w_i + \left(p_{os} - p_s^n \right) \bar{w}_s \end{aligned} \quad (12.13)$$

for $s = 1, \dots, M$ and

$$\sum_{i=1}^N \left(\frac{\partial \hat{r}_i^c}{\partial y} \cdot \Delta y + \frac{\partial \hat{r}_i^c}{\partial p} \cdot \Delta p \right) \frac{\partial \hat{r}_i^c}{\partial x_k} w_i = \sum_{i=1}^N \left(r_i^o - \hat{r}_i^c \right) \frac{\partial \hat{r}_i^c}{\partial x_k} w_i \quad (12.14)$$

for $k = 1, \dots, \ell - M$.

In equations (12.13) and (12.14), terms of order Δ^2 have been ignored in a similar fashion to the method of Least Squares outlined in section (3.3).

In matrix notation, equations (12.13) and (12.14) can be written more succinctly as

$$\begin{bmatrix} \Delta y \\ \Delta p \end{bmatrix}^{n+1} = \begin{bmatrix} A^T W A & A^T W B \\ B^T W A & B^T W B + \bar{W} \end{bmatrix}^{-1} \begin{bmatrix} A^T W \Gamma \\ B^T W \Gamma + \bar{W}(p_0 - p^n) \end{bmatrix} \quad (12.15)$$

where $A^T = [A_{ij}]$, $A_{ij} = \partial \hat{r}_i^c / \partial y_j$, $y_j \in y$ $i = 1, \dots, N$; $j = 1, \dots, \ell - M$

$$B^T = [B_{ij}], \quad B_{ij} = \partial \hat{r}_i^c / \partial p_j, \quad p_j \in \mathcal{P} \quad i = 1, \dots, N; \quad j = 1, \dots, M$$

$$\mathcal{P}_0 = [p_{0j}] \quad \text{and} \quad \mathcal{P}^n = [p_j^n], \quad j = 1, \dots, M.$$

This defines the normal equations involving constrained parameters. The method of solution of these parameters using multiple arcs can then be performed by applying equations (12.5) to (12.7). The straightforward method of least squares has been applied to A_1 and B_1 in CIRA 72 in conjunction with the summation formula of equation (12.1). Recovered values for A_1 and B_1 were as follows :-

$$A_1 = 38.45 \pm 0.21K,$$

$$B_1 = 0.0312 \pm 0.0004K.$$

Similarly, the method of least squares collocation has been applied to A'_1 , Z_1 , E_1 , A_2 and A_3 in JS84, again in conjunction with the summation formula of equation (12.1). Converged values for these parameters were as follows :-

$$A_1 = 87.09 \pm 1.50K,$$

$$Z_1 = 24.86 \pm 0.74m,$$

$$E_1 = 0.00105 \pm 0.00002,$$

$$A_2 = 0.338 \pm 0.005,$$

$$A_3 = 0.023 \pm 0.001.$$

Results of computing the orbits of Tables 12.1 and 12.2 with these estimated values are presented in Tables 12.6 and 12.7, respectively.

Table 12.6: Orbital results relative to CIRA 72 with K_p index, summation formula equation (12.1) and estimated values of 38.0K and 0.031K for A_1 and B_1 , respectively. Single drag coefficient estimated when using the GEM-T1 gravity field and NASA 'area tables' for SEASAT.

<u>Orbital Arc</u>	<u>Rms(m)</u>	<u>C_D</u>	<u>C_R</u>	<u>N_i</u>
1	1.20 (1.05)	3.53	1.59	972
2	3.18 (2.87)	2.54	0.56	1488
3	2.21 (1.98)	1.64	1.35	1481
4	3.87 (3.86)	1.74	0.43	1102
5	4.50 (4.97)	2.24	1.63	1993
6				
7	1.25 (1.52)	2.88	1.87	1005
8	0.96 (1.24)	3.80	1.70	978
9	1.87 (1.53)	2.92	1.76	933

Table 12.7: Orbital results relative to JS84 with K_p index, summation formula equation (12.1) and estimated values of 87.07K, 24.86m, 0.00105, 0.338 and 0.023 for A'_1 , Z_1 , E_1 , A_2 and A_3 , respectively. Single drag coefficient estimated when using the GEM-T1 gravity field and NASA 'area tables' for SEASAT.

<u>Orbital Arc</u>	<u>Rms(m)</u>	<u>C_D</u>	<u>C_R</u>	<u>N_i</u>
1	1.21 (1.09)	3.77	1.64	972
2	3.18 (2.90)	2.76	0.62	1488
3	2.39 (2.29)	1.65	1.34	1481
4	4.00 (3.88)	1.80	0.45	1102
5	4.64 (5.24)	2.32	1.65	1993
6				
7	1.30 (1.26)	2.82	1.87	1005
8	0.90 (1.25)	3.93	1.72	978
9	1.94 (1.54)	3.02	1.77	933

Comparison of Table 12.6 with 12.7 reveals little difference between the results when estimating either the coefficients A_1 and B_1 in CIRA 72 or $A'_1, Z_1, E_1, A_2,$ and A_3 in JS84, showing that the five coefficients in JS84 offer no advantage over the two in CIRA 72, when allowed to vary. Apparently, the JS84 coefficients are so inter-related that when constrained, the effect is the same as allowing total freedom in just two coefficients.

Comparison of Table 12.6 with Table 12.1 and Table 12.7 with Table 12.2, respectively, reveals that although some orbits improve in accuracy others deteriorate when computed using the estimated values for the model coefficients. In general, no model performs significantly better than any other, although by estimating the model parameters, a better overall fit is obtained. In detail, the rms of the orbits of Table 12.1 is 3.29m compared to 2.88m for those of Table 12.6. The reason that this improvement is not as significant as hoped, could be due to the poor fit of arc 5 in Table 12.1. It is by now well established that this arc performs badly with any model which utilizes K_p data as the measure of geomagnetic activity. Using this arc in the estimation process of the model coefficients will cause the solution to minimize the overall errors and in particular the large errors of this arc. The solution is thereby pulled in a direction which reduces the errors of arc 5 at the expense of the other arcs. Consequently, it was decided to omit arc 5 from the estimation process, estimate new model coefficients and recompute all eight arcs relative to these values. In the case of CIRA 72 the estimated coefficients were as follows :-

$$A_1 = 33.31 \pm 0.18K,$$

$$B_1 = 0.03355 \pm 0.0003K.$$

For JS84, the new values were :-

$$A'_1 = 72.42 \pm 1.23K,$$

$$Z_1 = 17.76 \pm 0.75m,$$

$$E_1 = 0.00082 \pm 0.00002,$$

$$A_2 = 0.358 \pm 0.005,$$

$$A_3 = 0.026 \pm 0.001.$$

Orbital rms values with these new models are given by the bracketed figures in Table 12.6 and 12.7. For brevity the model using CIRA 72, the K_p index, summation formula equation (12.1) and $A_1 = 33.31K$ and $B_1 = 0.03355K$ is hereafter labelled JHA_1B_1 .

Comparison of JHA_1B_1 with the rms results of Table 12.1 shows slight degradations for arcs 1, 2, 3 and 9, no change for arc 4, a slight improvement for arc 5 and vast improvement for arcs 7 and 8. Similarly for the new model with JS84, arcs 1, 2 and 3 deteriorate slightly, arc 4 remains unchanged, whilst arcs 5, 7, 8 and 9 all improve greatly, particularly arc 8, compared to the results of Table 12.2. Once again however, there is little to choose between the results from the CIRA 72 model (JHA_1B_1) or JS84 and consequently, subsequent analysis is restricted to the simpler JHA_1B_1 .

§12.4 Further Computations Using JHA_1B_1

Section 12.3 revealed that the model labelled JHA_1B_1 was possibly the best of those yet analysed. In order to assess its performance more thoroughly, various additional experiments have been run using arcs with both single and multiple drag coefficients. These arcs were not utilized in the estimation of the model coefficients A_1 and B_1 , so providing an independent check on the applicability of the model. For comparison, the arcs were also determined relative to the original version of CIRA 72.

One of the multiple drag coefficient arcs analysed spanned the six days from MJD 43776 to MJD 43782 so that the severe geomagnetic storm of MJD 43780 was covered. Daily drag coefficients were utilized throughout except on MJD 43780 when two half daily coefficients were estimated. Results of the orbital computations relative to both CIRA 72 and JHA_1B_1 using the GEM-T1 gravity field and NASA 'area tables' for SEASAT are presented in Table 12.8.

Table 12.8: Orbital results for MJD 43776 to MJD 43782 using multiple drag coefficients as described in the text.

<u>Model</u>	<u>Rms(m)</u>	<u>C_D Range</u>	<u>C_R</u>	<u>Number of Observations</u>
CIRA 72	1.10	2.76–5.74	1.67	1585
JHA ₁ B ₁	0.57	2.62–3.50	1.70	1585

Table 12.8 reveals that JHA₁B₁ has greatly improved the orbital fit to the laser range observations compared to CIRA 72. The reduced variation in the recovered drag coefficients when utilizing JHA₁B₁, shows that this model has accommodated the actual density variation more accurately than CIRA 72. Consequently, such a model for density should produce more reliable orbits from which to derive the density profiles of chapter 11, at least for periods of high geomagnetic variability. Therefore the two long-arcs of that chapter were recomputed relative to JHA₁B₁ and the recovered drag coefficients used to derive the density profiles as described previously. Resulting observed and modelled profiles are plotted graphically in Figures 12.5 to 12.8. Also plotted for comparison, are the profiles as derived from several other density models.

As expected, the observed profiles derived from JHA₁B₁ over both periods, are in good agreement with the observed profiles derived from other density models. Such agreement once more validates the method of relative density determination described in chapter 11. Of more significance however, is the modelled profile of JHA₁B₁ over the period MJD 43770 to MJD 43783 (Figure 12.6). The shape of this profile is very similar to that of the observed profiles (Figure 12.5) and explains the excellent fit of JHA₁B₁ over MJD 43776 to MJD 43782 (Table 12.8). In particular, it is noted that the model represents the persistence of MJD 43779 very accurately, showing that JHA₁B₁ performs very well over periods of high geomagnetic activity. However, for the earlier arc (Figure 12.8), the modelled profile from JHA₁B₁ is not in as good agreement with the observed profiles (Figure 12.7) as is the CIRA 72 modelled profile for instance, though much of the discrepancy is due to a scale

difference. Evidently, JHA_1B_1 represents density variation no better than CIRA 72 over periods of low geomagnetic activity.

Strictly speaking, the orbit of MJD 43776 to MJD 43782 does not provide an independent check on the applicability of JHA_1B_1 since the four day arc MJD 43778 to MJD 43782 was utilized within its derivation. Consequently, it was necessary to compare JHA_1B_1 and CIRA 72 using several 'independent' SEASAT arcs. At this point however, difficulties arise because SEASAT data becomes scarce or problematic. For instance, after the power failure on October 10, 1978 (MJD 43791), the solar panels must have ceased rotation, thus producing problems in the along-track SRP force modelling. Also, the data from the early part of SEASAT's operational lifetime is greatly influenced by small radial SRP perturbations coupled with relatively large along-track SRP perturbations. Any error in the modelling of the NASA 'area tables' will be particularly significant in the along-track direction over this period.

Despite these uncertainties, three additional orbital comparisons were made with SEASAT laser data. One arc spanned the six days from MJD 43700 to MJD 43706, another the six days from MJD 43716 to MJD 43722 and the third, the five days from MJD 43805 to MJD 43810. Of these three arcs, MJD 43716 to MJD 43722 is the least problematic in the sense described above. Results of the ensuing computations with CIRA 72 and JHA_1B_1 are presented in Table 12.9.

Figure 12.5 : Observed density profiles for the period MJD 43770 to MJD 43783.

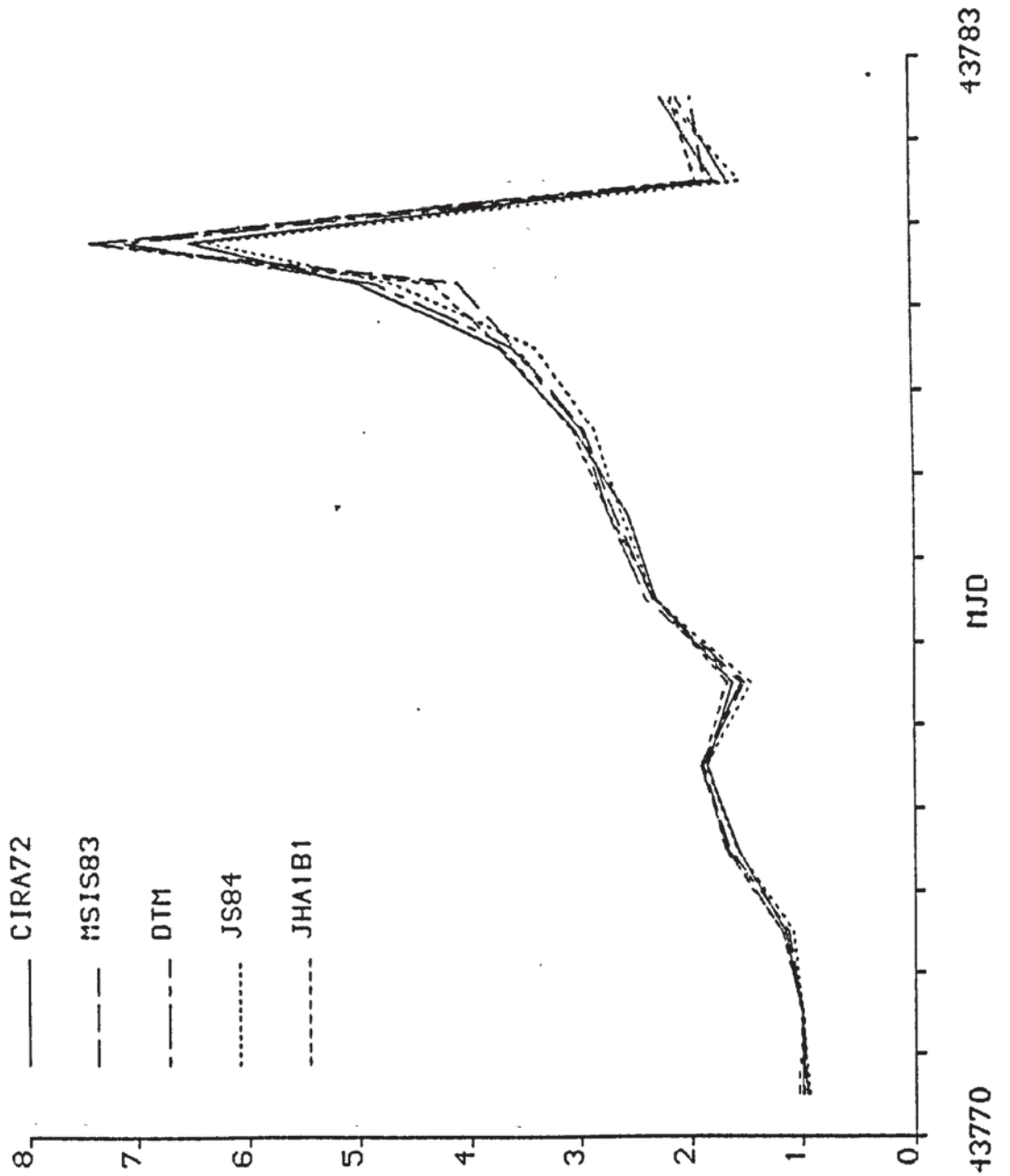


Figure 12.6 : Modelled density profiles for the period MJD 43770 to MJD 43783.

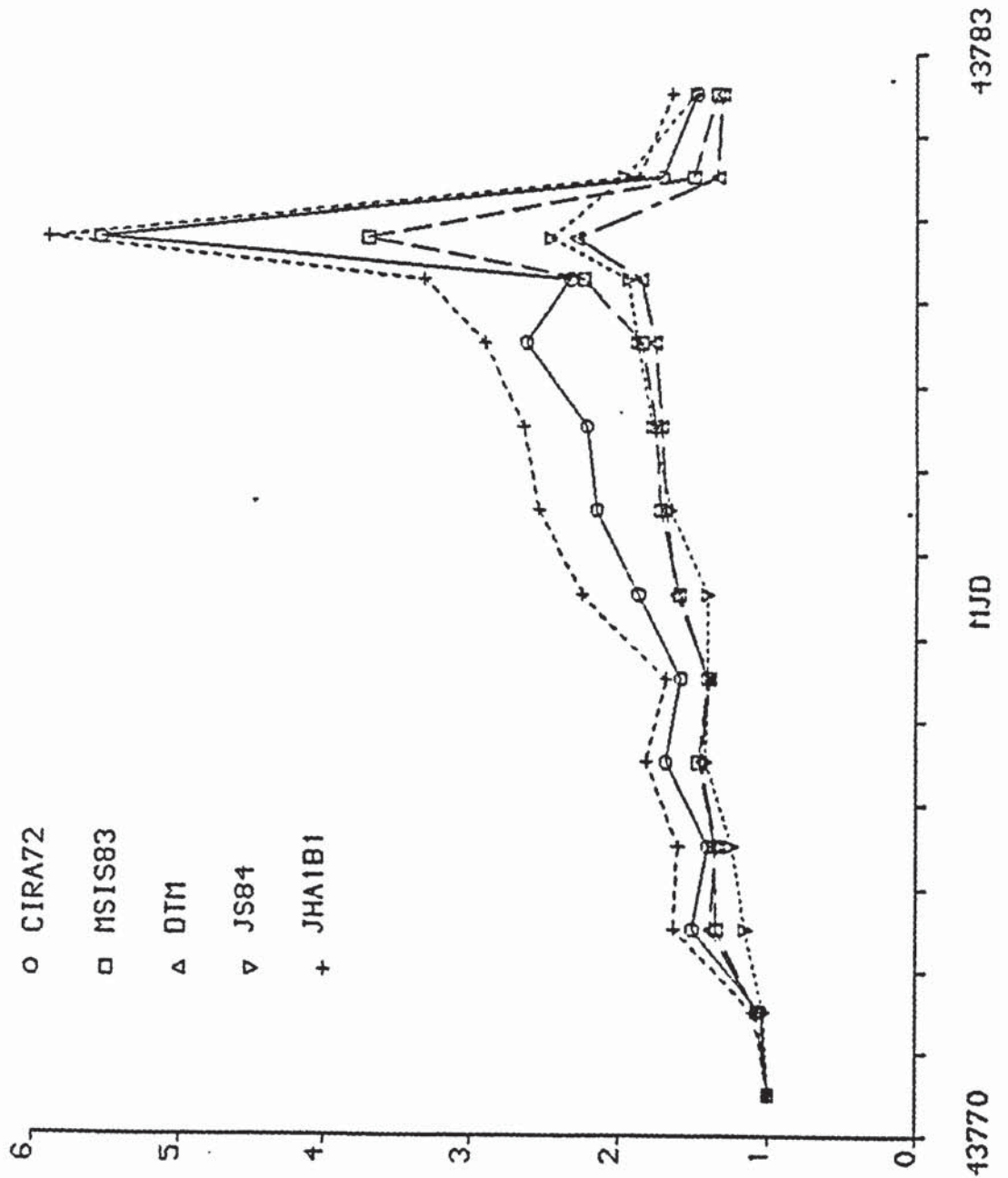


Figure 12.7 : Observed density profiles for the period MJD 43716 to MJD 43730.

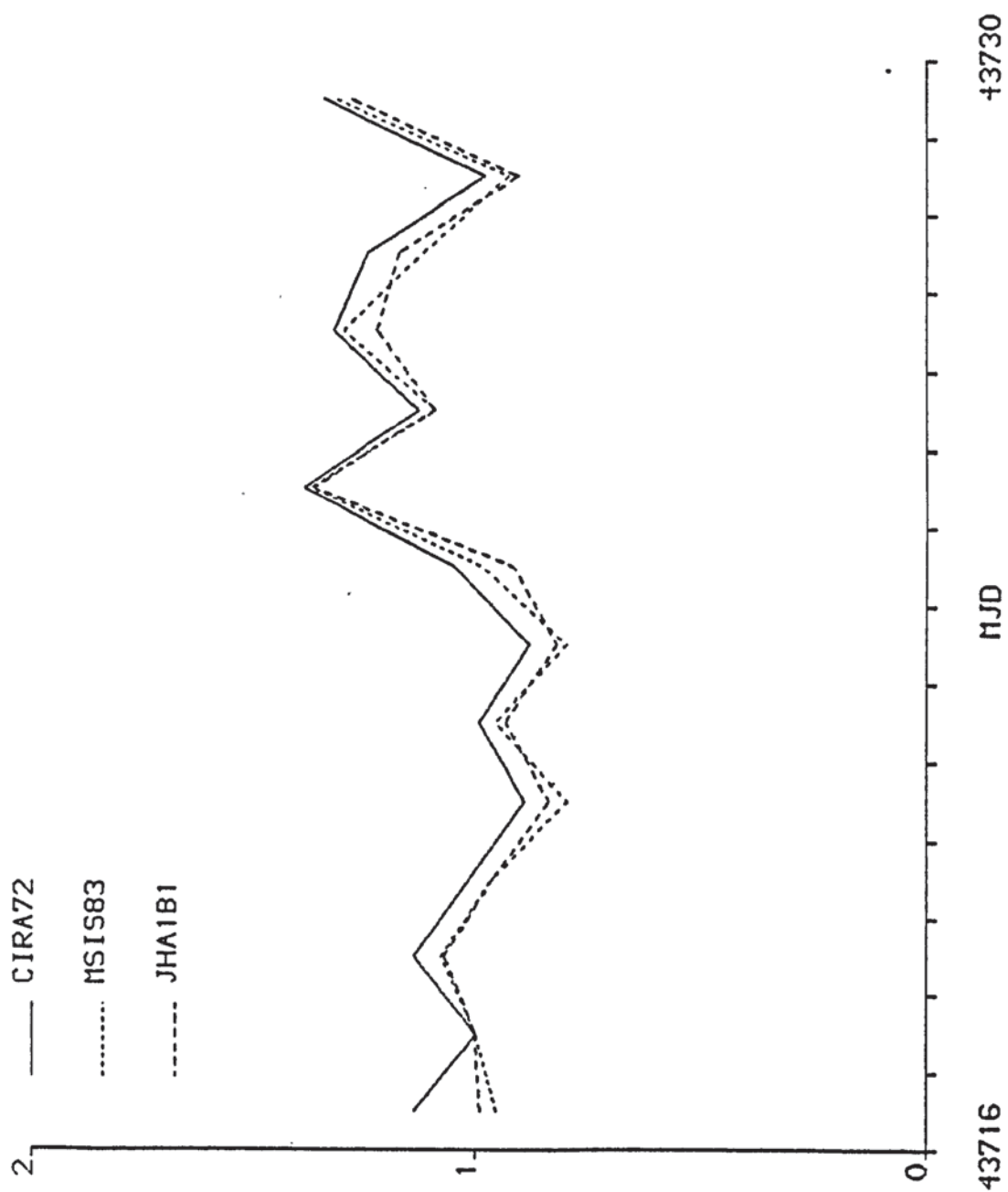


Figure 12.8 : Modelled density profiles for the period MJD 43716 to MJD 43730.

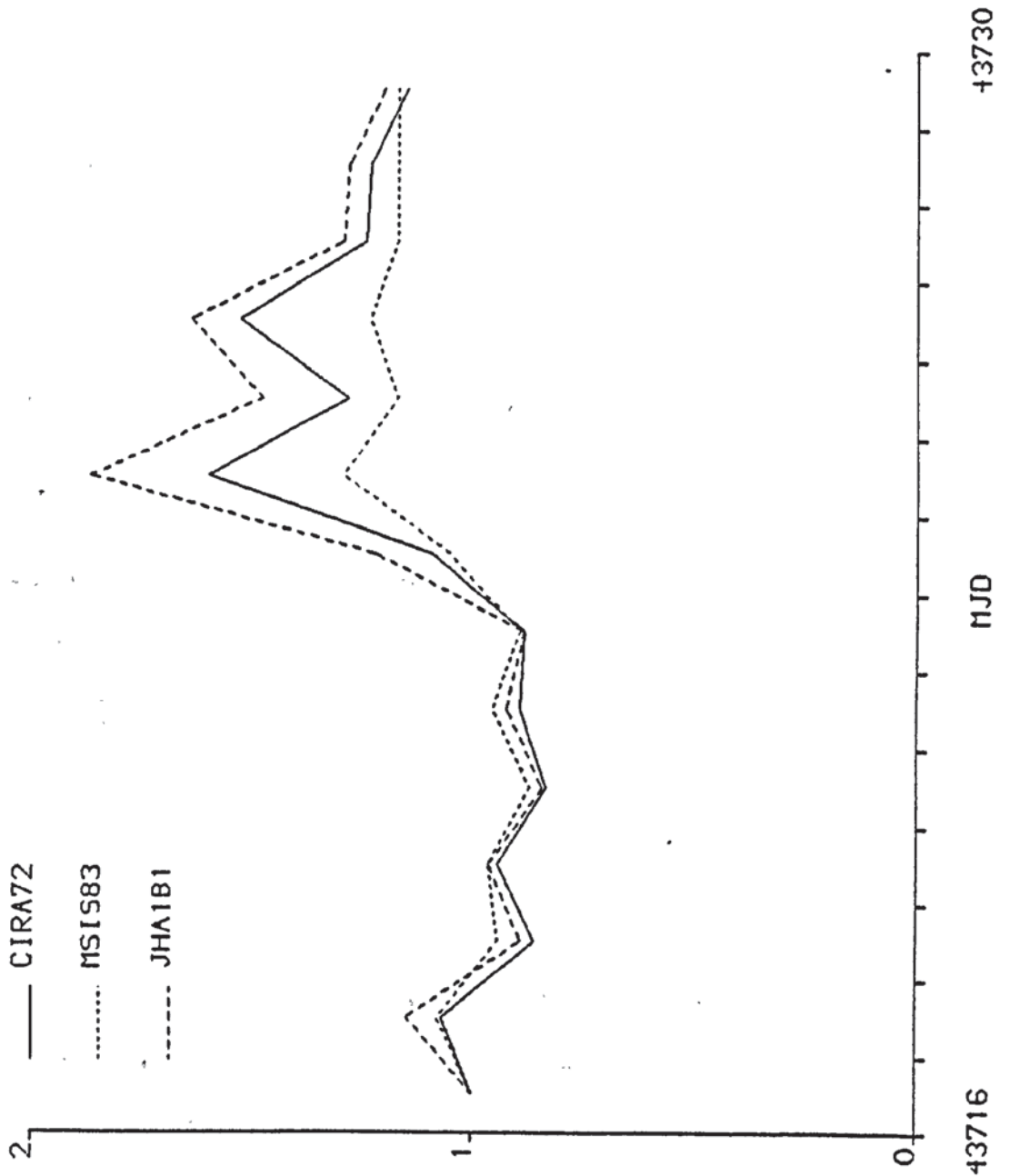


Table 12.9: Orbital results using CIRA 72 and JHA₁B₁ for three 'independent' SEASAT arcs.

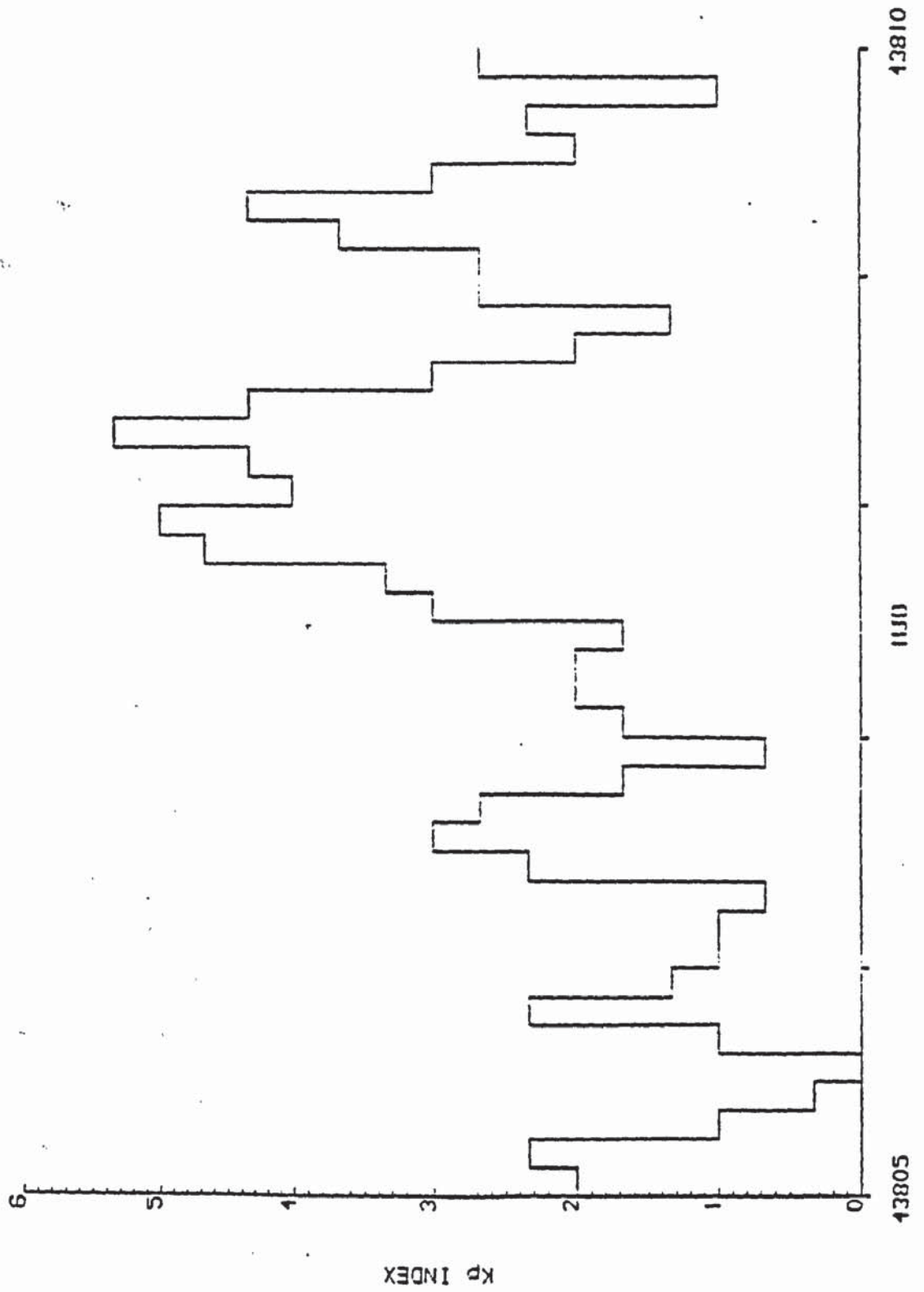
<u>Orbit</u>	<u>Rms(m)</u>	<u>C_D</u>	<u>C_R</u>	<u>Number or observations</u>
<u>43700–43706</u>				
JHA ₁ B ₁ (single C _D)	2.91	2.90	-0.46	1447
CIRA 72 (single C _D)	2.37	3.22	-0.14	1447
<u>43716–43722</u>				
JHA ₁ B ₁ (single C _D)	1.83	4.99	1.44	744
CIRA 72 (single C _D)	1.77	5.30	1.52	744
JHA ₁ B ₁ (daily C _D 's)	1.02	4.09–5.80	1.37	743
CIRA 72 (daily C _D 's)	1.02	4.19–6.01	1.37	743
<u>43805–43810</u>				
JHA ₁ B ₁ (single C _D)	0.97	3.35	1.50	665
CIRA 72 (single C _D)	3.06	3.66	1.49	665

It is seen that for the earliest arc, CIRA 72 performs better than JHA₁B₁, for MJD 43716–MJD 43722 there is little to choose between either model whereas for the latter arc, JHA₁B₁ performs significantly better than CIRA 72. As anticipated, the MJD 43700 to MJD 43706 orbital arc, when solving for a single drag coefficient, has experienced problems with the modelling of SRP with a high correlation (≈ 0.999) between C_R and C_D. Therefore it is dangerous to attach too much significance to the results of this orbit. For the least problematic of the three orbits (MJD 43716 to

MJD 43722), the results are very similar for both CIRA 72 and JHA_1B_1 as expected for a period of low geomagnetic variability (Figure 11.8). Conversely, the vast improvement of JHA_1B_1 over CIRA 72 for the last orbital arc is probably a consequence of the medium–high geomagnetic storm over this period (Figure 12.9).

Overall, these comparisons are not conclusive either in favour of JHA_1B_1 or CIRA 72, though for large, well–defined geomagnetic storms, JHA_1B_1 seems to be the most appropriate model to use. A more thorough examination of the applicability of JHA_1B_1 can only be achieved by analysing data from another satellite. The satellite chosen for this task was STARLETTE, spherical in shape of cross–sectional area 0.04524m^2 and mass 47.295kg [18]. Its orbit is at inclination $\sim 50^\circ$ with eccentricity ~ 0.02 and semi–major axis $\sim 7300\text{km}$ [69]. Since this orbit is of similar altitude to SEASAT's orbit, the coefficients of JHA_1B_1 should be applicable and a valid comparison of CIRA 72 with JHA_1B_1 can be made. However, STARLETTE was designed specifically for gravity field and tidal studies with minimal drag and SRP effects. Consequently, drag is less significant than for SEASAT by a factor of ten. Nevertheless, large geomagnetic disturbances need to be well modelled since they are still important. The amount of data available from STARLETTE provides sufficient coverage of geomagnetic disturbances, including one of very high severity over the period MJD 46467 to MJD 46473. In all, 17 STARLETTE orbits were analysed, 15 being consecutive (with the exception of data outages), the other two chosen to occur during high geomagnetic activity. The 15 orbits spanned the period 22 September, 1984 to 9 December 1984 (MJD 45965 to MJD 46043), each orbit being five days in length. The geomagnetic activity for this period, as measured by the K_p index, is plotted in Figure 12.10. As for the other two orbits, one was a six day arc spanning 6 February, 1986 to 12 February, 1986 (MJD 46467 to MJD 46473), the other a five day arc spanning 24 April, 1984 to 29 April, 1984 (MJD 45814 to MJD 45819). As shown in Figure 12.11, the six day arc occurred during the aforementioned severe geomagnetic storm.

Figure 12.9 : Geomagnetic planetary index, K_p for MJD 43805 to MJD 43810.



Six days were chosen for this arc length in order to constrain the solution after this geomagnetic event, in view of the sparse data on MJD 46472.

Comparisons of JHA_1B_1 with CIRA 72 for all 17 arcs relative to the GEM-T1 gravity field when employing single drag coefficients, can be found in Table 12.10, showing the recovered rms values only. For all arcs except the six day arc, C_R was held fixed at 1.14. For the six day arc, C_R had to be allowed to vary for a realistic solution to be obtained. Apparently, for both CIRA 72 and JHA_1B_1 there is contamination between drag and SRP during the severe geomagnetic storm of this period.

Table 12.10 reveals that JHA_1B_1 performs better than CIRA 72 in the majority of cases, with a significant improvement for the six day arc. Evidently, JHA_1B_1 has dramatically improved the modelling of severe geomagnetic storms without significantly deteriorating the modelling of low level geomagnetic activity.

The first 15 arcs of Table 12.10 were also employed in the estimation of the coefficients A_1 and C_R in a similar manner to the estimation of A_1 and B_1 in section 12.3. The resulting values were 34.80 and 1.25, respectively. B_1 could not be successfully recovered on account of the low sensitivity of STARLETTE to density variations. However, the results in no way contradict the values derived from SEASAT. Adding the final two arcs to the estimation process caused problems since they dominated the solution. Large correlations occurred between the drag coefficients of these arcs and A_1 , implying that separation was difficult. The value recovered for A_1 when using 17 arcs was 29.58 which is lower than anticipated, but all the drag coefficients increase correspondingly to compensate. Due to the high correlations, not much credence can be placed on this solution.

Of more importance are the improvements in the final two arcs over CIRA 72 when using JHA_1B_1 , showing that progress has been made in satellite drag modelling, at least over periods of high geomagnetic activity.

As a final test of JHA_1B_1 , the last two arcs of Table 12.10 were computed relative to MSIS-83A for comparison. The resulting rms values were 21.19cm for

the five day arc and 35.58cm for the six day arc, showing JHA₁B₁ to be slightly worse than MSIS-83A over the medium-high geomagnetic storm of the earlier arc and better over the severe geomagnetic storm of the later arc.

Table 12.10: Orbital rms results for 17 STARLETTE arcs. CIRA 72 versus JHA₁B₁ relative to the GEM-T1 gravity field and utilizing single drag coefficients.

<u>Arc (MJD)</u>	<u>rms for model (cm)</u>	
	<u>CIRA 72</u>	<u>JHA₁B₁</u>
45965-45970	28.41	27.68
45970-45975	26.51	26.92
45975-45980	16.81	16.70
45981-45986	32.50	32.39
45986-45991	17.29	17.31
45991-45996	22.65	22.16
45996-46001	20.53	20.99
46002-46007	18.80	18.30
46007-46012	21.88	21.76
46012-46017	22.88	22.81
46017-46022	19.30	19.68
46022-46027	18.89	18.89
46028-46033	19.23	19.27
46033-46038	33.30	33.03
46038-46043	17.93	17.98
46467-46473	41.64	30.94
45814-45819	28.37	25.65

Figure 12.10 : Geomagnetic planetary index, K_p , for MJD 45965 to MJD 46043.

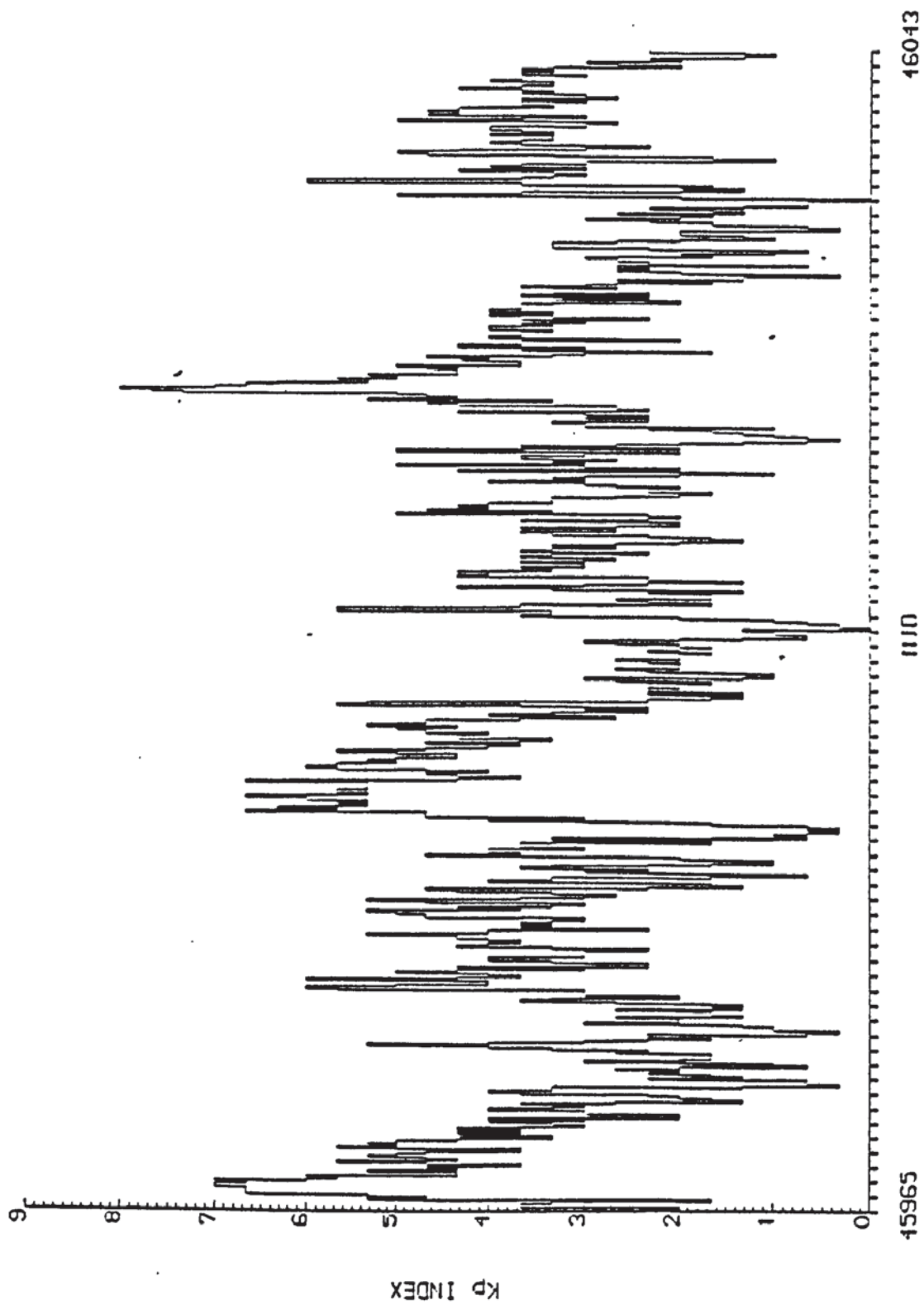


Figure 12.11 : Geomagnetic planetary index, K_p , for MJD 46467 to MJD 46473.

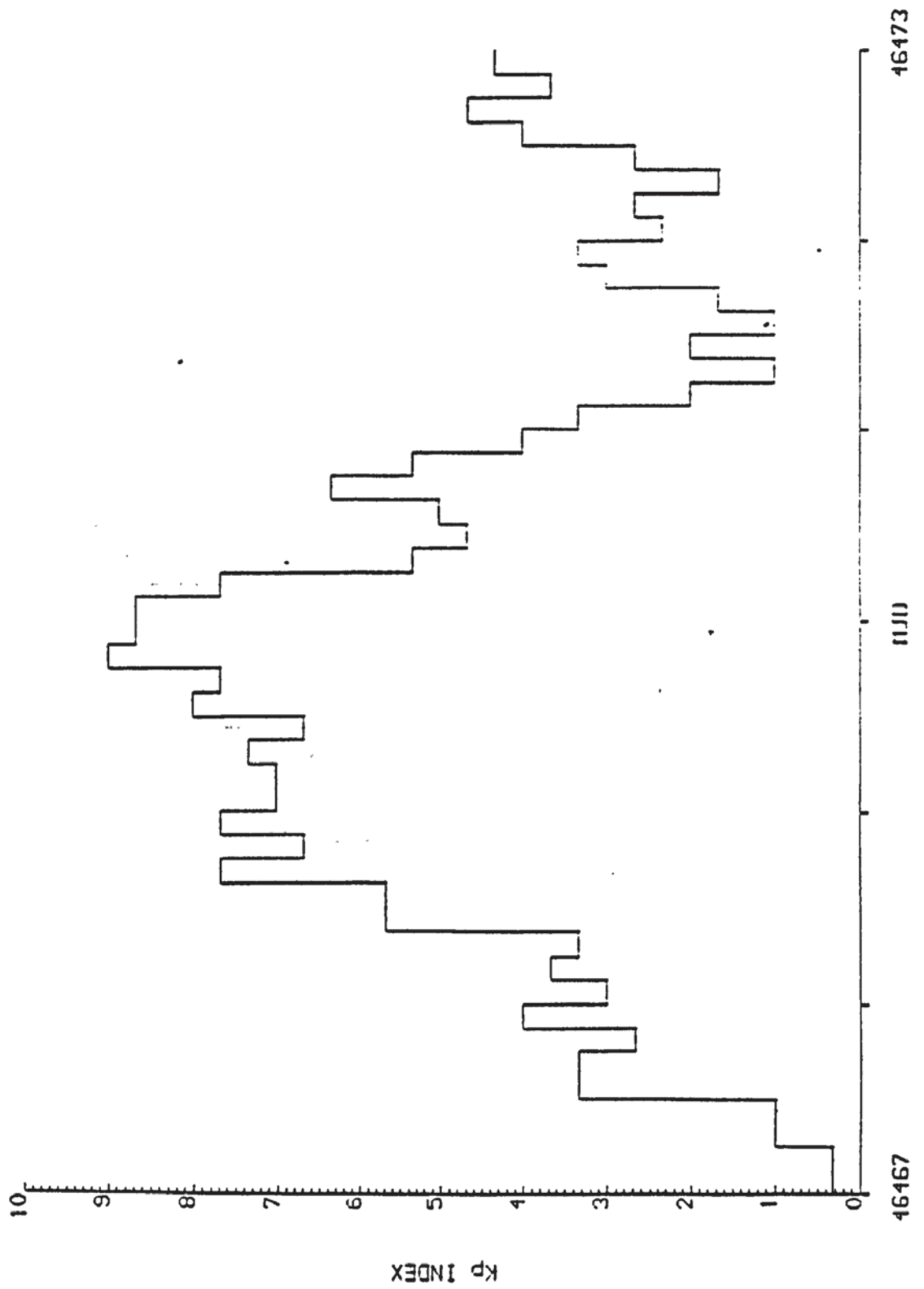
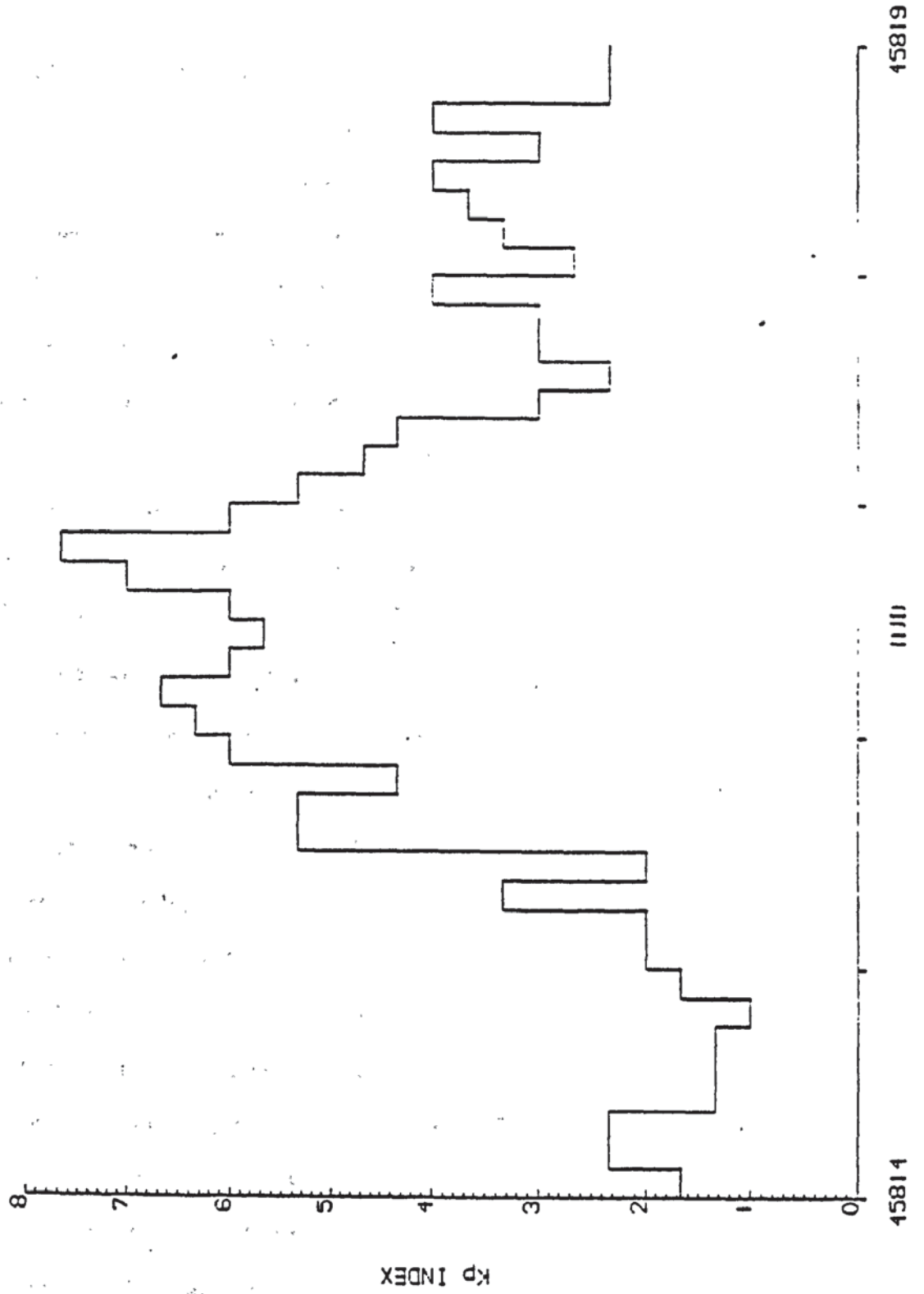


Figure 12.12 : Geomagnetic planetary index, K_p , for MJD 45814 to MJD 45819.



§12.5 A Note On The Use Of the NASA 'Area Tables' For Drag

During the preparation of this thesis a coding error in the utilization of the NASA 'area tables' for drag came to light. The error arose from a mistake in the GEODYN documentation which, in any case, is inappropriate for the SRP modelling as ascertained at the outset by discussion with GSFC personnel. That the error was inevident early on was a result of the limited effect of the variation in cross-sectional area on drag effects, any scaling error being absorbed in C_D whilst the say, 25% variation in area over an orbit being close to the sensitivity of the data. Correction of the coding error in no way invalidates any of the results of this study, being irrelevant for the effective density calculations of chapter 11 and having only a small qualitative effect in the comparisons of chapter 10 and modelling in chapter 12. Errors in the cross-sectional area were common to all comparisons, scaling the rms (and C_D values) by a common factor. This can be verified by comparing Tables 12.1 and 12.2 with the equivalent results in Tables 12.11 and 12.12, respectively, as derived from the corrected program. Qualitatively, the comparisons are unaltered, the rms values exhibiting identical trends for results for a particular arc. Furthermore, even excluding arc 9, being after the power failure anyway, the 'area tables' incorporated correctly, do not lead to any significant improvements compared with the incorrect version and for several arcs yield higher rms values. In fact, similar results could have been derived by using the spherical satellite approximation for drag, although the SRP accelerations are essential. It was evident from an early stage that incorrect alignment of the satellite body fixed axes as deduced from the GEODYN documentation lead to either zero or negative C_D values and/or negative C_R values. However, the insensitivity to area in drag modelling covered the drag coding error. It is clear from this work that adoption of 'black box' routines and tables from other institutions is hazardous and that derivation of 'in-house' software the best solution. However, the construction of equivalent area tables would have

been time consuming, drastically reducing the scientific output of this project and adding little to the results.

Table 12.11: Orbital results relative to CIRA 72 using the summation formula of equation (12.1) when solving for a single drag coefficient in conjunction with the GEM-T1 gravity field and the corrected NASA 'area tables' for SEASAT.

<u>Orbital Arc</u>	<u>Rms(m)</u>	<u>C_D</u>	<u>C_R</u>	<u>Number of Observations</u>
1	0.99	5.18	1.71	972
2	2.76	3.65	0.81	1488
3	1.74	2.37	1.43	1481
4	4.05	1.89	0.42	1101
5	5.05	2.46	1.73	1993
6				
7	2.11	3.54	2.18	1005
8	3.35	3.44	1.86	978
9	2.39	2.73	1.79	933

Table 12.12: As for Table 12.11 but using JS84.

<u>Orbital Arc</u>	<u>Rms(m)</u>	<u>C_D</u>	<u>C_R</u>	<u>Number of Observations</u>
1	0.85	6.22	1.71	972
2	2.41	4.45	0.99	1488
3	1.72	2.72	1.45	1481
4	4.07	2.06	0.47	1101
5	5.99	2.72	1.78	1993
6				
7	2.50	4.18	2.35	1005
8	5.31	3.84	1.94	978
9	3.10	3.04	1.78	933

Upon using the corrected program to estimate the model coefficients of section 12.3, the following values were obtained for JHA_1B_1 :-

$$A_1 = 35.77 \pm 0.20K,$$

$$B_1 = 0.0287 \pm 0.0003K.$$

These are in close agreement with the previous values of 33.31K for A_1 and 0.03355K for B_1 . Likewise, the recovered values of the coefficients in JS84 when using the summation formula equation (12.1) and the K_p index were :-

$$A'_1 = 76.73 \pm 1.13K,$$

$$Z_1 = 17.87 \pm 0.61m,$$

$$E_1 = 0.00088 \pm 0.00002,$$

$$A_2 = 0.327 \pm 0.004,$$

$$A_3 = 0.0253 \pm 0.0009.$$

which are also in very good agreement with their original counterparts. As for the STARLETTE comparisons, there are no significant changes to the orbital rms values when using JHA_1B_1 with these new coefficients. Over the severe geomagnetic storm (MJD 46467 to MJD 46473), the rms improves from 30.94cm to 30.18cm whilst for the medium-high storm (MJD 45814 to MJD 45819) the rms deteriorates from 25.65cm to 26.50cm. This does not alter any of the qualitative results or conclusions drawn from this analysis.

§12.6 Discussion

Part two of this thesis was concerned with computing orbital arcs using SEASAT laser range data relative to various models for atmospheric density and, in particular, geomagnetic activity. Evaluation of model performance was achieved by comparing orbital results when estimating for a single drag coefficient only, multiple coefficients absorbing drag modelling errors. Some of this work was presented in a paper entitled "A Comparison of Geomagnetic Activity Models using SEASAT Laser

Range Data" [26], which concluded that the modelling of geomagnetic activity was best performed using a summation technique on the effect rather than the index of activity. However, instances occur when this technique is still poor if used in conjunction with the geomagnetic planetary index, K_p . This motivated a new index, ΔE to be derived based on raw auroral electrojet (AE) data the use of which improved on the K_p index in certain instances. However, its overall performance was found to be less successful than K_p in modelling the exospheric temperature increase associated with a geomagnetic disturbance. Apparently, the 3 hour global index K_p is still to be preferred in orbital studies rather than the more detailed, but localized, AE index.

The most promising results were obtained upon estimating certain coefficients in the models for geomagnetic activity. Results of this work, presented in section 12.3, showed that many of the coefficients determined tended to increase the values of the modelled densities relative to the original model values. The inference is that the state-of-the-art density models under-estimate the density changes associated with geomagnetic activity at SEASAT heights. Such a phenomenon was observed in chapter 11 when modelled density profiles were compared to their observed counterparts.

A model, JHA_1B_1 , was derived in section 12.3 using data from seven SEASAT arcs, which consisted of a Hedin-type summation formula to represent persistence and required determination of the coefficients A_1 and B_1 in equation (9.5) for geomagnetic activity. In the majority of cases the model performs as good as CIRA 72, but over large, well-defined geomagnetic storms, it is significantly better. That this is the case is readily observed from Figure 12.6 where the modelled density profile of JHA_1B_1 is in excellent agreement with the observed profiles.

Further analysis of JHA_1B_1 required utilizing laser data obtained from the STARLETTE satellite, in an orbit of similar altitude to SEASAT. The results of this independent analysis confirmed the applicability of JHA_1B_1 for modelling severe geomagnetic activity. Evidently, the introduction of persistence modelling is very

important over periods of high geomagnetic activity; a criticism of CIRA 72. Conversely MSIS-83A accounts for geomagnetic persistence and for medium-high geomagnetic activity, performs as well, if not better than JHA_1B_1 (section 12.4). However, for the severe geomagnetic storm of MJD 46467 to MJD 46473, MSIS-83A performed noticeably worse. Apparently, there is a limit to the geomagnetic activity for which MSIS-83A is applicable, above which it begins to deteriorate in accuracy. Again this could be a consequence of the under-estimation of a density change associated with a geomagnetic disturbance at 800km, as observed in Figure 11.1, for all the density models. Estimation of the coefficients A_1 and B_1 was a direct attempt to overcome this deficiency and has succeeded for high geomagnetic activity. However, there has been no improvement for low geomagnetic activity which is hardly surprising since A_1 and B_1 are effectively biased towards high values of K_p only.

The results of this analysis have shown that satellite laser range data can be used to examine the deficiencies of current state-of-the-art atmospheric density models as well as determine atmospheric densities. The capability now exists to derive coefficients within atmospheric models which, with better data will produce more accurate models. It is anticipated and indeed hoped, that ERS-1 data will provide a more thorough investigation into the effects of geomagnetic activity on atmospheric densities, which in turn will produce even more accurate density models. A necessary pre-requisite for this analysis is the derivation of precise area modelling for the satellite, in both drag and SRP forces.

Although the density modelling techniques of this thesis, when used in conjunction with a single drag scale factor, have not produced the level of accuracy obtained from using multiple drag coefficients, in time it is hoped they will do so. Nevertheless, the model derived in this study, JHA_1B_1 , has still shown a dramatic improvement over current state-of-the-art models when used in conjunction with multiple drag coefficients as shown in Table 12.8.

CHAPTER 13

CONCLUSIONS AND RECOMMENDATIONS

§13.1 Conclusions

The SATAN software package has been modified to accept two additional types of satellite tracking data. As well as laser range observations, SATAN can now determine orbits using pure altimetry and crossover height differences. Extensive software has been written for the processing, utilization and analysis of these latter two types of tracking data. Software validation was achieved using data from the SEASAT satellite but modification to accept ERS-1 data is straightforward. Other software modifications include the implementation of multiple drag coefficients, the NASA 'area tables' for SEASAT and several atmospheric density models.

Investigation into the use of altimetry and crossovers for tracking purposes revealed that little additional information is obtained from an orbit computed using adequate laser range measurements. However, if only sparse laser data is available, supplementation with either altimetry or crossovers yields orbits of a similar quality to those derived from a good network of laser data. Such findings could prove beneficial in the tracking of ERS-1 for which as yet, it is unclear how much laser coverage there will be.

Apart from satellite tracking applications, altimetry and crossovers can be used to analyse certain orbital and oceanographic features. By analysing the frequencies of terms comprising the altimeter residuals, it is possible to determine which errors are orbital in nature and which are due to the geoid and/or sea surface topography. Such an analysis provided the means to determine a low degree and order sea surface topography model which was found to be in good qualitative agreement with the models derived by Engelis[50] and Marsh et al [48]. For a more detailed study however, it is necessary to separate high degree gravity field terms which requires the use of more extensive data, including land gravimetry.

Analysis of the crossover height residuals revealed that a north-south bias may occur in the orbit when utilizing poor laser data, a consequence of a time-dependent eccentricity error caused by a poorly determined solar radiation pressure coefficient, (Moore and Rothwell [47]). Supplementation of the orbit with either altimetry or crossovers reduced this bias. Also, being devoid of any geoid error, the rms of the crossover height residuals provides an independent check on global radial ephemeris accuracy.

The implementation of the GEM-T1 gravity field and associated laser station coordinates, the SEASAT 'area tables' for air-drag and normalized SRP accelerations and multiple drag coefficients into the SATAN software package has resulted in rms accuracies of between 50 and 60cm when computing six day SEASAT arcs. These values, which are confirmed by both the fit to laser range observations and the independent values derived from crossover height residuals, are in good agreement with those derived by Zandbergen et al [42] when computing three day arcs. Such precision is a vast improvement over the two metre rms accuracies which were obtained three years ago, at the outset, when employing the PGS-S3 gravity field and associated laser station coordinates, a spherical satellite approximation for cross-sectional area modelling and a linear rate of change for the drag parametrization. However, the decimetre accuracy required for optimum altimetric utilization has not as yet, been attained, primarily due to mis-modelling of the Earth's gravity field. It is anticipated that the introduction of the GEM-T3 gravity field and associated laser station coordinates into the SATAN package will help to alleviate this deficiency.

Other major sources of orbital error, at least for SEASAT, result from errors in the NASA 'area tables' for normalized SRP accelerations, particularly early on in SEASAT's operational lifetime and the modelling of atmospheric densities using static density models. Comparisons of state-of-the-art density models revealed deficiencies in several aspects, particularly the ability to represent density changes associated with geomagnetic activity. Variations within recovered drag coefficients from long-arc orbits are highly correlated with the geomagnetic planetary index, K_p ,

and motivated the determination of relative effective atmospheric densities at SEASAT heights, something that has never been previously attempted. The density profiles derived during this analysis revealed where a good fit to a single drag scale factor will occur and hence indicate which density models represent actual density variation. These profiles reveal that the state-of-the-art density models underestimate density changes associated with severe geomagnetic disturbances at SEASAT heights. It was seen here that, for such disturbances, persistence modelling is required, a deficiency of the CIRA 72 atmospheric model commonly adopted in orbital determinations. However, instances occur when the geomagnetic planetary index, K_p , does not represent density variations associated with geomagnetic activity, no matter which density model is employed. The use of a new index based on raw auroral electrojet data alleviated this problem in some cases, but on the whole was not as appropriate as K_p in representing density changes associated with geomagnetic activity.

Using a combination of laser data from several SEASAT arcs, it was shown that recovery of certain coefficients in the geomagnetic parametrization of CIRA 72 and its variants, was possible. When used in conjunction with a model for geomagnetic persistence, this method produced a new density model called JHA_1B_1 with coefficient values of 33.31K and 0.03355K for A_1 and B_1 of equation (9.5), respectively. The performance of this model is significantly better than CIRA 72 over periods of high geomagnetic activity without deteriorating in accuracy over periods of low geomagnetic activity. The general applicability of JHA_1B_1 at 800km and the validation of the coefficients A_1 and B_1 , were confirmed when similar conclusion were drawn from analysing STARLETTE data, showing that good progress has been made in the modelling of atmospheric densities at SEASAT heights. This progress could prove significant when JHA_1B_1 is applied in ERS-1 orbit determinations, ERS-1 having a similar altitude to that of SEASAT. It is anticipated that more progress will be made in density modelling using the techniques of this thesis, when data from ERS-1 is eventually analysed.

§13.2 Recommendations For Further Work

This research project has paved the way for several areas of further study. The implementation of altimetry into the software means there is the capability for further developments in oceanographic applications of satellite data. For instance, the groundwork in sea surface topography recovery has been undertaken and a more thorough analysis and simultaneous solution for gravity field coefficients is the next logical step. This will require the use of land gravimetry. Once this has been achieved, a sea surface topography model can be implemented into the altimeter data processing (equation (4.1)).

With the advent of more accurate tracking data, particularly laser range data, it should be possible to recover relative effective atmospheric densities over shorter time spans than one day. This requires that the drag coefficients be well determined which in turn requires very accurate along-track modelling of non-drag forces (gravity field and SRP). Such accuracies could be realized when GEM-T3 is applied to ERS-1 for instance. However, an accurate 'area table' for ERS-1 is a necessary pre-requisite for this work.

The analysis of a geomagnetic index based on raw auroral electrojet data was only briefly investigated. Further analysis could be performed with particular attention paid to the atmospheric response at the onset and decay of geomagnetic storms.

Finally, ERS-1 data could be utilized to determine new atmospheric density models and/or geomagnetic modelling coefficients, using the techniques developed in this thesis. It is hoped that ERS-1 will provide more data than did SEASAT during its three month operational lifetime, thereby producing more realistic models than those derived in this study.

REFERENCES

- [1] Tapley, B.D., and Born, G.H. The Seasat Precision Orbit Determination Experiment. *J. Astro. Sci.* Vol.XXVIII, No.4, pp.315-326, Oct-Dec, 1980.
- [2] Lerch, F.J., Marsh, J.G., Klosko, S.M. and Williamson, R.G. Gravity Model Improvement for Seasat. *J. Geophys. Res.*, Vol.87, pp.3281-3296, 1982.
- [3] Marsh, J.G., Lerch, F.J., Putney, B.H., Christodoulidis, D.C., Felsentreger, T.L., Sanchez, B.V., Smith, D.E., Klosko, S.M., Martin, T.V., Paulis, E.C., Robbins, J.W., Williamson, R.G., Colombo, O.L., Chandler, N.L., Rachlin, K.E., Patel, G.B., Bhatti, S. and Chinn, D.S. An improved model of the Earth's gravitational field GEM-T1, *J. Geophys. Res.*, Vol.93, pp.6169-6215, 1988.
- [4] Marsh, J.G., Lerch, F.J., Klosko, S.M. and Williamson, R.G. Orbit Determination for Altimeter Missions : The impact of new NASA/Goddard Space Flight Center Gravitational Models. Paper presented at the XXVII COSPAR, Espoo, Finland, July, 1988.
- [5] Wakker, K.F., Ambrosius, B.A.C., Zandbergen, R.C.A. and van Geldorp, G.H.M. Precise Orbit Computation, Gravity Model Adjustment and Altimeter Data Processing for the ERS-1 Altimetry Mission. ESA Contract Report, TU Delft, Feb. 1987.
- [6] Wakker, K.F., Ambrosius, B.A.C. and van der Ploeg, T. Seasat Orbit Determination from Laser Range Observations. Presented at SURGE discussion meeting, London, April 14-16, 1982.
- [7] Schutz, B.E. and Tapley, B.D. Orbit Accuracy Assessment for Seasat. *J. Astro. Sci.*, Vol.XXVIII, No.4, pp.371-390, Oct-Dec, 1980.
- [8] Martin, T.V., Eddy, W.F., Brenner, A., Rosen, B. and McCarthy, J. GEODYN SYSTEM DESCRIPTION, NASA Cont. No. NAS 5-22849, Task 054, 1980.
- [9] Sinclair, A.T. and Appleby, G.M. SATAN - Programs for the determination and analysis of satellite orbits from SLR data, SLR Tech. Note 9, RGO, Herstmonceaux, 1986.
- [10] Merson, R.H. Numerical Integration of the Equations of Celestial Mechanics, RAE Tech. Report 74184, 1975.
- [11] Jacchia, L.G. Atmospheric Models in the Region from 110 to 2000km. In CIRA 72, compiled by COSPAR Working Group 4, Akademie-Verlag, Berlin, 1972.
- [12] Slowey, J.W. Dynamic model of the Earth's upper atmosphere. NASA Cont. Report 3835, 1984.
- [13] Hedin, A.E., Salah, J.E., Evans, J.V., Reber, C.A., Newton, G.P., Spencer, N.W., Kayser, D.C., Alcayd e, D., Bauer, P., Cogger, L. and McClure, J.P. A Global Thermospheric Model Based on Mass Spectrometer and Incoherent Scatter Data MSIS1. N₂ Density and Temperature. *J. Geophys. Res.*, Vol.82, No.16, pp.2139-2147, 1977.

- [14] Hedin, A.E., Reber, C.A., Newton, G.P., Spencer, N.W., Brinton, H.C., Mayr, H.G. and Potter, W.E. A Global Thermospheric Model Based on Mass Spectrometer and Incoherent Scatter Data MSIS2. Composition. *J. Geophys. Res.*, Vol.82, No. 16, pp.2148–2156, 1977.
- [15] Hedin, A.E. A revised thermospheric model based on mass spectrometer and incoherent scatter data : MSIS–83. *J. Geophys. Res.*, Vol.88, pp.10170–10188, 1983.
- [16] Barlier, F., Berger, C., Falin, J.L., Kockarts, G. and Thuillier, G. A thermospheric model based on satellite drag data. *Ann. Geophys.* t.34, fasc.1, pp.9–24, 1978.
- [17] Rothwell, D.A. A Description of Altimeter and Crossover Processing Software. Internal Report, ESRU, Aston University, 1989.
- [18] Merit Standards, April 1983.
- [19] Sinclair, A.T. Earth Rotation and Reference Systems. Paper presented at Summer School in Space and Terrestrial Geodesy, Nottingham University, September, 1987.
- [20] Kaula, W.M. *Theory of Satellite Geodesy*. Blaisdell Publishing Company, Waltham, Massachusetts, 1966.
- [21] Brouwer, D. and Clemence, G.M. *Methods of Celestial Mechanics*. Academic Press, New York and London, 1961.
- [22] Lembeck, K. *The Earth's Variable Rotation Geophysical Causes and Consequences*. Cambridge University Press, Cambridge, 1980.
- [23] Melchior, P. *Tides of the Planet Earth*. Pergamon Press, Oxford, 1978.
- [24] Aksnes, K. Short-Period and Long-Period Perturbations of a Spherical Satellite due to Direct Solar Radiation. *Cel. Mech.*, Vol.13, pp.89–104, 1976.
- [25] Wakker, K.F., Ambrosius, B.A.C. and Aardoom, L. *Precise Orbit Determination for ERS–1*. ESA Contract Report, TU Delft, Aug., 1983.
- [26] Moore, P. and Rothwell, D.A. A Comparison of Geomagnetic Activity Models using SEASAT Laser Range Data. *Planet. Space Sci.*, Vol.37, No.6, pp.685–691, 1989.
- [27] Colquitt, E.S., Malyevac, C.W. and Anderle, R.J. Doppler Computed Seasat Orbits. *J. Astro. Sci.*, Vol. XXVIII, No. 4, pp.391–403, Oct–Dec., 1980.
- [28] Cook, G.E. Satellite Drag Coefficients. *Planet. Space Sci.*, Vol.13, pp.929–946, 1965.
- [29] *Geophysical Data Record (GDR) Users Handbook*. NASA document 622–97, Revision A, 15 Sept., 1980.
- [30] Born, G.H., Richards, M.A. and Rosborough, G.W. An empirical determination of the effects of sea state bias on SEASAT altimetry. *J. Geophys. Res.*, Vol.87, pp.3221–3226, 1982.
- [31] Torge, W. *Geodesy An Introduction*. De Gruyter, Berlin, New York, 1980.

- [32] Rothwell, D.A. and Moore, P. The Use of Altimetry as Tracking Data for Precise Orbit Determination. Paper presented at the UKGA-11, University of Durham, April, 1987.
- [33] Mohan, S.N., Bierman, G.J., Hamata, N.E. and Stavert, R.L. Seasat Orbit Refinement for Altimetry Application. *J. Astro. Sci.*, Vol.XXVIII, No. 4, pp.405-417, Oct-Dec., 1980.
- [34] Colombo, O.L. Altimetry, Orbits and Tides, NASA Technical Memorandum 86180, Nov., 1984.
- [35] Engelis, T. On the simultaneous improvement of a satellite orbit and determination of sea surface topography using altimeter data. *Manuscripta Geodaetica*, 13, pp.180-190, 1988.
- [36] Kozai, Y. The Earth Gravitational Potential Derived from Satellite Motion. *Space Science Reviews*, Vol.5, pp.818-879, 1966.
- [37] Gedeon, G.S. Tesseral Resonance Effects on Satellite Orbits. *Cel. Mech.*, Vol.1, pp.167-189, 1969.
- [38] Marsh, J.G. and Williamson, R.G. Precision Orbit Analyses in Support of the Seasat Altimeter Experiment. *J. Astro. Sci.*, Vol.XXVIII, No. 4, pp.345-369, Oct-Dec., 1980.
- [39] Wagner, C.A. Radial Variations of a Satellite Orbit Due to Gravitational Errors : Implications for Satellite Altimetry. *J. Geophys. Res.*, Vol.90, No. B4, pp.3027-3036, March, 1985.
- [40] Engelis, T. Radial Orbit Error Reduction and Sea Surface Topography Determination Using Satellite Altimetry, Report 377, Dept. of Geodetic Science and Surveying, The Ohio State University, Columbus, 1987.
- [41] Cook, G.E. Perturbations of Near-Circular Orbits by the Earth's Gravitational Potential. *Planet. Space Sci.*, Vol.14, pp.433-444, 1966.
- [42] Zandbergen, R.C.A., Wakker, K.F. and Ambrosius, B.A.C. Application of Satellite Altimeter Data to Orbit Error Correction and Gravity Model Adjustment. Paper presented at 27th COSPAR meeting, Espoo, Finland, July, 1988.
- [43] Ponman, T. The analysis of periodicities in irregularly sampled data. *Mon. Not. R. Ast. Soc.*, Vol.196, pp.583-596, 1981.
- [44] Lerch, F.J., Putney, B.H., Wagner, C.A. and Klosko, S.M. Goddard Earth Models for Oceanographic Applications (GEM 10B and 10C). *Marine Geodesy*, Vol.5, No. 2, pp.145-187, 1981.
- [45] Heiskanen, W.A. and Moritz, H. *Physical Geodesy*. Freeman, San Francisco, 1967.
- [46] Sandwell, D.T., Milbert, D.G. and Douglas, D.C. Global Nondynamic Orbit Improvement for Altimetric Satellites. *J. Geophys. Res.*, Vol.91, No. B9, pp.9447-9451, 1986.
- [47] Moore, P. and Rothwell, D.A. A Study of Gravitational and Non-Gravitational Modelling Errors in Crossover Differences. Unpublished.

- [48] Marsh, J.G., Koblinsky, C.J., Lerch, F.J., Klosko, S.M. and Robbins, J.W. Direct use of Satellite Altimeter Data for Orbit Determination, Gravitational Modelling Improvements and Recovery of Dynamic Topography. Paper presented at the 27th COSPAR meeting, Espoo, Finland, 1988.
- [49] Burden, R.L. and Faires, J.D. Numerical Analysis (Third Edition). Prindle, Weber and Schmidt, Boston, 1985.
- [50] Engelis, T. Analysis of Sea Surface Topography using Seasat Altimeter Data. NOAA Contract No. 78-4326, March, 1983.
- [51] Lerch, F.J. and Klosko, S.M. Gravity Model Improvement Using Laser Data : Progress Report. Paper presented at First Crustal Dynamics Working Group Meeting, Goddard Space Flight Center, Greenbelt, MD 20771, Sept., 1981.
- [52] Rapp, R.H. Tidal Gravity Computations Based on Recommendations of the Standard Earth Tide Committee. Paper presented at the XVIII General Assembly of IUGG, Hamburg, 1983.
- [53] Engelis, T. and Knudsen, P. Orbit improvement and determination of the ocean geoid and topography from 17 days of Seasat data. Manuscripta Geodaetica, Vol.14, pp.193-201, 1989.
- [54] Rowlands, D. The Adjustment of Seasat Altimeter Data on a Global Basis for Geoid and Sea Surface Topography Determinations, OSU Report No 325, Columbus, Ohio, 1981.
- [55] Levitus, S. Climatological Atlas of the World Ocean. NOAA Geophysical Fluid Dynamics Lab., Profess. Paper 13, Rockville, Maryland, 1982.
- [56] Walker, J.C.G. Analytic Representation of Upper Atmospheric Densities Based on Jacchia's Static Diffusion Models. J. Atmospheric Sci., July, 1965.
- [57] Bartels, J. The Geomagnetic measures for the time-variations of solar corpuscular radiation, described for use in correlation studies in other geophysical fields. Ann. Int. Geophys. Vol.4., pp.227-236, 1957.
- [58] Slowey, J.W. The geomagnetic variation in the upper atmosphere. Adv. Space Res., Vol.3, pp.67-73, 1983.
- [59] Noomen, R. Aerodynamic drag and geomagnetic perturbations : their modelling and effect on spacecraft dynamics. Technical Thesis, Delft University, 1983.
- [60] Oliver, W.L. A procedure for the efficient calculation of atmospheric density. COSPAR paper II. 2.8, Ottawa, 1982.
- [61] Jacchia, L.G. Thermospheric Temperature, Density and Composition : New Models. SAO, Special Report 375, 1977.
- [62] Hedin, A.E. MSIS-86 Thermospheric Model. J. Geophys. Res., Vol.92, No. A5, pp.4649-4662, 1987.
- [63] King-Hele, D. Satellite Orbits in an Atmosphere, Theory and Applications. Blackie, Glasgow and London, 1987.

- [64] Rothwell, D.A. and Moore, P. The Determination of Relative Effective Atmospheric Densities at 800km using SEASAT Laser Range Data. Planet. Space Sci., to be published.
- [65] Berger, C. and Barlier, F. Response of the equatorial thermosphere to magnetic activity analysed with accelerometer total density data. Asymmetrical structure. J. Atmos. and Terr. Phys., Vol.43, pp.121-133, 1981.
- [66] Rishbeth, H and Garriott, O.K. Introduction to Ionospheric Physics. Academic Press, New York, London, 1969.
- [67] Nisbet, J.S., Stehle, C. and Bleuler, E. Initial tests of an index based on AL Values for modelling magnetic storm related perturbations of the thermosphere. J. Geophys. Res., Vol.88, No. A3, pp.2175-2180, 1983.
- [68] Mortiz, H. Advanced Physical Geodesy, Abacus Press, Tunbridge Wells, Kent, England, 1980.
- [69] King-Hele, D.G., Pilkington, J.A., Hiller, H. and Wakker, D.M.C. The RAE Table of Earth Satellites, 1957-1980. Macmillan Reference Books, London, 1981.

Appendix 1: Definitions Of Orbital Elements And Geometry

Figure A.1

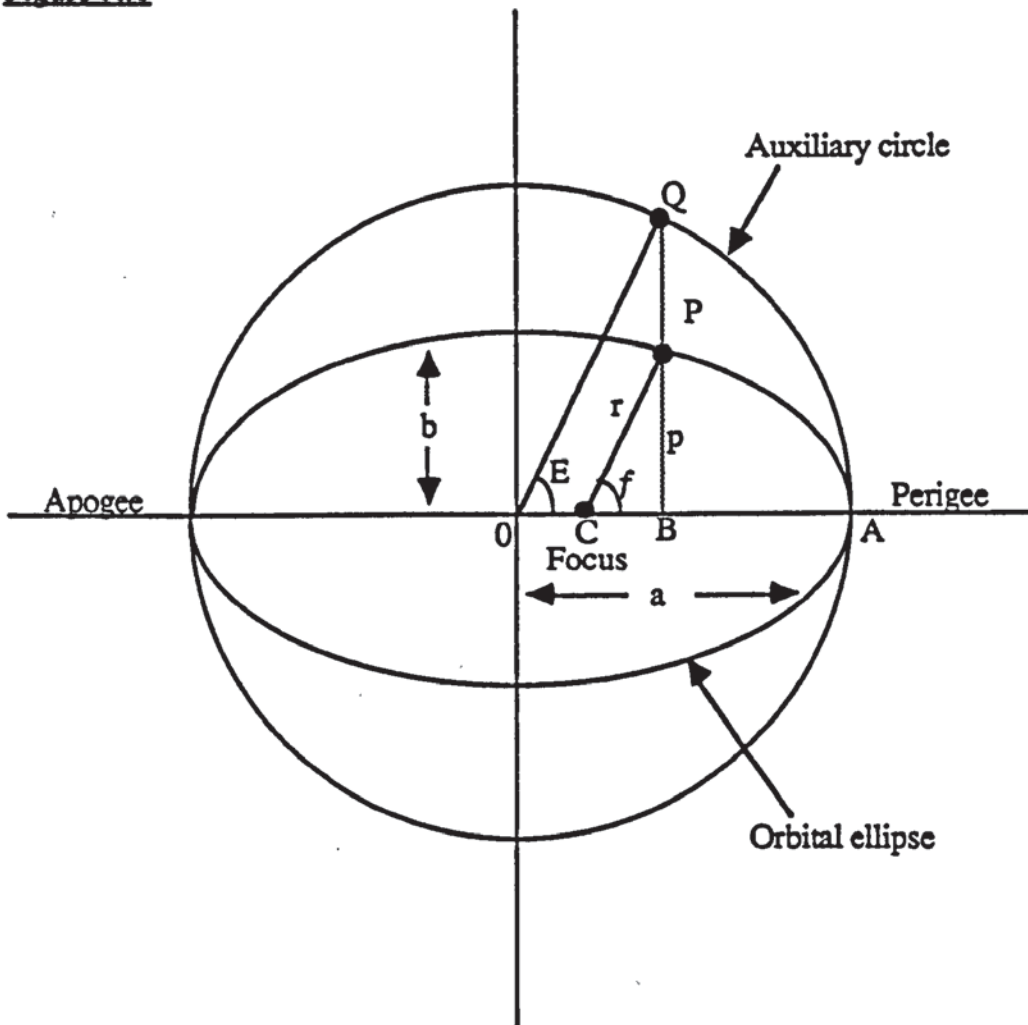


Figure A.1 depicts the orbital ellipse and its associated auxiliary circle of radius a , the length of the semi-major axis. The eccentricity, e , of the ellipse, with focus at C , is defined to be the ratio OC/OA . Hence C is at a distance ae from O , the centre of the auxiliary circle. A point, P , on the ellipse can be identified using two quantities, r and f , as shown where

$$r = \frac{p}{1 + e \cos f} \quad (A.1)$$

The angle f is termed the true anomaly of the point, P ; p is the semi-latus rectum, equal to $a(1 - e^2)$. If BP is projected vertically upwards, it intersects the auxiliary circle at a point Q . The angle $\hat{A}OQ$ defines the eccentric anomaly, E .

Assuming the point P moves round the ellipse in time T , the period of the motion, the mean motion, n , is defined by

$$n = 2\pi/T. \quad (\text{A.2})$$

If the time of perigee passage is τ then after a time interval $t - \tau$, the point P will have swept through an angle f . However, if the rate this angle had been swept out, was equal to n , then it would be different from f . This angle is denoted by M and is called the mean anomaly. Mathematically,

$$M = n(t - \tau). \quad (\text{A.3})$$

Figure A.2

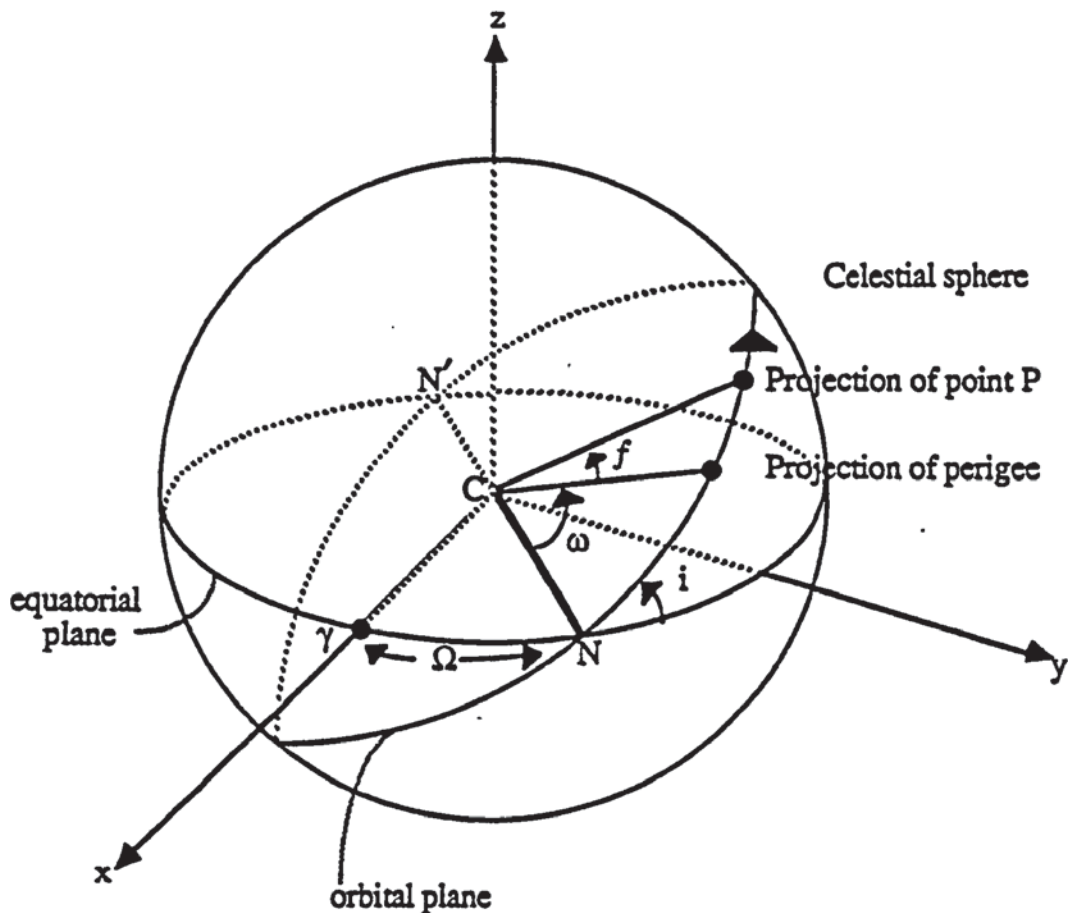


Figure A.2 depicts the orientation of the orbital plane relative to the equatorial plane of the earth. The x -axis points along the direction to the First Point of Aries, γ , a fixed point on the celestial sphere. The y - and z -axes are constructed so that z points to the North Pole and all three axes form a right handed system. NN' defines the line of nodes, the intersection of the orbital plane with the equatorial plane, N ,

being the ascending node, N' the descending node. The angle $\gamma^{\wedge}CN$ defines Ω , the argument of the ascending node whilst the inclination, i , is given by the angle between the equatorial and orbital planes. The argument of perigee, ω , is the angle between N and the projection of perigee onto the celestial sphere, as shown. Hence the point P can be identified by six quantities called Keplerian elements. They are a , e , M , Ω , ω and i . The first three elements relate to the size and shape of the orbital ellipse as well as the position within this ellipse. The latter three elements relate to the orientation of this ellipse in space. Such a set of Keplerian elements is not unique.

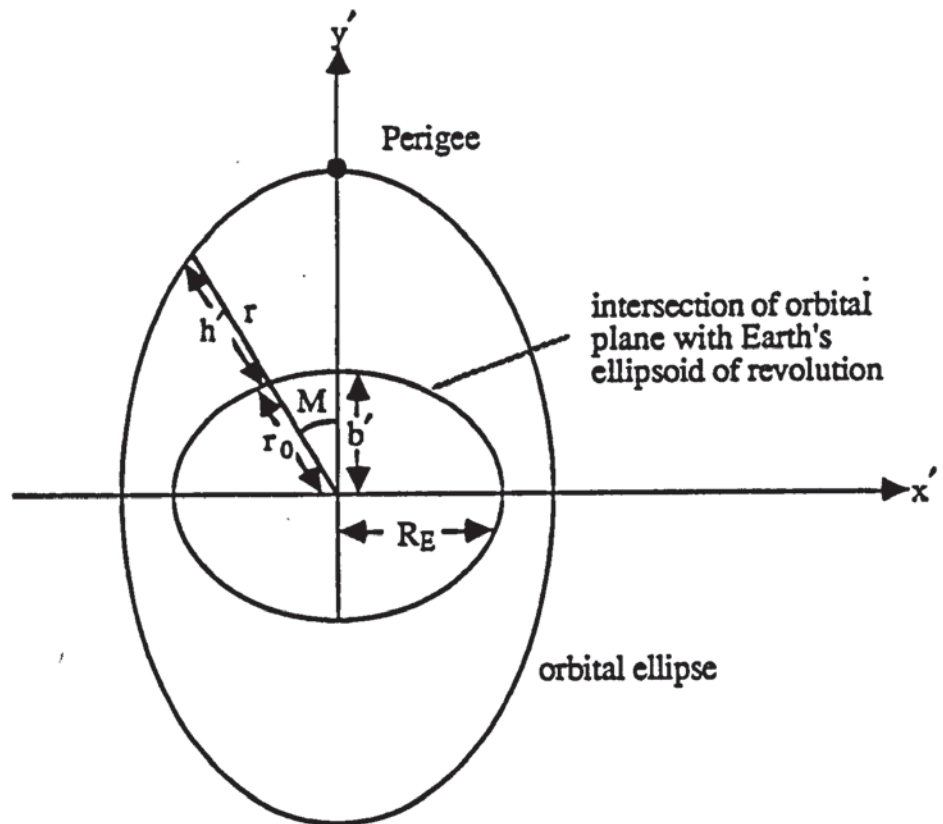
Figure A.3

Figure A.3 shows in simple form, the orbital ellipse in relation to an ellipsoidal section through the earth. For a near circular orbit with perigee frozen at $\pi/2$ r is given by

$$r \approx a(1 - e \cos M) \quad (\text{A.4})$$

where a is the semi-major axis of the orbital ellipse of eccentricity e . M is the mean anomaly (approximately equal to the angle shown in the diagram). Then from Figure A.3

$$h' \approx r - r_0 \quad (\text{A.5})$$

where h' is the radial height of the orbit above the earth's surface with r_0 as shown. Note that h' is not as measured by the altimeter height which is effectively normal to the ellipsoid of revolution. However, for a first order analysis it is assumed that h'

is the measured altimeter height. The equation of the section through the Earth's ellipsoid shown in Figure A.3 is

$$\frac{x'^2}{R_E^2} + \frac{y'^2}{b'^2} = 1 \quad (\text{A.6})$$

where $x' = r_0 \sin M$ and $y' = r_0 \cos M$. Substituting these into equation (A.6) and solving for r_0 yields

$$r_0 = \frac{R_E b'}{(b'^2 \sin^2 M + R_E^2 \cos^2 M)^{\frac{1}{2}}} \quad (\text{A.7})$$

From equations (A.4), (A.5) and (A.7)

$$h' = a(1 - e \cos M) - \frac{R_E b'}{(b'^2 \sin^2 M + R_E^2 \cos^2 M)^{\frac{1}{2}}} \quad (\text{A.8})$$

It is desired to find the number of maxima and minima in the error function $\Delta h'$ of h' , due to an error in the time tag of the altimeter measurements, Δt . Now

$$M = nt \quad (\text{A.9})$$

so that $\Delta M = n\Delta t$. Therefore

$$\Delta h' \approx a \sin M (n\Delta t) + R_E \frac{b' \sin M \cos M (b'^2 - R_E^2)}{D^{\frac{3}{2}}} (n\Delta t) \quad (\text{A.10})$$

where $D = b'^2 \sin^2 M + R_E^2 \cos^2 M$. The maxima and minima of $\Delta h'$ are found by

differentiating with respect to t and equating to zero. Hence

$$\begin{aligned} \frac{d}{dt} (\Delta h') &= -a e \cos M \Delta M n + \frac{R_E b' \cos 2M (b'^2 - R_E^2)}{D^{\frac{3}{2}}} \Delta M n \\ &\quad - \frac{3}{4} (b'^2 - R_E^2) \frac{\sin^2 2M R_E b'}{D^{\frac{5}{2}}} \Delta M n \equiv 0. \end{aligned} \quad (\text{A.11})$$

Assuming $D \approx R_E^2$ (since the Earth is spherical to first approximation) and e small, equation (A.11) can be written

$$0 = \frac{b'(b'^2 - R_E^2)}{R_E^2} \Delta M \left[\cos 2M - \frac{3}{4} \left(\frac{b'^2 - R_E^2}{R_E^2} \right) \sin^2 2M \right] \quad (\text{A.12})$$

or

$$0 = \frac{b'(b'^2 - R_E^2)}{R_E^2} \Delta M \left[\frac{3}{4} \left(\frac{b'^2 - R_E^2}{R_E^2} \right) (\cos^2 2M - 1) + \cos 2M \right]. \quad (\text{A.13})$$

Equation (A.13) has solution

$$\cos 2M = \frac{-1 + \sqrt{1 + 4K^2}}{2K} \quad (\text{A.14})$$

taking the + sign only, where $K = \frac{3}{4} \left(\frac{b'^2 - R_E^2}{R_E^2} \right)$.

Therefore there are four stationary points as M travels through one orbital revolution. From equation (A.11) it can be shown that for $\Delta M > 0$

$$\begin{aligned} \frac{d}{dt} (\Delta h') &< 0 && \text{for } M = 0 \\ \frac{d}{dt} (\Delta h') &> 0 && \text{for } M = \pi/2 \\ \frac{d}{dt} (\Delta h') &< 0 && \text{for } M = \pi \\ \text{and} \quad \frac{d}{dt} (\Delta h') &> 0 && \text{for } M = \frac{3\pi}{2} \end{aligned}$$

with the converse for $\Delta M < 0$.

Hence these four stationary points define maxima and minima, two of each. Thus a time tag error on the altimeter measurements manifests itself in the form of a twice per revolution radial error.

Appendix 3: Helmert-Wolf Blocking

This method is used to determine a number of arc-independent parameters from multiple arcs by removing from each arc the dependent parameters.

Assume that the normal equations from a particular arc, k , can be written as

$$N^{(k)}\Delta\mathbf{x} = \mathbf{b}^{(k)} \quad (\text{A.15})$$

where $N^{(k)}$ is the matrix of partial derivatives, $\Delta\mathbf{x}$ the vector of corrections (to be determined) and $\mathbf{b}^{(k)}$ is the vector involving the residuals. [See equation (3.19) for a full definition of the normal equations.] Then equation (A.15) can be separated into arc-dependent (inner) parameters and arc-independent (outer) parameters thus

$$\begin{pmatrix} N_{II} & N_{I0}^T \\ N_{I0} & N_{00} \end{pmatrix}^{(k)} \begin{pmatrix} \Delta\mathbf{x}_I^{(k)} \\ \Delta\mathbf{x}_0 \end{pmatrix} = \begin{pmatrix} \mathbf{b}_I^{(k)} \\ \mathbf{b}_0 \end{pmatrix} \quad (\text{A.16})$$

with I denoting the inner parameters and 0 the outer parameters. Expanding (A.16) gives

$$N_{II}^{(k)} \Delta\mathbf{x}_I^{(k)} + N_{I0}^{T(k)} \Delta\mathbf{x}_0 = \mathbf{b}_I^{(k)} \quad (\text{A.17})$$

$$N_{I0}^{(k)} \Delta\mathbf{x}_I^{(k)} + N_{00}^{(k)} \Delta\mathbf{x}_0 = \mathbf{b}_0^{(k)} \quad (\text{A.18})$$

From equation (A.17)

$$\Delta\mathbf{x}_I^{(k)} = \left(N_{II}^{(k)}\right)^{-1} \left(\mathbf{b}_I^{(k)} - N_{I0}^{T(k)} \Delta\mathbf{x}_0\right) \quad (\text{A.19})$$

since $N_{II}^{(k)}$ is invertible, and on substituting (A.19) into (A.18)

$$N^{*(k)} \Delta\mathbf{x}_0 = \mathbf{b}^{*(k)} \quad (\text{A.20})$$

where $N^{*(k)} = \left(N_{00} - N_{I0} N_{II}^{-1} N_{I0}^T \right)^{(k)}$ and $\underline{b}^{*(k)} = \left(\underline{b}_0 - N_{I0} N_{II}^{-1} \underline{b}_I \right)^{(k)}$.

The combination of the normal equations from each arc, k , is then simply performed by adding all the $N^{*(k)}$ matrices and all the $\underline{b}^{*(k)}$ vectors, respectively, so that

$$\left(\sum_k N^{*(k)} \right) \Delta \underline{x}_0 = \sum_k \underline{b}^{*(k)} \quad (\text{A.21})$$

which yields the solution

$$\Delta \underline{x}_0 = \left(\sum_k N^{*(k)} \right)^{-1} \left(\sum_k \underline{b}^{*(k)} \right). \quad (\text{A.22})$$

United Kingdom Geophysical Assembly - 11

University of Durham - April 1987

THE USE OF ALTIMETRY AS TRACKING
DATA FOR PRECISE ORBIT DETERMINATION

D A Rothwell and P Moore

Earth Satellite Research Unit
Department of Computer Science & Applied Mathematics
Aston University
United Kingdom

The University of Aston in Birmingham
Precise Orbit Determination and Analysis
from Satellite Altimetry and Laser Ranging
D.A.Rothwell
Doctor of Philosophy
1989

Abstract

Precise orbit determination is becoming increasingly a pre-requisite for optimal utilisation of satellite-borne experimentation.

The most accurate tracking data of satellites is obtained by laser ranging, but for long-arc determination a good geographical distribution of ground stations is essential. For satellites carrying an altimeter as well as laser retro-reflectors the altimeter data can be used to supplement the laser data in the dynamical solution. Results of experiments will be presented using laser and altimeter data from SEASAT. Selection criterion and appropriate weighting for the data will be discussed. In particular it will be seen that accurate ephemerides can be obtained from a limited number of laser passes supplemented with altimeter data. Applications to ERS-1 will be discussed.

1. Introduction

Precise orbit determination is rapidly becoming a pre-requisite for many oceanographic and geodetic purposes. For example the European remote sensing satellite, ERS1, and the polar platform of Columbus will demand high accuracies in satellite positioning, particularly the radial measurement, during the next decade. Accuracy of satellite ephemerides depends not only on expertise in modelling orbital perturbations but also on a global distribution of high quality tracking data.

Of the tracking data available, the laser ranger is the most precise with current range measurements accurate to within 5cm. Unfortunately laser ranging is expensive, restricted by weather and occasional operational problems, whilst the distribution of sites gives incomplete global coverage. It is important to recognise that, although a computed orbit may fit the tracking data in the sense that the range residuals are 'small', the true orbit may differ appreciably from the computed orbit particularly over regions of the world where no tracking data is available. The rms of fit of tracking data is effectively a measure of local rather than global accuracy, especially for sparse data.

Other tracking data include unified S-band range-rate measurements. These have the advantage of all weather capability but the precision is downgraded by atmospheric effects. Doppler data derived from an extensive global network of stations is an alternative to the above types but again the accuracy is impaired by atmospheric refraction.

For satellites carrying a radar altimeter it has been demonstrated (Wakker et al, 1983) that altimeter measurements over the sea surface can be used as tracking data. The altimeter measures the satellite height to the instantaneous sea surface. Although theoretically accurate to near 10cm the measurement relative to a reference ellipsoid, as required

for precise orbit determination, involves knowledge of the mean sea-surface height, ie the geoid. Quoted accuracies for the geoid eg GEM10C (Lerch et al, 1981) are in the order of 1m rms, but individual values may be in error by 5m or more over ocean mounts or trenches. Effectively altimetry is a radial measurement although along-track orbital information is derived by frequent sampling of the available data set. No cross-track information can be recovered, however. In the following experiments altimeter data is used to supplement laser range data for Seasat (7806401) for both long and medium arcs. It will be seen, in confirmation of the results obtained by Wakker et al (1983), that sparse laser data augmented by altimeter data can give orbital accuracies comparable to those derived from an extensive network of laser-ranging sites.

Seasat was the first satellite launched specifically for oceanographic monitoring and represented a proof-of-the-concept mission. During its 78 day operational life before a short-circuit terminated all activity, the satellite relayed an unparalleled quantity of data from on-board instrumentation, including the altimeter. Launched on 26 June 1978, the satellite orbited at an inclination of 108° , at a height of near 790 km. Initially the satellite was placed into an orbit, the so-called launch orbit, that nearly repeated its ground-track every 17 days. A series of manoeuvres initiated on 18 August and completed on 10 September gave a precise repeat ground-track of period 3 days. The arc selected for analysis corresponds to the launch orbit.

2. Computational Procedure

Analysis was undertaken by implementation of the SATAN satellite analysis software produced at the RGO (Sinclair and Appleby, 1986) and modified at Aston University. Computation within the package is by means of a Gauss-Jackson 8th order numerical integrator using a step-length of 0.5 min in this instance. The package is implemented on a VAX 8650. The computational model is in strict accordance with the MERIT standards (Melbourne et al, 1983)

and is summarised in Table 1.

For experimental purposes data was selected for a 5 day period corresponding to the 17 day repeat orbit. The five day arc MJD 43728-MJD 43733 exhibited fair global coverage with data from 8 laser stations, with data from Arequipa available for at least 2 passes/day. Two types of orbit were considered, namely long-arcs and medium arcs. Typically a long-arc is of length several days or more, the incomplete tracking data necessitating arcs of this length. This places considerable burden on orbital modelling, particularly the gravity field and atmospheric drag. A medium arc, here defined to be of length of a few revolutions of the satellite, depends to a greater extent on the availability of dense tracking data and is less susceptible to dynamic modelling errors.

Given that the true orbit is unknown a reference orbit for comparative purposes was computed using the laser-range data and criteria summarised in Table 2. The data per pass was restricted by regular sampling to give a degree of equality between stations and passes. A priori observational standard deviations (sd) were ascribed to the stations in accordance with the accepted accuracies of the data in 1978. The NASA stations were the most accurate whilst the European and SAO stations were each ascribed accuracies of 70cm except for Arequipa where 50cm was assumed. The rms range residuals after fit testify to the greater reliability of the NASA stations. At the time of computation the Orroal data had not been corrected for the range-dependent error resulting from incorrect instrumentation (Latimer 1979).

For each long-arc computation a state vector at epoch, 5 daily drag coefficients, and a solar reflectivity coefficient were estimated. The estimation of daily drag coefficients is an artificial device to give a good degree of fit, however its use can be easily justified. The computational model utilised a constant area to mass ratio for air-drag and solar radiation. Given the time dependence of the space-craft geometry the assumption of uniformity is clearly inappropriate. However, the model allows for estimation of daily drag

coefficients is not the uncertainty in the effective cross-sectional area but deficiencies in the atmospheric model associated with short-term disturbances particularly those indicated by variations in the geomagnetic indices Ap or Kp. Without these extra degrees of freedom the rms for the laser range residuals is unrealistically high. Figure 1 shows the orbital differences between the reference orbit and an orbit computed using the same data but where only a single drag coefficient was adjusted.

3. Altimetry and precise orbit determination

To utilise altimeter measurements as tracking data corrections for atmospheric refraction, ocean tides, atmospheric pressure, the geoid etc. are applied to the processed altimeter data. All corrections were taken from the Seasat Geophysical Data Record (GDR) tape unless stated otherwise. In particular the so called GEM-10BD geoid was used. During its operational life the altimeter on Seasat yielded an unequalled amount of data. Used in its entirety the data would dominate the solution unless a minute weight was assigned. For some applications, eg gravity field determination, regular sampling of the altimeter data may lead to correlations with short-wavelength geoidal model errors. This is not a problem if only a state vector and drag and solar reflectivity coefficients are solved for. In the subsequent computations altimeter data was selected at least 1 or 2 minutes apart, although 0.5 min and 10 min intervals were used on occasions. The total number of data points at the sampling intervals is summarised in Table 2. Also given there is an indication of the number of altimeter data points processed; the actual number will depend on the weighting strategy and the quality and quantity of the laser data.

To illustrate the effect of augmenting sparse laser tracking data an orbit was computed using the 11 passes from Arequipa. Comparison against the reference orbit, computed by attaching zero weight or infinite s.d. to the altimeter data, is summarised in Table 3. Surprisingly, the orbital differences were relatively small particularly in the radial and cross-track directions. Augmenting the laser data with altimeter data leads to a substantial improvement along track and, to a lesser extent, cross-track. Computations using various observational standard deviations are summarised in Table 3.

Decreasing the observational standard deviation from 2m to 1m, that is placing a greater emphasis on the altimeter data, leads to over 15% improvements in the along-track and cross-track directions although the radial accuracy worsens. For the computation with a sampling interval of 10 min the observational standard deviation was increased to 0.44m to give equality of weighting with altimeter data at 1 min interval and sd 1.4m. The computed orbits are nearly identical with max/rms differences between the orbits of 0.08/0.03; 1.05/0.21; 0.02/0.01 metres respectively in the radial, along-track and cross-track orbital directions.

Figure 2 typifies the orbital differences.

A more stringent test on the influence of altimetry was provided by deletion of the second of three passes on MJD 43730. The computations using just the 10 remaining passes over Arequipa and altimeter data are summarised in Table 4. Using only the laser data the orbit differs by 2.55m and 24.8m rms from the reference orbit in the radial and along-track directions. Processing altimeter data yields substantial improvement in the orbit. The along-track improvement is further qualified by the observation that 3 of 5 daily drag coefficients for the orbit derived from just laser data are negative; a situation remedied by adding altimeter data.

The drag coefficients are discussed further in Chapter 5.

Inspection of Table 4 reveals that the orbital differences decrease as the observational standard deviations are reduced. For a standard deviation of 0.5m the altimeter and laser data points are each of equal weight, whilst the ratio of altimeter to laser range measurements is of the order 10:1. Despite the predominance of altimetry the laser range measurements are still able to constrain the inclination, i , and right ascension of the ascending node, Ω , ie the cross-track orbital elements. However, when the a priori standard deviation for the altimeter was set at 0.1m the laser data had minimal effect and the computer run failed to converge. Comparison of iterations exhibited a strong-oscillation cross-track indicative of data yielding only radial and along-track information.

Three computer runs were undertaken using different sampling strategies for the altimeter data but with the observational standard deviation adjusted accordingly to compensate for the varying quantity of data. The results identified by an asterisk in Table 4 exhibit remarkable similarity. In detail, a comparison of the results using 1 and 10 min sampling periods yielded maximum differences of 0.14m, 2.31m and 0.01m respectively in the radial, along-track and cross-track direction; the rms difference being 0.52m along-track. Evidently, within certain bounds, it is the effective weighting of altimetry to laser range data that is important, rather than the sampling frequency of the altimeter data set. Figure 3 illustrates the orbital differences for altimetry and 10 passes of 7907 data relative to the reference orbit.

4. The geoid

Inaccurate knowledge of the geoid is the principle source of error in the altimeter tracking data. Throughout the computations the GEM-10BD geoidal heights, as available on the GDR tape, were utilised. The so-called GEM-10B detailed geoid is based on the GEM-10B gravity field (Lerch et al, 1981) augmented by $1^\circ \times 1^\circ$ gravimetric data. As an alternative to GEM-10BD, geoidal heights derived from PGS-S3 were used in one experiment. PGS-S3 (Lerch et al, 1982) was computed by combining the gravity model normal equations for GEM-10B, which included GEOS3 altimetry, with Unified S Band and laser tracking data for Seasat. The more refined PGS-S4 gravity field, derived by supplementing the PGS-S3 normal equations with Seasat altimetry, was not available at Aston at the time of writing.

The degree of fit of the altimeter measurements to the reference orbit using GEM-10BD and PGS-S3 was obtained by assigning infinite observational standard deviation, ie zero weight, to the altimeter data. The results of Table 5 give the rms of fit of the altimeter measurements, this value being the rms difference of the computed height minus the observed height of the satellite above the geoid, with all residuals in excess of 7m deleted. Contributions to the rms of fit arise from both radial errors in the derived satellite position and to errors in the applied corrections. The results using PGS-S3 are significantly better in the rms of fit and the number of altimeter data points within $\pm 7m$ of the reference orbit. Wakker et al (1983) showed similar improvement with the PGS-S4 geoid. The latter is more expected given the use of Seasat altimetry within its formulation.

Further experiments were undertaken to quantify the effect of altimetry on sparse laser tracking data when the geoid, and other corrections, are known precisely or exhibit a random error. Using the reference orbit a set of altimeter data residuals was computed. When added to the observed

measurements a data set called 'exact altimetry' was constructed, with zero rms error relative to the reference orbit .

Orbits were computed with the exact altimeter data set and only 5 passes of 7907 laser data; the passes one for each day of MJD 43728-MJD 43733, being selected to lie as near midday as possible. The results are summarised in Table 6 and illustrated in figure 4. It is seen that for exact altimeter measurements, ie geoid known precisely, excellent ephemerides can be derived from a small number of laser passes. Modifying the exact altimeter data set by allowing for a random error of rms 0.6m, i.e. $\pm 1m$, resulted in negligible change. Although hyperthetical and idealistic, these results indicate the level of accuracy achievable with sparse laser tracking when the geoidal height, is known to within the tolerance of the altimeter.

5. Drag and Solar reflectivity coefficients

Estimation of drag coefficients within the data reduction procedure absorbs along-track modelling errors that result from deficiencies in the gravity field as well as errors in the atmospheric model and effective cross-sectional area. Daily drag coefficients and the solar reflectivity coefficient derived in the aforementioned data reductions are summarised in Table 7. The high correlations between the estimated daily drag coefficients and the along-track orbital differences of figures 2-4 is self-evident. Little variation is observed in the solar-reflectivity coefficient.

6. Medium-length arcs

To investigate the influence of altimetry on arcs over shorter periods two medium-length arcs were selected from the five day long arc, the tracking data being summarised in Table 8. Each arc of time span 0.2 day was approximately 2.75 orbital revolution, Seasat having orbital period 104 min. For each arc a state vector at epoch was estimated; the drag coefficient and solar reflectivity coefficient being taken from the long-arc solution.

The small number of altimeter measurements necessitated relatively high weights to affect the data reduction procedure. Accordingly observational standard deviations of 0.5m or 0.1m were ascribed to the altimeter data.

Orbital differences relative to the long-arc solution for the various weighting strategies are summarised in Table 9 and illustrated in figure 5. Again the influence of altimetry is positive leading to substantial improvements in the radial and along-track directions. Inspection of Table 9 reveals that decreasing the observational standard deviation leads to contradictory results. This may be coincidental and anyway is not considered significant along-side the overall improvement. However, it must be remembered that arcs of this length are more susceptible to vagaries in the tracking data than long-arcs.

7. Conclusions and applications to future altimetry missions

eg ERS 1

- (1) The usefulness of the altimeter as a tracking device has again been demonstrated. Long-arc solutions determined from tracking data from one or two laser stations augmented with altimeter data closely approximate orbits generated from a dense network of laser sites. As the gravity fields tailored for Seasat yield radial errors of order 1m rms the differences in Table 3 are not significant. The short-periodic differences of figures 2-4 are once per revolution effects, the long-periodic differences the effect of variations in the daily drag coefficients.
- (2) The geoidal height corrections are well-known to be the principle error in altimeter tracking data. More accurate geoid models would greatly improve the practicability of altimetry for precise orbits. The PGS-S3 geoid derived from the gravity field of that name is apparently more accurate, at least for the ground-track of Seasat, than the GEM-10BD geoid tabulated on the Seasat GDR tape. Experiments using exact altimetry establish that a few passes of laser data from one station and precise altimetry at say 1 min intervals yields minimal radial error.
- (3) Altimetry improves the along-track determinations and daily drag coefficient 'estimation' for long-arc solutions.
- (4) Altimeter tracking data can have significant implications for precise orbit determinations over arc-lengths of a small number of orbital revolutions.

(5) The optimum weighting strategy for the altimeter and laser data is a complex issue dependent on several orbit related specifications, notably the quality, quantity and distribution of the laser tracking data and the accuracy of the geoid along the satellite ground-track. However, the sampling interval appears to be unimportant as near identical orbits can be derived by adjusting the weight of the altimeter measurements accordingly.

(6) The empirical approach adopted in this study is invaluable for insight into the utilisation of altimetry as tracking data. Future studies could investigate errors in the radial and along-track directions perhaps using the correlation-covariance matrices of the data reduction procedure.

Acknowledgements

The authors wish to express their gratitude to Andrew Sinclair and Graham Appleby, RGO, Herstmonceux for the original version of the SATAN software; to Delft University of Technology for supplying the laser tracking data and to the Institute for Oceanographic Sciences, Bidston for the altimeter data.

References

- J H Latimer, Smithsonian Astrophysical Observatory, Letter to investigators using laser data from Orroral, September 1979.
- F J Lerch, B H Putney, C A Wagner and S M Klosko (1981), Goddard Earth Models for Oceanographic Applications (GEM 10B and 10C), Marine Geodesy, 5, 145.
- F J Lerch, J G Marsh, S M Klosko and R G Williamson (1982), Gravity Model Improvement for Seasat, J Geophys. Res., 87, 3281.
- W Melbourne, R Anderle, M Feissel, R King, D McCarthy, B Tapley and R Vicente (1983), Project MERIT Standards, U.S. Naval Obs. Circular No 167.
- A T Sinclair and G M Appleby (1986) SATAN-Programs for the Determination and Analysis of Satellite Orbits from SLR Data, SLR Tech. Note No.9, RGO, Hertmanceusc.
- K F Wakker, B.A.C. Ambrosius and L Aardoom (1983) Precise Orbit Determination for ERS 1, Delft University of Technology, The Netherlands.

Table 1

The SATAN computational model utilised in the Seasat analysis.

Force model and constants

Gravity field PGS-S3

$$a_e = 6378.138 \text{ Km}; GM = 398600.64 \text{ Km}^3/\text{s}^2; C = 299792.458 \text{ Km/s}$$

Atmospheric model Jacchia 1971

$$S = 25.3\text{m}^2, \quad m = 2216.7 \text{ Kg}$$

Third body attraction (sun, moon and planets) JPL DE-96 ephemeris.

Solar radiation (direct, Earth reflected and infra-red radiation)

$$S = 25.3\text{m}^2; \text{ pressure at 1 AU} = 4.5605 \times 10^{-6} \text{ N/m}^2$$

Body Tides

Force $K_2 = 0.3$, Wahr's frequency dependence

Station displacement $h_2 = 0.609$, $l_2 = 0.0852$

Ocean Tides $S_{SA}, M_m, M_f, Q_1, O_1, P_1, K_1, N_2, M_2, S_2, K_2$

Schwiderski amplitudes and phases.

Nutation Wahr

Polar motion and UTI data BIH

Parameters estimated

State vector at epoch

Daily drag coefficients, C_D

Solar reflectivity coefficient, C_R

Table 2

Laser data summary. Reference arc

MJD 43728 - MJD 43733

Maximum no. of observations/pass 55

Rejection criterion 5m

Station No.	Location	No of Passes	Total no of observations/ observations processed	rms range residual after fit (m)	a priori sd (m)
7062	Otay	10	886/414	0.56	0.15
7067	Bermuda	6	297/114	0.82	0.15
7069	Patrick AFB	5	996/241	0.64	0.15
7907	Arequipa	11	458/438	1.71	0.50
7801	Helwan	3	98/35	2.09	0.70
7833	Kootwijk	2	50/50	1.52	0.70
7929	Natal	1	12/12	0.97	0.70
7943	Orroral*	4	116/53	3.41	0.70

* not corrected for known range dependent error.

Altimeter data summary.

Rejection criterion 7m

Sampling interval (min)	Total no of data points	Approx. no processed (orbit dependent)
1	5785	4000
2	3040	2000
10	645	440

Table 3

Summary of orbital differences between orbits computed from altimetry and 11 passes of Arequipa laser range data and the reference orbit. 458 laser range measurements processed.

Altimeter sd (m)	data sampling interval (min)	Orbital differences radial (m)	max/rms differences along-track (m)	cross-track (m)
∞	-	1.22/0.57	27.57/7.62	1.41/0.96
2.0	1	1.10/0.50	20.45/5.38	1.23/0.83
1.4	1	1.17/0.53	18.43/4.79	1.15/0.78
1.0	1	1.23/0.55	16.85/4.38	1.05/0.71
0.44	10	1.18/0.53	18.79/4.74	1.13/0.76

Table 4

Summary of orbital differences between orbits computed using 10 passes(425 observations) of Arequipa laser range data with altimetry and the reference orbit.

sd (m)	Altimeter data Sampling interval (min)	Orbital differences max/rms		
		radial (m)	along-track (m)	cross-track (m)
∞	-	5.66/2.55	117.2/24.81	0.95/0.66
2	1	1.62/0.68	29.85/6.24	1.13/0.77
* 1.4	1	1.41/0.60	21.69/4.90	1.09/0.74
1.0	1	1.32/0.58	17.43/4.32	1.00/0.68
0.5	1	1.35/0.60	12.01/3.64	0.52/0.35
* 1.0	2	1.36/0.61	19.83/4.68	1.08/0.73
* 0.44	10	1.46/0.61	21.31/4.82	1.10/0.74

* equivalent weighting of altimeter data relative to laser range data

Table 5

Effect of the adopted geoid on the altimeter measurement residuals.
 (All residual in excess of 7m discarded)

Geoid	Altimeter sd (m)	data Sampling interval (min)	Observations	rms of fit of altimeter data (m)
PGS-S3	∞	2	2086	2.28
GEM-10BD	∞	2	2027	2.69

Table 6

Summary of orbital differences between orbits computed from exact altimetry and 5 passes (221 observations) of Arequipa laser data and reference orbit

	sd (m)	Altimeter data sampling interval (min)	Orbital differences radial	Orbital differences along-track	max/rms cross-track
Exact altimetry	1	2	0.26/0.08	9.77/4.30	0.30/0.20
	2	2	0.84/0.23	27.13/6.60	0.25/0.16
Random error (rms-0.60m)	2	2	0.87/0.23	28.07/6.68	0.28/0.18

Table 8 Summary of data for medium-arc analyses

ARC 1 MJD 43729.0 - MJD 43729.2

Laser range data

Station	observations	a priori sd (m)	span of observations (MJD 43729)(days)
7067	9	0.15	0.0287-0.0302
7907	18	0.50	0.0371-0.0395
7062	54	0.15	0.1689-0.1708

Altimeter data: 2 min interval, 10m rejection level 92 observations

ARC 2 MTD 43730.0 - MJD 43730.2

Laser range data

Station	observations	a priori sd (m)	span of observations (MJD 43730)(days)
7067	51	0.15	0.0053-0.0095
7907	47	0.50	0.0134-0.0190
7069	55	0.15	0.0753-0.0795
7062	34	0.15	0.1457-0.1468

Altimeter data: 2 min interval, 10m rejection level 69 observations

Table 9 Summary of orbital differences between medium arc solutions and reference arc.

	Altimeter data sd (m)	radial (m)	Orbital differences along-track (m)	max/rms cross-track (m)
ARC 1	∞*	2.89/1.96	11.80/5.79	6.37/4.41
	0.5	0.86/0.53	3.45/1.79	4.79/3.32
	0.1	0.70/0.44	3.20/1.43	3.56/2.55
ARC 2	∞*	1.79/1.22	7.24/4.40	1.79/1.25
	0.5	0.61/0.40	2.43/1.31	1.46/1.01
	0.1	0.98/0.62	3.51/1.58	2.88/1.99

* zero weight altimetry

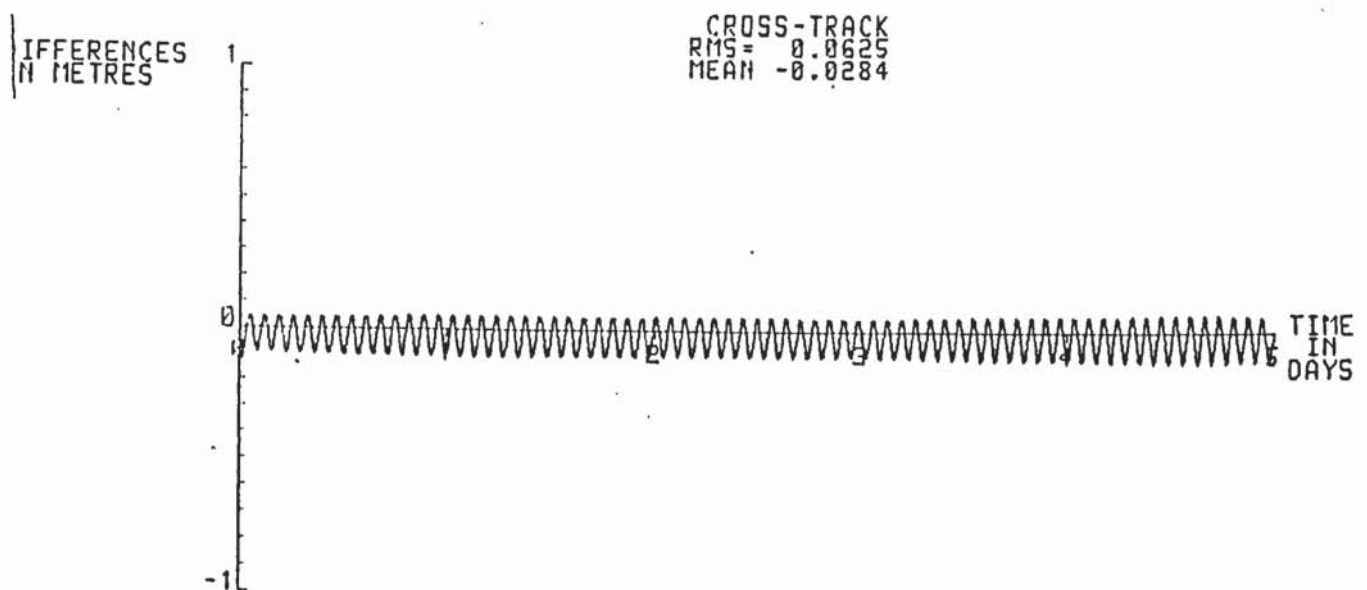
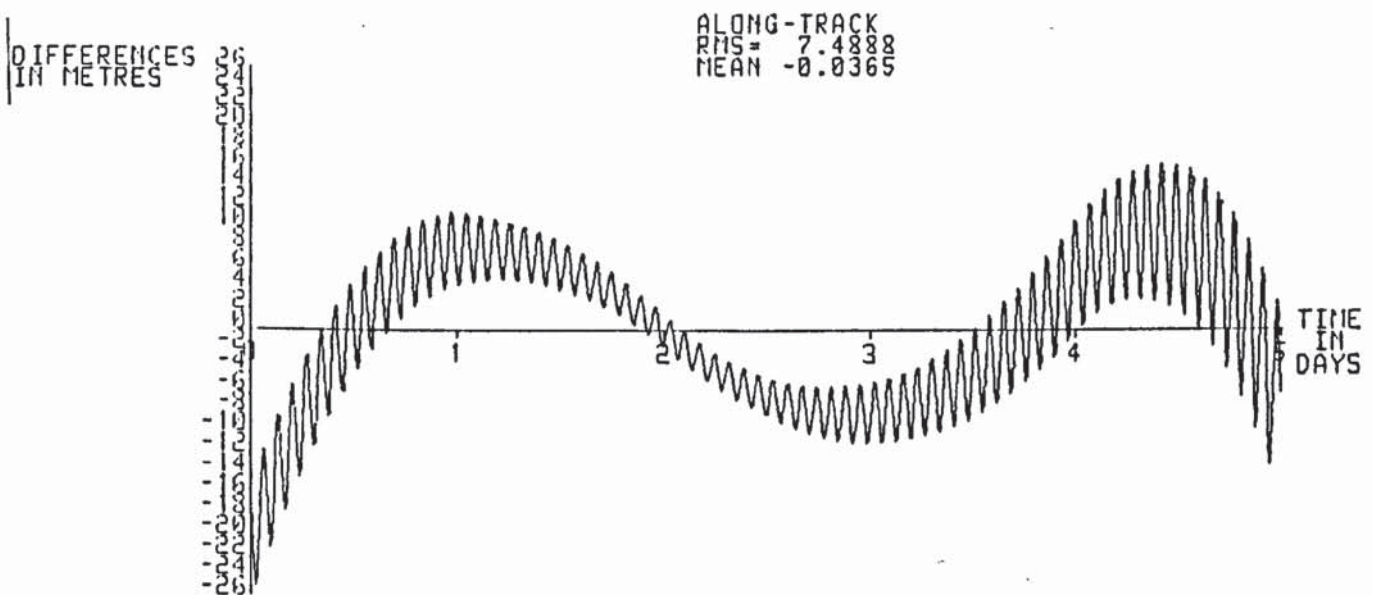
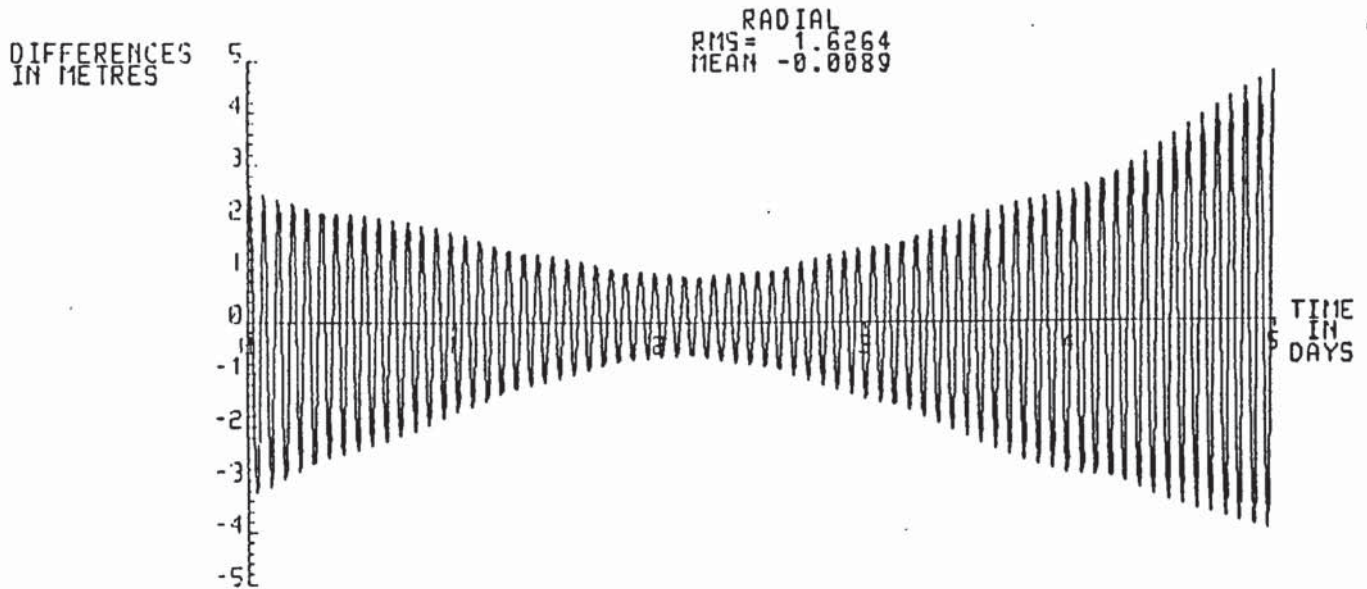
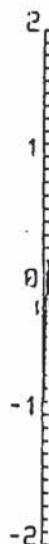
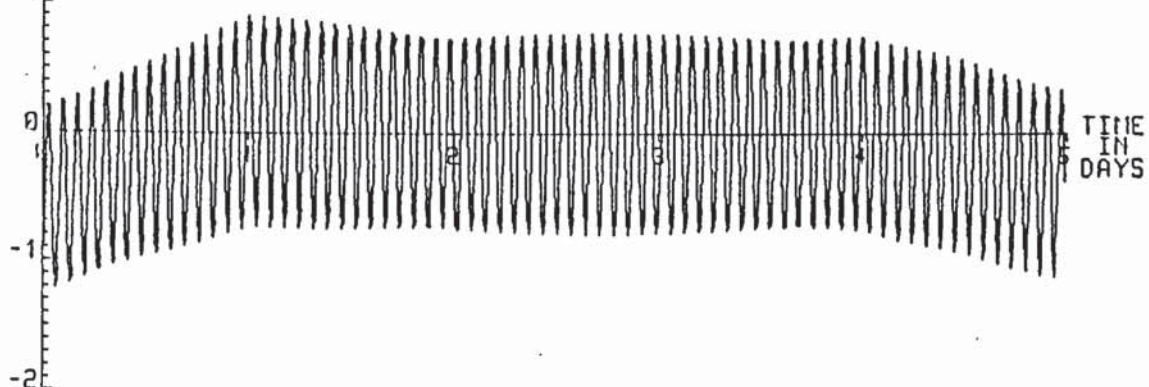


Figure 1: The radial, along-track and cross-track differences for an orbit computed using a single drag coefficient versus the reference orbit with daily drag coefficients.

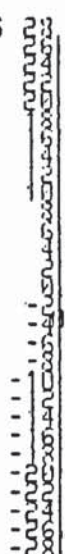
DIFFERENCES
IN METRES



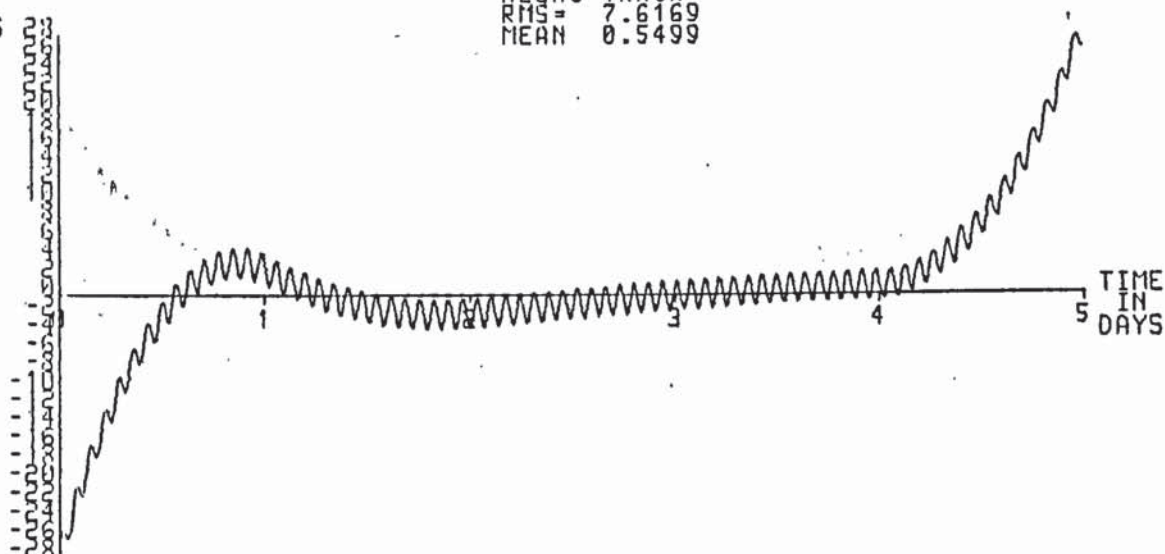
RADIAL
RMS = 0.5719
MEAN -0.0794



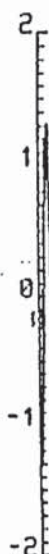
DIFFERENCES
IN METRES



ALONG-TRACK
RMS = 7.6169
MEAN 0.5499



DIFFERENCES
IN METRES



CROSS-TRACK
RMS = 0.9568
MEAN -0.0041

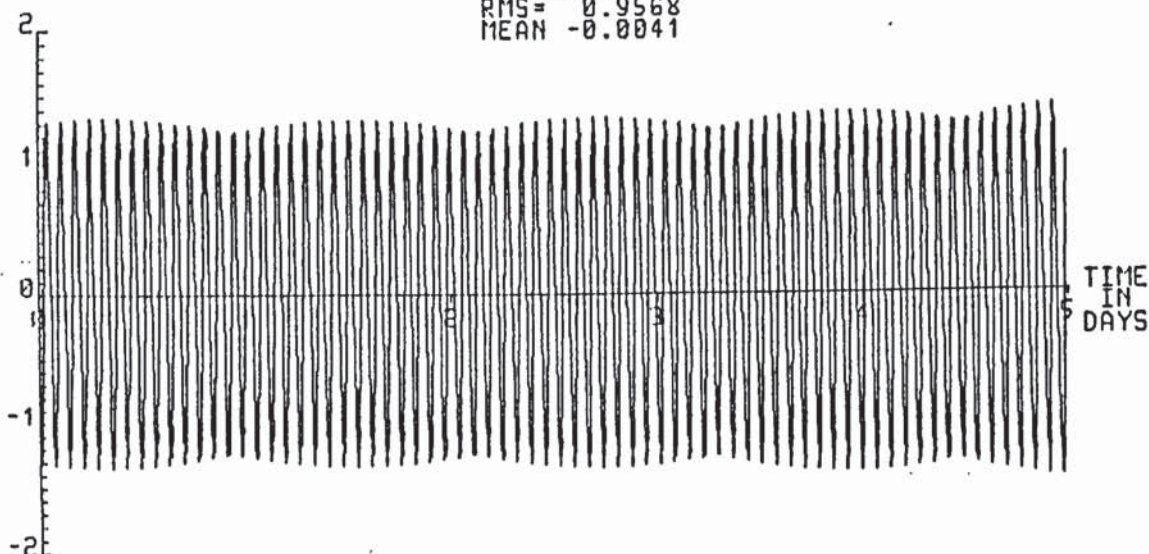


Figure 2a: The radial, along-track and cross-track differences for an orbit computed from 11 passes of Arequipa laser data versus the reference orbit.

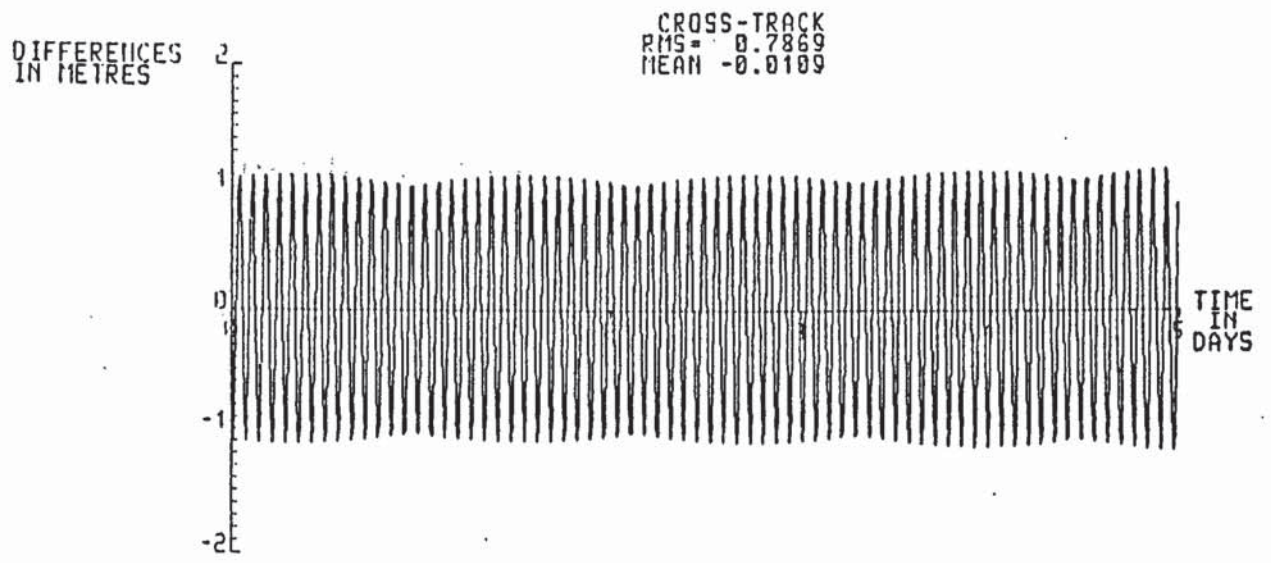
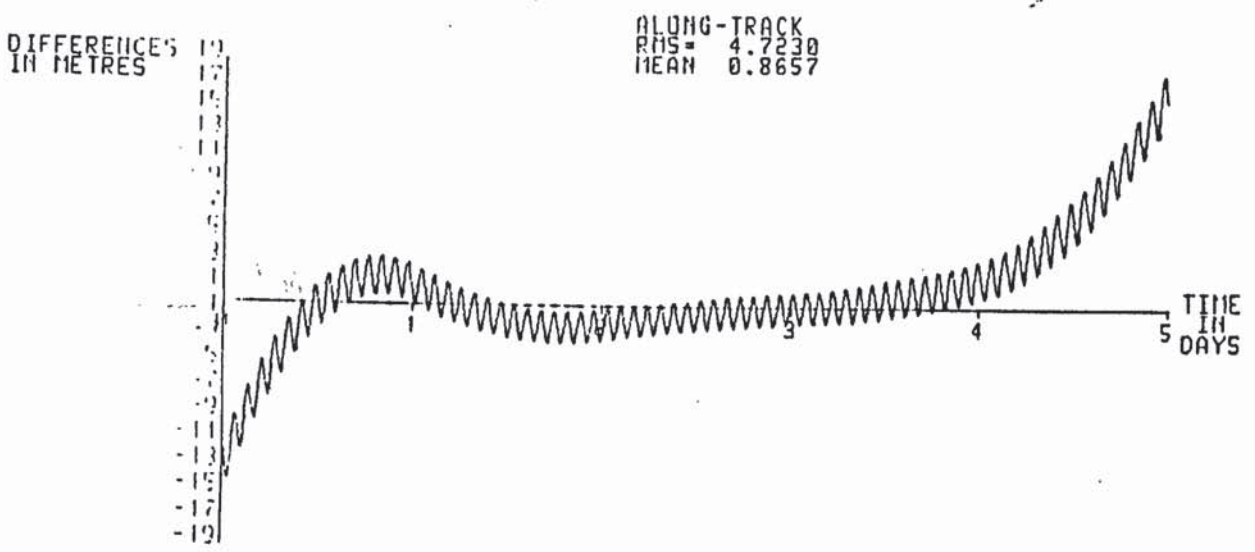
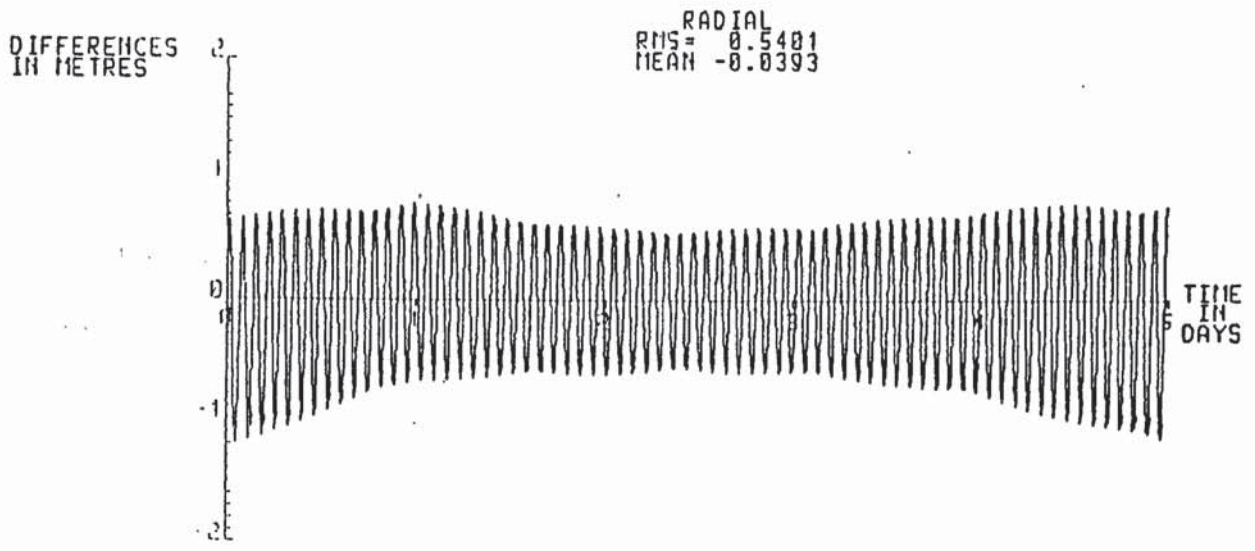
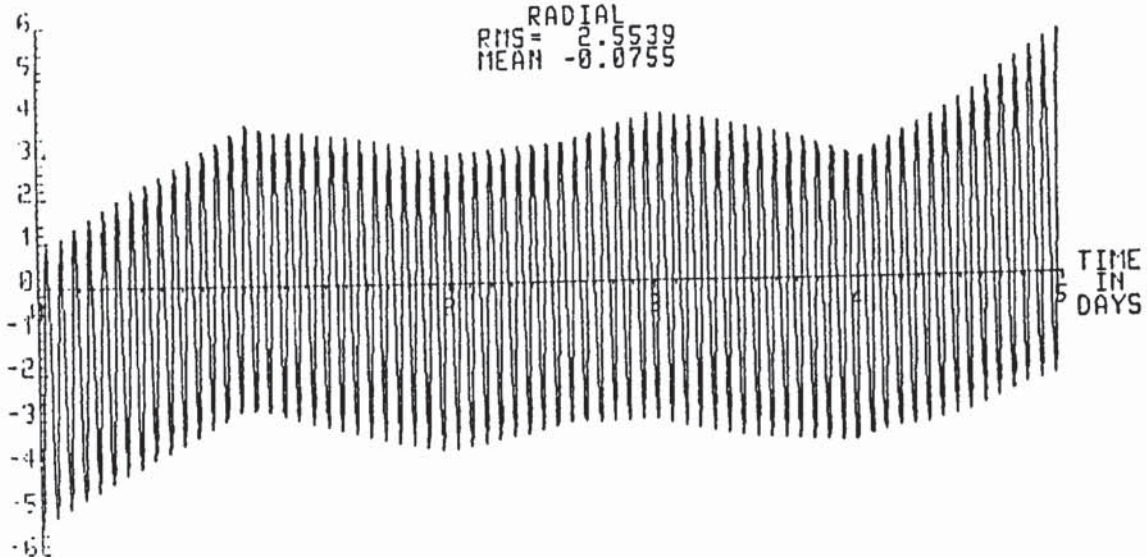
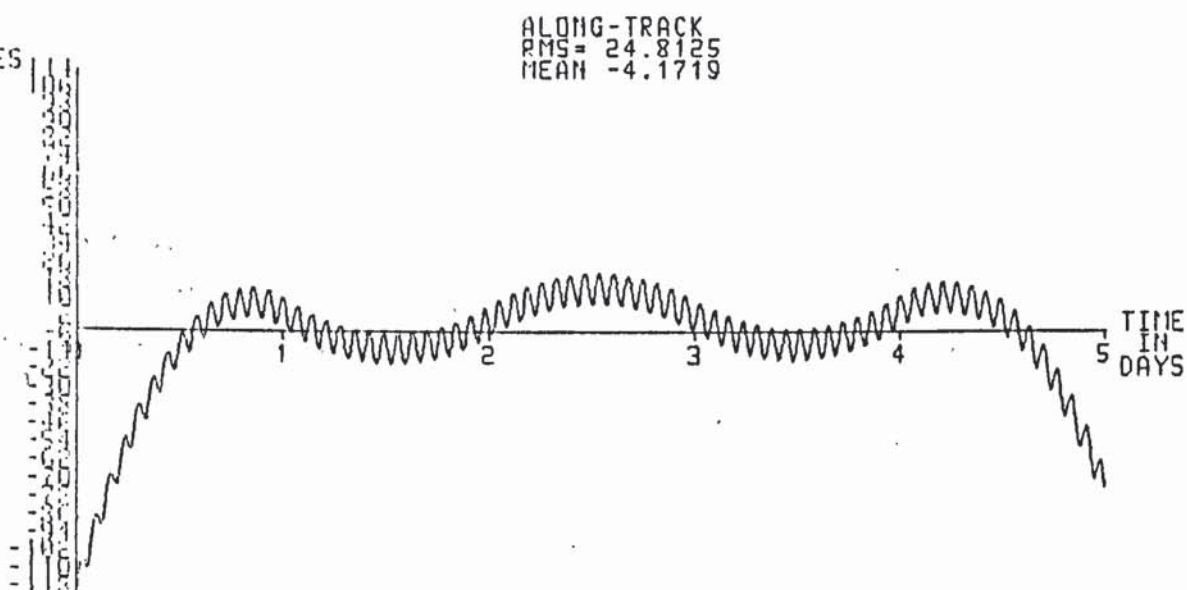


Figure 2b: The radial, along-track and cross-track differences for an orbit computed from 11 passes of Arequipa laser data and one-per-2min altimeter measurements with 1m sd versus the reference orbit.

DIFFERENCES
IN METRES



DIFFERENCES
IN METRES



DIFFERENCES
IN METRES

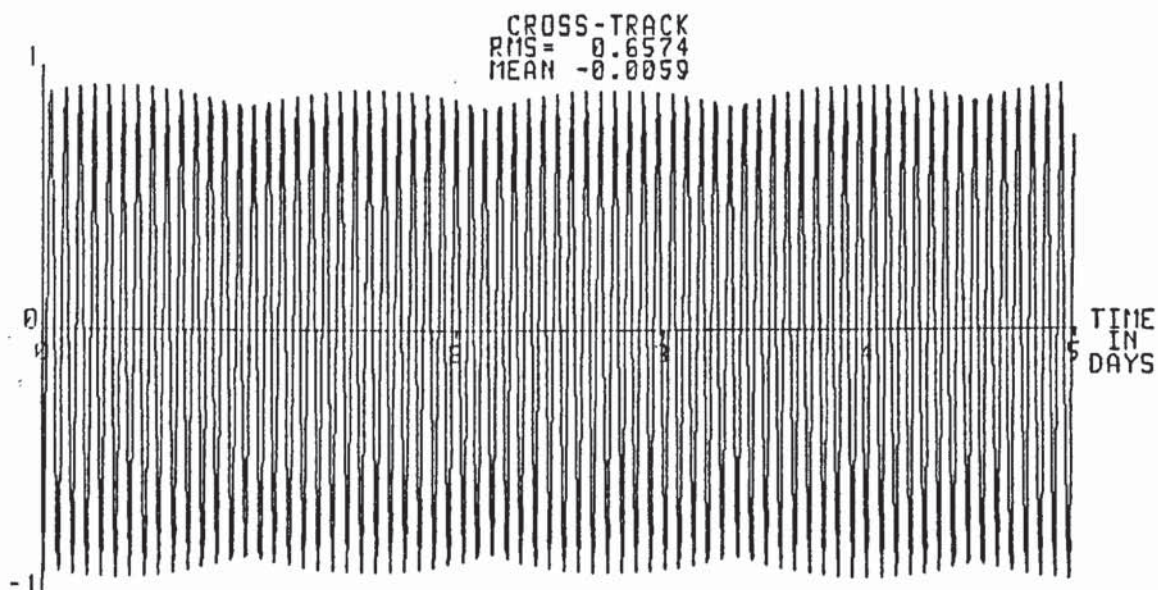


Figure 3a: The radial, along-track and cross-track differences for an orbit computed from 10 passes of Arequipa laser data versus the reference orbit.

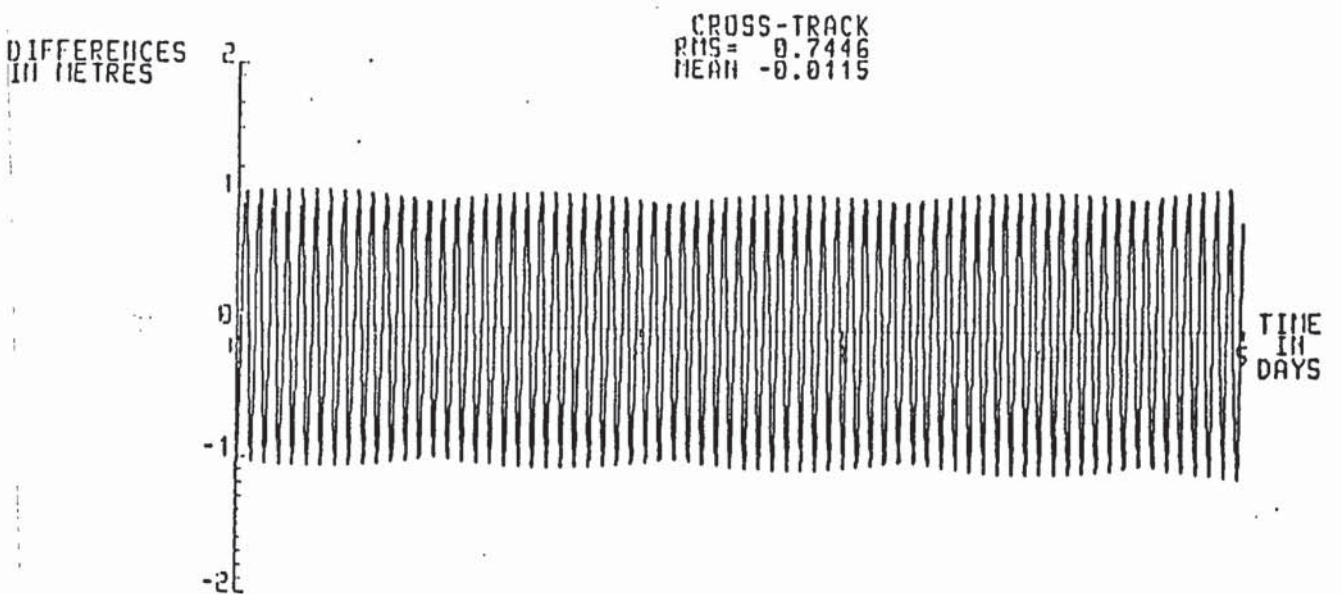
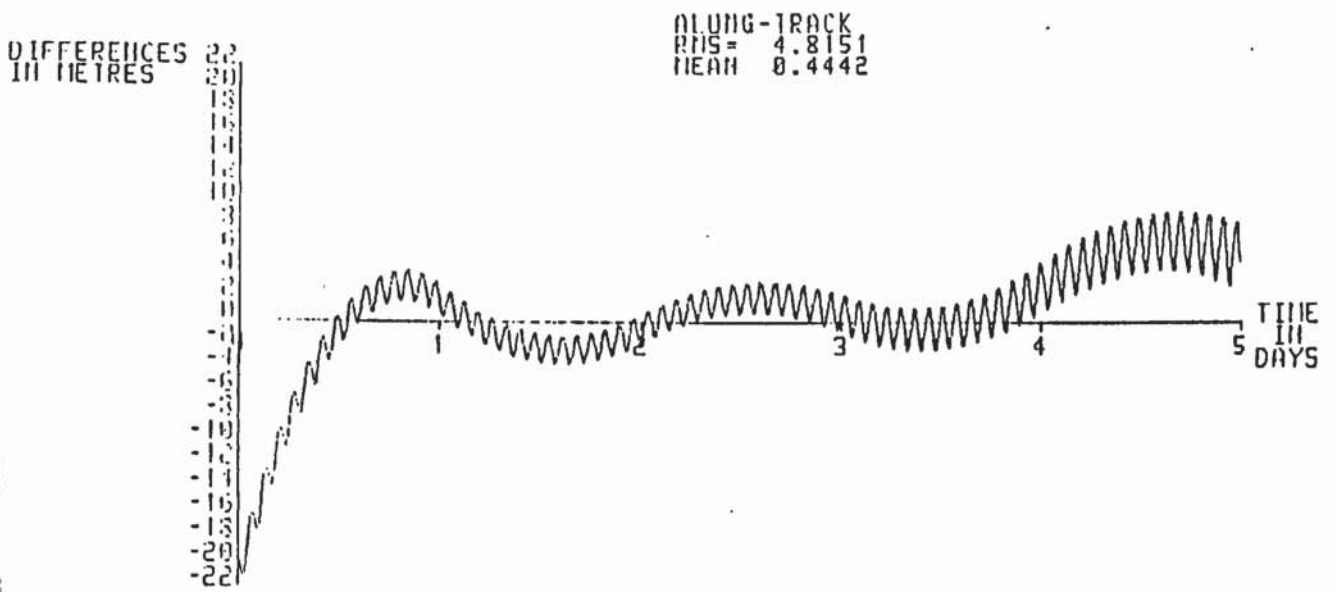
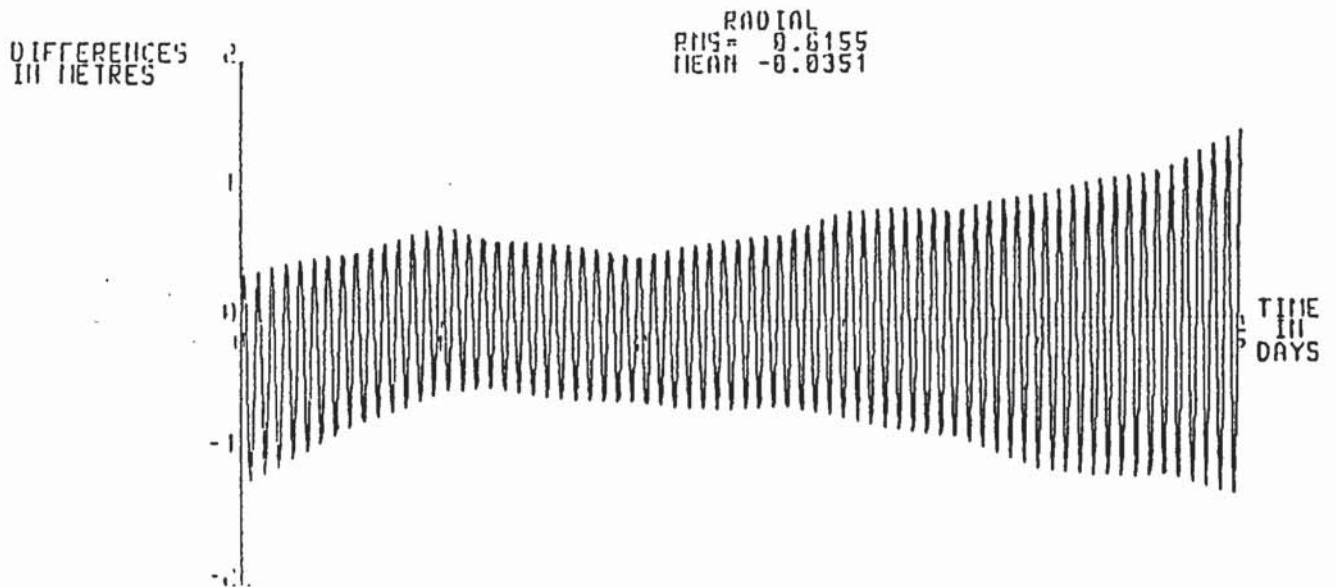
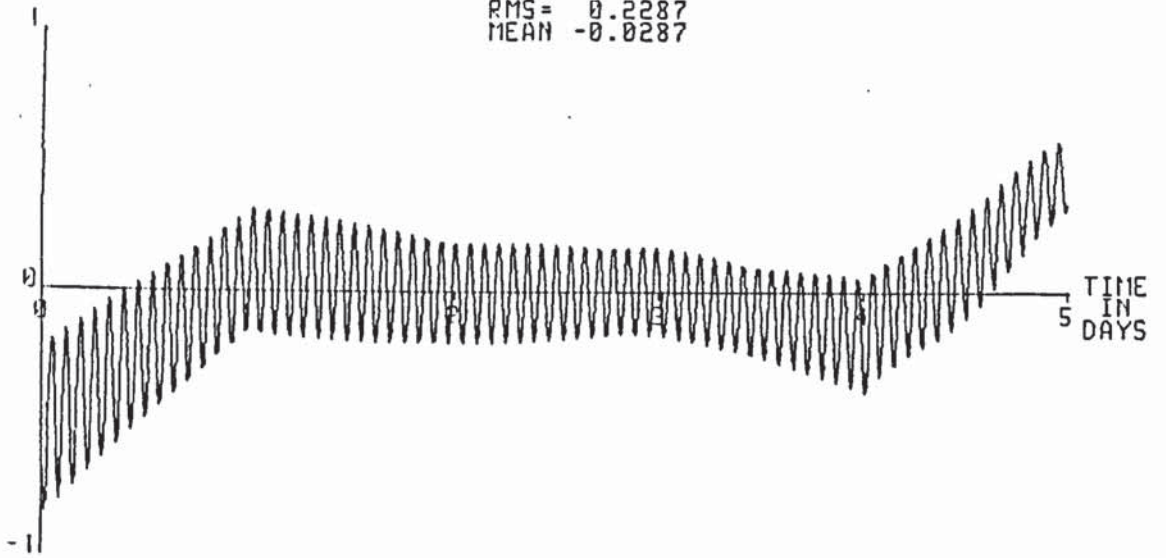


Figure 3b: The radial, along-track and cross-track differences for an orbit computed from 10 passes of Arequipa laser data and one-per-2min altimeter measurements with 1m sd versus the reference orbit.

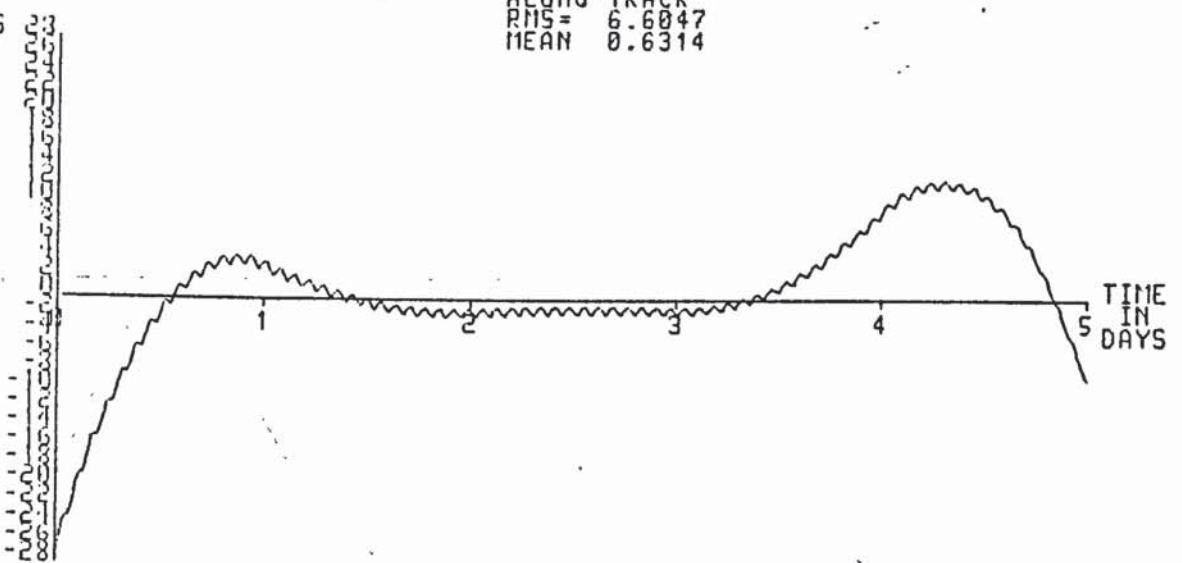
DIFFERENCES
IN METRES

RADIAL
RMS = 0.2287
MEAN -0.0287



DIFFERENCES
IN METRES

ALONG-TRACK
RMS = 6.6047
MEAN 0.6314



DIFFERENCES
IN METRES

CROSS-TRACK
RMS = 0.1435
MEAN 0.0012

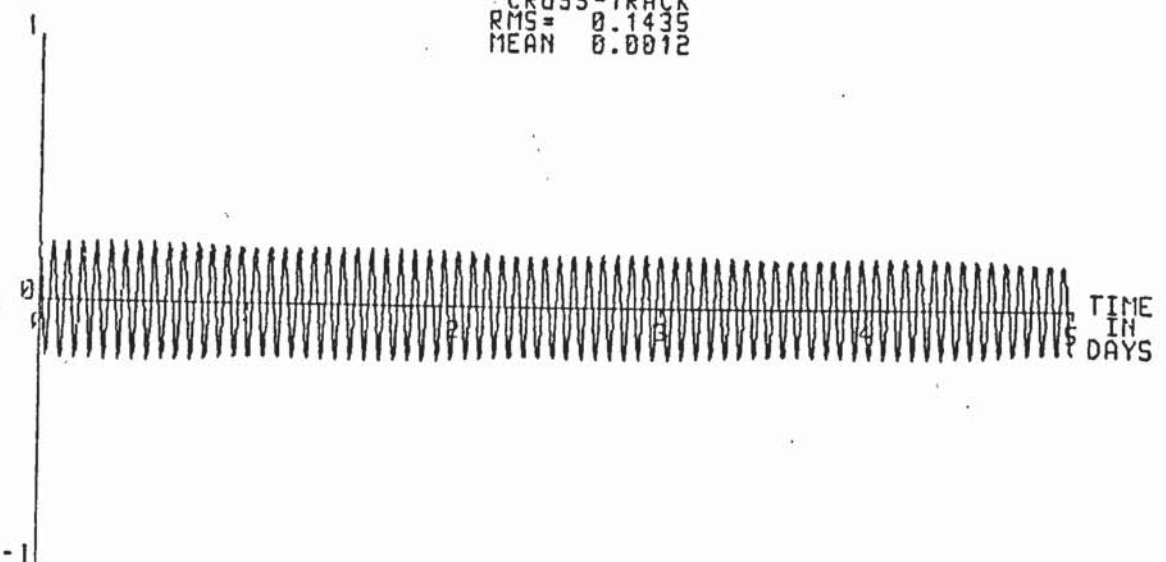


Figure 4: The radial, along-track and cross-track difference for an orbit computed from 5 passes of Arequipa laser data and one-per-2min 'exact' altimeter measurements with 2m sd versus the reference orbit.

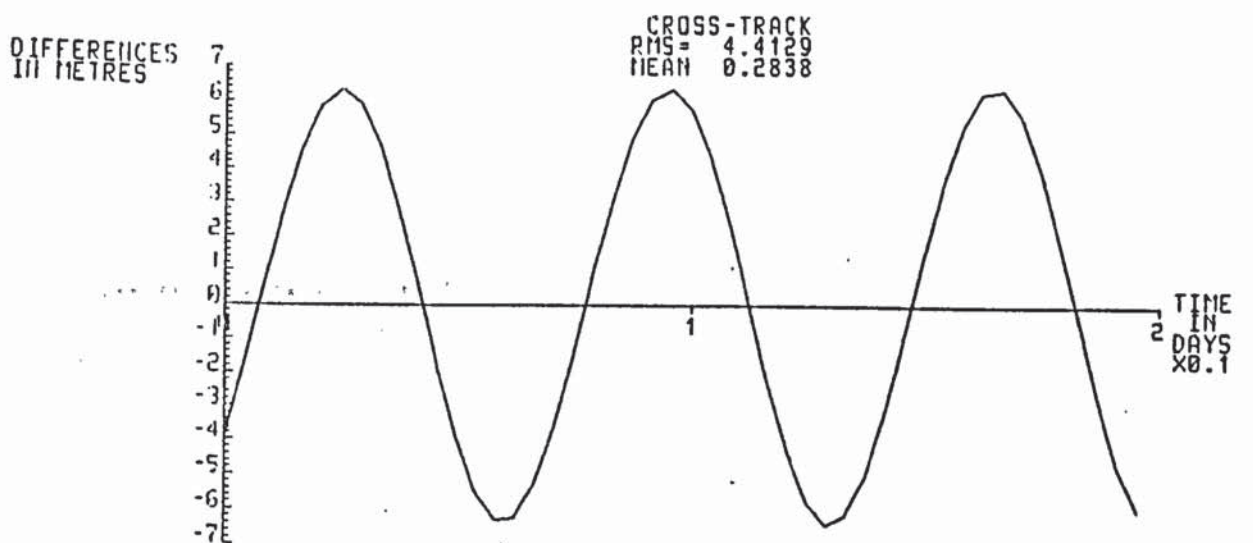
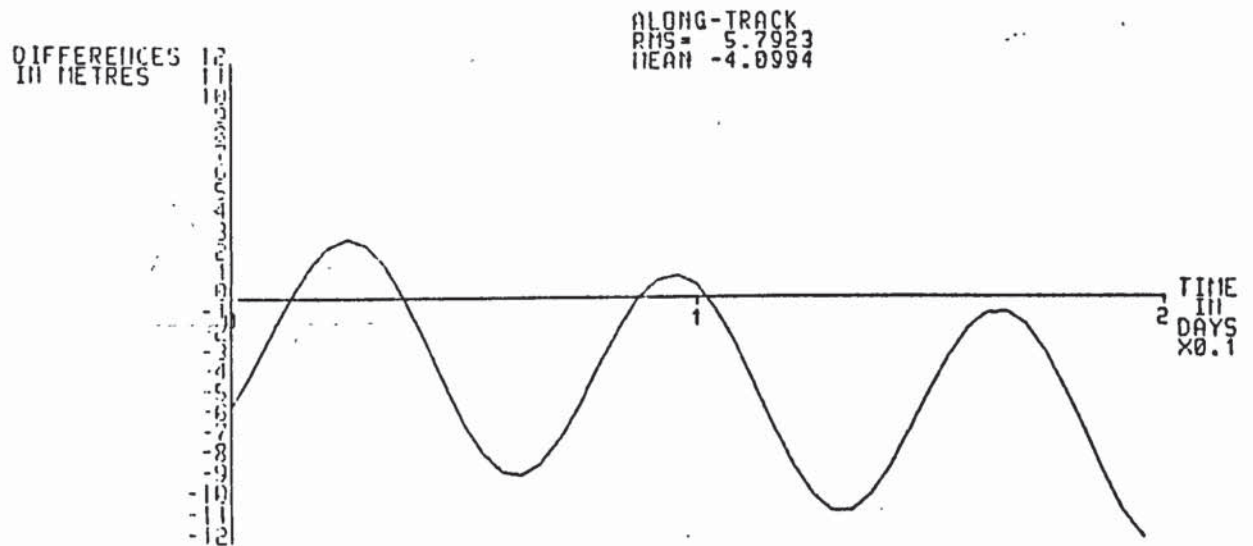
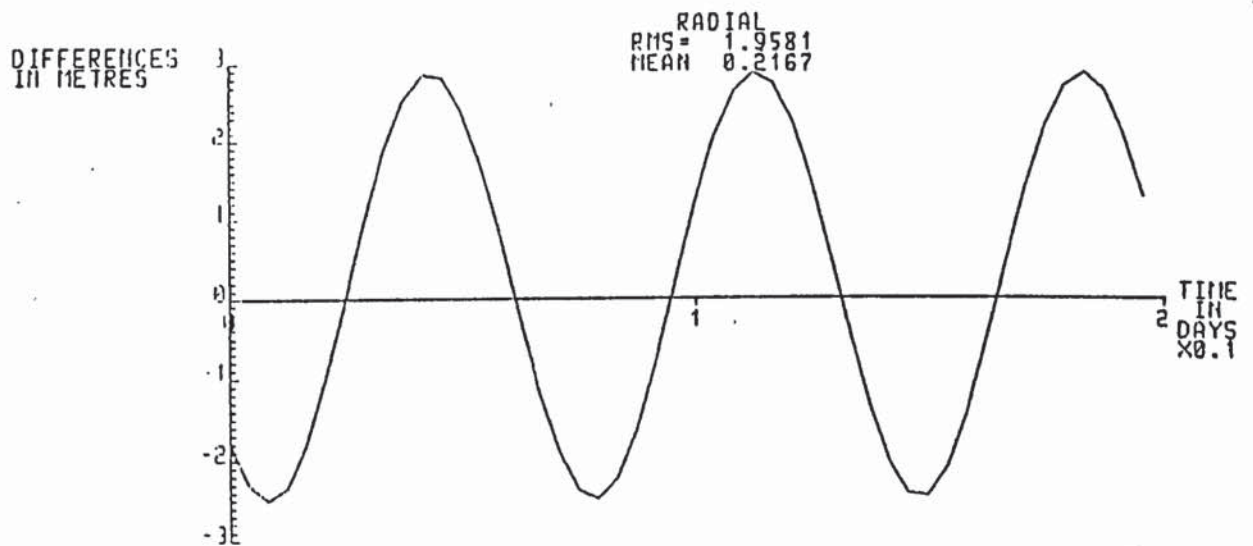
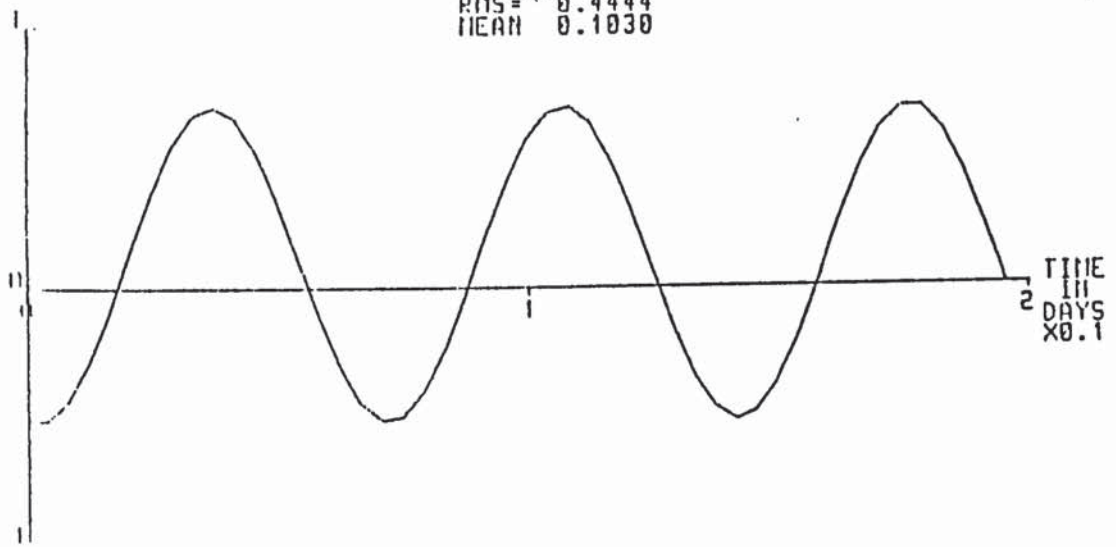


Figure 5a: The radial, along-track and cross-track difference for an orbit computed from laser data versus the reference orbit over the time interval MJD 43729.0 to MJD 43729.2

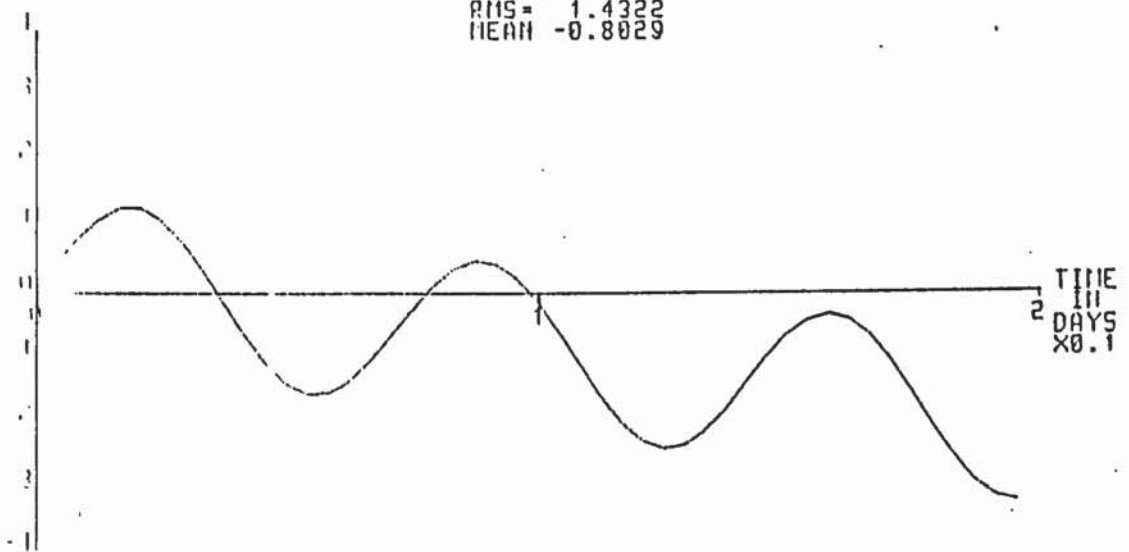
DIFFERENCES
IN METRES

RADIAL
RMS = 0.4444
MEAN 0.1030



DIFFERENCES
IN METRES

ALONG-TRACK
RMS = 1.4322
MEAN -0.8029



DIFFERENCES
IN METRES

CROSS-TRACK
RMS = 2.5538
MEAN -0.0721

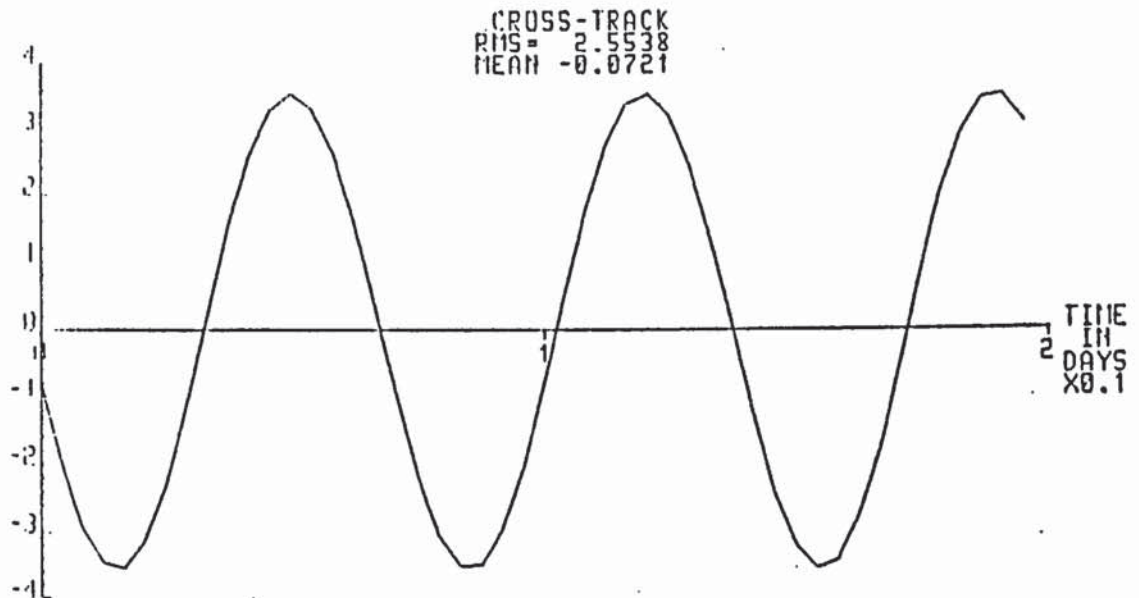


Figure 5b: The radial, along-track and cross-track differences for an orbit computed from laser data and one-per-2min altimeter measurements with 0.1m sd versus the reference orbit over the time interval MJD 43729.0 to MJD 43729.2

Pages removed for copyright restrictions.

```

E=CH(6)
DO 610 K=1,10
NI=K-1
WRITE (S3,51) NI
IF (S3.EQ.E) THEN
    J=NI
    GOTO 620
END IF
610 CONTINUE
620 CONTINUE
    J=J+1
    WRITE (CH(6),51) J
    CH(7)='0'
    GOTO 700
END IF
IF (J.EQ.100) THEN
    CH(5)='1'
    CH(6)='0'
    CH(7)='0'
END IF
700 CONTINUE
IF (N.EQ.NFILE) STOP 'FINISHED NUMBER OF FILES'
N=N+1
GOTO 201
13 CONTINUE
C
CLOSE(UNIT=2)
CLOSE(UNIT=5)
C CLOSE(UNIT=20)
C
STOP.
END

```

```

C      PROGRAM TO FIND THE CROSSOVER HEIGHT DIFFERENCES
C
C      INPUT FILES      :      EPH.DAT   - EPHEMERIS
C                       :      ORBIT.DAT  - NO. OF STEPS
C                       :      REDIN.DAT  - TIME SPAN
C
C      WORKFILES       :      EQUAT.CRS  - EQUATOR CROSSINGS
C                       :      REV.DAT   - ORBIT IN HALF REVS
C
C      OUTPUT FILES    :      HDIFF.DAT  - CROSSOVER DIFFERENCES
C
C      DOUBLE PRECISION XX1(3),XX2(3),ST(2),T1,T2,T
1      ,X1,X2,Y1,Y2,Z1,Z2,X,Y,LAMDA,FACTOR,PI,PI2
2      ,DUM1,DUM2
C
C      COMMON/TIME/NREV,NST,ILNG,HMIN,IND,PI,PI2
DATA PI/3.1415926536D0/
PI2=2.D0*PI
C
C      OPEN (UNIT=6,NAME='[-]ORBIT.DAT',TYPE='OLD')
6      READ(6,6) HMIN,NST
      FORMAT(/F10.2,I6)
      CLOSE(UNIT=6)
C
C      GET LENGTH OF HALF REVOLUTION -
C      SEASAT'S PERIOD IS APPROXIMATELY 101 MINUTES.
C      THIS NUMBER SHOULD BE CHANGED FOR ERS_1
C
      ILNG=101*INT(0.5/HMIN)
C
C      OPEN (UNIT=1,NAME='EPH.DAT',FORM='UNFORMATTED',TYPE='OLD'
1      ,ACCESS='DIRECT',RECL=14,MAXREC=NST)
      OPEN (UNIT=3,NAME='[-]REDIN.DAT',TYPE='OLD')
      READ(3,'(A)') JUNK
      READ(3,11) STMJD,ENDMJD
- 11      FORMAT(2F9.2)
      CLOSE(UNIT=3)
C
C      NUMBER OF HALF REVOLUTIONS FOR SEASAT.
C      AGAIN THIS SHOULD BE CHANGED FOR ERS_1
C
      NREV=NINT(43./3.*(ENDMJD-STMJD)+0.5)*2
2      OPEN (UNIT=9,NAME='EQUAT.CRS',FORM='UNFORMATTED',TYPE='UNKNOWN'
      ,ACCESS='DIRECT',RECL=4,MAXREC=NREV-1)
C
      DO 13 I=1,NREV-1
      ST1=0.0
13      WRITE(9'I)ST1
      CONTINUE
      INDEX=0
      IE=0
      IT=1
      5      READ(1'IT) ST(1),(XX1(I),I=1,3)
      IF (IT.EQ.NST) GOTO 101
      IT=IT+1
      IF (XX1(3).LT.0.D0) IEQ1=0
      IF (XX1(3).GT.0.D0) IEQ1=1
      IF (XX1(3).EQ.0.D0) THEN
          IE=1
          GOTO 20
      END IF
C
10      READ (1'IT) ST(2),(XX2(I),I=1,3)
      IF (IT.EQ.NST) GOTO 101
      IT=IT+1
      IF (XX2(3).LT.0.D0) IEQ2=0

```

```

IF (XX2(3).GT.0.D0) IEQ2=1
IF (XX2(3).EQ.0.D0) THEN
  IE=2
  GOTO 20
END IF
C
IF (IEQ1.EQ.IEQ2) THEN
  DO 30 J=1,3
  XX1(J)=XX2(J)
  30 CONTINUE
  ST(1)=ST(2)
  GOTO 10
END IF
C
C
C COME HERE IF AN EQUATOR CROSSING HAS OCCURRED
C
20 CONTINUE
IF (IE.EQ.1) THEN
  T=ST(1)
  Y=XX1(2)
  X=XX1(1)
  LAMDA=DATAN2(Y,X)
  LAMDA=DMOD((LAMDA+PI2),PI2)
  INDEX=INDEX+1
  WRITE(9'(INDEX)) T,LAMDA
  GOTO 40
END IF
C
IF (IE.EQ.2) THEN
  T=ST(2)
  Y=XX2(2)
  X=XX2(1)
  LAMDA=DATAN2(Y,X)
  LAMDA=DMOD((LAMDA+PI2),PI2)
  INDEX=INDEX+1
  WRITE(9'(INDEX)) T,LAMDA
  GOTO 40
END IF
C
C
C INTERPOLATE LINEARLY TO FIND TIME AND LONGITUDE OF CROSSING
C
Z1=XX1(3)
Z2=XX2(3)
T1=ST(1)
T2=ST(2)
T=T2-Z2*(T2-T1)/(Z2-Z1)
X1=XX1(1)
X2=XX2(1)
Y1=XX1(2)
Y2=XX2(2)
FACTOR=(T2-T)/(T2-T1)
X=X2-(X2-X1)*FACTOR
Y=Y2-(Y2-Y1)*FACTOR
LAMDA=DATAN2(Y,X)
LAMDA=DMOD((LAMDA+PI2),PI2)
INDEX=INDEX+1
WRITE(9'(INDEX)) T,LAMDA
40 CONTINUE
C
GOTO 5
101 CONTINUE
C
C
C ARRANGE EPHEMERIS INTO HALFRV REVOLUTIONS
C
CALL HALFRV
C

```

```

C      CALCULATE THE CROSSOVERS
C
C      CALL CROSSO
C
C      CALCULATE THE CROSSOVER HEIGHT DIFFERENCES
C
C      CALL CHT
C
C      STOP
C      END
C
C      *****
C
C      SUBROUTINE HALFRV
C
C      SUBROUTINE TO ARRANGE EPHEMERIS INTO HALF REVOLUTIONS
C
C      DOUBLE PRECISION X(3),ST,LAMDA,A(200),B(200),PI,PI2
C
C      COMMON/TIME/NREV,NST,ILNG,HMIN,IND,PI,PI2
C
C      OPEN (UNIT=10,NAME='REV.DAT',FORM='UNFORMATTED',TYPE='UNKNOWN'
1 ,ACCESS='DIRECT',RECL=4*ILNG,MAXREC=NREV)
C
C      II=1
C      N=1
C      IT=1
C      READ(1'IT) ST,(X(I),I=1,3)
C      IT=IT+1
C      LAMDA=DATAN2(X(1),X(2))
C      A(II)=DMOD((LAMDA+PI2),PI2)      ! CONVERT TO 0-2PI RANGE
C      B(II)=ST
C      II=II+1
C      IF(X(3).GT.0.DO)IND=1 ! STARTING POSITION IN NORTHERN HEMISPHERE
C      IF(X(3).LE.0.DO)IND=2 ! STARTING POSITION IN SOUTHERN HEMISPHERE
10 CONTINUE
C      IF (X(3).GT.0.DO) THEN
30 READ(1'IT) ST,(X(I),I=1,3)
C      IF (IT.EQ.(NST)) GOTO 101
C      IT=IT+1
C      LAMDA=DATAN2(X(2),X(1))
C      IF (X(3).LE.0.DO) THEN
C      IF ((II-1).LE.ILNG) THEN
C      WRITE(10'N) (B(J),A(J),J=1,II-1)
C      ELSE
C      TYPE*, 'ARRAY TOO SMALL AT',N
C      STOP
C      END IF
C      II=1
C      A(II)=DMOD((LAMDA+PI2),PI2)
C      B(II)=ST
C      II=II+1
C      N=N+1
C      GOTO 10
C      END IF
C      A(II)=DMOD((LAMDA+PI2),PI2)
C      B(II)=ST
C      II=II+1
C      GOTO 30
C      END IF
C
C      IF (X(3).LE.0.DO) THEN
40 READ(1'IT) ST,(X(I),I=1,3)
C      IF (IT.EQ.(NST)) GOTO 101
C      IT=IT+1
C      LAMDA=DATAN2(X(2),X(1))

```

```

IF (X(3).GT.0.DO) THEN
  IF ((II-1).LE.ILNG) THEN
    WRITE(10'N) (B(J),A(J),J=1,II-1)
  ELSE
    TYPE*, 'ARRAY TOO SMALL AT', N
    STOP
  END IF
  II=1
  A(II)=DMOD((LAMDA+PI2),PI2)
  B(II)=ST
  II=II+1
  N=N+1
  GOTO 10
END IF
A(II)=DMOD((LAMDA+PI2),PI2)
B(II)=ST
II=II+1
GOTO 40
END IF
C
101 CONTINUE
IF ((II-1).LE.ILNG) THEN
  WRITE(10'N) (B(J),A(J),J=1,II-1)
ELSE
  TYPE*, 'ARRAY TOO SMALL AT', N
  STOP
END IF
RETURN
END
C
C
C *****
C
C SUBROUTINE CROSSO
C
C SUBROUTINE TO CALCULATE THE CROSSOVERS
C
C INPUT FILES : REV.DAT - TIMES OF EACH INTEGRATED POSITION
C              :           SPLIT INTO HALF REVOLUTIONS
C              : EQUAT.CRS - TIMES AND LATITUDES OF EQUATOR
C              :           CROSSINGS
C              : EPH.DAT - EPHEMERIS FILE AT EACH INTEGRATION
C              :           STEP
C
C WORKFILE : CROSS.DAT - DATES OF CROSSOVERS
C
C OUTPUT FILE : REJCRO.DAT - CROSSOVER INFORMATION
C
C
C DOUBLE PRECISION L1,L2,L3,L4,L5,L6,T1,T2,T3,T4,T5,T6,LL(2,200)
1 ,ST(2,200),LAM(4),TL(4),L(2,2),T(2,2),LT(4),EE,E(2,8)
2 ,SX,SY,SZ,SXD,SYD,SZD,C(8),R2,DSXY,LD(2,8),PHI(2,8),DLDX,DLDY
3 ,DPDX,DPDY,DPDZ,DLIDT(2,8),DPIDT(2,8),DL(2,2),DP(2,2),DETIJ,DTI
4 ,DTJ,D(8),PI,PI2,TI,P(2,2),SXY,LTP1,LTP2,L12,P12,H7,LAMD(4)
5 ,LSUM,PIBY2
C
C
C COMMON/TIME/NREV,NST,ILNG,HMIN,IND,PI,PI2
DATA D/-5040.DO,720.DO,-240.DO,144.DO
1 , -144.DO,240.DO,-720.DO,5040.DO/
C
C NUMBER=0
C PIBY2=PI/2.DO
C
C H7=DBLE(HMIN)**7
C NOS=0
C

```



```

1 LAM(4)).AND.(LAM(2).LE.LAM(3)))THEN
  L(1,1)=DMOD((LSUM-PIBY2+PI2),PI2)
  GOTO 49
  END IF
C
  IF ((LAM(1).LT.LAM(2)).AND.(LAM(3).LT.LAM(4)).AND.(LAM(1).LE.
1 LAM(4)).AND.(LAM(3).LE.LAM(2))) THEN
  L(1,1)=DMOD((LSUM+PI+PI2),PI2)
  GOTO 49
  END IF
C
  IF ((LAM(1).LT.LAM(2)).AND.(LAM(4).LT.LAM(3)).AND.(LAM(1).LE.
1 LAM(4)).AND.(LAM(2).LE.LAM(3))) THEN
  L(1,1)=DMOD((LSUM+PIBY2+PI2),PI2)
  GOTO 49
  END IF
C
  IF ((LAM(2).LT.LAM(1)).AND.(LAM(4).LT.LAM(3)).AND.(LAM(4).LE.
1 LAM(1)).AND.(LAM(2).LE.LAM(3))) THEN
  L(1,1)=DMOD((LSUM+PI2),PI2)
  GOTO 49
  END IF
C
  IF ((LAM(2).LT.LAM(1)).AND.(LAM(3).LT.LAM(4)).AND.(LAM(4).LE.
1 LAM(1)).AND.(LAM(3).LE.LAM(2))) THEN
  L(1,1)=DMOD((LSUM+PIBY2+PI2),PI2)
  GOTO 49
  END IF
C
  IF ((LAM(1).LT.LAM(2)).AND.(LAM(4).LT.LAM(3)).AND.(LAM(4).LE.
1 LAM(1)).AND.(LAM(3).LE.LAM(2))) THEN
  L(1,1)=DMOD((LSUM-PIBY2+PI2),PI2)
  GOTO 49
  END IF
C
C
C
C
  CONDITIONS FOR A DOUBLE CROSSOVER
C
  IF ((LAM(1).LT.LAM(2)).AND.(LAM(3).LT.LAM(4)).AND.(LAM(1).LE.
1 LAM(4)).AND.(LAM(2).LE.LAM(3))) THEN
  L(1,1)=DMOD((LSUM+PI2),PI2)
  L(2,1)=DMOD((LSUM+PI+PI2),PI2)
  GOTO 47
  END IF
C
  IF ((LAM(1).LT.LAM(2)).AND.(LAM(3).LT.LAM(4)).AND.(LAM(4).LE.
1 LAM(1)).AND.(LAM(3).LE.LAM(2))) THEN
  L(1,1)=DMOD((LSUM+PI2),PI2)
  L(2,1)=DMOD((LSUM+PI+PI2),PI2)
  GOTO 47
  END IF
C
  L(1,1)=DMOD((LSUM+PIBY2+PI2),PI2)
  L(2,1)=DMOD((LSUM-PIBY2+PI2),PI2)
  ICR=2
  L(2,2)=L(2,1)
C
  49 CONTINUE
  L(1,2)=L(1,1)
C
C
C
  ICR= NUMBER OF CROSSOVERS BETWEEN TWO REVS (1 OR 2)
  DO 50 K=1,ICR
  ND=0
  DO 100 JJ=1,2

```

```

IF (JJ.EQ.1) THEN
  J1=J+1
  I1=I+1
ELSE IF (JJ.EQ.2) THEN
  J1=I+1
  I1=J+1
END IF

C
READ (10'J1) ((ST(JJ, LN), LL(JJ, LN)), LN=1, ILNG)
LL(JJ, 1)=DMOD((LL(JJ, 1)+PI2), PI2)
LTP2=DMOD((L(K, JJ)+(PI2-LL(JJ, 1))), PI2)
DO 60 LN=1, ILNG
LL(JJ, LN)=DMOD((LL(JJ, LN)+PI2), PI2)

C
C
C
C
MOVE ORIGIN TO START OF REVOLUTION TO COMPARE LAMDA'S

IF (LN.EQ.1) THEN
  LTP1=PI2
ELSE IF (LN.GT.1) THEN
  LTP1=DMOD((LL(JJ, LN)+(PI2-LL(JJ, 1))), PI2)
END IF
IF (ST(JJ, LN).EQ.0.DO) THEN
  LK=LN-1
  IF (DABS(LL(JJ, LK)-L(K, JJ)).LT.0.015D0) GOTO 61
  IF (DABS(LL(JJ, 1)-L(K, JJ)).LT.0.015D0) GOTO 261
  STOP 'ERROR SOMEWHERE'
END IF
IF (LTP1.GT.LTP2) GOTO 60 ! SEASAT IS IN A RETROGRADE ORBIT
T(K, JJ)=(ST(JJ, LN)+ST(JJ, LN-1))/2.DO
GOTO 70
60 CONTINUE
LK=ILNG
DUM1=DABS(LL(JJ, LK)-L(K, JJ))
DUM2=DABS(LL(JJ, 1)-L(K, JJ))
IF (DUM1.LT.0.015D0) GOTO 61
IF (DUM2.LT.0.015D0) GOTO 261
TYPE *, DUM1, DUM2
STOP 'ERROR IN APPROXIMATE LAMDA'
61 CONTINUE
T(K, JJ)=ST(JJ, LK)+DBLE(HMIN)/2.DO
GOTO 70
261 T(K, JJ)=ST(JJ, 1)-DBLE(HMIN)/2.DO
70 CONTINUE
100 CONTINUE

C
72 CONTINUE
DO 300 JJ=1, 2
IF (JJ.EQ.1) THEN
  J1=J+1
  I1=I+1
ELSE IF (JJ.EQ.2) THEN
  J1=I+1
  I1=J+1
END IF

C
DO 65 M=(ILNG*(J1-2)+1), ILNG*(J1+1)
READ(1'M) EE
IF (EE.LT.T(K, JJ)) GOTO 65
IF (EE.GE.T(K, JJ)) THEN
  DO 66 N=1, 8
  IF ((M+N).LT.6.OR.(M+N).GT.(NST+5)) STOP 'OUT OF LIMITS'
  READ (1'(M-5+N))E(JJ, N), SX, SY, SZ, SXD, SYD, SZD
  R2=SX*SX +SY*SY +SZ*SZ
  SXY=SX*SX +SY*SY

```

```

DSXY=DSQRT(SXY)
LD(JJ,N)=DATAN2(SY,SX)
LD(JJ,N)=DMOD((LD(JJ,N)+PI2),PI2)
PHI(JJ,N)=DATAN2(SZ,DSXY)
DLDX=-SY/SXY
DLDY=SX/SXY
DLIDT(JJ,N)=DLDX*SXD +DLDY*SYD
DPDX=-SZ*SX/(R2*DSXY)
DPDY=DPDX*SY/SX
DPDZ=DSXY/R2
DPIDT(JJ,N)=DPDX*SXD +DPDY*SYD +DPDZ*SZD
66 CONTINUE
GOTO 80
END IF
65 CONTINUE
TYPE *,EE,T(K,JJ)
GO TO 50
C STOP 'LAMDA NOT FOUND'
80 CONTINUE
300 CONTINUE
C
C WORK OUT INTERPOLATION COEFFICIENTS
C
71 DO 200 JJ=1,2
TI=T(K,JJ)
DO 68 N=1,8
C(N)=(TI-E(JJ,1)) *(TI-E(JJ,2)) *(TI-E(JJ,3)) *(TI-E(JJ,4))
1 *(TI-E(JJ,5)) *(TI-E(JJ,6))* (TI-E(JJ,7)) *(TI-E(JJ,8))/
2 ((TI-E(JJ,N))*D(N)*H7)
68 CONTINUE
C
C IF INTERPOLATION RANGE IS GREATER THAN 180 DEGREES ADD ON 360
C DEGREES TO ALL POINTS BELOW 180 DEGREES SO THAT WE GET A
C CONTINUOUS FUNCTION FOR INTERPOLATION
C
C
IF (DABS(LD(JJ,1)-LD(JJ,8)).GT.PI) THEN
DO 76 N=1,8
IF (LD(JJ,N).LT.PI) LD(JJ,N)=LD(JJ,N)+PI2
76 CONTINUE
END IF
L(K,JJ)=DMOD((LD(JJ,1)*C(1) +LD(JJ,2)*C(2) +LD(JJ,3)*C(3)
1 +LD(JJ,4)*C(4) +LD(JJ,5)*C(5) +LD(JJ,6)*C(6) +LD(JJ,7)*C(7)
2 +LD(JJ,8)*C(8)),PI2)
C
P(K,JJ)=PHI(JJ,1)*C(1) +PHI(JJ,2)*C(2) +PHI(JJ,3)*C(3)
1 +PHI(JJ,4)*C(4) +PHI(JJ,5)*C(5) +PHI(JJ,6)*C(6) +PHI(JJ,7)*C(7)
2 +PHI(JJ,8)*C(8)
C
DL(K,JJ)=DLIDT(JJ,1)*C(1) +DLIDT(JJ,2)*C(2) +DLIDT(JJ,3)*C(3)
1 +DLIDT(JJ,4)*C(4) +DLIDT(JJ,5)*C(5) +DLIDT(JJ,6)*C(6)
2 +DLIDT(JJ,7)*C(7) +DLIDT(JJ,8)*C(8)
C
DP(K,JJ)=DPIDT(JJ,1)*C(1) +DPIDT(JJ,2)*C(2) +DPIDT(JJ,3)*C(3)
1 +DPIDT(JJ,4)*C(4) +DPIDT(JJ,5)*C(5) +DPIDT(JJ,6)*C(6)
2 +DPIDT(JJ,7)*C(7) +DPIDT(JJ,8)*C(8)
C
200 CONTINUE
C
IF (DABS(L(K,1)-L(K,2)).GT.PI) THEN
DO 212 N=1,2
IF (L(K,N).LT.PI) L(K,N)=L(K,N)+PI2
212 CONTINUE
END IF
C

```

```

C      CHANGE IN TIMES
C
L12=L(K,1) -L(K,2)
P12=P(K,1) -P(K,2)
DETIJ=-DL(K,1)*DP(K,2) +DL(K,2)*DP(K,1)
DTJ=(-DP(K,2)*L12 +DL(K,2)*P12)/DETIJ*1440.DO
DTI=(-DP(K,1)*L12 +DL(K,1)*P12)/DETIJ*1440.DO
C
T(K,1)=T(K,1) -DTJ
T(K,2)=T(K,2) -DTI
IF (DABS(DTI).GE.DBLE(HMIN/2.0).OR.DABS(DTJ).GE.DBLE(HMIN/2.0))
1 THEN
    ND=ND+1
    IF (ND.GT.2) THEN
        NDELT=NDELT+1
        WRITE(8,303) T(K,1),J,T(K,2),I
303    FORMAT(D20.12,I6,2X,D20.12,I6)
        GOTO 50
    END IF
    GOTO 72
END IF
C
IF (DABS(DTJ).GT.1.D-09.OR.DABS(DTI).GT.1.D-09) THEN
    NUMBER=NUMBER+1
    GOTO 71
END IF
NUMBER=0
C
WRITE(5,110) T(K,1),J,T(K,2),I
110  FORMAT (D20.12,I6/D20.12,I6)
    NACC=NACC+1
50   CONTINUE
40   CONTINUE
30   CONTINUE
C
C
C      REPEAT FOR SOUTHERN HEMISPHERE
C
IF (NOS.LT.2) THEN
    IF (IND.EQ.1) THEN
        IND=2
        GOTO 22
    ELSE IF (IND.EQ.2) THEN
        IND=1
        GOTO 22
    END IF
END IF
C
WRITE(8,301) NDELT,NACC
301  FORMAT(// ' TOTAL NUMBER OF CROSSOVERS REJECTED DUE TO
1 CHANGE IN INTERPOLATION INTERVAL = ',I6//
2 ', ' TOTAL NUMBER OF ACCEPTED CROSSOVERS = ',I6)
CLOSE(UNIT=8)
CLOSE(UNIT=10,DISPOSE='DELETE')
CLOSE(UNIT=9,DISPOSE='DELETE')
CLOSE(UNIT=1)
RETURN
END
C
C
C      *****
C
C      SUBROUTINE CHT
C
C      SUBROUTINE TO INTERPOLATE THE CROSSOVER HEIGHTS

```



```

20      READ(4,20)DBASE,TSTART
        FORMAT(2D12.5)
        DAY=DBASE+TSTART/1440.DO
        DATE1=DAY+12.DO*H
        DATE2=DAY+DBLE(STLNTH)
        MBASE=IDINT(DBASE)
C
C      SET UP LEAP SECONDS
C
        MLA=0
        VALUE=0.0
30      CONTINUE
        MLB=MLA
        READ(1,40,END=50)MLA,VALUE
40      FORMAT(2X,I5,3X,F7.4)
        IF(MLA.LE.MBASE) GOTO 30
        GOTO 60
50      MLA=60000      ! DUMMY END VALUE
60      CONTINUE
C
        CLOSE (UNIT=1)
        CLOSE (UNIT=4)
C
C      PUT CROSSOVER TIMES INTO CHRONOLOGICAL ORDER
C
        CALL CHRONO (T,IX,K)
C
        GDRDAT='[-.TAPES] '//CHAR
        M=1
        OPEN (UNIT=2,NAME=GDRDAT,TYPE='OLD',FORM='UNFORMATTED')
        DO 200 I=1,K
5      IEND=0
        READ (2,END=101) (II(J),J=1,8),(JI(J),J=9,31),(KI(J),J=32,33)
C      IF(KI(32).NE.0) GOTO 5
C      AGC=JI(25)*1.E-02
C      IF (AGC.GT.36.0) GOTO 5
C
        I1=II(1)
        I2=II(2)
        CALL DATES (I1,I2,DATE)
        DATE=(DATE-DBASE)*1440.DO      ! TIME IN MINUTES FROM BASE EPOCH
        IF (DATE.LE.DATEB) GOTO 5
        IF (IRETURN.EQ.1) THEN
            IRETURN=0
            GOTO 5
        END IF
        IF (IRETURN.EQ.2) GOTO 202
        IF (DATE.LT.T(I)) THEN
            ST(1)=ST(2)
            MM1=M
            ST(2)=DATE
            DATEB=DATE
            MM2=M
            DO 140 N=1,8
                IJ(N,1)=IJ(N,2)
                IJ(N,2)=II(N)
140         CONTINUE
            DO 150 N=9,31
                JJ(N,1)=JJ(N,2)
                JJ(N,2)=JI(N)
150         CONTINUE
            GOTO 5
        END IF
C
        IF (DATE.GT.T(I)) THEN
            ST(3)=DATE

```

```

DATEB=DATE
MM3=M
DO 160 N=1,8
160 IJ(N,3)=II(N)
CONTINUE
DO 170 N=9,31
170 JJ(N,3)=JI(N)
CONTINUE
IEND=1
105 READ (2,END=101) (IJ(J,4),J=1,8),(JJ(J,4),J=9,31)
1 (KI(J),J=32,33)
C IF(KI(32).NE.0) GOTO 105
C AGC=JJ(25,4)*1.E-02
C IF (AGC.GT.36.0) GOTO 105
C

I1=IJ(1,4)
I2=IJ(2,4)
CALL DATES (I1,I2,DATE)
IF (IRETURN.EQ.2) GOTO 202
DATE=(DATE-DBASE)*1440.DO ! TIME IN MINUTES FROM EPOCH
IF (DATE.LT.DATEB) GOTO 105
ST(4)=DATE
DATEB=DATE
MM4=M
END IF

C IF (DATE.EQ.T(I)) THEN
DATEB=DATE
CALL RAM (II,JI,VAL,R)
T(I)=T(I)/1440.DO +DBASE
WRITE(7) T(I),VAL,IX(I)
GOTO 200
END IF

C NOW WE HAVE CROSSOVER IN THE MIDDLE OF THE INTERPOLATION RANGE
C
360 CONTINUE
IF (INTERP.EQ.2) GOTO 301
DO 300 N=1,3
IF ((ST(N+1)-ST(N)).GT.0.100) THEN
NREJ=NREJ+1
GOTO 200
END IF
300 CONTINUE
301 CONTINUE

C CALCULATE ALTIMETER HEIGHT
C
DO 210 N=1,4
DO 230 J=1,8
230 II(J)=IJ(J,N)
CONTINUE
DO 240 J=9,31
240 JI(J)=JJ(J,N)
CONTINUE
CALL RAM (II,JI,VAL,R)
HT(N)=VAL
C RT(N)=R
210 CONTINUE
C
C INTERPOLATE USING EITHER CUBIC LAGRANGE OR LINEAR INTERPOLATION
C
TI=T(I)
IF (INTERP.EQ.1) CALL CUBIC (TI,ST,HT,VAL,VALDOT,IERR)
IF (INTERP.EQ.2) THEN
STL(1)=ST(2)

```

```

        STL(2)=ST(3)
        IF ((STL(2)-STL(1)).GT.0.1D0) THEN
            NREJ=NREJ+1
            GOTO 200
        END IF
        HTL(1)=HT(2)
        HTL(2)=HT(3)
        CALL LINEAR (TI,STL,HTL,VAL,VALDOT,IERR)
    END IF
    IF (IERR.EQ.1) THEN
        TYPE*, 'ERROR IN INTERPOLATION TIMES AT LOCATION', I, M
        STOP
    END IF
    TI=TI/1440.D0 +DBASE
    WRITE(7) TI,VAL,VALDOT,IX(I)
    GOTO 200
101  CONTINUE
    CLOSE(UNIT=2)
    IF (M.EQ.NFILE) GOTO 202
    M=M+1
    IF (CH(5).EQ.'0'.AND.CH(6).EQ.'0') GOTO 400
    IF (CH(5).EQ.'0') GOTO 500
    C=CH(5)//CH(6)//CH(7)
    DO 330 KK=1,200
        NI=KK
        WRITE (S1,325) NI
325  FORMAT (I3)
        IF (S1.EQ.C) THEN
            J=NI
            GOTO 401
        END IF
330  CONTINUE
401  CONTINUE
        J=J+1
        J1=MOD(J,10)
        J2=MOD((J-J1),100)/10
        J3=(J-10*J2-J1)/100
        WRITE (CH(5),51) J3
        WRITE (CH(6),51) J2
        WRITE (CH(7),51) J1
51  FORMAT (I1)
        GOTO 700
C
500  CONTINUE
        D=CH(6)//CH(7)
        DO 510 KK=1,99
            NI=KK
            WRITE (S2,520) NI
520  FORMAT (I2)
            IF (S2.EQ.D) THEN
                J=NI
                GOTO 530
            END IF
510  CONTINUE
530  CONTINUE
                J=J+1
                IF (J.EQ.100) GOTO 600
                J1=MOD(J,10)
                J2=(J-J1)/10
                WRITE (CH(6),51) J2
                WRITE (CH(7),51) J1
                GOTO 700
C
400  CONTINUE
        E=CH(7)
        DO 410 KK=1,10

```

```

        NI=KK-1
        WRITE (S3,51) NI
        IF (S3.EQ.E) THEN
            J=NI
            GOTO 420
        END IF
410    CONTINUE
420    CONTINUE
        J=J+1
        IF (J.EQ.10) GOTO 600
        WRITE (CH(7),51) J
        GOTO 700
C
600    CONTINUE
        IF (J.EQ.10) THEN
            E=CH(6)
            DO 610 KK=1,10
                NI=KK-1
                WRITE (S3,51) NI
                IF (S3.EQ.E) THEN
                    J=NI
                    GOTO 620
                END IF
            CONTINUE
610    CONTINUE
620    CONTINUE
            J=J+1
            WRITE (CH(6),51) J
            CH(7)='0'
            GOTO 700
        END IF
        IF (J.EQ.100) THEN
            CH(5)='1'
            CH(6)='0'
            CH(7)='0'
        END IF
700    CONTINUE
        IF (CHAR.EQ.'T01_114.DAT') CHAR='T02_001.DAT'
        IF (CHAR.EQ.'T02_112.DAT') CHAR='T03_001.DAT'
        IF (CHAR.EQ.'T03_078.DAT') GOTO 202
        GDRDAT='[-.TAPES] '//CHAR
        OPEN(UNIT=2,NAME=GDRDAT,TYPE='OLD',FORM='UNFORMATTED')
        IF (IEND.EQ.1) THEN
            IEND=0
            READ (2) (IJ(J,4),J=1,8),(JJ(J,4),J=9,31)
            ,(KI(J),J=32,33)
            IF(KI(32).NE.0) GOTO 105
            AGC=JJ(25,4)*1.E-02
            IF (AGC.GT.36.0) GOTO 105
C
C
C
            I1=IJ(1,4)
            I2=IJ(2,4)
            CALL DATES (I1,I2,DATE)
            IF (IRETURN.EQ.2) GOTO 202
            DATE=(DATE-DBASE)*1440.D0 ! TIME IN MINUTES FROM BASE EPOCH
            IF (DATE.LE.DATEB) GOTO 105
            ST(4)=DATE
            DATEB=DATE
            MM4=M
            GOTO 360
        END IF
        GOTO 5
200    CONTINUE
202    CONTINUE
C
        CLOSE(UNIT=2)
        REWIND(UNIT=7)

```

```

C      CALL HDIFF
C      CLOSE(UNIT=7,DISPOSE='DELETE')
C      CLOSE(UNIT=16)
C
C      RETURN
C      END
C
C      *****
C
C      SUBROUTINE RAM (II,JI,VAL,R)
C
C      DOUBLE PRECISION RAMM,GEOHT,BARC,SETC,OETC,DIONC,DRYTC,WETTC
1      ,VAL,DHGHT,HTT(9:18),DAE,DF,DF2,DCF,DC2,DSF,DS2,DSL,DCL,X,Y,Z
2      ,R,RDDG,FI,LONG,EN,DCC,DCS,ENT,SWH
C
C      INTEGER*4 II(8)
C      INTEGER*2 JI(9:31)
C
C      DAE=63781370.D-07
C      DF=298257.D-03
C      RDDG=1.745329251994D-02
C      FI=(DFLOTJ(II(3))-90.D06)*1.D-06*RDDG
C      LONG=DFLOTJ(II(4))*1.D-06*RDDG
C      DF2=(1.D0-1.D0/DF)*(1.D0-1.D0/DF)
C      DCF=DCOS(FI)
C      DC2=DCF*DCF
C      DSF=DSIN(FI)
C      DS2=DSF*DSF
C      DCL=DCOS(LONG)
C      DSL=DSIN(LONG)
C      DCC=DCF*DCL
C      DCS=DCF*DSL
C      EN=DAE/DSQRT(DC2+DF2*DS2)
C
C      CALCULATE ALTIMETER HEIGHT
C
C      RAMM=DFLOTJ(II(5))*1.D-03 ! RAW HT IN METRES
C
C      GEOHT=(DFLOTJ(II(8))-15.D+04)*1.D-03 ! GEOID HT IN METRES
C
C      DO 10 J=9,18
C      HTT(J)=(DFLOTI(JI(J))-15000.D0)*1.D-03 ! CORRECTIONS
10     CONTINUE
C      SWH=DFLOTI(JI(20))*1.D-02 ! SIGNIFICANT WAVE HEIGHT
C
C      BARC =HTT(9) ! BAROMETRIC CORRECTION IN METRES
C      SETC =HTT(10) ! SOLID EARTH TIDE CORRECTION IN METRES
C      OETC =HTT(11) ! OCEAN TIDE CORRECTION IN METRES
C      DIONC =HTT(13) ! IONOSPHERIC CORRECTION IN METRES
C
C      IF(HTT(15).NE.9.999) THEN
C         WETTC=HTT(15)
C      ELSE
C         WETTC=HTT(14)
C      END IF
C
C      WETTC =HTT(14) IS FNWC WET TROPOSPHERIC CORRECTION IN METRES
C      WETTC =HTT(15) IS SMMR WET TROPOSPHERIC CORRECTION IN METRES
C
C      DRYTC =HTT(16) ! FNOC DRY TROPOSPHERIC CORRECTION IN METRES
C
C      DINSTC=HTT(18) ! NET INSTRUMENT CORRECTION IN METRES
C
C      DHGHT=RAMM+GEOHT+BARC+SETC+OETC+DIONC+HTT(14)+DRYTC+DINSTC ! METRE
C      DHGHT=DHGHT-0.07D0*SWH

```

```

C      VAL=DHGHT*1.D-06 ! ALTIMETER HT IN MEGAMETRES
C
C      RETURN
C      END
C
C      *****
C
C      SUBROUTINE CHRONO (T,IX,K)
C
C      PUTS CROSSOVER TIMES INTO CHRONOLOGICAL ORDER
C
C      DOUBLE PRECISION T(20000),B,D
C      DIMENSION IX(20000)
C
C      REWIND (5)
C      K=1
5      READ(5,10,END=101) T(K)
10     FORMAT(D20.12)
C      IX(K)=K
C      K=K+1
C      GOTO 5
101    CONTINUE
C      K=K-1
C      N=K
C
C      100    CONTINUE
C      B=T(1)
C      J=1
C      DO 20 I=2,N
C      D=T(I)
C      IF (B.GE.D) GOTO 20
C      B=T(I)
C      J=I
20     CONTINUE
C
C      INTERCHANGE BIGGEST WITH LAST
C
C      T(J)=T(N)
C      T(N)=B
C      L=IX(J)
C      IX(J)=IX(N)
C      IX(N)=L
C      N=N-1
C      IF (N.GT.1) GOTO 100
C
C      CLOSE(UNIT=5,DISPOSE='DELETE')
C      RETURN
C      END
C
C      *****
C
C      SUBROUTINE CUBIC (T,ST,H,VAL,VALDOT,IERR)
C
C      INTERPOLATES THE CROSSOVER HEIGHTS USING THE DATA FROM
C      THE ALTIMETER GDR'S
C
C      DOUBLE PRECISION T,ST(4),H(4),VAL,D(4),C(4),VALDOT,DC(4)
1     ,TST(4),ST12,ST13,ST14,ST23,ST24,ST34
C      COMMON/DINFO/DATE1,DATE2,MLA,IRETURN,I,M
C
C      IERR=0
C      IF (T.LT.ST(4).AND.T.LT.ST(3).AND.T.GT.ST(2).AND.
1     T.GT.ST(1)) GOTO 10
C      IERR=1
C      RETURN
C
C

```

```

10 CONTINUE
   ST12=ST(1)-ST(2)
   ST13=ST(1)-ST(3)
   ST14=ST(1)-ST(4)
   ST23=ST(2)-ST(3)
   ST24=ST(2)-ST(4)
   ST34=ST(3)-ST(4)
   D(1)=ST12*ST13*ST14
   D(2)=-ST12*ST23*ST24
   D(3)=ST13*ST23*ST34
   D(4)=-ST14*ST24*ST34
C
   DO 15 N=1,4
   DC(N)=0.D0
   TST(N)=T-ST(N)
15 CONTINUE
   DO 20 N=1,4
   C(N)=TST(1)*TST(2)*TST(3)*TST(4)/(TST(N)*D(N))
   DO 30 M=1,4
   IF (M.EQ.N) GOTO 30
   DC(N)=DC(N) +C(N)/TST(M)
30 CONTINUE
20 CONTINUE
C
   VAL=H(1)*C(1) +H(2)*C(2) +H(3)*C(3) +H(4)*C(4)
   VALDOT=H(1)*DC(1) +H(2)*DC(2) +H(3)*DC(3) +H(4)*DC(4)
C
   RETURN
   END
C
C *****
C
C SUBROUTINE DATES (I1,I2,DATE)
C
C COMPUTES THE MJD OF THE CROSSOVER
C
C DOUBLE PRECISION DATE,DATE1,DATE2,DDY,DBASE,FDDY,FRDY
C
C INTEGER*4 I1,I2
C
C COMMON/DINFO/DATE1,DATE2,MLA,IRETURN,I,M
C
10 DDY=DFLOTJ(I1)/86400.D0 ! INTEGER PART OF TIME TAG IN DAYS
   FDDY=DFLOTJ(I2)*1.D-06/86400.D0 ! FRACTIONAL PART
   DDY=DDY+FDDY
   IDY=IDINT(DDY)
   MJD=IDY +43509 ! MJD OF START OF 1978 IS 43508
   FRDY=DDY-DBLE(IDY)
C
   IF(MJD.GT.MLA)FRDY=FRDY +1.D0/86400.D0 ! ADDING LEAP SECOND
   DATE=DBLE(FLOAT(MJD)) +FRDY
   IF (DATE.LT.DATE1) THEN
     IRETURN=1
     RETURN
   END IF
   IF (DATE.GT.DATE2) THEN
     TYPE*,' EXCEEDED TIME SPAN AT TAPE',M
     TYPE*,I
     IRETURN=2
   END IF
   RETURN
   END
C
C *****
C
C SUBROUTINE HDIFF

```

```

C
C   COMPUTES THE CROSSOVER DIFFERENCE AFTER MATCHING THEM UP
C   AGAIN
C
1  DOUBLE PRECISION T(20000),H(20000),TT,HT,DIFF,HDOT(20000)
   ,DIFDOT,HD
   DIMENSION IND(20000)

```

```

C
5  I=1
   READ (7,END=101) T(I),H(I),HDOT(I),IND(I)
   I=I+1
   GOTO 5
101 CONTINUE

```

```

C
   I=I-1
   N=I
10  CONTINUE
   L=IND(1)
   M=1
   DO 20 J=2,N
   IF (L.GE.IND(J)) GOTO 20
   L=IND(J)
   M=J
20  CONTINUE

```

```

C
   IND(M)=IND(N)
   IND(N)=L
   TT=T(M)
   T(M)=T(N)
   T(N)=TT
   HT=H(M)
   H(M)=H(N)
   H(N)=HT
   HD=HDOT(M)
   HDOT(M)=HDOT(N)
   HDOT(N)=HD
   N=N-1
   IF (N.GT.1) GOTO 10

```

```

C
C   HEIGHTS ARE NOW IN ASCENDING ORDER OF INDEX - COMPARE
C

```

```

DO 40 J=1,I
IF (MOD(IND(J),2).EQ.0) GOTO 40
IF (IND(J+1).EQ.IND(J)+1) THEN
  DIFF=H(J)-H(J+1)
  DIFDOT=HDOT(J)-HDOT(J+1)
  WRITE(16,60) DIFF,DIFDOT,T(J),T(J+1)
  FORMAT(4F20.12)
60  END IF
40  CONTINUE
RETURN
END

```

```

C
C   *****
C

```

```

C   SUBROUTINE LINEAR (T,S,H,VAL,VALDOT,IERRL)
C
C   SIMILAR TO SBR CUBIC EXCEPT THE INTERPOLATION IS LINEAR.
C
C   DOUBLE PRECISION T,S(2),H(2),VAL,D(2),C(2),VALDOT
C
C   IERRL=0
C   IF (T.LT.S(2):AND.T.GT.S(1)) GOTO 10
C   IERRL=1
C   RETURN
10  CONTINUE

```

```
C      D(1)=S(1)-S(2)
      D(2)=-D(1)
      DO 20 N=1,2
      C(N)=(T-S(1))*(T-S(2))/((T-S(N))*D(N))
20    CONTINUE
C      VAL=C(1)*H(1) +C(2)*H(2)
      VALDOT=(H(1)-H(2))/D(1)
C      RETURN
      END
```

```

SHB=HTT(12)
GA=VAL
GOTO 100
101 CONTINUE
CLOSE(UNIT=6)
C
IF (CH(5).EQ.'0'.AND.CH(6).EQ.'0') GOTO 400
IF (CH(5).EQ.'0') GOTO 500
C=CH(5)//CH(6)//CH(7)
DO 330 K=1,200
NI=K
WRITE (S1,325) NI
325 FORMAT (I3)
IF (S1.EQ.C) THEN
    J=NI
    GOTO 401
END IF
330 CONTINUE
401 CONTINUE
J=J+1
J1=MOD(J,10)
J2=MOD((J-J1),100)/10
J3=(J-10*J2-J1)/100
WRITE (CH(5),51) J3
WRITE (CH(6),51) J2
WRITE (CH(7),51) J1
51 FORMAT (I1)
GOTO 700
C
500 CONTINUE
D=CH(6)//CH(7)
DO 510 K=1,99
NI=K
WRITE (S2,520) NI
520 FORMAT (I2)
IF (S2.EQ.D) THEN
    J=NI
    GOTO 530
END IF
510 CONTINUE
530 CONTINUE
J=J+1
IF (J.EQ.100) GOTO 600
J1=MOD(J,10)
J2=(J-J1)/10
WRITE (CH(6),51) J2
WRITE (CH(7),51) J1
GOTO 700
C
400 CONTINUE
E=CH(7)
DO 410 K=1,10
NI=K-1
WRITE (S3,51) NI
IF (S3.EQ.E) THEN
    J=NI
    GOTO 420
END IF
410 CONTINUE
420 CONTINUE
J=J+1
IF (J.EQ.10) GOTO 600
WRITE (CH(7),51) J
GOTO 700
C
600 CONTINUE
IF (J.EQ.10) THEN

```

```

SHB=HTT(12)
GA=VAL
GOTO 100
101 CONTINUE
CLOSE(UNIT=6)
C
IF (CH(5).EQ.'0'.AND.CH(6).EQ.'0') GOTO 400
IF (CH(5).EQ.'0') GOTO 500
C=CH(5)//CH(6)//CH(7)
DO 330 K=1,200
NI=K
WRITE (S1,325) NI
325 FORMAT (I3)
IF (S1.EQ.C) THEN
J=NI
GOTO 401
END IF
330 CONTINUE
401 CONTINUE
J=J+1
J1=MOD(J,10)
J2=MOD((J-J1),100)/10
J3=(J-10*J2-J1)/100
WRITE (CH(5),51) J3
WRITE (CH(6),51) J2
WRITE (CH(7),51) J1
51 FORMAT (I1)
GOTO 700
C
500 CONTINUE
D=CH(6)//CH(7)
DO 510 K=1,99
NI=K
WRITE (S2,520) NI
520 FORMAT (I2)
IF (S2.EQ.D) THEN
J=NI
GOTO 530
END IF
510 CONTINUE
530 CONTINUE
J=J+1
IF (J.EQ.100) GOTO 600
J1=MOD(J,10)
J2=(J-J1)/10
WRITE (CH(6),51) J2
WRITE (CH(7),51) J1
GOTO 700
C
400 CONTINUE
E=CH(7)
DO 410 K=1,10
NI=K-1
WRITE (S3,51) NI
IF (S3.EQ.E) THEN
J=NI
GOTO 420
END IF
410 CONTINUE
420 CONTINUE
J=J+1
IF (J.EQ.10) GOTO 600
WRITE (CH(7),51) J
GOTO 700
C
600 CONTINUE
IF (J.EQ.10) THEN

```

```

C      CALCULATE ALTIMETER HEIGHT
C
C      RAMM=DFLOTJ(II(5))*1.D-03 ! RAW HT IN METRES
      HTB=RAMM
C
C      SEAHT1=(DFLOTJ(II(7))-15.D+04)*1.D-03
C
C      GEOHT=(DFLOTJ(II(8))-15.D+04)*1.D-03 ! GEOID HT IN METRES
C
      IF (IGEOID.EQ.2) THEN
129      READ(20,129) NNN,VAL
          FORMAT(I6,D12.6)
          IF (NNN.NE.NUM) STOP 'ERROR IN INDICES'
          DIFG=GEOHT-VAL
          GB=VAL
      END IF
C
      DO 200 J=9,18
200      HTT(J)=(DFLOTI(JI(J))-15000.D0)*1.D-03 ! CORRECTIONS IN METRES
          CONTINUE
          HTT(12)=HTT(12)*1.D+01 ! SEASAT MEAN SEA SURFACE
          SWH=DFLOTI(JI(20))*1.D-02 ! SIGNIFICANT WAVE HEIGHT
          SHB=HTT(12)
          DHDT=9999.D0
          IF (NUM.NE.1) THEN
              DEN=(DB-DA)*86400.D0
              IF (DEN.LE.1.5D0) THEN
                  DHDT=(HTB-HTA)/DEN
              END IF
          END IF
          JORNO=JI(31)
          HTT(17)=HTT(17)*1.D+01 ! RADIAL S/C DIFFERENCE (DOD-GSFC)
          DODGOD=SNGL(HTT(17))
          SCHT=DFLOTJ(II(6))*1.D-03 ! COMPUTED S/C HT WRT REF ELLIPSOID
          WRITE(5,701) SCHT,NUM,DODGOD,JORNO,DHDT
701      FORMAT(D20.12,I6,F12.5,I6,D16.8)
C
          BARC =HTT(9) ! BAROMETRIC CORRECTION IN METRES
          SETC =HTT(10) ! SOLID EARTH TIDE CORRECTION IN METRES
          OETC =HTT(11) ! OCEAN TIDE CORRECTION IN METRES
          DIONC =HTT(13) ! IONOSPHERIC CORRECTION IN METRES
C
          IF(HTT(15).NE.9.999) THEN
              WETTC=HTT(15)
          ELSE
              WETTC=HTT(14)
          END IF
C
          WETTC =HTT(14) IS FNWC WET TROPOSPHERIC CORRECTION IN METRES
          WETTC =HTT(15) IS SMMR WET TROPOSPHERIC CORRECTION IN METRES
C
          DRYTC =HTT(16) ! FNOC DRY TROPOSPHERIC CORRECTION IN METRES
          DINSTC=HTT(18) ! NET INSTRUMENT CORRECTION IN METRES
C
          IF (IGEOID.EQ.2) GEOHT=VAL
          DHGHT=RAMM+GEOHT+BARC+SETC+OETC+DIONC+HTT(14)+DRYTC+DINSTC ! METRES
          DHGHT=DHGHT-0.07D0*SWH ! SEA STATE BIAS CORRECTION
          DHGHT=DHGHT-DELHC ! SOLID EARTH TIDE CONSTANT OFFSET RE-INSTATED
          DDHT=DHGHT*1.D-06 ! ALTIMETER HT IN MEGAMETRES
          DIFF=DHGHT-SCHT
C
C
300      WRITE(2,300)DATE,NUM,DDHT,FI,LONG
          FORMAT(F20.12,I6,D17.9,2(1X,F12.8))
C
          NUM=NUM+1

```

```

40 READ(1,40,END=50)MLA,VALUE
   FORMAT(2X,I5,3X,F7.4)
   IF(MLA.LE.MBASE) GOTO 30
   GOTO 60
50 MLA=60000 ! DUMMY END VALUE
60 CONTINUE
C
   CLOSE (UNIT=1)
   CLOSE (UNIT=3)
   CLOSE (UNIT=4)
C
   N=1
   TYPE*, 'WHAT IS THE FIRST FILE TO BE READ IN?'
   READ (6,110) STRING
   WRITE (CHAR,110) STRING
110 FORMAT (A11)
   TYPE*, 'HOW MANY FILES ARE REQUIRED?'
   ACCEPT*, NFILE
201 CONTINUE
   IF (CHAR.EQ.'T01_114.DAT') CHAR='T02_001.DAT'
   IF (CHAR.EQ.'T02_112.DAT') CHAR='T03_001.DAT'
   IF (CHAR.EQ.'T03_078.DAT') STOP 'NO MORE ALTIMETER DATA FROM
1 SEASAT'
   GDRDAT='[ROTHWELLDATA.TAPES] '//CHAR
C
   OPEN(UNIT=6,NAME=GDRDAT,TYPE='OLD',FORM='UNFORMATTED')
100 READ(6,END=101)(II(J),J=1,8),(JI(J),J=9,31),(KI(J),J=32,33)
   IF(KI(32).NE.0) GOTO 100
   AGC=JI(25)*1.E-02
   IF (AGC.GT.36.0) GOTO 100
   AGCS=JI(26)*1.E-02
C
C   COMPUTE TIMES OF ALTIMETER MEASUREMENTS
C
77 DDY=DFLOTJ(II(1))/86400.D0 ! INTEGER PART OF TIME TAG IN DAYS
   FDDY=DFLOTJ(II(2))*1.D-06/86400.D0 ! FRACTIONAL PART
   DDY=DDY +FDDY
   IDY=IDINT(DDY)
   MJD=IDY +43509 ! MJD OF START OF 1978 IS 43508
   FRDY=DDY-DBLE(IDY)
C
   IF(MJD.GT.MLA)FRDY=FRDY +1.D0/86400.D0 ! ADDING LEAP SECOND
   DATE=DBLE(FLOAT(MJD)) +FRDY
   IF (DATE.LE.DATEB) GOTO 100
   IF (DATE.LT.DATE1) GOTO 100
   IF (DATE.GT.DATE2) THEN
     TYPE*, ' EXCEEDED TIME SPAN'
     GOTO 13
   END IF
   DATEB=DATE
   IF (DABS(DATE-DLAST).GE.DIV) THEN
     DLAST=DATE
     GOTO 111
   END IF
   DA=DATE
   HTA=DFLOTJ(II(5))*1.D-03 ! RAW HT IN METRES
   GOTO 100
111 CONTINUE
   DB=DATE
   FI=(FLOAT(II(3))-90.E6)*1.E-06 ! FIRST APPROX TO PHI USED IN RGO
C
C   CALCULATION OF GEOCENTRIC SOLID EARTH TIDE
C   (REF.:- GDR USERS HANDBOOK)
C
   DELHC=0.202D0*(1.5D0*SIND(FI)*SIND(FI) - 0.5D0)*H2
C
   LONG=FLOAT(II(4))*1.E-06 ! NADIR LONGITUDE

```

```

PROGRAM CONVERT
C
C   REVISED AUGUST, 1989.
C
C   TO CONVERT THE ALTIMETER GDR TO THE REQUIRED SATAN USABLE
C   FORMAT.
C
REAL LONG
DOUBLE PRECISION HTT(9:18),DDY,FDDY,FRDY,RAMM,GEOHT,BARC,
1  SETC,OETC,DIONC,WETTC,DRYTC,DINSTC,DHGHT,DBASE,DATE,DDHT,SCHT
2  ,TSTART,H,HMIN,DAY,DATE1,DATE2,DLAST,DIV,DIFF,DREJ,DIF,VAL
3  ,DIFG,DATEB,DA,DB,HTA,HTB,SHA,SHB,GA,GB,DHDT,DEN,SWH,H2,DELHC
C
CHARACTER*11 CHAR,STRING,CH(11)*1,S1*3,C*3,S2*2,D*2,S3*1
1  ,E*1,GDRDAT*19
INTEGER*4 II(8)
INTEGER*2 JI(9:31)
BYTE      KI(32:33)
EQUIVALENCE (CHAR,CH(1))
DATA H2/0.609D0/
C
OPEN(UNIT=1,NAME='STEPS.DAT',TYPE='OLD')
OPEN(UNIT=2,NAME='ALTOBS.DAT',TYPE='NEW',FORM='FORMATTED')
OPEN(UNIT=3,NAME='ORBIT.DAT',TYPE='OLD')
OPEN(UNIT=4,NAME='START.DAT',TYPE='OLD')
OPEN(UNIT=5,NAME='SCHT.DAT',TYPE='NEW',FORM='FORMATTED')
C
11  TYPE*,'ENTER IN A 1 TO USE GDR GEOID'
TYPE*,'ENTER IN A 2 TO USE OWN GEOID'
ACCEPT*,IGEOID
IF (IGEOID.NE.1.AND.IGEOID.NE.2) GOTO 11
IF (IGEOID.EQ.2) OPEN(UNIT=20,NAME='[.EXS]INTERP.DAT',TYPE='OLD'
1  ,FORM='FORMATTED')
WRITE (5,14) IGEOID
14  FORMAT (I1)
C
TYPE*,'TYPE IN MINIMUM TIME INTERVAL BETWEEN MEASUREMENTS'
TYPE*,'(INTERVAL MUST BE IN MINUTES BUT CAN BE FRACTIONS OF A
1  MINUTE)'
ACCEPT*,TIME
DIV=DBLE(TIME)/1440.D0
RESID=0.D0
DSUM=0.D0
NUM=1
DATEB=0.D0
READ(3,'(A)') EPHEMFILE
READ(3,'(A)') FIELD
250 READ(3,250) HMIN,LENGTH
FORMAT(D10.2,I6)
H=HMIN/1440.D0
STLNTH=FLOAT(LENGTH)*SNGL(H)
READ(4,10)JUNK
10  FORMAT(A1)
READ(4,20)DBASE,TSTART
20  FORMAT(2D12.5)
DAY=DBASE+TSTART/1440.D0
DATE1=DAY+12.D0*H
DATE2=DAY+DBLE(STLNTH)
MBASE=IDINT(DBASE)
C
C   SET UP LEAP SECONDS
C
MLA=0
VALUE=0.0
30  CONTINUE
MLB=MLA

```

```

C
C   CALCULATE ALTIMETER HEIGHT
C
RAMM=DFLOTJ(II(5))*1.D-03 ! RAW HT IN METRES
HTB=RAMM
C
SEAHT1=(DFLOTJ(II(7))-15.D+04)*1.D-03
C
GEOHT=(DFLOTJ(II(8))-15.D+04)*1.D-03 ! GEOID HT IN METRES
C
IF (IGEOID.EQ.2) THEN
129   READ(20,129) NNN,VAL
      FORMAT(I6,D12.6)
      IF (NNN.NE.NUM) STOP 'ERROR IN INDICES'
      DIFG=GEOHT-VAL
      GB=VAL
END IF
C
DO 200 J=9,18
200   HTT(J)=(DFLOTI(JI(J))-15000.D0)*1.D-03 ! CORRECTIONS IN METRES
      CONTINUE
      HTT(12)=HTT(12)*1.D+01 ! SEASAT MEAN SEA SURFACE
      SWH=DFLOTI(JI(20))*1.D-02 ! SIGNIFICANT WAVE HEIGHT
      SHB=HTT(12)
      DHDT=9999.D0
      IF (NUM.NE.1) THEN
          DEN=(DB-DA)*86400.D0
          IF (DEN.LE.1.5D0) THEN
              DHDT=(HTB-HTA)/DEN
          END IF
      END IF
      JORNO=JI(31)
      HTT(17)=HTT(17)*1.D+01 ! RADIAL S/C DIFFERENCE (DOD-GSFC)
      DODGOD=SNGL(HTT(17))
      SCHT=DFLOTJ(II(6))*1.D-03 ! COMPUTED S/C HT WRT REF ELLIPSOID
701   WRITE(5,701) SCHT,NUM,DODGOD,JORNO,DHDT
      FORMAT(D20.12,I6,F12.5,I6,D16.8)
C
      BARC =HTT(9) ! BAROMETRIC CORRECTION IN METRES
      SETC =HTT(10) ! SOLID EARTH TIDE CORRECTION IN METRES
      OETC =HTT(11) ! OCEAN TIDE CORRECTION IN METRES
      DIONC =HTT(13) ! IONOSPHERIC CORRECTION IN METRES
C
      IF(HTT(15).NE.9.999) THEN
          WETTC=HTT(15)
      ELSE
          WETTC=HTT(14)
      END IF
C
      WETTC =HTT(14) IS FNWC WET TROPOSPHERIC CORRECTION IN METRES
      WETTC =HTT(15) IS SMMR WET TROPOSPHERIC CORRECTION IN METRES
C
      DRYTC =HTT(16) ! FNOC DRY TROPOSPHERIC CORRECTION IN METRES
      DINSTC=HTT(18) ! NET INSTRUMENT CORRECTION IN METRES
C
      IF (IGEOID.EQ.2) GEOHT=VAL
      DHGHT=RAMM+GEOHT+BARC+SETC+OETC+DIONC+HTT(14)+DRYTC+DINSTC ! METRES
      DHGHT=DHGHT-0.07D0*SWH ! SEA STATE BIAS CORRECTION
      DHGHT=DHGHT-DELHC ! SOLID EARTH TIDE CONSTANT OFFSET RE-INSTATED
      DDHT=DHGHT*1.D-06 ! ALTIMETER HT IN MEGAMETRES
      DIFF=DHGHT-SCHT
C
C
300   WRITE(2,300)DATE,NUM,DDHT,FI,LONG
      FORMAT(F20.12,I6,D17.9,2(1X,F12.8))
C
      NUM=NUM+1

```

```

40 READ(1,40,END=50)MLA,VALUE
   FORMAT(2X,I5,3X,F7.4)
   IF(MLA.LE.MBASE) GOTO 30
   GOTO 60
50 MLA=60000 ! DUMMY END VALUE
60 CONTINUE
C
   CLOSE (UNIT=1)
   CLOSE (UNIT=3)
   CLOSE (UNIT=4)
C
   N=1
   TYPE*, 'WHAT IS THE FIRST FILE TO BE READ IN?'
   READ (6,110) STRING
   WRITE (CHAR,110) STRING
110 FORMAT (A11)
   TYPE*, 'HOW MANY FILES ARE REQUIRED?'
   ACCEPT*, NFILE
201 CONTINUE
   IF (CHAR.EQ. 'T01_114.DAT') CHAR='T02_001.DAT'
   IF (CHAR.EQ. 'T02_112.DAT') CHAR='T03_001.DAT'
   IF (CHAR.EQ. 'T03_078.DAT') STOP 'NO MORE ALTIMETER DATA FROM
1 SEASAT'
   GDRDAT='[ROTHWELLDATA.TAPES] '//CHAR
C
   OPEN(UNIT=6,NAME=GDRDAT,TYPE='OLD',FORM='UNFORMATTED')
100 READ(6,END=101)(II(J),J=1,8),(JI(J),J=9,31),(KI(J),J=32,33)
   IF(KI(32).NE.0) GOTO 100
   AGC=JI(25)*1.E-02
   IF (AGC.GT.36.0) GOTO 100
   AGCS=JI(26)*1.E-02
C
C COMPUTE TIMES OF ALTIMETER MEASUREMENTS
C
77 DDY=DFLOTJ(II(1))/86400.D0 ! INTEGER PART OF TIME TAG IN DAYS
   FDDY=DFLOTJ(II(2))*1.D-06/86400.D0 ! FRACTIONAL PART
   DDY=DDY +FDDY
   IDY=IDINT(DDY)
   MJD=IDY +43509 ! MJD OF START OF 1978 IS 43508
   FRDY=DDY-DBLE(IDY)
C
   IF(MJD.GT.MLA)FRDY=FRDY +1.D0/86400.D0 ! ADDING LEAP SECOND
   DATE=DBLE(FLOAT(MJD)) +FRDY
   IF (DATE.LE.DATEB) GOTO 100
   IF (DATE.LT.DATE1) GOTO 100
   IF (DATE.GT.DATE2) THEN
       TYPE*, ' EXCEEDED TIME SPAN'
       GOTO 13
   END IF
   DATEB=DATE
   IF (DABS(DATE-DLAST).GE.DIV) THEN
       DLAST=DATE
       GOTO 111
   END IF
   DA=DATE
   HTA=DFLOTJ(II(5))*1.D-03 ! RAW HT IN METRES
   GOTO 100
111 CONTINUE
   DB=DATE
   FI=(FLOAT(II(3))-90.E6)*1.E-06 ! FIRST APPROX TO PHI USED IN RGO
C
C CALCULATION OF GEOCENTRIC SOLID EARTH TIDE
C (REF.: - GDR USERS HANDBOOK)
C
DELHC=0.202D0*(1.5D0*SIND(FI)*SIND(FI) - 0.5D0)*H2
C
LONG=FLOAT(II(4))*1.E-06 ! NADIR LONGITUDE

```

A Description of Altimeter and Crossover Processing Software

D.A. Rothwell

Internal Report for ESRU, Aston University

August, 1989

**The University of Aston In Birmingham
Precise Orbit Determination and Analysis
from Satellite Altimetry and Laser Ranging
D.A.Rothwell
Doctor of Philosophy
1989**

1. Introduction

This document is intended to give a brief description of the altimeter and crossover processing software required to produce satellite observational data compatible with the SATAN software package [1]. Also contained herein are computer listings of the programs CONVERT (altimetry) and CROSS (crossovers).

2. The program CONVERT

CONVERT is a FORTRAN program to transform the altimeter data from GDR [2] format into SATAN [1] usable form. It is designed to be run interactively since various "TYPE *" statements appear, which require responses. Several input files are required by the program, namely STEPS.DAT (giving the times of leap seconds in the UTC system, where UTC \equiv Universal Time (Coordinated) [3]), START.DAT (giving the epoch for the UTC scale), INTERP.DAT (if it is desired to use a derived geoid) and obviously the altimeter GDR's. More information on the GDR's can be found in section 4. Prior to running CONVERT, the above files should contain the required information for the orbital arc to be analysed.

Upon running CONVERT, the first "TYPE *" statement asks to which geoid the altimeter measurements should be referred. A response of '1' indicates that the GEM-10BD geoid [4], that which is on the GDR tapes, should be utilized whilst a response of '2' specifies using that which is contained in the file INTERP.DAT (see section 5).

The next "TYPE *" statement asks for the sampling interval in minutes, the minimum value possible, being $1/60$. An interval of 1 or 2 minutes usually provides an adequate sample of data with a higher sampling rate not necessarily adding any extra orbital information, whilst greatly slowing down the processing. Also it should be noted that a large amount of altimetry, can 'swamp' other observational data unless it is down-weighted appropriately in the data reduction program.

The final "TYPE *" statement asks for the name of the first GDR file to be processed, together with the total number of files. The response must be made in the T Ø * - i j k.DAT format (see section 4). The number of files specified should be sufficient to span the length of the orbital arc to be analysed.

The program processes the GDR files until one of two conditions occurs. It will stop when it has either processed all the input files, or it has reached the end of the orbital arc length. If the former of these conditions occurs, the message "FINISHED NUMBER OF FILES" will appear on the screen. This could mean that insufficient data was input to the program so it is necessary to check the time of the last altimeter observation in the output file ALTOBS.DAT. A large time difference between this and the end of the orbital arc means that the program should be re-run inputting more GDR files. If the message "EXCEEDED TIME SPAN" appears, then enough data was input to the program.

The output file ALTOBS.DAT contains the date, index, altimeter height measurement, latitude and longitude of each sampled observation. This file is used in program SORTS to chronologically order the altimeter observations with other observational data and in the data reduction program to minimize the altimeter residuals. The output file SCHK.DAT contains information on the NASA GSFC and DOD computed orbits for each sampled altimeter observation. It too, is used in the data reduction program.

3. Algorithms within CONVERT

CONVERT contains two main algorithms, one to determine dh°/dt , h° being the observed altimeter height and one to process the altimeter measurement itself. The value of dh°/dt is written as DHDT in the program and is used in the data reduction program to determine a timing error on the altimeter. The algorithm in CONVERT is

$$DHDT = (HTB - HTA) / DEN \quad (1)$$

where HTB is the raw altimeter measurement at the point in question, HTA is the same at the previous measured point and DEN is the time span between the two in seconds. If DEN is larger than 1.5 seconds, DHDT is flagged as unreliable, being given the value 9999.DØ. Such a value is not used to determine the timing bias. Typically DEN = sampling interval of GDR tape.

The altimeter observation is written as DHGHT within the program. It is evaluated using the following algorithm :-

$$DHGHT = RAMM + GEOHT + BARC + SETC + OETC + DIONC + WETTC + DRYTC + DINSTC - 0.07 * SWH - DELHC \quad (2)$$

where	RAMM	is the raw altimeter measurement
	GEOHT	is the geoid height with respect to the reference ellipsoid
	BARC	is the barotropic correction
	SETC	is the solid earth tide correction
	OETC	is the ocean earth tide correction
	DIONC	is the ionospheric correction
	WETTC*	is the wet tropospheric correction
	DRYTC	is the dry tropospheric correction
	DINSTC	is the instrument correction
and	SWH	is the significant wave height, $h_1 \cdot \frac{1}{3}$

All of these terms are contained on the GDR files except perhaps the geoid height which could be read from INTERP.DAT if this is desired.

Further, $DELHC = 0.202 \left(\frac{3}{2} \sin^2 \phi - \frac{1}{2} \right) h_2$, ϕ being the geocentric latitude (taken as the geodetic latitude within the program) and h_2 is the second order Love number ($h_2 = 0.609$).

*WETTC can be chosen from two values, the FNWC or SMMR value. Both exist on the GDR files but data outages occur for the SMMR value. Hence the FNWC value is used throughout.

This algorithm does not account for sea surface topography, but once a model for this is derived, a term can be added to equation (2).

4. The GDR files

The GDR files were originally recorded on three magnetic tapes in binary format. They were converted to decimal integer format as explained in [2]. To remain consistent with the original numbering system the files are named TØ* - i j k.DAT where * represents 1, 2 or 3, indicating the tape number and i j k is an integer ranging from ØØ1 to 113, for the file number of that specific tape. Since the altimetry spans July 6 to October 9, TØ1 - ØØ1.DAT corresponds to data beginning on July 6. The rest follow in chronological order. To identify which files correspond to a particular time period, it is necessary to check the printouts which give the first five records of each file on each of the three tapes.

The first integer of each record corresponds to the observation time, in seconds, from the start of 1978. This can be readily converted to MJD format thus identifying the first GDR file needed as input to CONVERT.

5. Derived geoids

The FORTRAN program LEG [5] is used to compute the height of the geoid above the reference ellipsoid, given any set of geopotential coefficients, i.e. the gravity field. The output from this program, LEG.DAT, contains this geoid information for a $\frac{1^\circ}{2} \times \frac{1^\circ}{2}$ grid on the earth's surface. In order to compute the derived geoid height at each altimeter observation time, it is necessary to first run CONVERT (to get the observation times) and then to run INTERP which interpolates the geoid heights at these times. The output from this program, INTERP.DAT, can then be used in CONVERT if desired. Note that this process involves running CONVERT twice so it is essential that the same sampling interval is used in both instances. Also, the procedure can be performed once a converged orbit has been obtained. The reduction program is run using altimetry referred to each derived geoid in turn. There is no need to re-run the orbit generation program. Analysis of the differences in the results from using different geoids can give insight into the errors therein.

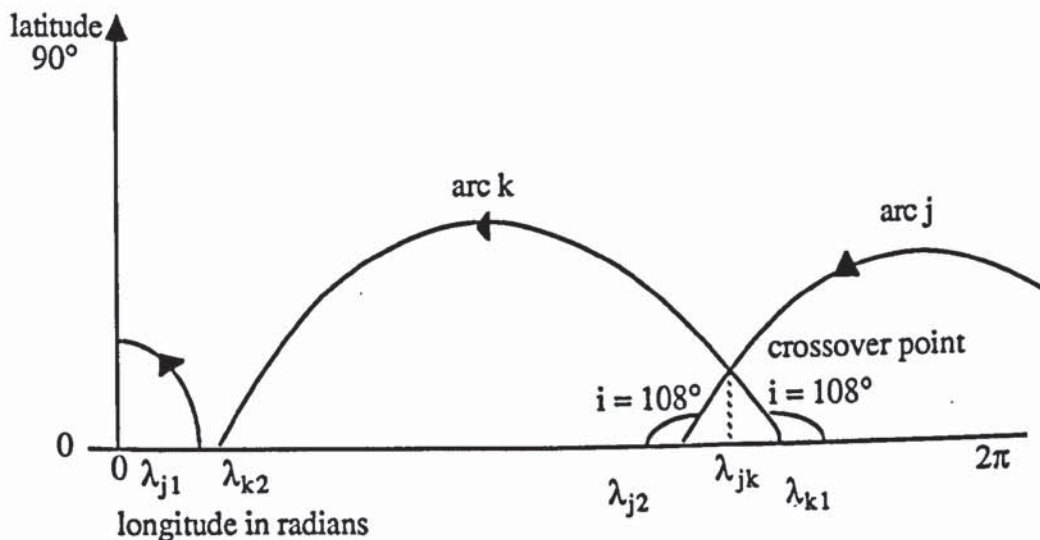
6. The program CROSS

The method adopted to determine the position of the crossover points is a geometrical one due to Rowlands [6]. The processing is executed in the FORTRAN program CROSS which also calculates the crossover height differences at these points for any given ephemeris.

Initially, the ephemeris is read in from the file EPH.DAT, an output file from the orbit generation program. This is used to determine the equator crossings of the orbit, by checking for a change in sign of the z-coordinate of position. The two points either side of the equator, are then used to linearly interpolate the time and longitude of the actual crossing. The equator crossings divide the ephemeris into half revolution arcs, the start and end of each arc being identified by one crossing. Since northern hemisphere arcs can only intersect with other northern hemisphere arcs and likewise for the southern hemisphere, data from each hemisphere is processed separately.

Subsequent processing involves comparing every arc from one hemisphere with every other arc from the same hemisphere. Using the longitude of the equator crossings of two arcs it is possible to approximate the longitude of the crossover point between them (see Figure (1)).

Figure 1: Schematic description of crossover point in northern hemisphere



The approximate longitude, λ_{jk} , of the crossover point between arcs j and k can quite easily be found from the geometry, as shown in Figure 1. However, care is needed in deriving a mathematical formula for λ_{jk} in terms of λ_{j1} , λ_{j2} , λ_{k1} , λ_{k2} due to the discontinuity at the Greenwich Meridian. Simply averaging all four values as Rowlands does, could give anomalous results. In practice, it turns out that there are six different situations which can arise, giving rise to six different mathematical formulae for a single crossover between any two arcs. For a double crossover (which can arise because $\lambda_{k1} - \lambda_{k2} > 180^\circ$) four extra conditions could arise. All need to be checked.

Once calculated, the approximate longitude, λ_{jk} , is compared to a time-longitude map derived from the ephemeris, to find the approximate times t_j and t_k of the crossover on arcs j and k , respectively. The position and velocity at t_j (respectively t_k) are then used to calculate λ_j (respectively λ_k), a more accurate longitude of the crossover point, ϕ_j (respectively ϕ_k), the latitude of the crossover and $\partial\lambda_j/\partial\underline{x}$, $\partial\phi_j/\partial\underline{x}$, (respectively $\partial\lambda_k/\partial\underline{x}$ and $\partial\phi_k/\partial\underline{x}$).

These values are used to differentially correct the times t_j and t_k to give more accurate values. The procedure depends on the fact that the latitude and longitude of the crossover point is the same on each arc.

Assume that t'_j , t'_k are the corrected crossover times on the two arcs. These give rise to the more accurate values of latitude and longitude, ϕ'_j , ϕ'_k and λ'_j , λ'_k respectively. Then

$$\phi'_j = \phi'_k \quad (3)$$

and
$$\lambda'_j = \lambda'_k \quad (4)$$

where
$$\phi'_j = \phi_j - dt_j \left(\frac{d\phi_j}{dt} \right) \quad (5)$$

and
$$dt_j = t_j - t'_j.$$

Similar equations to (5) exist for ϕ'_k , λ'_j , λ'_k . On substituting these into (3) and (4)

$$\lambda_j - dt_j \left(\frac{d\lambda_j}{dt} \right) = \lambda_k - dt_k \left(\frac{d\lambda_k}{dt} \right), \quad (6)$$

$$\phi_j - dt_j \left(\frac{d\phi_j}{dt} \right) = \phi_k - dt_k \left(\frac{d\phi_k}{dt} \right), \quad (7)$$

the solution of which is given by

$$\begin{pmatrix} dt_j \\ dt_k \end{pmatrix} = \begin{pmatrix} d\lambda_j/dt & -d\lambda_k/dt \\ d\phi_j/dt & -d\phi_k/dt \end{pmatrix}^{-1} \begin{pmatrix} \lambda_j - \lambda_k \\ \phi_j - \phi_k \end{pmatrix} \quad (8)$$

Then $t'_j = t_j - dt_j$ and $t'_k = t_k - dt_k$.

New values of λ'_j , λ'_k , etc. are found by interpolating within the ephemeris at t'_j and t'_k , respectively. The procedure is repeated until some prescribed tolerance level on $|dt_j|$ and $|dt_k|$ is attained.

Finally, the crossover times t_j , t_k are used to interpolate, either linearly or cubically, in the GDR files to find the pseudo-altimeter height at each point. The observed crossover height difference is then the difference between the two pseudo-altimeter measurements.

A note on running CROSS: There is an input file to CROSS called TAPE.DAT. This contains the information about how to interpolate within the altimeter GDR's as well as which GDR file is the first to be used as input. These parameters should be checked prior to running CROSS, which is most conveniently performed as a background job due to its processing time.

7. Running the programs

- 1) Obtain appropriate state-vector named START.DAT.
- 2) Edit REDIN.DAT, ORBIT.DAT accordingly.
- 3) Run OBSSEL to select laser observations for required period.
- 4) Run NØ6Q to obtain planetary polynomial data for same.
- 5) Edit REDIN.DAT to accept OBS.DAT the output from OBSSEL.
- 6) Run PASS, to sample the laser data, output in OBSERV.DAT.
- 7) Edit REDIN.DAT to accept OBSERV.DAT.
- 8) Check for first altimeter GDR file to be read.
- 9) Run CONVERT ensuring that enough GDR files are input.
- 10) Run CROSS to obtain crossover data output to HDIFF.DAT (note this needs ephemeris data from a previous run of the orbit generator).
- 11) Run SORTS incorporating any/all data types (laser data should always be incorporated).
- 12) Run orbit generator.
- 13) Run data reduction program solving for certain parameters, output to SOLNCP.DAT.
- 14) Rename SOLNCP.DAT to START.DAT.
- 15) Go to 12).
- 16) Repeat steps 12) to 15) until convergence is attained.

References

- [1] Sinclair, A.T. and Appleby, G.M. SATAN-Programs for the determination and analysis of satellite orbits from SLR data. SLR Tech. Note 9, RGO, Herstmonceaux, 1986.
- [2] Geophysical Data Record (GDR) Users Handbook. NASA document 622-97, Revision-A, 15 Sept., 1980.
- [3] Bomford, G. Geodesy (4th Edition), Clarendon Press, Oxford, 1980.
- [4] Lerch, F.J., Putney, B.H., Wagner, C.A. and Klosko, S.M. Goddard Earth Models for Oceanographic Applications (GEM-10B and 10C). Marine Geodesy, Vol.5, No. 2, pp 145-187, 1981.
- [5] Hyde, J.H. Calculation of the Geoid. Final year project, Aston University, 1986.
- [6] Rowlands, D. The Adjustment of SEASAT Altimeter Data on a Global Basis for Geoid and Sea Surface Topography Determinations. OSU Report No. 325, Columbus, Ohio, 1981.